Insight into a fossil plate interface: unraveling the P-T-t-d evolution of the Akeyasi metamorphic belt in southwest Tianshan (NW China).

Léa Bayet

Dissertation submitted to obtain the academic degree of

Doktor der Naturwissenschaften (Dr. rer. nat.)

To the department of Earth Sciences of

Freie Universität Berlin

Berlin, June 2018

Reviewers:

1. Erster Gutacher: Prof. Dr. Timm John

Institut für Geologische Wissenschaften
Freie Universität Berlin
Malteserstrasse 74-100, Haus N
23349 Berlin, Germany

2. Zweiter Gutacher: Prof. Dr. Philippe Agard

Sorbonne Université, CNRS-INSU
Institute des Sciences de la Terre à Paris (ISTeP)
4 place Jussieu (Tour 46-00 3E)
75252 Paris, France

Date of defense : 18.07.2018

Erklärung

Hiermit Erkläre ich, Léa Bayet, dass die vorliegende Arbeit ausschließlich auf Grundlage der angebenen Hilfsmittel selbständig von mir verfasst wurde. Alle Stellen der Arbeit die aus anderen Werken dem Wortlaut oder dem Sinne nach entnommen sind, wurden eindeutig unter Angabe der Quellen als Entlehhung gekennzeichnet. Diese Arbeit ist nicht in einem früheren Promotionsverfahren engereicht worden.

Berlin, den 04.06.2018

Léa Bayet

Abstract

Subduction zones represent important tectonic boundaries and are the scene of devastating geohazards. In subduction zones, most of the fluid and material transfer, deformation, and earthquakes occur at the plate interface. Although the geometry of the plate interface is partly constraint by geophysical data, the fate of deeply buried material and the processes occurring at depth remain uncertain. In particular, the deep burial of large volumes of sediments poses a conundrum on the role of buoyancy, coupling-decoupling transitions, and their origin. Indeed, material incorporated in a subduction zone may derive from various sources, depending for instance on the subduction type (accretion versus erosion), the nature of the trench infill, and the formation of mélanges (tectonic or sedimentary). Fossil subduction zones provide key information on processes occurring at depth, recorded in rocks through their burial and exhumation.

The Akezayi metamorphic complex (AMC) or southern Tianshan metamorphic belt (Tianshan, northwest China) represents such a fossil plate interface. Controversial models depicted the AMC as resulting from a tectonic mélange, with juxtaposition of rocks from various depths or as consisting of two units: the high-pressure (H*P*) and the ultra-high-pressure (UH*P*) units. The AMC consists of a greenschist-facies unit in the north and south and a H*P* to UH*P* (H*P*-UH*P*) unit in its central part. The greenschist-facies unit consist of metasediments typically composed of green amphibole, chlorite, and albite ± white mica. The H*P*-UH*P* unit represents a ~4-5 km volcano-clastic sequence. Lithology in the H*P*-UH*P* unit is characterized by an intimate interlayering of micaschists and mafic rocks. Rock composition varies between ‘pure’ micaschist and ‘pure’ mafic components. The detailed mapping of the lithology highlighted a global compositional gradient from more pelitic in the north to more psammitic and mafic in the south.

The H*P*-UH*P* sequence exhibits pervasive deformation with the identification of a minimum of five stages. The first, only visible on the microscopic level, is represented by a rotative schistosity of quartz inclusion in garnets, and is attributed to burial. This stage is followed by a pervasive schistosity, observed at various scales (from cm- to km-scale), subsequently reworked by crenulation schistosity and folding. Pervasive shearing of both, the schistosity and crenulation schistosity, occurred later during exhumation, as indicated by the pervasive glaucophane lineation. Some of the shear zones reach a km-scale extent and structurally divide the H*P*-UH*P* unit in five sub-units. Finally, C’ structures define the latest observed deformation stage and formed during greenschist-facies conditions.

The determination of the peak pressure-temperature (*P*-*T*) conditions was conducted in a systematic way, on spatially distributed samples using robust thermobarometric methods. The peak temperature was estimated by applying the Raman spectroscopy on carbonaceous material

(RSCM; T_C) and Zr in rutile thermometry (T_{Zr}). Results yield a homogeneous distribution of peak temperature combining both T_{Zr} and T_C, with an average of 538 ± 12 °C for the H*P*-UH*P* unit. Minimum peak pressure was estimated using quartz in garnet (QuiG) and phengite barometry. Coesite identified in several samples indicates a minimum pressure of 2.7 GPa for a given temperature of ~540 °C. Combining coesite occurrence, QuiG and phengite barometry revealed a rather coherent pressure distribution of 2.52 ± 0.25 GPa, i.e., widespread UH*P* metamorphic conditions.

A review of the previous metamorphism age estimates revealed peak condition ages of 320.5 ± 6.6 Ma (2σ) using garnet Lu-Hf and Sm-Nd, zircon and rutile U-Pb, and Rb-Sr white mica dating. The present study yielded similar ages with three well-constrained isochrons giving a date of 321.6 ± 1.9 Ma (2σ). A fourth sample yielded an age of 315.9 ± 1.8 Ma, still in agreement with the peak metamorphism estimates within error. Post-peak conditions have been estimated to around 311 Ma, mainly based on Rb-Sr, Ar-Ar and K-Ar white mica dating. We thus interpret the age of 310.0 ± 2.5 Ma of the last sample as reflecting post-peak conditions, which is supported by the presence of retrograde paragonite finely interlayered with phengite.

Combining field data, peak *P*-*T* estimates, and Rb-Sr dating lead to the conception of a new geodynamic model for the AMC. We suggest that the volcano-clastic rocks derive from the sedimentary cover of the oceanic plate, parts of an eroded accretionary prism and trench infill containing ashes from arc volcanism. The material was buried, detached, and stacked, near greenschist-facies levels and at H*P*-UH*P* conditions. The deeper stacking occurred in several successive slices thrusted on top of each other at a depth of ~80km (2.5-2.7 GPa), previously inferred as a decoupling-coupling transition. Although buoyant and given that a duration of a few million years was estimated for such a stacking, this volcano-clastic sequence remained relatively cold (540 °C) and did not undergo diapirism. The temperatures were likely shielded by the presence of a mantle wedge cold nose, intensive fluid circulation and/or a thickened overriding plate. We suggest that diapirs most likely form deeper down and/or farther away from the plate interface.

This stacking formed a coherent and single unit, as attested by the rather homogeneous peak *P*-*T*-*t* conditions between the structural sub-units. The sequence was subsequently detached from the upper plate and exhumed to blueschist-facies conditions, where thrusts were reactivated in major shear zones with a normal movement. The thickness of each slice (< 1km), and the shearing and thinning of the ~4-5 km sequence during exhumation may reflect a thin plate interface thickness, as suggested by geophysical data (~2-5 km).

The pillow basalt unit, located in the southernmost part of the belt, was detached at last, together with the rest of the sequence at UH*P* conditions, or during exhumation of sequence at H*P* conditions. The present-day geometry reveals a dome-like structure of the greenschist-facies unit, suggesting its exhumation prior to or simultaneous with the exhumation of the H*P*-UH*P* unit.

Zusammenfassung

Subduktionszonen stellen wichtige tektonische Grenzen dar und sind Schauplätze verheerender Naturkatastrophen. In den Subduktionszonen treten die meisten Fluid- und Materialtransfers, Deformationen und Erdbeben entlang der Plattengrenzfläche auf. Obwohl die Geometrie der Plattengrenzfläche durch geophysikalische Daten teilweise bekannt ist, sind die Entwicklung tief subduzierter Gesteine und die zugrunde liegenden Prozesse kaum erforscht. Insbesondere die tiefe Subduktion großer Sedimentvolumina wirft Fragen nach den Rollen von Auftrieb, Kopplungs-Entkopplungs-Übergängen und ihrer Ursprünge auf. Tatsächlich kann das Material, das in eine Subduktionszone eingebracht wird, aus verschiedenen Quellen stammen - abhängig vom Subduktionstyp (Akkretion versus Erosion), der Art der Tiefseegrabensedimente und der Bildung von Mélangen (tektonisch oder sedimentär). Fossile Subduktionszonen liefern wichtige Informationen über Vorgänge in der Tiefe, welche in Gesteinen während der Versenkung und Exhumierung aufgezeichnet wurden.

Der Akezayi Metamorphic Complex (AMC) oder südliche Tianshan Metamorphic Belt (Tianshan, Nordwestchina) repräsentiert eine solche fossile Plattengrenze. Umstrittene Modelle interpretieren den AMC als das Ergebnis einer tektonischen Mélange, in der Gesteine aus verschiedenen Tiefen vermengt wurden, oder welche aus zwei Einheiten besteht: einer Hochdruck- (H*P*) und einer Ultrahochdruck- (UH*P*) -Einheit. Der AMC besteht aus einer Grünschiefer-faziellen Einheit im Norden und Süden, und einer H*P*-UH*P*-Einheit (H*P*-UH*P*) im zentralen Teil. Die Grünschiefer-fazielle Einheit besteht aus Metasedimenten, die typischerweise grünen Amphibol, Chlorit und Albit ± weißem Glimmer führen. Die H*P*-UH*P*-Einheit ist eine ~ 4-5 km vulkanisch-klastische Abfolge. Die Lithologie in der H*P*-UH*P*-Einheit ist durch eine Zwischenschicht von Glimmerschiefern und mafischen Gesteinen charakterisiert. Die Gesteinszusammensetzung variiert zwischen rein pelitischen und rein mafischen Komponenten. Die detaillierte Kartierung der Lithologie offenbarte einen globalen Zusammensetzungsgradienten von pelitisch im Norden zu psamititisch und mafisch im Süden.

Die Sequenz der H*P*-UH*P*-Einheit zeugt von einer durchdringenden Deformation, welche in mindestens fünf Stufen unterteilt werden kann. Die erste, welche nur mikroskopisch sichtbar ist, wird durch eine rotierende Schieferung von Quarzeinschlüssen in Granaten dargestellt und wird der Versenkung zugeschrieben. Diesem Stadium folgte eine durchdringende Schieferung, die auf verschiedenen Skalen (von cm- bis km-Skala) beobachtet wird und anschließend durch Krenulations-Schieferung und Faltung überprägt wird. Die durchdringende Scherung von beidem, der Schieferung und der Krenulations-Schieferung, erfolgte später während der Exhumierung wie durchdringende Glaukophan-Lineationen anzeigen. Einige der Scherzonen erreichen eine

Ausdehnung im km-Bereich und teilen die H*P*-UH*P*-Einheit strukturell in fünf Untereinheiten. Schließlich zeigen C'-Strukturen das letzte beobachtbare Deformationsstadium an, welches unter Grünschiefer-faziellen Bedingungen ablief.

Die Bestimmung der Peak-Drücke (*P*) und -Temperaturen (*T*) wurde systematisch an Hand von räumlich verteilten Proben mittels robusten thermobarometrischen Methoden durchgeführt. Die Peak-Temperaturen wurde durch Raman-Spektroskopie an kohlenstoffhaltigem Material (RSCM; T_{C}) und Zr in Rutil-Thermometrie (T_{Zr}) bestimmt. Die Ergebnisse zeigen eine homogene Verteilung der Peak-Temperaturen mit durchschnittlich 538 ± 12 ° C für die H*P*-UH*P*-Einheit aus der Kombination von T_{Zr} und T_{C} an. Der minimale Spitzendruck wurde unter Verwendung von Quarz in Granat- (QuiG) und Phengit-Barometrie geschätzt. Coesit, der in mehreren Proben identifiziert wurde, zeigt einen Mindestdruck von 2,7 GPa für die gegebene Temperatur von ca. 540 ° C an. Durch die Kombination des Vorhandenseins von Coesit, QuiG- und Phengit-Barometer konnte eine ziemlich kohärente Druckverteilung von 2.52 ± 0.25 GPa bestimmt werden, d.h. UH*P*-metamorphe Bedingungen.

Eine Überprüfung früherer Altersschätzungen ergab ein Alter von 320,5 ± 6,6 Ma (2σ) für die metamorphen Peak-Bedingungen unter Verwendung von Granat Lu-Hf- und Sm-Nd-, Zircon und Rutil U-Pb-, und Rb-Sr-Hellglimmer-Datierungen. Die vorliegende Studie erzeugte ähnliche Daten mit drei gut definierten Isochronen, welche ein Alter von 321,6 ± 1,9 Ma (2σ) definieren. Eine vierte Probe ergab ein Datum von 315,9 ± 1,8 Ma, welches innerhalb des Fehlers ebenfalls mit den Schätzungen des Alters der metamorphosen Peak-Bedingungen übereinstimmen. Post-Peak-Bedingungen wurden in älteren Studien auf etwa 311 Ma geschätzt und die Alter basieren hauptsächlich auf Rb-Sr-, Ar-Ar- und K-Ar-Weißglimmer-Datierungen. Wir ordnen somit das Alter von 310,0 ± 2,5 Ma der letzten Probe den Post-Peak-Bedingungen zu, was durch die Anwesenheit von retrogradem Paragonit, welcher mit Phengit verwachsen ist, unterstützt wird.

Die Kombination aus Geländedaten, Peak-*P*-*T*-Abschätzungen und Rb-Sr-Datierungen führte zur Konzeption eines neuen geodynamischen Modells für den AMC. Wir vermuten, dass die vulkanisch-klastischen Gesteine von der sedimentären Bedeckung der ozeanischen Platte, Teilen eines erodierten Akkretionsprismas, und der Tiefseegrabenfüllung, welche Asche vom Bogenvulkanismus enthält, stammen. Das Material wurde in der Folge subduziert, abgeschert und gestapelt, jeweils unter Grünschiefer-faziellen- und H*P*-UH*P*-Bedingungen. Die tiefere Stapelung erfolgte durch die Überschiebung mehrerer aufeinanderfolgenden Schollen in einer Tiefe von ca. 80 km (2,5-2,7 GPa), welche zuvor als Entkopplungs-Kopplungs-Übergang gedeutet wurde. Trotz Auftriebs und der Tatsache, dass für eine solche Stapelung eine Dauer von einigen Millionen Jahren angenommen wird, blieb diese vulkanisch-klastische Abfolge relativ kalt (540 ° C) und erfuhr keinen Diapirismus. Die relativ geringen Temperaturen wurden wahrscheinlich durch das Vorhandensein einer „kalten Nase“ des Mantelkeils, einer intensiven Fluidzirkulation und/ oder einer verdickten, hängenden Platte begünstigt. Wir vermuten, dass Diapire sich wahrscheinlich tiefer und/ oder weiter von der Plattengrenzfläche entfernt bilden.

Die gestapelten Schollen bildeten eine kohärente und einzelne Einheit während der Subduktion, was durch die homogenen Peak-*P*-*T*-*t* Bedingungen in den strukturellen Untereinheiten gestützt wird. Die Sequenz wurde anschließend von der hängenden Platte gelöst und bis in blauschiefer-fazielle Tiefen exhumiert, wo Überschiebungen in großen Scherzonen mit einer normalen Bewegungsrichtung reaktiviert wurden. Die Mächtigkeit jeder tektonischen Scholle (<1km), und das Scheren und die Ausdünnung der 4-5 km mächtigen Sequenz während der Exhumierung kann eine dünne Plattengrenzflächenmächtigkeit widerspiegeln, wie auch durch geophysikalische Daten (*ca.* 2-5 km) angedeutet wurde.

Die Kissenbasalteinheit, die sich im südlichsten Teil des Gürtels befindet, wurde schließlich zusammen mit dem Rest der Sequenz unter UH*P*-Bedingungen oder während der Exhumierung der Sequenz bei H*P* Bedingungen abgeschert. Die heutige Geometrie zeigt eine domartige Struktur der Grünschiefer-faziellen Einheit, was auf eine Exhumierung vor oder zusammen mit der H*P*-UH*P*-Einheit hindeutet.

To my grandmother, who raised me and thanks to whom I became the person I am today. You are not there today for this important achievement, but you are and will always be in my heart and in my thoughts.

Table of Contents

Chapter 1

Introduction

1.1 Subduction zones and plate interface

1.1.1 Plate tectonics and subduction

The first concept of plate tectonics was introduced by Alfred Wegener (1912), with the theory of the continental drift: “Die Entstehung der Kontinente und Ozeane” (Wegener, 1929). The definition and principles of plate tectonics were later refined during the 60’s, with the description of plates and plate boundaries (Le Pichon, 1968; McKenzie and Parker, 1967). Plates are considered as rigid blocks undergoing plastic deformation, while plate boundaries define elastic deformable areas (Dickinson, 1974; Le Pichon, 1968; McKenzie, 1972; McKenzie and Parker, 1967; Wilson, 1965).

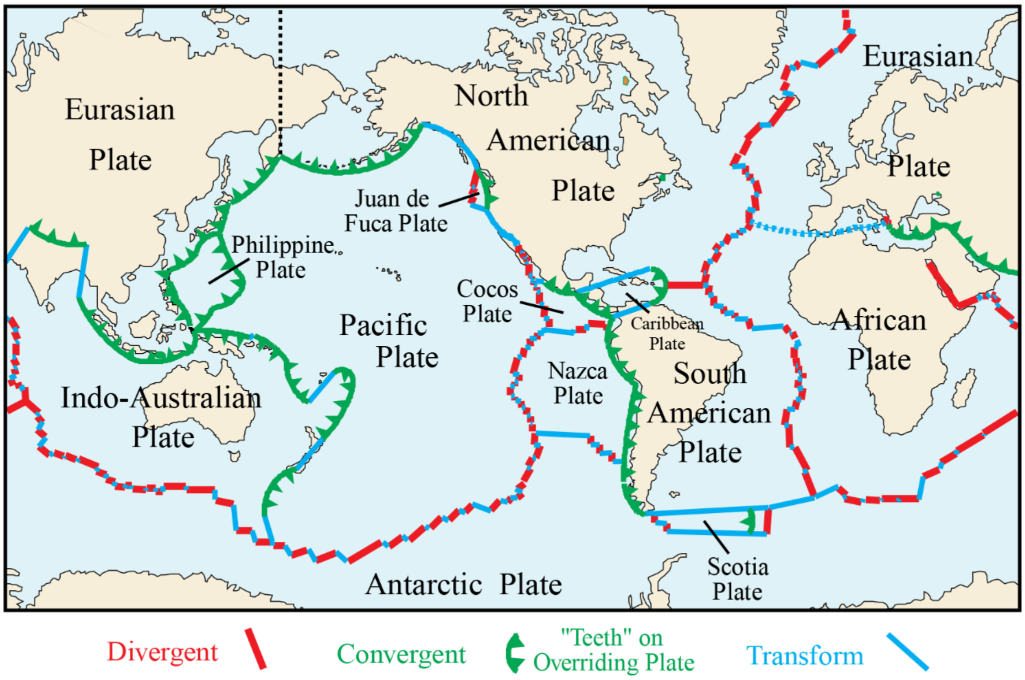

Figure 1.1: Map of plate tectonics, with the representation of the different plates and divergent (red), convergent (green) and transform (blue) plate boundaries. Subduction zone belong to the convergent plate boundaries. Image: USGS.

Plate boundaries are classified in three main types:

1) Transform boundaries (Fig. 1.1, blue lines), where two plates slide along each other, at the oceanic level (e.g., the Clipperton Fault; Gallo et al., 1986) and at the intra-continental faults (e.g., San Andreas Fault; Okubo and Aki, 1987; Wallace, 1990);

2) Divergent boundaries (Fig. 1.1, red lines), representing areas of extension and production of oceanic lithosphere at the oceanic ridges (e.g., Atlantic ridge; Cannat et al., 1995; Frey et al.,

1974; Vine and Matthews, 1963; White, 1984) and continental rifts (e.g., East-African rift; Chorowicz, 2005; Fairhead and Stuart., 1982; Jestin et al., 1994);

3) Convergent plate boundaries (Fig. 1.1, green lines), with areas of continental collision, e.g., the Alps (e.g., Agard and Lemoine, 2005; Coward and Dietrich, 1989; Dal Piaz, 2001; Handy et al., 2010) or in the Himalaya (e.g., Molnar and Tapponnier, 1977, 1975a), and subduction zones where material created at oceanic ridges is destroyed, as along the South American west coast (e.g., Oncken et al., 2006).

Subduction zones consist of an oceanic lower plate sinking underneath an oceanic or continental upper plate. Wadati (1935) and Benioff (1949) first characterized the geometry of the downgoing plate (or slab) as a planar zone, based on the geometry of earthquake seismicity. Over the past decades, geophysical techniques improved in tomography, seismic reflexion, and seismic refraction permitted to increase the resolution of the slab geometry (e.g., Abers, 2005; Abers et al., 2006; Bostock et al., 2002; Calahorrano et al., 2008; Calvert, 2004; Ferris et al., 2003; Peacock et al., 2011; Yuan et al., 2000).

Subduction zones are of key importance for the Earth system, as they play a major role in geochemical cycles, plate tectonics, and geohazards such as earthquakes, tsunamis, or volcanism. These areas represent areas of efficient recycling of material and fluids between Earth's surface and interior (e.g., Hacker, 2008; Hacker et al., 2003a, 2003b; John et al., 2012; Philippot, 1993; Scambelluri et al., 2004; Tatsumi, 1989; Zack and John, 2007). Although these phenomena happen at large scales (hundreds of kilometers), recycling, and processes triggering geohazards, such as earthquakes and volcanism, mainly occur in a narrow area of subduction zones: the plate interface.

1.1.2 Plate Interface

The plate interface, often referred to as a subduction channel, represents the area between the lower and upper plate, where most of the deformation, exchange of fluids and materials occurs (e.g., Agard et al., 2018; Bebout and Penniston-Dorland, 2016; Guillot et al., 2009; Hacker et al., 2003a; Kirby, 1983; Scambelluri and Philippot, 2001; Wada et al., 2008; Fig. 1.2a, b). The interface is characterized by an area of slow seismic velocity above the downgoing plate (Abers, 2005, 2000; Yuan et al., 2000). Although the characterization of the plate interface geometry improved with time, its thickness remains debated. However, Many studies agree that the average thickness is limited around < 10 km (e.g., Calahorrano et al., 2008; Calvert, 2004; Chuang et al., 2017; Cloos and Shreve, 1996; Rowe et al., 2013; St. Clair et al., 2016; Toda et al., 2008) and receiver function images advocate for a more precise thickness estimated around 2-5 km (Abers, 2005; Fig. 1.2c).

Friction between the upper and the lower plate induces important strain accumulation concentrated at the plate interface, with numerical modelling and geophysical data interpreting the plate interface itself a large-scale shear zone (e.g., Cloos and Shreve, 1996; Raimbourg et al., 2007; Rowe et al., 2013; von Huene et al., 2004; Wakabayashi, 2015). At the plate interface, shearing and friction behavior compete with mechanical lubrication induced by buoyant sediments entering the subduction zone and serpentine along the interface (e.g., Cloos and Shreve, 1996; England and Holland, 1979; Guillot et al., 2001; Tan et al., 2012). This competition results in alternating phases of coupling and decoupling between the lower and the upper plate (e.g., Agard et al., 2018; Duarte et al., 2013; Fig. 1.2d).

At shallow depth, the upper and lower plates are seismically coupled with the locking of some areas, for instance due to the entering of seamounts in the subduction zone (Kato and Hirasawa, 1997; Scholz, 1998; Scholz and Small, 1997; Tichelaar and Ruff, 1993). These lock zones, previously thought to occur all along the plate interface, have been redefined as locked patches, involving coupling of several small areas, while the rest of the interface remains decoupled (Kaneko et al., 2000; Métois et al., 2016, 2012; Moreno et al., 2010; Schurr et al., 2014; Fig. 1.2e).

During the plates locking, the accumulated energy is fully to partially released during an earthquake rupture, with brittle deformation of the surrounding rock, and the formation of tectonic breccias (e.g., Angiboust et al., 2012a; Locatelli et al., 2018; Sibson, 1986) and/or pseudotachylites (Allen, 2005; Austrheim and Andersen, 2004; Ferré et al., 2015; John et al., 2009; John and Schenk, 2006; Thielmann et al., 2015).

At depth between ca. 35 km and 70-80 km, the descending slab and overriding plate are mechanically decoupled and move independently from each other (Agard et al., 2018; Aygül and Oberhänsli, 2017; Pacheko et al., 1993; Syracuse et al., 2010; Wada and Wang, 2009). From ca. 80 km depth and beyond, inferred as the maximum depth of slab–mantle decoupling, the lower and upper plate become fully coupled, as shown by numerical models, geophysics and recovered exhumed rocks from these depth (e.g., Abers et al., 2017, 2006; Agard et al., 2018; Syracuse et al., 2010; Wada and Wang, 2009). The coupling/decoupling transition depths and impacts on subduction zone processes are discussed later in this chapter.

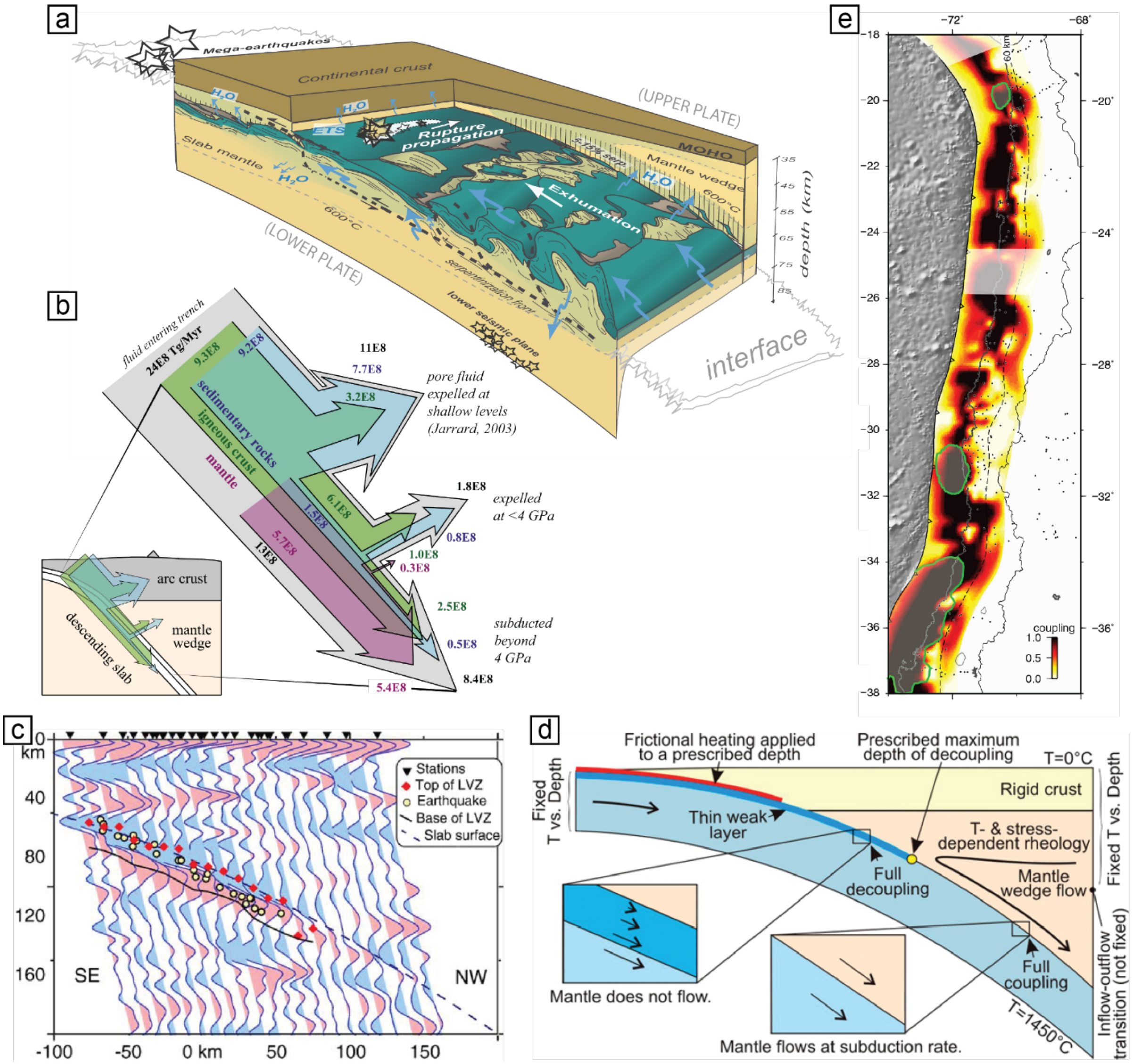

Figure 1.2: **(a)** Sketch of a subduction zone (from ~30 to ~100 km depth) showing an inferred geometry of the plate interface at depth (grey lines). Deformation at the plate interface is marked by thrust sheets, slicing (black doted lines), and shearing (black arrows). Earthquakes (black stars) rupture as mega-earthquakes at shallow depth (~30 km) and at intermediate depth (45-50 km) along the plate interface, and at larger depth (80-100 km) in a lower seismic plane of the slab. Fluid release is illustrated on this figure (blue arrows), showing lateral, and upward fluid circulation along the plate interface and in the overriding plate mantle wedge. Modified after Angiboust et al. (2012). **(b)** Sketch of the global H_2O flux in subduction zones for oceanic lithosphere. Flux magnitudes are represented by the widths of arrows. After Hacker, 2008. **(c)** Seimic images from receiver function showing a low velocity zone (LVZ) corresponding to the top of the subducting plate (Ferris et al., 2003, Abers et al., 2006). **(d)** Geodynamic model showing the alternating coupling/ decoupling transitions along the plate interface (Wada and Wang, 2009). **(e)** Best coupling distribution in the Andes, with rupture zones of three major earthquakes (green ellipses). Note that coupling zones are distributed in patches, instead of a fully coupled subduction plate interface (Métois et al., 2016).

1.2 Subduction processes

1.2.1 Numerical models vs natural laboratory

Given that no direct access to the plate interface exists, one must rely on numerical modelling, geophysical data, and observations from natural laboratories where exhumation has occurred. Fossil subduction zones give access to information on detailed processes happening at small time and space scales while numerical models and geophysical data provide a bigger picture and rough information at the larger scale.

Numerical models can predict parameters such as the depth of some mineral reactions, rheology, and the depth of the seismic zone, based on the thermal regime (Agard and Vitale-Brovarone, 2013; Arcay et al., 2005; Hyndman and Wang, 1993; Kincaid and Sacks, 1997; Peacock and Hyndman, 1999; van Keken et al., 2008). Mineral reactions, and thus water release, highly depend on temperature and pressure (e.g., Bebout, 2007; Connolly, 1990; Hacker et al., 2003b; Holland and Powell, 1998; Thompson, 1955; Whitney, 1975). As later explained in this chapter, mineral reactions are key factors for fluid-related processes, rock rheology (density), and earthquake inception. The rheological behavior of subducted rocks highly depends on temperature, with a brittle regime at low temperature and a ductile regime at high temperature varying according to a given thermal state of the subducting slab (e.g., Arcay et al., 2005; Burov, 2011; Byerlee, 1993; Kirby, 1983). Finally, the mechanisms influencing coupling and decoupling processes and their transition depths at the plate interface can be characterized using numerical modelling (Syracuse et al., 2010; Wada and Wang, 2009).

Natural laboratories represent key areas to observe processes in both active and passive subduction zones. On the one hand, active subduction zone investigation rely mainly on geophysical data providing information such as the geometry and some physical parameters of subduction zones, using tomography, seismic images and relocalisation of earthquake hypocenters (e.g., Abers, 2005; Abers et al., 2006; Bostock et al., 2002; Calvert, 2004; Ferris et al., 2003; Igarashi et al., 2001).

On the other hand, reconstructing the tectono-metamorphic evolution of fossil subduction zones give precious information on detailed processes occurring at depth, depending on the rock record. Exhumed rocks record conditions they experienced in the subduction zone including: 1) pressure, which can be converted to depth depending on the rock density, 2) temperature giving information on the thermal state of the plate interface at some depths, 3) timing of burial, stacking and exhumation, 4) fluid-rock interactions and their effect on the geochemical cycle and mineral transformation, and 5) structures observed in the field to understand the different deformation stages and states at the plate interace. Furthermore, some subduction zones comprise tectonic breccias or pseudotachylites, which provide information on earthquake genesis (Allen, 2005; Angiboust et al., 2012a; John et al., 2009; John and Schenk, 2006; Locatelli et al., 2018; Rowe et al., 2005; Sibson, 1986; Thielmann et al., 2015).

1.2.2 Impact of metamorphism and fluid-rock interactions on subduction processes

Changes in temperature and pressure with depth induce a change of the mineral composition, which affects the rheology of the slab and surrounding rocks. During metamorphism from greenschist-, to blueschist-, and eclogite-facies conditions, rock properties such as viscosity, density, and rheology are modified (Bebout, 2007; Connolly and Kerrick, 2002; Hacker et al., 2003a; Kirby et al., 1996; Poli and Schmidt, 2002; Yuan et al., 2000). Eclogitization resulting in the densification of the slab is observed in tomography where the slab can no longer be distinguished from the surrounding mantle, as it acquires a similar density (e.g., Bjørnerud, 2002; Hacker et al., 2003a; Halpaap et al., 2018; Lloyd et al., 2011; Yuan et al., 2000).

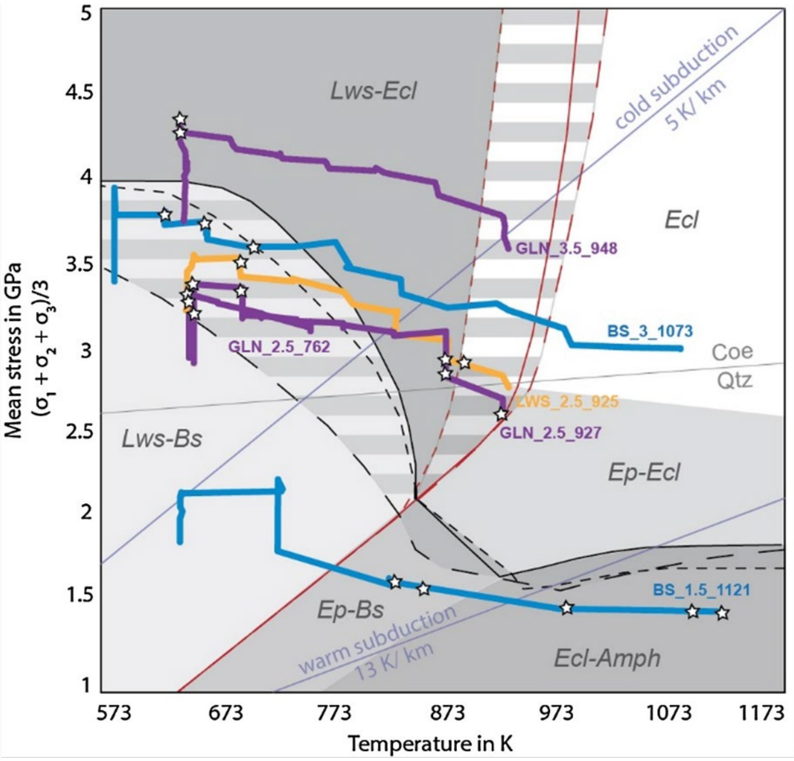

Figure 1.3: Diagram of mean stress versus temperature, showing the corresponding P-T pseudosection. Stars represent acoustic emissions (AEs), assimilated to small earthquakes. The Amp- and the Lws-out reactions (Gorczyk et al., 2007; Gerya et al., 2008) are shown on this figure. Note that the second high-temperature cluster of AEs correlates with the breakdown of Lws. Modified from Incel et al. (2017).

Fluid release is associated to mineral reactions occurring along the plate interface and in the mantle, some of which trigger earthquakes due to mineral breakdown (e.g., Ferrand et al., 2017;

Green, 2007; Hacker et al., 2003b; Hyndman and Peacock, 2003; Incel et al., 2017; Peacock, 2001, Fig. 1.3). One of the fluid related mechanisms involved in earthquake genesis is the fluid overpressure, as fluid pore pressure reaches near lithostatic values (Audet et al., 2009; Peacock et al., 2011). The release of fluid in the overriding plate is a key parameter for the formation of magmas in the mantle wedge, as this will enhance melting (Arcay et al., 2005; Bebout and Penniston-Dorland, 2016; Hacker, 2008; Keken et al., 2002; Peacock, 1990; Tatsumi, 1989, 1986; van Keken et al., 2011).

Fluid-rock interaction is of importance for the geochemical cycle, with the mobilization of various chemical species during mineral reactions (e.g., Hermann et al., 2006; John et al., 2011b; Scambelluri et al., 2008; Scambelluri and Philippot, 2001) leading to the formation of new minerals and/or a free fluid phase (e.g., John et al., 2008; Zack and John, 2007). Indeed, several hydrous phases, such as lawsonite, amphibole, antigorite and white micas represent water and various species are carriers which will liberate this water and some chemical species during their breakdown, which will later be involved in fluid transfer from crust to mantle (e.g., John et al., 2011b; Pawley and Holloway, 1993; Philippot, 1993; Poli and Schmidt, 2002, 1995; Scambelluri et al., 2004).

1.2.3 Material recycling

1.2.3.1 Subduction input: material origin

The origin of the material entering the subduction zone influences the burial and exhumation mechanisms along with other processes occurring at depth.The material conveyed in the subduction zone derives both from the lower and the upper plate (Guillot et al., 2009; Karig and Sharman, 1975; Vannucchi et al., 2012). On the one hand, the lower plate provides oceanic material (e.g., basalts, gabbros), sedimentary material from the oceanic cover, and potentially seamounts formed on the ocean floor (John et al., 2010; Kopp et al., 2006; Lallemand and Le Pichon, 1987; Oxburgh and Parmentier, 1977; Scholz and Small, 1997). On the other hand, the material deriving from the upper plate varies according to parameters such as weathering, transportation of ashes from volcanic arcs, and subduction type (erosive versus accretionary). Erosion and weathering of mountain ranges produce sedimentary and detrital material, possibly transferred to the trench (e.g., Huang et al., 1992; VanLaningham et al., 2006). Ashes generated during the formation of arc volcanism can be transported over long distances (e.g., Kutterolf et al., 2008a, 2008b), and potentially incorporated into the trench.

Finally, the subduction type, i.e., accretionary or erosive, plays a key role on material recycling in subduction zones (Clift and Vannucchi, 2004; Cloos and Shreve, 1996, 1988a, 1988b; Kopp et al., 2006; Remitti et al., 2011; von Huene and Scholl, 1991; Fig. 1.4).

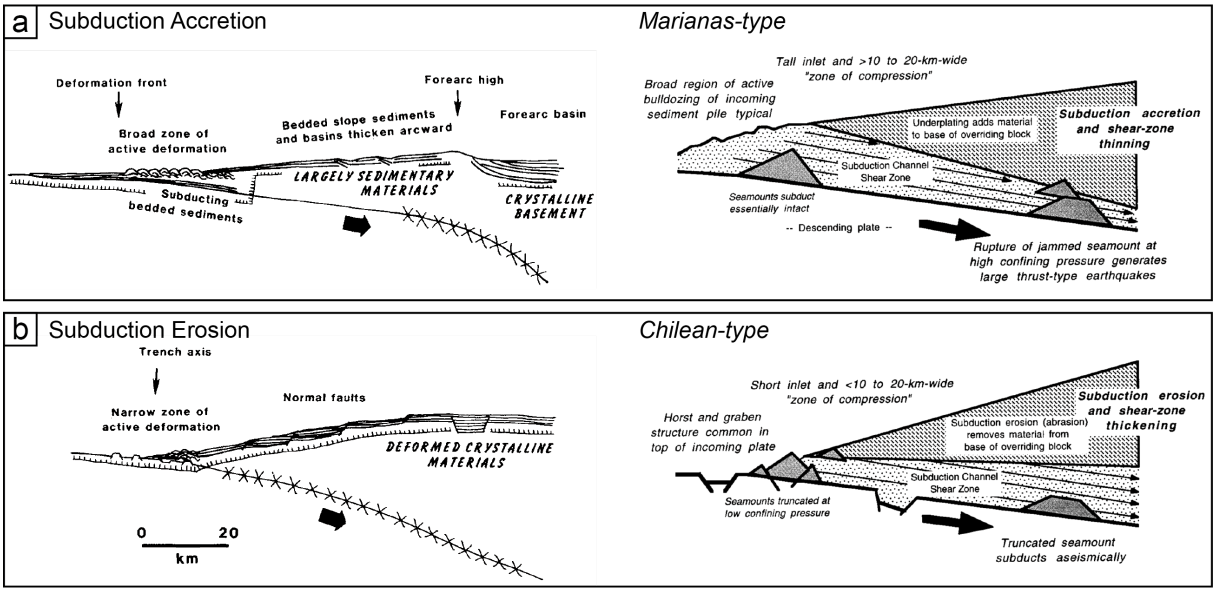

Figure 1.4: Sketch of subduction accretion versus erosion, inducing deformation and variations in material incorporation in the subduction zone, after Cloos and Shreve (1996, 1988b). (a) Model of subduction accretion, with the Marianas subduction as an example; creation of a large accretionnary prism mainly composed of sedimentary material, a broad zone of active deformation at the deformation front, and a wide seduction channel shear zone, thinning downwards (b) Model of subduction erosion, with the Chilean subduction as an example; the area of active dformation at the deformation front is narrow, with mainly basement material and absence of large amounts of sedimentary material, and a thin shear zone widening downwards, the erosion of seamounts, and high deformation.

In their paper, Clift and Vannucchi (2004) defined accretionnary and erosive subduction types according to “whether the net volume of crust in a forearc wedge is growing or decreasing … over long periods of geologic time”. Thus, accretionnary systems are defined by the growth of the forearc with increasing material supplied to the overriding plate material and the formation of an accretionnary prism. Conversely, erosive systems present a net loss of material from the overriding plate, with the destruction of material from the overriding plate by basal and frontal erosion, and the retreat of the forearc front.

Furthermore, the type of subduction will affect the geometry and thickness of the subudction channel. As an example, the Marianas represent a typical accretionnary subduction zone, with a wide subduction channel made from a thick accretionnary prism thinning downwards (Fig. 1.4a; Cloos and Shreve, 1996, 1988b). Parts of the prism are transported into the trench by debris flow or erosion into the subduction zone, further subducting on top of the down-going plate (Clift and Vannucchi, 2004; Currie et al., 2007; Plank and Langmuir, 1998; von Huene, 1986; Wakita and Metcalfe, 2005). In the case of an erosive subduction system, such as the Chilean subduction system (Fig. 1.4b), the subduction channel is represented by a thick shear zone. In this case, material supply consists of psammitic and detrital material scrapped off the upper plate by frontal erosion, or crustal material scrapped off by basal erosion (Clift and Vannucchi, 2004; Cloos and Shreve, 1996, 1988a, 1988b; Vannucchi et al., 2012; von Huene et al., 2004; von Huene and Culotta, 1989; von Huene and Scholl, 1991).

1.2.2.2 Diapiric, sedimentary and tectonic mélanges

Material supply can undergo sedimentary mélange near the surface or at shallow depths. Sedimentary mélange takes place when sedimentary debris flows are mixed with exotic blocks via "processes of slope failure, sediment transport, and deposition" , which was inferred, e.g., in the Franciscan (e.g., Festa et al., 2010; Gucwa, 1975; Wakabayashi, 2015). This mélange undergoes further metamorphism and deformation while buried in the subduction zone. It is important to note that sedimentary mélange occurs prior to burial, while further mélange is possible at depth along the plate interface, with diapirism and/or tectonic mélange.

Diapir mélange results from a density inversion due to primary density contrasts or secondary processes such as fluid overpressure, metamorphic or tectonic processes (e.g., Festa et al., 2012; Kopf, 2002). Buoyant mélanges composed of both basic and sedimentary components form above the slab and are transported into the mantle wedge as diapirs (Castro et al., 2010; Marschall and Schumacher, 2012; Marsh, 1977). They are further melted as the dehydration and partial melting occurs, which induces a change in the geochemical arc signature, which is overprinted by a sedimentary signal, in addition of the mafic signal (e.g., Marschall and Schumacher, 2012; Nielsen and Marschall, 2017; Plank and Langmuir, 1998, 1993; Spandler and Pirard, 2013; Woodhead and Fraser, 1985; Fig. 1.5). As a consequence, the geochemical fingerprint of these magmas presents trace-element characteristics deriving from both slab derived fluids, depleted mantle wedge peridotites and sediments (e.g., Marschall and Schumacher, 2012; Nielsen and Marschall, 2017).

Alternatively, rocks can undergo tectonic mélange, with material from various depths and origins mixed in a buoyant matrix while undergoing deformation (e.g., Festa et al., 2012, 2010; Grigull et al., 2012; Raymond, 1975). Tectonic mélanges present typical features, with a buoyant less competent matrix (sediments, serpentinite) displaying layer-parallel shearing, while more competent rocks develop boudinage structures (Festa et al., 2012; Kimura and Mukai, 1991; Lash, 1987; Onishi and Kimura, 1995).

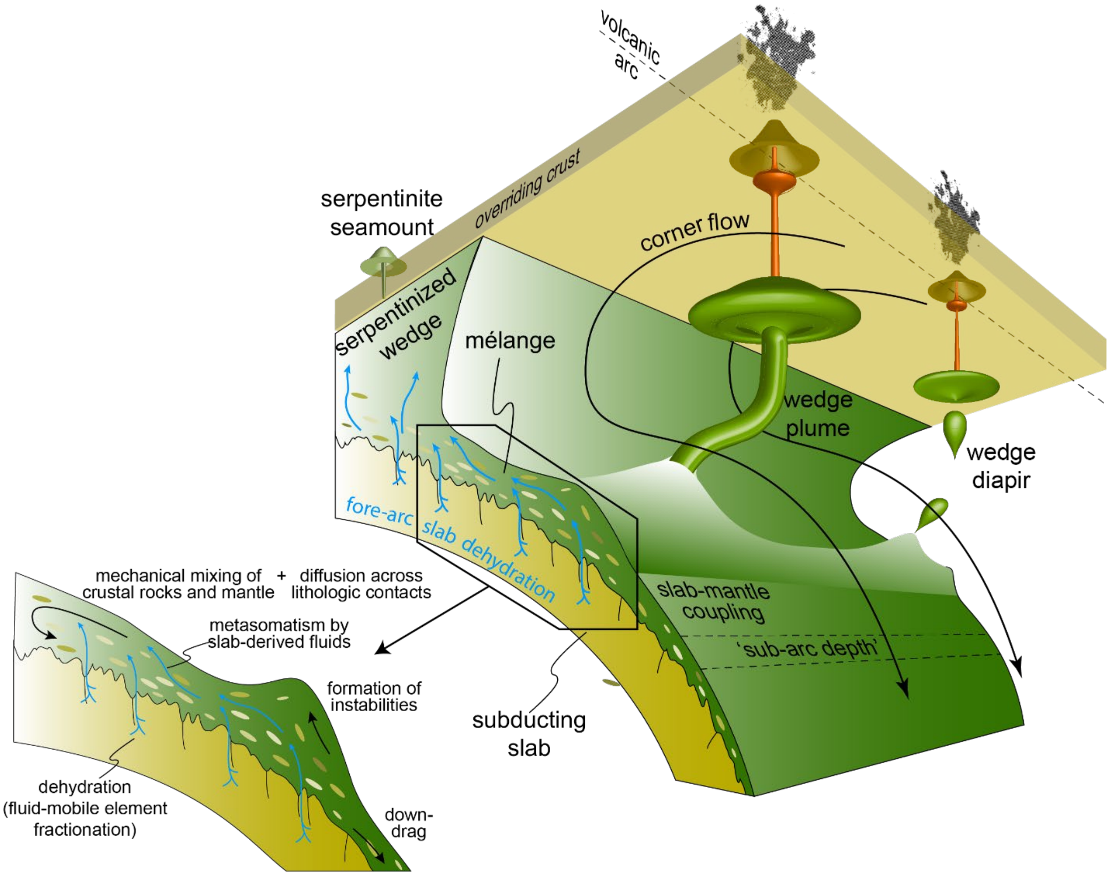

Figure 1.5: 3D schematic drawing of a subduction zone illustrating the mélange-diapir model of Marschall and Schumacher (2012), with fluid flow (blue arrows) and solid mass (black arrows). The mantle wedge plumes derive from the formation of sedimentary diapirs rising in the mantle wedge corner, where they subsequently get melted and mixed with peridotite. The melt produces arc-volcanism with a mixed geochemical signature. The zoom depicts the key processes operating at the slab–mantle interface.

1.2.3.3 Fate of the subducted material – burial and exhumation

As aforementioned, the fate of the subducted material depends on its nature (and buoyancy), but also on coupling-decoupling mechanisms and thermal state of the subduction zone. Coupling and decoupling between the upper and lower plates lead to the transfer of material via detachment, stacking, burial, and exhumation of material along the plate interface (e.g., Agard et al., 2009; Bebout and Penniston-Dorland, 2016; Guillot et al., 2009; Plunder et al., 2015; Vannucchi et al., 2012; von Huene, 1986).

Although exhumed rocks record key information during their burial and exhumation, only an infinitesimal part is exhumed, and it is unclear whether exhumation occurs pulse-like or continuously (e.g., Agard et al., 2018, 2009; Guillot et al., 2009). Slab material is buried continuously, while detachment and exhumation seem to occur only at preferential levels and under specific conditions. Detachment of mafic rocks from the lower plate is inferred to occur as slices are further stacked to the upper plate (Angiboust and Agard, 2010; Guillot et al., 2009; Plunder et al., 2015), and results from shearing in the subduction channel and a strong mechanical coupling between the upper and lower plates (Agard et al., 2018).

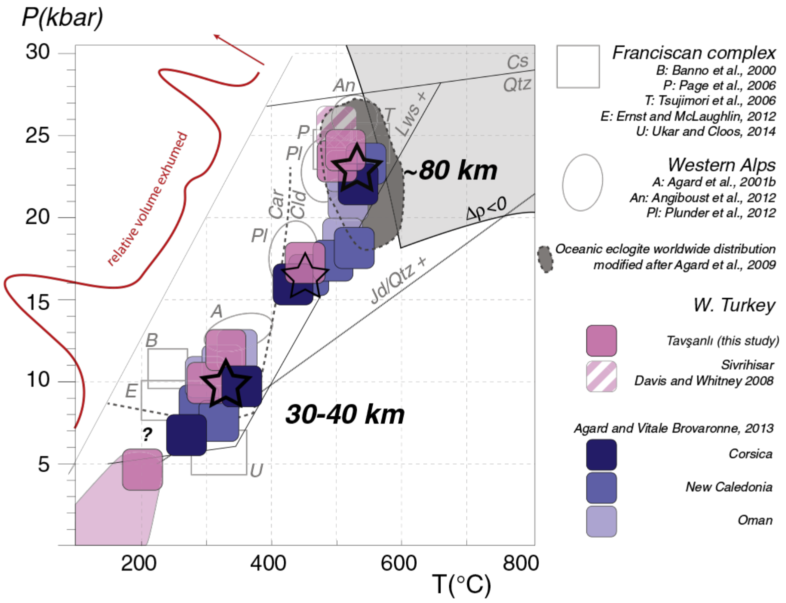

Figure 1.6: Pressure-temperature diagram compiling peak burial of oceanic rocks by Plunder et al. (2015). The rock record of maximal burial shiws two clusters: one around 30-40 km depth and another around 80 km depth (Agard et al., 2018). The grey top right corner represent the area where oceanic rocks become denser than the surrounding mantle, interpreted as the depth of "no return".

In their review paper based on numerous field data and numerical models, Agard et al. (2018) point out two main thresholds for material detachment from the slab: around 30-40 km and 80 km depth (Fig. 1.6). The first threshold is deduced from the rock record with the recovery of many rocks with conditions attesting a maximum burial at ca. 30-40 km (e.g., Platt, 1986; Grove et al., 2008; Plunder et al., 2012; Angiboust et al., 2018). No rock record attests from a detachment between ca. 30-40 km and ca. 80 km, likely due to the decoupling between both plates.

The second threshold of ca. 80 km depth is inferred from geophysical data, numerical models and field data, with a coherent transition from decoupling to full coupling at ca. 80 km depths (e.g., Abers et al., 2017, 2006, Agard et al., 2018, 2009; Burov, 2011; Furukawa, 1993;

Kato and Hirasawa, 1997; Syracuse et al., 2010; Wada and Wang, 2009; Fig. 1.2d). Furthermore, exhumed oceanic rocks from high pressure/low temperature fossil subduction zones record maximum pressure of 2.7-2.8 GPa (Chopin, 1984; Smith, 1984). This maximal depth record implies that the subducted rocks pass a “point of no return” at ca. 80 km depth and cannot be recovered after this point (Agard et al., 2018, 2009; Angiboust et al., 2012b; Aygül and Oberhänsli, 2017; Whitney et al., 2014). Exhumation of such dense rocks is possible due to the presence of buoyant material such as sediments or serpentine which allows the decoupling and exhumation of both the mafic bodies and buoyant material (Agard et al., 2009; Angiboust and Agard, 2010; Gerya et al., 2002). Additionally, corner flow (e.g., England and Holland, 1979; Shreve and Cloos, 1986), changes in rheology (e.g., Yamato et al., 2008), slab roll-back (e.g., Brun and Faccenna, 2008; Husson et al., 2009; Ring et al., 2010) or slab breakoff (e.g., Davies and von Blanckenburg, 1995; Ernst et al., 1997), are other mechanisms potentially responsible for the exhumation of deeply buried rocks in the subduction channel.

1.3 Aims and questions

The aim of this study is to decipher the nature and behavior of the plate interface at great depth (60-90km). The main questions addressed in this thesis are:

- What are the origins and fate of the subducted material?
- How to refine the constraints on burial, exhumation, and recycling processes involved at the plate interface?
- How well constrained are processes occurring at depth? In particular, do numerical and geochemical models fit to reality?
- What is the impact of coupling-decoupling mechanisms on burial and exhumation?
- How precisely can we reconstruct the geodynamic evolution of a plate interface?
- Which information can be extracted from field and analytical data?

The Southern Tianshan metamorphic belt (STMB) or Akeyasi metamorphic complex (AMC) in China represents a fossil subduction zone and a key area for investigating processes occurring at the depth of the plate interface. Indeed, the AMC contains large volumes of fresh and well-preserved rocks deeply buried at UHP metamorphic conditions.

Furthermore, the complex deformation history, good exposure, intensive fluid circulation, and various rock mineral assemblages designate the AMC as an ideal field laboratory to study processes occurring at depth and shed light on regional scale issues.

1.4 Scope of the thesis

The main chapters of the thesis aim to reconstruct the geodynamic evolution of the AMC and shed light on the processes occurring at depth at the plate interface. As exhumed rocks record information during burial and exhumation, they are valuable to interpret processes occurring along the plate interface. Therefore, we use the AMC as an ideal study case of a fossil plate interface, as it contains fresh and well preserved eclogite- and blueschist-facies rocks. We combine detailed mapping of the structure and lithology with an estimation of the pressure-temperature-time (P-T-t) constraints of the AMC.

Chapter 4: Massive sediment accretion at ~ 80 km depth along the subduction interface : Evidence from the southern Chinese Tianshan

This chapter is published as:

Bayet, L., *John, T., Agard, P., Gao, J., Li, J., 2018. Massive sediment accretion at ~ 80 km depth along the subduction interface : Evidence from the southern Chinese Tianshan. Geology https://doi.org/10.1130/G40201.1*

In this chapter of the thesis, I focus on the fate of subducted sediments at depth of ca. 80 km. The Southern Tianshan Metamorphic belt serves as an example of deeply buried metasediments, attested by homogeneous pressure-temperature (P-T) estimates and coesite findings. We report, for the first time, the stacking of a ca. 4-5 km thick massive sequence of sediments sudbucted to ca. 80 km depth, and discuss the implication on plate interface and diapir formation processes.

Timm John and Philippe Agard designed the project. Léa Bayet, Timm John, and Philippe Agard collected the samples, wrote the manuscript, and conceptualized the model. Ji-Lei Li and

Jun Gao helped to collect the samples and organize the fieldwork. Léa Bayet processed the field data, and estimated the P-T conditions using electron microprobe and Raman spectroscopy.

Chapter 5: Tectonic evolution of the HP-UHP southern Tianshan metamorphic belt (NW China)

This chapter is in revisions for Lithos as:

***Bayet, L.**, Agard, P., John, T., Menneken M., Zhou T., Gao, J. Tectonic evolution of the HP-UHP southern Tianshan metamorphic belt (NW China).*

This chapter presents a tectono-metamorphic study of the AMC. We analyze and discuss the mapping of the structures and lithologies at various scales. Detailed petrological study is carried out using electron microprobe analysis and microscopic observations. P-T estimates are presented with additional peak pressure estimates from chapter 1. The rock protoliths, structure formation, and P-T conditions are discussed in this chapter. Finally, we present a new geodynamic model for the AMC and discuss the existing models previously presented in the literature and implications for subduction zone processes.

Léa Bayet, Timm John, and Philippe Agard designed the project, collected the samples, and wrote the manuscript. Tan Zhou and Jun Gao helped to collect the samples and organize the fieldwork. Léa Bayet analyzed the field data to build the geological maps, estimated the P-T conditions using electron microprobe and Raman spectroscopy, and analyzed the samples for a petrological study. Martina Menneken helped to acquire Raman spectroscopy data.

Chapter 6: A Rb-Sr perspective on the timing of peak burial for the HP-UHP Akeyazi metamorphic complex (Tianshan, NW China).

This chapter is in preparation for submission to Contribution to Mineralogy and Petrology as:

***Bayet, L.,** John, T., Harry Becker, Elis Hoffmann, Agard, P., Gao, J. A Rb-Sr perspective on the timing of peak burial for the HP-UHP Akeyazi metamorphic complex (Tianshan, NW China).*

This chapter presents new Rb-Sr data on six selected samples to better constrain the timing of burial and exhumation of the AMC. Isochrons are based on Rb-Sr dating on white mica, using various white mica fractions and an additional phase to constrain the low intercept of the isochrons. Electron microprobe and microscopic analysis were carried out to determine the paragenesis of the white micas. I used the new decay constant for ^{87}Rb to recalculate isochrons from this study and past studies in the AMC.

Léa Bayet, Timm John, Harry Becker, and Elis Hoffmann designed the project and wrote the manuscript. Léa Bayet, Timm john and Philippe Agard collected the samples. Harry Becker and Elis Hoffmann helped to interpret and process Rb-Sr data and Elis Hoffmann (*together with Monika Feth*) helped during sample preparation and analysis. Jun Gao assisted by organizing the fieldwork. Léa Bayet prepared the samples via mineral separation including jaw crusher, handpicking, lab chemistry (sample weighing, dissolution and column separation) and prepared, realized and processed thermal ionization mass spectroscopy analysis. She further realized a petrological study using electron microprobe and microscopy.

Chapter 2

The Tianshan metamorphic belt

2.1 Regional setting

2.1.1 The Central Asian Orogenic Belt

The Tianshan belongs to the Central Asian Orogenic Belt (CAOB) in its southwestern part (e.g., Jahn et al., 2000; Fig. 2.1). The CAOB was first described by Sengor (1987) as an accretion of continental blocks, also named Altaids. The CAOB results from the convergence of the Siberia, Kazakh, and Tarim plates and is composed of six terranes: the Altay, the East and West Junggar basin, the East and West Tianshan and the North Tarim (Hu et al. 2000). The Devonian-Carboniferous climax eruption of the Bogda-arc is referred to as the Pan-Asian thermal event (e.g., Charvet et al., 2011, 2007; Coleman, 1989), which resulted in the emplacement of "juvenile" material (calc-alkaline volcanic rocks and A-types granites).

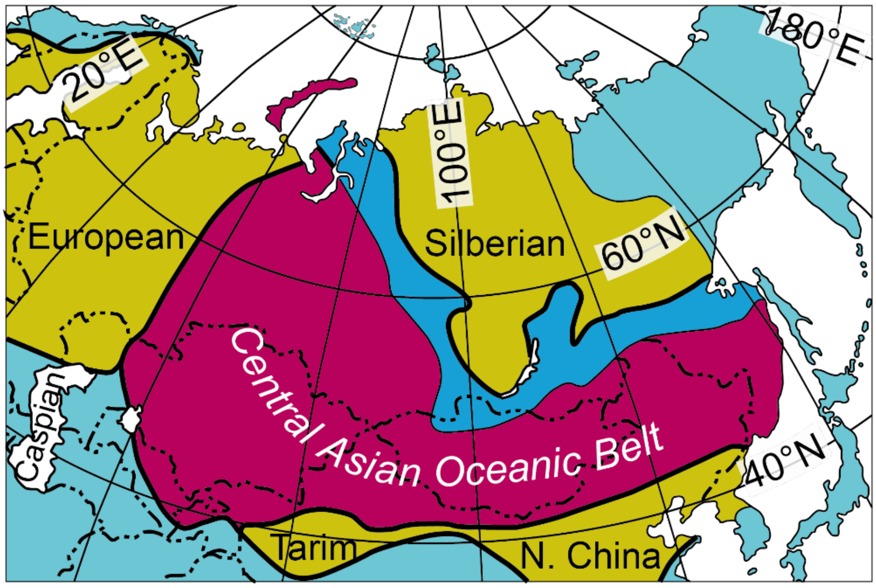

Figure 2.1: Geological map of the Central Asian Orogenic Belt (CAOB), modified after Gao et al. (2011)

Additionally, the CAOB contains several ophiolite belts parallel to the Tarim and Junggar plates, as shown by the numerous suture zones in the Kazakhstan-Yili Block; the North Margin of Tarim Block; the Central Tianshan Arc Terrane and Junggar Terrane (Allen et al., 1993; Long et al., 2011). Therefore, several authors interpreted the CAOB as a subduction/accretion complex (Sengor et al., 1993), arc complex accretion (Jahn et al., 2000), and accretion of a "young" subduction complex with "older" continental blocks (Hu et al., 2000). The India-Eurasia collision reactivated all the older strike-slip and thrust structures in central Asia, via a northward horizontal transmission of the stress (e.g., Burchfiel et al., 1999; Hu et al., 2000; Jolivet et al., 2010; Molnar and Tapponnier, 1975).

2.1.2 The Tianshan orogenic belt

The Tianshan orogenic belt extends East-West for ~2500 km in central Asia and formed by the collision between the Tarim, Kazazh(-Issyk)-Yili and Junggar plates (Gao et al., 2009; Han et al., 2011; Long et al., 2011; Xiao et al., 2009; Fig. 2.2). The Tianshan comprises several suture zones, activated at different periods, including the North Central Tianshan Suture (NCTS) and the South Central Tianshan Suture (SCTS; Fig. 2.2). The NCTS (younger) represents the collision of a former southward subduction between an island arc in the North and an active continental margin in the South in the late Carboniferous (Windley et al., 1990). The SCTS (older) represents a former northward subduction of the Tianshan Ocean, during the Silurian to Late Devovian (Gao et al., 1995; Gao and Klemd, 2003, 2000). The subsequent collision between the North Tarim and the Yili-Central Tianshan plates resulted in a ~7.5 km wide zone of thrust sheets. The suture has been later reactivated in a ~0.5 km wide sinistral strike-slip shear zone, resulting from the India-Eurasia collision (Gao et al., 1995; Gao and Klemd, 2000).

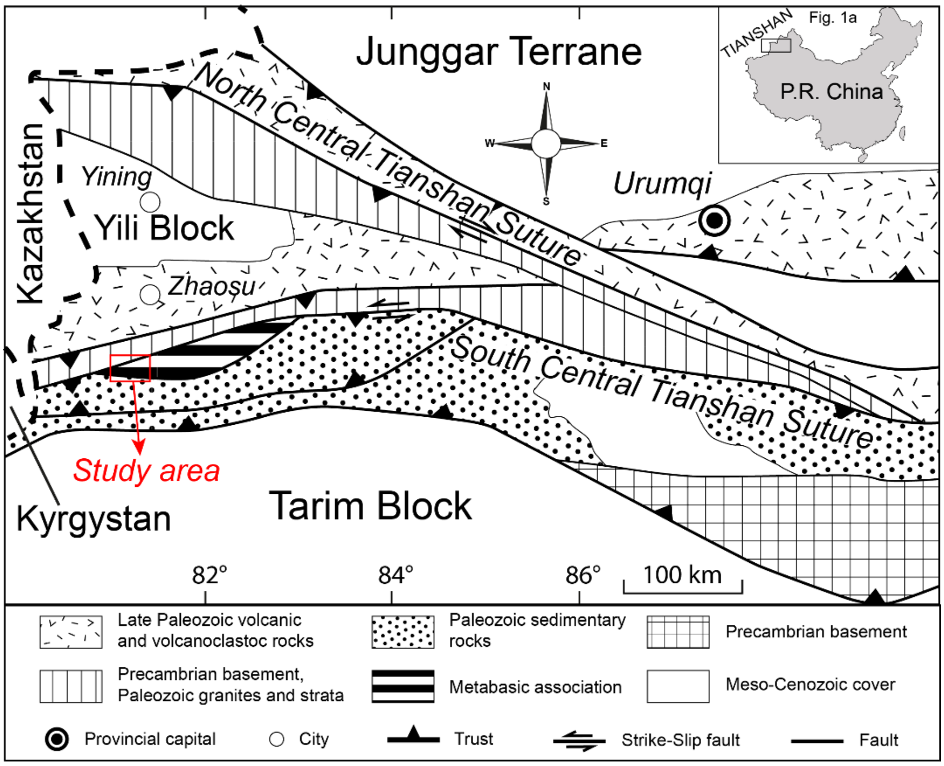

Figure 2.2: Geological regional map of the western Tianshan orogenic belt (NW China), resulting from the collision of the Tarim block in the South with the Yili-Tianshan plate in the North, modified after Gao et al. (1999)

The southern Tianshan metamorphic belt (STMB) lies along the SCTS over ~1500 km from NW China to Tajikistan (Gao et al., 1998, 1995; Hegner et al., 2010; Volkova and Budanov, 1999; Fig. 2.2). North to the STMB lies the Yili-Tianshan plate, composed of a Proterozoic basement and Paleozoic sediments mainly present as turbidites (e.g., Allen et al., 1993; Charvet et al., 2007; Gao et al., 1998). The basement consists of volcanic and volcanoclastic rocks, comprising granite, diorite, and granodiorite (Gao et al., 2009; Gao and Klemd, 2003; Long et al., 2011; Xia et al., 2014). The south of the Southern Tianshan metamorphic belt is separated from the Tarim plate by the Northern Haerkeshan Peak Fault (NHPF; Fig. 2.3; Gao et al., 1999; van der Straaten et al., 2008). The Tarim plate is referred to as a passive continental margin and consists of unmetamorphosed Palaeozoic sedimentary strata (e.g., Allen et al., 1993; Carroll et al., 1995).

The subduction polarity of the Tianshan ocean remains debated, between a northward subduction polarity, i.e., subducted underneath the Yili plate (e.g., Gao et al., 1998, 1995; Soldner et al., 2017; Xiao and Santosh, 2014), or southward polarity, i.e., underneath the Tarim plate (e.g., Charvet et al., 2011; Wang et al., 2011).

2.2 The Akeyazi metamorphic complex

The studied area, named the southern Tianshan metamorphic belt (STMB) or Akeyazi metamorphic complex (AMC; Klemd et al., 2015; Tan et al., 2017), is located in northwestern China, close to the border of Kazakhstan. The AMC consists of two units, with the high- to ultra-high-pressure (HP-UHP)/low temperature unit boarded by the greenschist-facies (GS) unit in the North and in the South (e.g., Gao and Klemd, 2000). The GS unit is dominated by metasediments, while the HP-UHP unit consists of metavolcanoclastic and metapelitic rocks (e.g., Gao and Klemd, 2003). Eclogite boudins are widespread, with a large body of pillow basalts located in the South (e.g., Gao et al., 1999; van der Straaten et al., 2008).

Previous pressure-temperature-time (P-T-t) conditions have been estimated without a systematic rock sampling strategy using various analytical methods. The results of these studies provided scattered peak P-T estimates in the range of 330 to 650 °C at 1.4 to 3.2 GPa for peak burial conditions (Gao and Klemd, 2000; Klemd et al., 2011, 2005, Lü et al., 2012b, 2009, Wei et al., 2009, 2003; Appendix B2, B3). Radiometric data also revealed a wide range of peak burial conditions between ~315 Ma and ~328 Ma, with a main cluster around 320 Ma, and post-peak metamorphic conditions around 311 Ma (Klemd et al. 2005). Overall structural data remain poorly constrained at the scale of the area, with only a few schistosity measurements reported (e.g., Gao et al., 1999, Soldner et al., 2017; Tian and Wei, 2013). Previous P-T-t estimate details are reported in chapters 4 to 6.

Several studies focused on local fluid-rock interaction processes of well-preserved blueschist- and eclogite-facies rocks. Rocks in the AMC underwent intense fluid circulation during burial and exhumation, as shown by the occurrence of veins, fluid channels, and reaction selvages (e.g., Beinlich et al., 2010; John et al., 2012; Lü et al., 2012b; van der Straaten et al., 2012, 2008). Eclogitic veins in blueschist host rocks in the AMC result from: 1) internal dehydration of the blueschist forming halos as a consequence of temperature and pressure increase during burial (Gao and Klemd, 2001) or 2) infiltration of metasomatic fluids inducing dissolution-precipitation reactions forming eclogitic veins (Beinlich et al., 2010). In either case, the reaction occurred near peak metamorphic conditions. Similarly, omphacite veins in an eclogite host rock were interpreted as HP eclogitic veins recrystallizing in UHP eclogitic host rocks (Lü et al., 2012b). Even though omphacite from both the vein and the host preserve similar jadeite composition, Lü et al. (2012b) concluded that fluid channel infiltrated the host rock during exhumation, given the mobilization of trace elements such as Ba and the textural difference observation. Alternatively, eclogites are occasionally rehydrated by fluid infiltration during exhumation, as shown in the blueschist rims of eclogite-facies pillow basalts (van der Straaten et al., 2012, 2008). The fluid infiltration event induced high element mobility, with an increase of Ba and K in the blueschists resulting in the formation of ankerite and calcite.

2.3 HP/UHP vs Mélange

Fluid-rock interactions were broadly investigated and numerous studies attempted to estimate the P-T-t conditions of the AMC. However, scattered results together with a lack of detailed structural and lithological data at the scale of the area led to the conception of contradictory models.

The AMC is interpreted either as a tectonic mélange or as a sub-belts model. The first concept (tectonic mélange) involves mafic blocks deriving from various depths (UHP and HP conditions), juxtaposed and mixed during exhumation in a metavolcano-sedimentary matrix (Klemd et al., 2011; Meyer et al., 2016). This "block-in-matrix" mélange type is inferred to derive from a tectonic mélange during subduction. This concept is based on field observations of mafic blocks or boudins wrapped in a metasedimentary matrix. Conversely, Lü et al. (2012a) proposed a sub-belt model consisting of an UHP unit in the North and a HP unit in the South juxtaposed during exhumation. The sub-belt model is based on the occurrence of coesite findings in the north of the belt, while the south only contains blueschist-facies rocks lacking UHP indicator. Both units were hypothetically separated by a major shear zone, as inferred from coesite findings. The tectonic mélange and sub-belt models have different consequences on burial and exhumation mechanisms, and source and fate of the material involved. Thus, it is of prime importance to unravel the geodynamic evolution of the AMC.

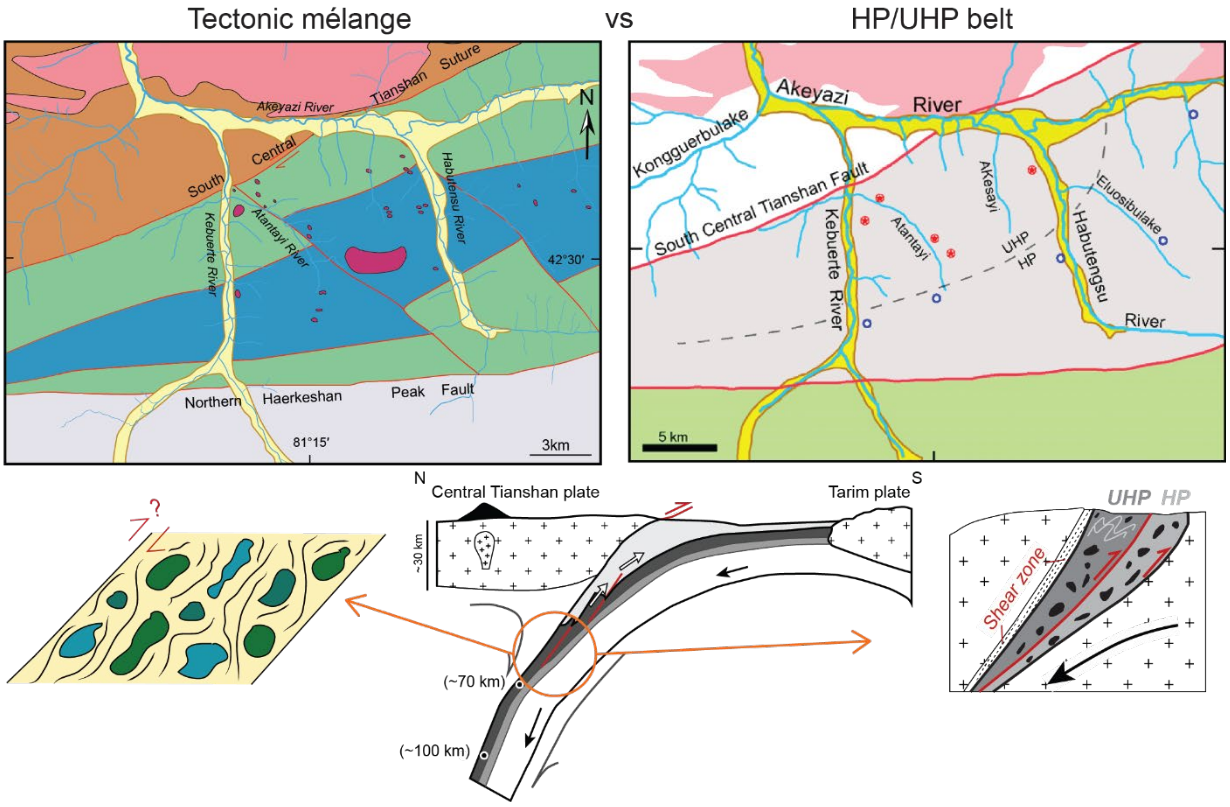

Figure 2.3: Geological maps (modified after Gao et al., 1998 and Tan et al, 201, left; and Lü et al., 2012, right) and conceptual models of the AMC, viewed as a tectonic mélange, with rocks originating from various depths (left) or as consisting of a sub-belt with a HP and UHP units (right, after Lü et al., 2008). Schematic drawing of the Tianshan subduction zone modified after Klemd et al. (2011).

Chapter 3

Methods

To unravel the geodynamic evolution of the AMC, systematic methodology has been applied and is summarized in figure 3.1. Analytical methods for Raman spectroscopy, microprobe analysis, TIMS and the use of the software are detailed in the different chapters in the section method.

3.1 Field work

Two field campaigns were undertaken in 2014 and 2015, aiming to: 1) identify deformation features at various scales, 2) a detailed mapping of structures and lithologies, and 3) collect samples for further analyses. An area of ca. 75 km² (~10 km by 7.5 km area; ca. 300 GPS data points) was mapped via N-S transects along the Akesayi (E), Muzetekexie (center) and Atantayi (W) valleys. The southern part of the study area was unfortunately not accessible, due the presence of a large glacier.

About 400 samples from 180 localities have been analyzed to: 1) constrain pressure-temperature-time conditions (P-T-t), 2) characterize textures, mineral assemblages and mineral chemistry, and 3) study deformation at the thin section scale.

3.2 Methods for constraining P-T conditions

3.2.1 Carbonaceous material thermometry

Metasedimentary rocks often contain organic matter, which progressively transforms into graphite with increasing metamorphic grade. This process of graphitization induces a reorganization of the carbonaceous material (CM), deriving from organic matter. Beyssac et al. (2002) developed a geothermometer based on the graphitization of the CM, using Raman spectroscopy. The degree of graphitization is quantified by the relative area of the defect band (R2 ratio), and is not reversible, as retrogressed eclogites show the same peak temperatures than fresh eclogites. The R2 ratio is defined as D1⁄(G+D1+D2), with the G, D1 and D2 representing the area under the Raman peak shifts of the CM (Fig. 3.2a). For low temperature samples, an additional D3 band appears (Fig. 3.2a). The G band develops with increasing temperature, while bands D1, D2 and D3 disappear (Fig. 3.2b). This is due to increasing crystallinity of the graphite, reducing the space for D bands, which reflect structure defaults.

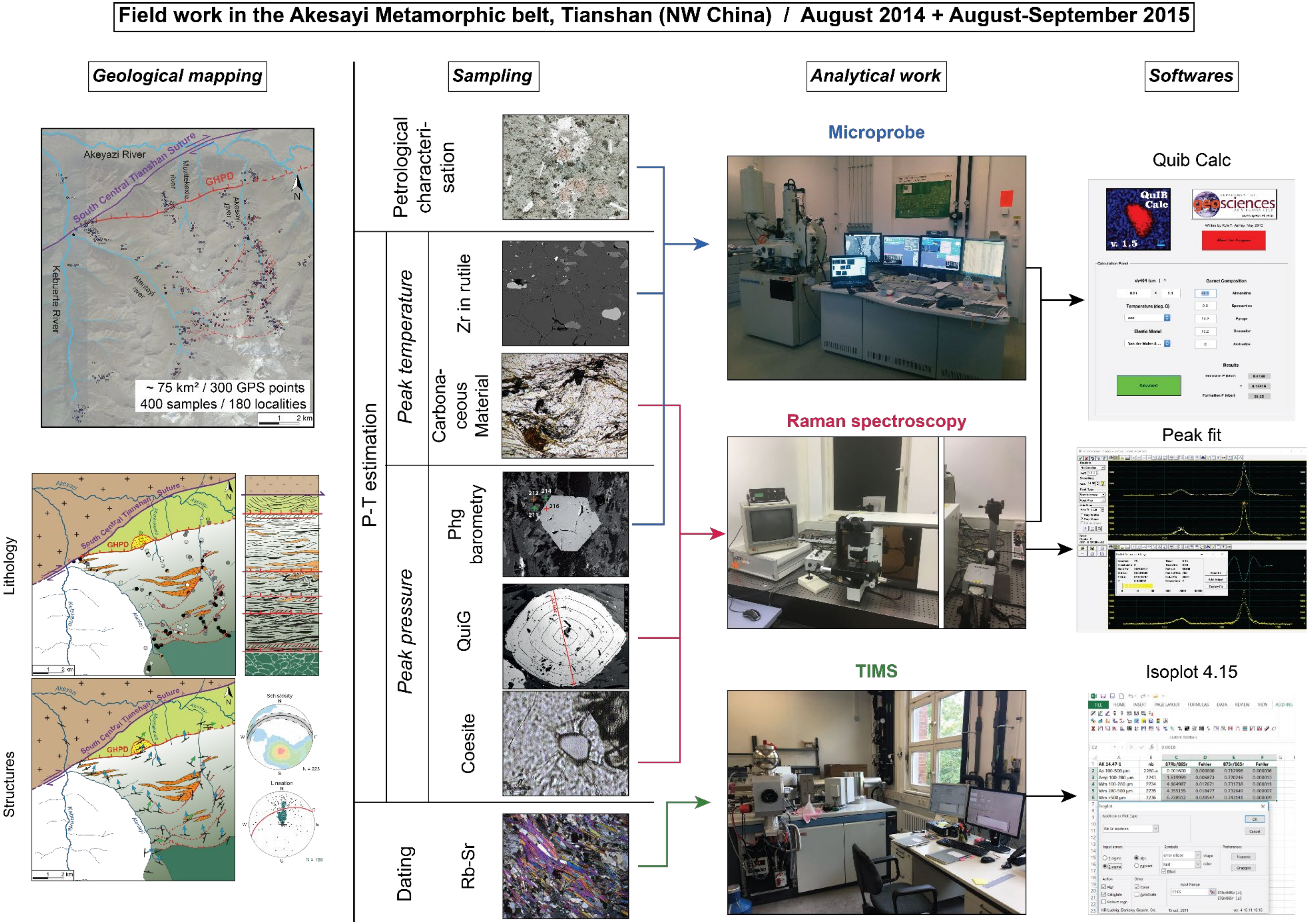

Figure 3.1. : Overview of the methods used to reconstruct the geodynamic evolution of the Akeyasi metamorphic belt

To calculate the R2 ratio, it is necessary to obtain the peak and area under the peak of each band. To do so, the spectra were fitted using the program PeakFit 3.0 (Jandel Scientific) with a Voigt function. An automatic regression calculation was applied, reiterated until obtaining a regression coefficient $r^2 > 0.985$. The R2 ratio and peak temperature correlate linearly, according to the equation: $T(°C) = -445 \times R2 + 641$ (Beyssac et al., 2002). Application of Raman spectroscopy on carbonaceous material and THERMOCALC pseudosection calculation on rocks from the Zermatt-Saas ophiolitic unit gave similar results (Angiboust et al., 2009). Temperature estimations range from 330 to 650 °C with an absolute error (accuracy) of ±50 °C due to the use of natural samples. However, despite its poor accuracy, the method allows to identify inter sample variations with a high precision of ±10-15 °C (Aoya et al., 2010; Beyssac et al., 2004).

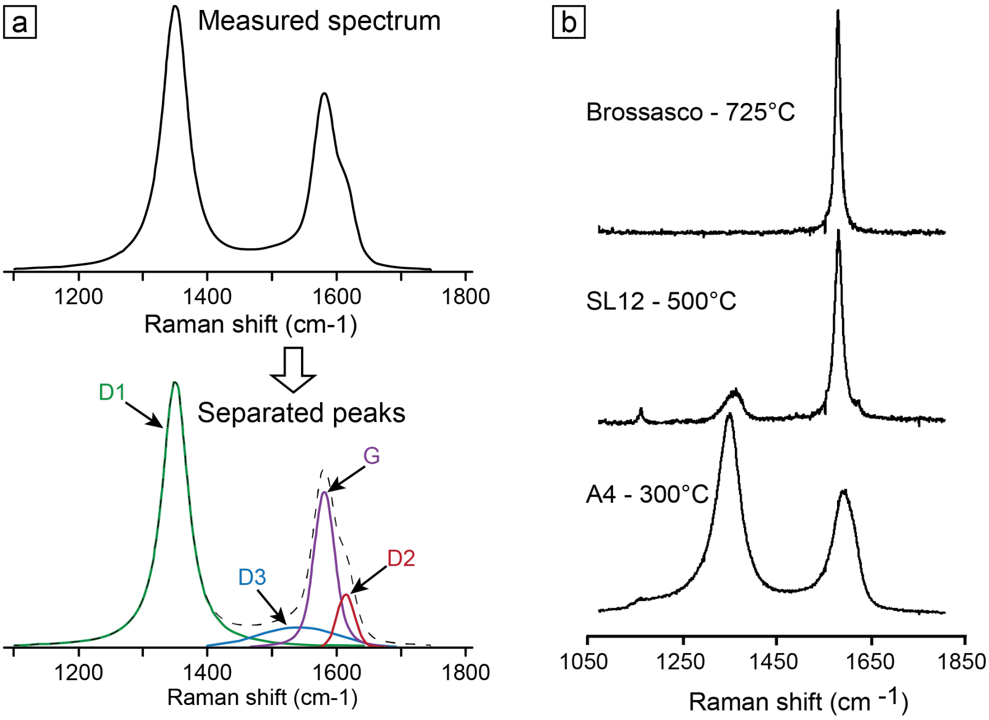

Figure 3.2: Raman spectra of carbonaceous material. **(a)** Schematic illustration of peak deconvolution from a measured Raman spectrum. The R2 ratio is defined as the area ratio D1⁄(G+D1+D2). **(b)** Natural example of peak transformation with increasing temperature after Beysssac et al. (2002).

3.2.2 Zr content in rutile geothermometry

Diffusion of Zr in rutile depends on both oxygen fugacity and temperature, via interstitial tetravalent ion migration (Sasaki et al., 1985). Zack et al. (2004, 2002) observed the temperature dependence of Zr incorporation in rutile and proposed a thermometer. This empirical thermometer is based on Zr incorporation in rutile and is calibrated on natural rocks, with temperatures ranging from 430 to 1100 °C. Electron microprobe analysis (EMPA) is used to measure the Zr concentration in rutile grains, which is log-linear correlated to temperature according to the equation:

$$T(in\ °C) = 127.8 \times ln(Zr\ in\ ppm) - 10$$

Watson et al. (2006) proposed a new calibration for the Zr in rutile thermometer from natural and synthetic rutiles in the presence of quartz, in the range of 470 to 1450 °C. Ferry and Watson (2007) updated the equation to:

$$\log(Zr\ in\ ppm) \times \log a_{SiO_2} = A + \frac{B}{T}(in\ K)$$

with A = 7.420 ± 0.105 and B = –4530 ± 111. The activity of the quartz was assumed =1, as quartz is always present in our samples, resulting in:

$$T(in\ °C) = \left(\frac{4530}{7.420 - \log(Zr\ in\ ppm)}\right) - 273$$

3.2.3 QuiG geobarometry

Inclusions enclosed in host minerals potentially retain the entrapment conditions. The quartz inclusion in garnet (QuiG) barometer (Enami et al., 2007) is an excellent method for our study, as garnet is ubiquitous in the studied rocks and often contains quartz inclusions. The main bands of α-quartz are located at about 464, 205, and 128 cm-1, with the most intensive peak for the 464 band. Increasing pressure induces stress on the quartz, resulting in the rearrangement of the quartz crystal lattice (e.g., Rosenfeld, 1969).

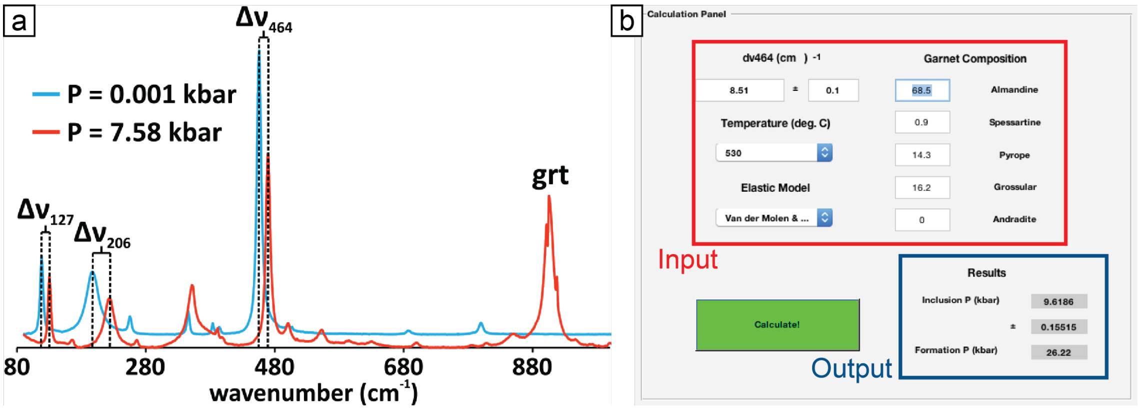

dv464 (cm) -1: 8.51 ± 0.1

Temperature (deg. C): 530

Elastic Model: Van der Molen & ...

Garnet Composition

68.5	Almandine
0.9	Spessartine
14.3	Pyrope
16.2	Grossular
0	Andradite

Results

Inclusion P (kbar): 9.6186 ± 0.15515

Formation P (kbar): 26.22

Figure 3.3: **(a)** Example Raman spectra at room temperature of quartz and 1 bar (blue) and from an inclusion that is completely encapsulated (red; calculated P=7.58 kbar), after Ashley et al. (2014a). **(b)** Screen capture of the QuIB Calc program window. Input and output are highlighted, with an example calculation shown.

This change induces a peak shift towards higher wave numbers (Fig. 3.3a), with Δv464 defined as the difference between the 464 band of quartz at atmospheric pressure and quartz under confinement pressure (e.g., Ashley et al., 2014a; Enami et al., 2007). Quartz growing at depth and entrapped in garnet, will retain this entrapment pressure to some extent. Indeed, the resulting confining pressure depends on garnet elasticity, which is a function of the garnet composition. Therefore, quartz will relax to a certain degree depending on garnet composition (Enami et al., 2007; Rosenfeld, 1969). Accordingly, only the highest estimated pressure must be taken into account, providing a minimum estimation of the peak pressure. Peak pressure was determined using the QuiBCalc program (Ashley et al., 2014b) and the state equation of Van der Molen and Van Roermund (1986). Garnet compositions have been determined by single spot EMPA at the location of the inclusion or by extrapolation from chemical maps together with line scans from EMPA. Input parameters are presented on Fig. 3.3b.

3.2.4 Conventional geothermobarometry

Additionally to QuiG barometry, conventional thermobarometry was used to determine peak pressure using the phengite barometer of Ravna and Terry (2004). This thermobarometer is based on garnet-omphacite-phengite equilibrium reactions. Reactions involve the end members grossular (Grs) and pyrope (Prp) in garnet, diopside (Di) in clinopyroxene and muscovite (Ms) and celadonite (Cel) in phengite, following the equation:

$$6CaMgSi_2O_6 + 3KAl_2AlSi_2O_{10}(OH)_2 = Mg_3Al_2Si_3O_{12} + 2Ca_3Al_2Si_3O_{12}3 + 3KMgSi_4O_{10}(OH)_2$$

$$6\,diopside \;\; + 3\,muscovite \qquad = \text{pyrope} \qquad + 2\ \text{grossular} \qquad + 3\,Celadonite$$

The pressure and temperature at equilibrium are calculated iteratively for the given garnet, omphacite, and phengite compositions. However, temperatures estimated depend on the garnet-clinopyroxene thermometer, based on the ferric iron content of garnet and omphacite(e.g., Ellis and Green, 1979). The Fe2O3 component is not measured directly using EPMA, which leads to error in calculating the ferric iron content and overestimation of the temperatures. Given this overestimation, we decided to use the aforementioned techniques of RSCM and Zr-in-rutile as equilibrium peak temperature.

3.3 Rb-Sr geochronology

Rubidium-strontium dating is based on the ^{87}Sr decays to ^{87}Rb according to the equation:

$$\left(\frac{^{87}Sr}{^{86}Sr}\right)_t = \left(\frac{^{87}Sr}{^{86}Sr}\right)_0 + \left(\frac{^{87}Rb}{^{86}Sr}\right)_t \left(e^{\lambda t} - 1\right)$$

With λ (decay constant) $= 1.3972 \times 10^{-11}$ yr^{-1}; t = present time; 0 = initial time.

For dating purpose, samples were crushed after removal of the weathered parts. Crushed parts were sieved at 100 µm, 280 µm and 500 µm mesh size and cleaned with ethanol to avoid contamination from sieving and water cleaning. Mineral separates have been processed to avoid disequilibrium potentially coming from bulk rock analysis. For a better spread of the isochron, we used several fractions of white mica and an additional apatite, amphibole, or omphacite fraction (depending on sample) to constrain the lower intercept. White mica was separated first for each fraction. To ensure a pure phengite fraction a Franz magnetic separator has been used. Iron-rich minerals were extracted applying a strong intensity current (0.4-0.9 Amp), varying among sample. We further separated phengite from paragonite with a low intensity current (~1.0-1.2 Amp), as phengite contains iron contrary to the nominally iron-free paragonite. White mica separates were ground to remove potential inclusion, separated once more in the Franz separator, and checked and picked using optical microscopy to ensure a pure white mica fraction.

The residual of each fraction was further separated into different magnetic fractions, from iron-rich (mainly garnet, >0.4 Amp) to iron-free (e.g., quartz, zircon, apatite, <2.5 Amp). Amphibole and omphacite (100-280 µm) were collected from magnetic fractions between 0.4 and 0.9 Amp, depending on samples. Both were carefully handpicked under a binocular microscope. Apatite was extracted with a heavy liquid procedure in two steps. First, the heavy minerals with a density >2.82, i.e. zircon and apatite, were separated from lighter minerals. Zircon and apatite were separated in a second step, using diiodomethane with a density of 3.30 to 3.32. Apatite was collected from the light residual. To ensure a proper hand picking for the apatites, several grains from the separation were analyzed by Raman spectroscopy and used to verify apatite grains during hand picking. Mineral separates were weighted on a microscale according to the mineral phase, to ensure a good spiking calibration. For isotopic work, all Rb and Sr concentrations were determined by isotope dilution, using a set of mixed ^{87}Rb–^{84}Sr spikes.

3.4 X-Ray Fluorescence Spectrometry (XRF)

Major (wt% oxide) and trace elements (ppm) of the six samples presented in chapter 6 were determined using X-ray fluorescence (XRF; Panalytical PW2404) at the GFZ Potsdam. Whole rock samples were crushed with a steel jaw crusher and milled until obtaining a fine powder (grain sizes <62 µm). The powdered samples were dried, weighed, and further fused at 1050 °C to a glass disc of Li tetraborate–metaborate (FLUXANA FX-X65, sample-to-flux ratio 1:6).

Concentrations were calculated using a Panalytical Axios Advanced wavelength-dispersive spectrometer and matrix correction ion programs. H_2O and CO_2 concentrations were calculated as loss on ignition.

Chapter 4

Massive sediment accretion at ~80 km depth along the subduction interface: Evidence from the southern Chinese Tianshan

4.1 Abstract

Sediment burial to depths beyond 60 km is documented by rare exposures and inferred from mass-balance calculations, element recycling, and numerical modeling. Although thermomechanical and geochemical models have suggested potential diapirism of subducted metasediments, natural evidence of this remains scarce, especially for large volumes. The southern Tianshan metamorphic belt (northwest China) represents a unique example of a deeply buried, ~4–5-km-thick, coesite-bearing sequence dominated by trench infill metasediments, with kilometer-scale variations in volcanoclastic and pelitic components. We demonstrate that these rocks were subducted down to ~80 km, as shown by evenly distributed pressure-temperature conditions of 2.5 ± 0.2 GPa and 536 ± 11 °C. Considering sedimentary budgets and geophysical constraints on subduction channel thickness (<2–5 km), this sequence likely detached as several 0.5–1-km-thick individual slices, and later accreted to the upper plate within >2 m.y. Results show that temperatures were buffered and cold (<550 °C), suggesting continuous refrigeration (by incoming cold material from the slab, juxtaposition to a mantle wedge “cold nose”, presence of a thick overriding plate, and/or fluid circulation along the plate interface). The absence of evidence for diapirism in this buoyant metasedimentary package, at ~540 °C and 80 km depth, suggests that metasedimentary diapirs may occur only at greater depth and/or farther away from the plate interface.

4.2 Introduction

Subduction zones play a key role in material recycling into the mantle, calling for a detailed understanding of the fate of subducted material. Of particular importance is the fate of low-buoyancy (meta)sediments during oceanic subduction, as they get metamorphosed along the plate interface, change rheology and density, and may, in cases, change composition via metasomatism (e.g., forming hybridized rocks such as chlorite schists; Marschall and Schumacher, 2012). Field data reveal partial offscraping and exhumation of sediments (<<25%; Agard et al., 2009) at shallow depths (10–15 km; e.g., in the Apennines, Italy, Vannucchi et al., 2008) and down to depths of ~50–60 km (Raspas complex, Ecuador, John et al., 2010). This partial recovery and the lack of significant amount of sediments returned from deeper down, except as thin sedimentary veneers associated with oceanic crustal fragments (e.g., Lago di Cignana, Italy, Reinecke, 1998), advocates for deep sediment subduction. Alternatively, or in part, sediments could also rise as diapirs feeding arcs (Behn et al., 2011; Marschall and Schumacher, 2012) or relaminate at the base of the upper plate (Hacker et al., 2011). Unfortunately, field evidence for voluminous deeply subducted sediments is rare, preventing direct assessment of the extent of mechanical and/or chemical disruption of the uppermost slab cover. Numerical models, on the other hand, are not (yet) discriminating, as they predict both sedimentary offscraping and deep burial of sediments along the plate interface (Gerya et al., 2008; Ruh et al., 2015). To constrain these processes, we conducted a detailed study in the southern Tianshan metamorphic belt (TMB), northwest China, where a unique 4–5-km-thick belt of eclogite-facies metasedimentary/metavolcanoclastic rocks (some of which are coesite-bearing) is exposed. Using internally consistent geothermobarometry, we provide regional-scale pressure-temperature (*P-T*) distribution maps, and document for the first time the existence of a several-kilometer-thick stacking of metasedimentary material at depths of ~80 km, and discuss implications for present-day subduction dynamics.

4.3 Geological overview

The Chinese Tianshan belongs to the central Asian orogenic belt and formed during the Paleozoic by the collision between the Tarim, Yili, and Junggar plates (e.g., Gao et al., 2009; Han and Zhao, 2017; Fig. 4.1a). In the southwest, the South Central Tianshan Suture (SCTS) exposes a metamorphic belt composed of high- to ultrahigh-pressure (HP-UHP)/low-temperature rocks, consisting of fresh blueschist- to eclogite-facies metavolcanoclastic and metasedimentary rocks bounded by greenschist-facies units (Gao and Klemd, 2000; Li et al., 2015; Wei et al., 2009; Fig. 4.1b). These high-pressure rocks correspond to the vanished South Tianshan oceanic crust and sedimentary cover (i.e., interleaved pillow basalts and radiolarian cherts, mostly at the base of the section; (Fig. 4.1c) and to trench infill sediments, which were subducted northward underneath the Yili-plate (e.g., Soldner et al., 2017; Xiao and Santosh, 2014).

Although a detailed account of tectonic features is beyond the scope of the present paper, new observations (Figs. 4.1b and 4.1c) suggest the existence of (1) lithological horizons more continuous than previously thought (e.g., >1–2 km in places; Figs. 4.1b and 4.1c), (2) a southward decrease of the pelitic component and increase of the mafic and psammitic components across the 4–5-km-thick metavolcanoclastic-metasedimentary sequence, (3) kilometer-scale blueschist-facies shear zones with glaucophane lineations separating mappable sub-units, and a major

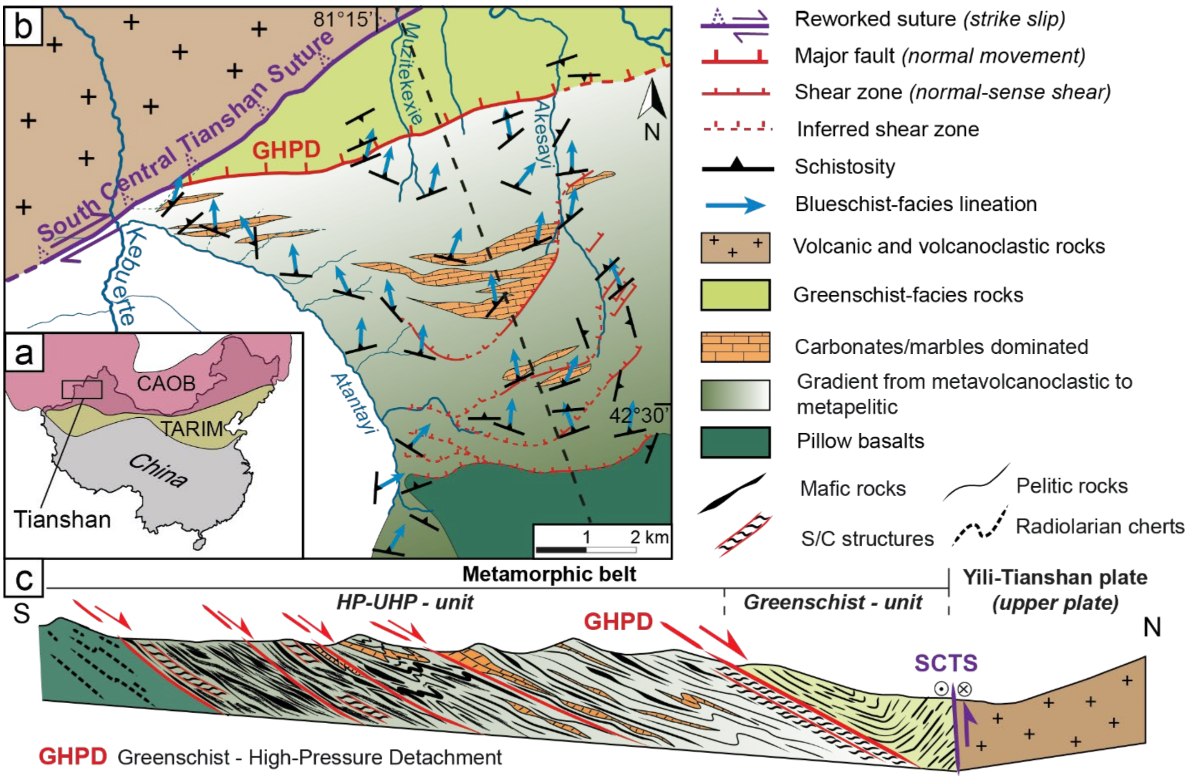

Figure 4.1: **(a)** Tectonic map of the Central Asian Orogenic Belt (CAOB). **(b)** Geological map of the high-pressure–ultrahigh-pressure (HP-UHP)/low-temperature metamorphic belt (northwest China), showing the dominant lithologies and structures, featuring the main contacts (red and purple lines), the schistosity (black symbols), and the blueschist-facies lineation (blue arrows) measurements. **(c)** Schematic north-south cross section of the study area, outlining northward, gradual changes from more mafic and psammitic to more politic, and showing the slicing of the sequence. Location of the cross section is represented black dotted line in B. TARIM—Tarim Block; SCTS—South Central Tianshan Suture.

extensional detachment to the north (i.e., relocated Greenschist–High-Pressure Detachment [GHPD]; Fig. 4.1c), and (4) a lowermost (hence latest) underplated unit composed of ~500-m-thick pillow basalts.

The latter observation advocates for ongoing subduction rather than collision at the time of high-pressure metamorphism (in addition, no basement rock was found in the high-pressure units). Recent radiometric data indicate peak burial at ca. 318 Ma, exhumation at lower but still eclogite-facies conditions at ca. 315 Ma, and reaching blueschist-facies conditions at ca. 311 Ma and greenschist-facies conditions at ca. 303 Ma (e.g., Klemd et al., 2011, 2005; Tan et al., 2017). The transition from oceanic subduction to continental collision, at ca. 315–300 Ma, was followed by the emplacement of A-type granitoids marking post-collisional intra-plate extension (until ca. 270 Ma; Han and Zhao, 2017). P-T constraints vary considerably, from 420 to 640 °C and 1.4–3.2 GPa, with 530 ± 50 °C and 2.1 ± 0.3 GPa as the most accepted conditions for the metamorphic peak (e.g., Gao and Klemd, 2000; Klemd et al., 2011; Lü et al., 2009; Wei et al., 2009). This large spread of P-T estimates arises from the use of disparate geothermobarometric methods (Appendix B2, B3), earlier focus on geochemistry or geochronology of eclogites and fluid-rock interactions (e.g., van der Straaten et al., 2008), and a lack of systematic petrological and structural data at the scale of the area. Two opposing geodynamic interpretations have thus emerged, with contrasting implications for mechanisms and depths of burial and decoupling from the slab: the TMB being either viewed as (1) a tectonic mélange with pieces originating from various depths juxtaposed during exhumation (e.g., Klemd et al., 2011), or (2) two distinct units, the coesite-bearing UHP unit (in the north) being separated from the coesite-free HP unit by a major shear zone (e.g., Lü et al., 2009; Lü and Zhang, 2012).

4.4 Estimation of peak metamorphic conditions

Compared to previous studies providing scattered peak *P-T* estimates, our results are based on a systematic approach and internally consistent methods applied to evenly distributed samples. Peak temperatures have been estimated for carbonaceous material (C) based on graphitization of the organic matter using Raman spectroscopy (e.g., Beyssac et al., 2002). Estimated temperatures (TC) lie between 525 °C and 553 °C (Fig. 4.2a), with an intra-sample error of 15–32 °C and a regional average of 537 ± 13 °C, with two samples slightly off the main cluster (sample AT 14.30: 509 ± 20 °C; AK 14.10–1: 573 ± 29 °C). The thermometer based on Zr content in rutile (TZr;

Ferry and Watson, 2007) was used on 10 samples lacking carbonaceous material and for comparison.

TZr values exhibit a slightly narrower range, between 520 °C and 543 °C (with an error of 14–22 °C within individual samples) and a slightly lower regional average of 530 ± 7 °C than for TC, but differences lie within the errors of the methods (Fig. 4.2b). Minimum peak pressures (PR) were determined using the Raman wave shift of quartz inclusions in garnet and calculated using the program QuIB Calc (Ashley et al., 2014b). Entrapment temperatures for each inclusion were cautiously estimated considering (1) the garnet nucleation temperature, (2) the linear temperature increase from core to rim using compositional zoning of garnet, and (3) the estimated peak temperature (Fig. 4.2c). Partial to full relaxation of quartz inclusions involves a loss of entrapment pressure, thus placing only a lower bound on the peak pressure experienced by the samples. Only the highest calculated pressures P_R (i.e., the least relaxed) are therefore used to estimate the minimum peak pressure experienced by the rocks, which ranges for the whole region between 2.1 and 2.8 GPa (±0.2 GPa).

The presence of coesite (identified by Raman spectroscopy; Fig. 4.3b, Lü et al., 2009; Lü and Zhang, 2012; this study) in our samples also provides a minimum pressure of 2.7 GPa at ~540 °C. A minimum peak pressure of 2.7 GPa was therefore considered for coesite-bearing samples with estimated P_R < 2.7 GPa, resulting in a new average effective P_R of 2.5 ± 0.2 GPa for the studied area, close to or at the quartz-coesite transition. In each sample, the highest P_R values as well as coesite are found in the mantle zone close to the garnet rim (Fig. 4.2d). The regional

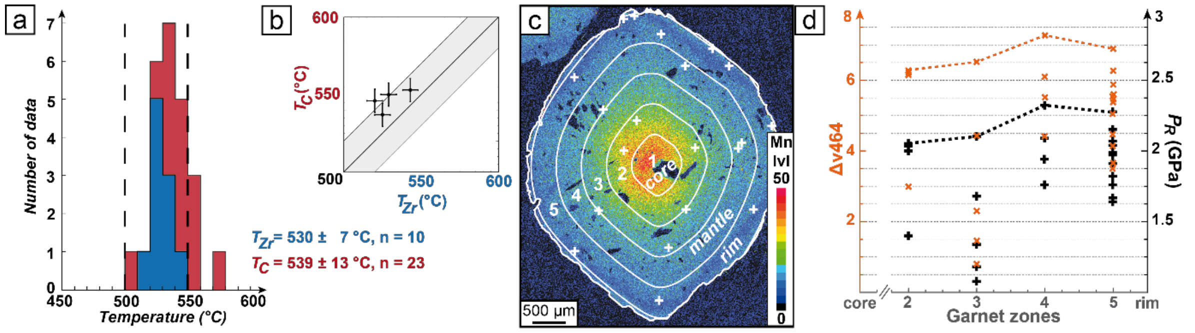

Figure 4.2: **(a)** Histogram of average temperature T_C (carbonaceous material, red) and T_{Zr} (Zr in rutile, blue) for all samples. **(b)** Comparison of T_C versus T_{Zr} thermometers on samples for which both were applied, with the 1:1 line (black) and method uncertainty (gray area). **(c)** Mn chemical map (color-coding after signal intensity) showing core to rim prograde growth zoning in garnet (sample AK14.35–1). White crosses show location of quartz inclusions in zones 1–5. **(d)** Raman shift (Δv464) for each of these quartz inclusions (orange, left axis) and corresponding calculated pressure (black, right axis) by garnet zone.

distribution of maximum temperatures (combining both T_{Zr} and T_C) and pressures and coesite occurrences is remarkably coherent (Fig. 4.3), demonstrating that the entire metavolcanoclastic-metasedimentary sequence south of the GHPD was buried to similar UHP conditions.

4.5 Deep burial of a thick volcanoclastic sequence

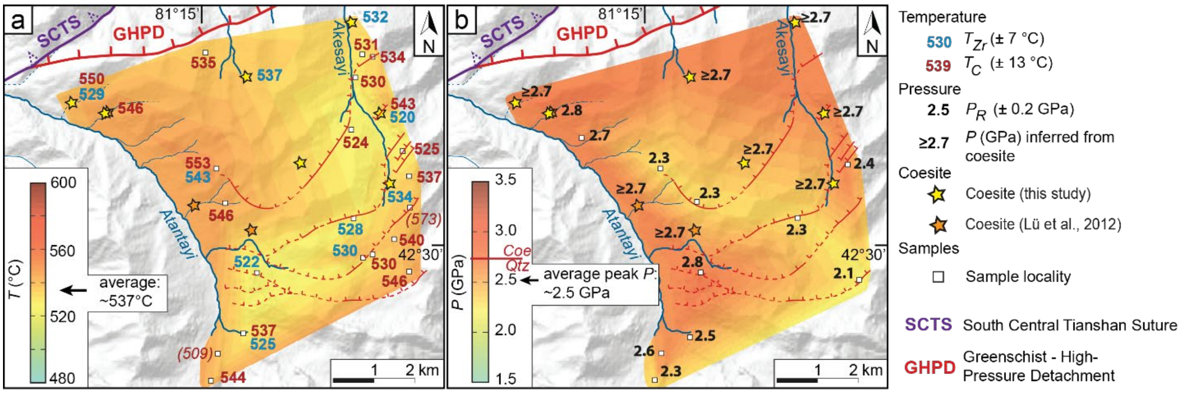

Figure 4.3: **(a)** Spatial distribution of averaged peak temperature T_C (carbonaceous material, red) and T_{Zr} (Zr in rutile, blue). **(b)** Pressure (*P*) inferred from quartz (Raman shift) or coesite inclusions in garnet (see text).

The lithological variations across the metavolcanoclastic-metasedimentary sequence, from more pelitic to more mafic and psammitic (from top to bottom) suggests an increasing input of proximal greywackes and volcanoclastic arc material with time into the trench. Two scenarios are possible to account for the existence of this 4–5-km-thick lithological sequence: (1) the sequence was subducted as a single package, or (2) it was formed by juxtaposition of several slices at depth. Based on average values for present-day subduction zones, and using estimates of porosity loss for pelitic material during compaction (i.e., 50–60%; Bond and Kominz, 1984; Syracuse et al., 2010), a 7–10-km-thick sedimentary pile would have had to enter the trench to produce a final 4–5-km-thick sequence. Sediment inputs in subduction zones vary between 0.4 and 2.5 km (Syracuse et al., 2010) and geophysical constraints show that the maximum thickness of the subduction plate interface lies between 2 and 5 km (Abers, 2005). It is therefore unlikely that the TMB derived from a single thick metasedimentary sequence overlying the sinking oceanic crust. Using average estimates of subducted sediment thickness (i.e., 500–1000 m; Syracuse et al., 2010), it is plausible instead that this material was dragged down and detached as 10 ± 5 successive tectonic slices.

Detachment from the slab occurred at a depth of ~80 km, as shown by the numerous coesite findings and minimum peak pressures of ~2.5 GPa throughout.

These homogeneous P-T estimates indicate that the UHP metasedimentary slices were underplated and successively stacked at almost invariant conditions, the final slice comprising fragments of mafic oceanic crust (i.e., pillows and cherts located in the south). Thrusts in between the slices, which formed during stacking (i.e., south-vergent), were likely reworked on exhumation and are only elusive. Some of the blueschist-facies, top-to-the-north extensional shear zones affecting earlier fabrics (e.g., rootless isoclinal, hectometer-scale eclogitic folds), across which lithological contrasts can be observed, may correspond to former thrusts (Fig. 4.1c).

The relative homogeneity of peak *P*-*T* conditions across the area, however, suggests that offsets across the blueschist-facies shear zones are only moderate (<1–5 km, within uncertainties of *P*-*T* estimates). The similarity in P_{max} and T_{max} history also suggests the existence of key coupling/decoupling processes at a threshold depth of ~80 km, as already inferred by geophysical studies (e.g., Abers et al., 2006; Wada and Wang, 2009). Considering average convergence rates and slab dip angles (i.e., 30–90 km/m.y. and 25–65°), 2 ± 1 m.y are needed to bury an individual slice down to 80 km depth, and 5 m.y. for the entire sequence (for a minimum of five slices). This stands in contradiction with the predictions of Behn et al. (2011) suggesting diapir formation in <1 m.y. for a 4–5-km-thick buoyant pile of sediments at 540 °C and 80 km. Our study, indeed,

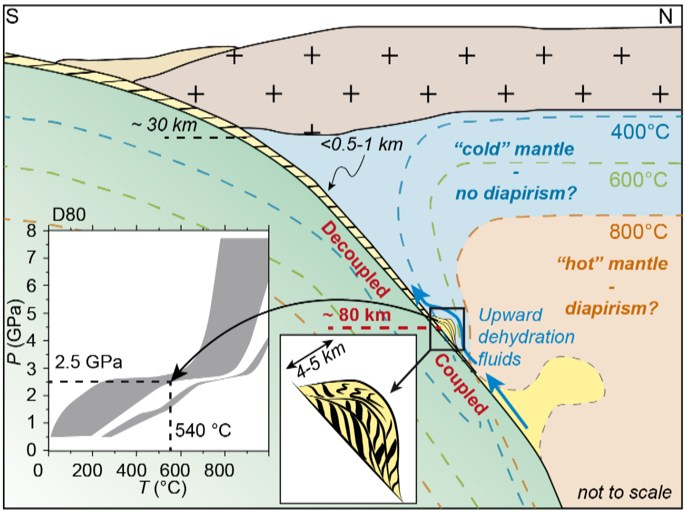

Figure 4.4: Sketch depicting the deep burial of metasediments detached as several tectonic slices of ~1-km-thickness each at ~80 km depth. Pressure-temperature (*P*-*T*) conditions for the Tianshan metamorphic belt are reported on the *P*-*T* array for worldwide subduction zones (Syracuse et al., 2010, their model D80). The recorded *T* (~constant and <550 °C) suggests continuous refrigeration (see text). Mélange diapirs could develop deeper down or farther away from the plate interface.

shows that an important portion (4–5 km), if not all, of a metasedimentary UHP metamorphic sequence remained accreted for at least a few million years without undergoing diapirism (Fig. 4.4). Similarly, neither chlorite schists nor mélange zones hypothesized to produce new hybrid rock compositions and make up diapiric material (Marschall and Schumacher, 2012) were observed in the studied area.

In the absence of significant heating after peak burial, we envision that (1) this deep metasedimentary stack remained close to the refrigerated plate interface and was returned relatively rapidly (i.e., <~5 m.y.), and (2) diapirs may form only deeper down and/or farther away from the plate interface (Fig. 4.4). The "cold" peak temperatures could either testify the presence of a mantle wedge "cold nose", with $T < 600–800$ °C down to ~80 km depth (Abers et al., 2006), a thickened overriding plate (e.g., Ruh et al., 2015), or efficient fluid circulation along the plate interface (e.g., van der Straaten et al., 2008), shielding the TMB from the overlying hot mantle and consequently keeping it "cold".

4.6 Acknowledgements

We thank E. Schwarzenbach and H. Vrijmoed, R. Milke, M. Menneken, and J. Berndt-Gerdes for helpful comments and support during the analytical work. This research received funding from the People Programme (Marie Curie Actions) of the European Union's Seventh Framework Programme FP7/2017–2013/under REA grant agreement no. 604713, 'Zooming in between Plates (ZIP)'.

Chapter 5

Tectonic evolution of the HP-UHP southern Tianshan metamorphic belt (NW China)

5.1 Abstract

The South Tianshan orogen (northwest China) comprises a *thick volcanoclastic* HP-UHP metamorphic belt exhibiting well-preserved eclogite- and blueschist-facies rocks and pervasive deformation throughout all units. Despite many previous studies, the tectonic evolution of this fossil subduction zone remains controversial due to the lack of extensive field observations combining structural and petrological data. In order to contribute to clarifying this issue, we herein present the results of extensive mapping of lithologies, deformation patterns and petrological evolutions.

The STMB is composed of a high-pressure (HP) to ultra-high-pressure (UHP) central domain separated by a major detachment from a greenschist-facies (GS) one above, both in the North and South. A gradational transition in lithologies (i.e., interlayered micaschists, volcanoclastic, and mafic rocks) is observed within the HP-UHP unit, from more pelitic in the North to more mafic in the South. Tectonic patterns and contrasting lithologies allow to recognize five distinct sub-units stacked at HP to UHP depths. Pervasive ductile deformation revealed by penetrative schistosities, folding, shear planes and boudinage structures is characterized by successive deformation stages which are attributed to burial (D_{n-1}), peak deformation accompanying detachment from the slab and/or deep nappe stacking (D_n, D_{n+1}) and exhumation (D_{n+2}, D_{n+3}). During exhumation under blueschist-facies conditions, the HP-UHP nappe stack underwent pervasive shearing, in particular across km-scale extensional shear zones with consistent top to the north shear senses reworking inherited thrust contacts. The HP-UHP unit reached peak metamorphic conditions at ~2.5 GPa and ~540 °C. Peak pressures of 2.52 ± 0.25 GPa, consistent with the widespread occurrence of coesite in the HP-UHP unit, suggest a maximum burial depth of ~80 km which is thought to reflect a transition between mechanical coupling and decoupling at the plate interface. This tectono-metamorphic evolution is set back in a tentative geodynamic model.

5.2 Introduction

Over the past three decades numerous occurrences of ultra-high-pressure terranes have been reported worldwide (Chopin, 1984; Gillet et al., 1984; Liou et al., 2004; Smith, 1984), continuously questioning the mechanisms of burial and exhumation (e.g., Agard et al., 2009; Chopin, 2003; Guillot et al., 2009). Subducted material can be derived from both the lower and the upper plate, involving material of different composition. Various compositions influence viscosity and density, and thus buoyancy, thereby leading to different behavior along the plate interface.

In a generalized view, the uppermost part of a subducting oceanic slab consists of cover sediments and basaltic oceanic crust, some of which are seamounts (e.g., Ranero et al., 2008). Upper plate material may consist of ashes from arc-volcanism (e.g., Kutterolf et al., 2008b), sediments from the accretionary prism and trench infill, and basement material if basal erosion occurs (Scholl et al., 1980). Whether subduction is primarily in accretion or erosion mode partly controls what kind of material is supplied to the plate interface, as both provide different types of material (Clift and Vannucchi, 2004; Cloos and Shreve, 1988a, 1988b). In either case, material from both the lower and upper plate will be transported on top of the downgoing plate into subduction and may be stripped from the slab as tectonic slices (e.g., Angiboust and Agard, 2010; Laurent et al., 2016), mélanges (Festa et al., 2012; Grigull et al., 2012; Lázaro et al., 2009) and/or possibly get mixed via deformation and fluid-rock interaction processes (e.g., Bebout and Penniston-Dorland, 2016; Marschall and Schumacher, 2012). Burial and exhumation at the plate interface are accompanied by intense deformation, so that the plate interface is regarded by many as a large-scale shear zone (e.g., Cloos and Shreve, 1996; Raimbourg et al., 2007; Rowe et al., 2013; von Huene et al., 2004; Wakabayashi, 2015).

To unravel the fate of subducted material during burial and further constrain exhumation processes, we herein present a tectono-metamorphic study of the Southern Tianshan metamorphic belt (STMB, northwest China), which is characterized by an unusually thick pile of well-preserved high- to ultra-high-pressure (HP-UHP) metasedimentary and metavolcanoclastic rocks with numerous coesite findings (Bayet et al., 2018; Chen et al., 2011; Li et al., 2012; Lü et al., 2009; Lü and Zhang, 2012; Tian and Wei, 2013). Despite several attempts to reconstruct pressure-temperature-time evolution pathways (e.g. Tan et al., 2017 and references therein; Fig. 5.1a) and studies in the STMB focused on petrology, geochemistry and fluid-rock interaction (Beinlich et al., 2010; John et al., 2012; Lü et al., 2009; van der Straaten et al., 2008; Wei et al., 2003), the regional structures remain poorly studied (except from local studies in the Kebuerte and Atantayi valleys: Soldner et al., 2017; Tan et al., 2017). This lack of distributed petrological and structural data over the area along with scattered P-T-t estimates has led to two contradictory concepts for the structural evolution of the STMB. It is considered either as 1) a tectonic mélange, with rocks originating from various depths, subsequently juxtaposed during exhumation (e.g., Klemd et al., 2011, Fig. 5.1b), or 2) consisting of two sub-units separated by a km-scale shear zone: a HP-UHP unit in the North (based on coesite findings) and a HP unit (coesite-free) in the South (Lü et al., 2012a, Fig. 5.1b).

We herein present a detailed study of the structural and lithological relationships together with peak P-T estimates and propose a new geodynamic evolution for the STMB. Extensive mapping of tectonic boundaries, internal structures, and deformation stages, in association with determining P-T conditions allows to constrain accretion mechanisms at depth and the regional scale geodynamic evolution.

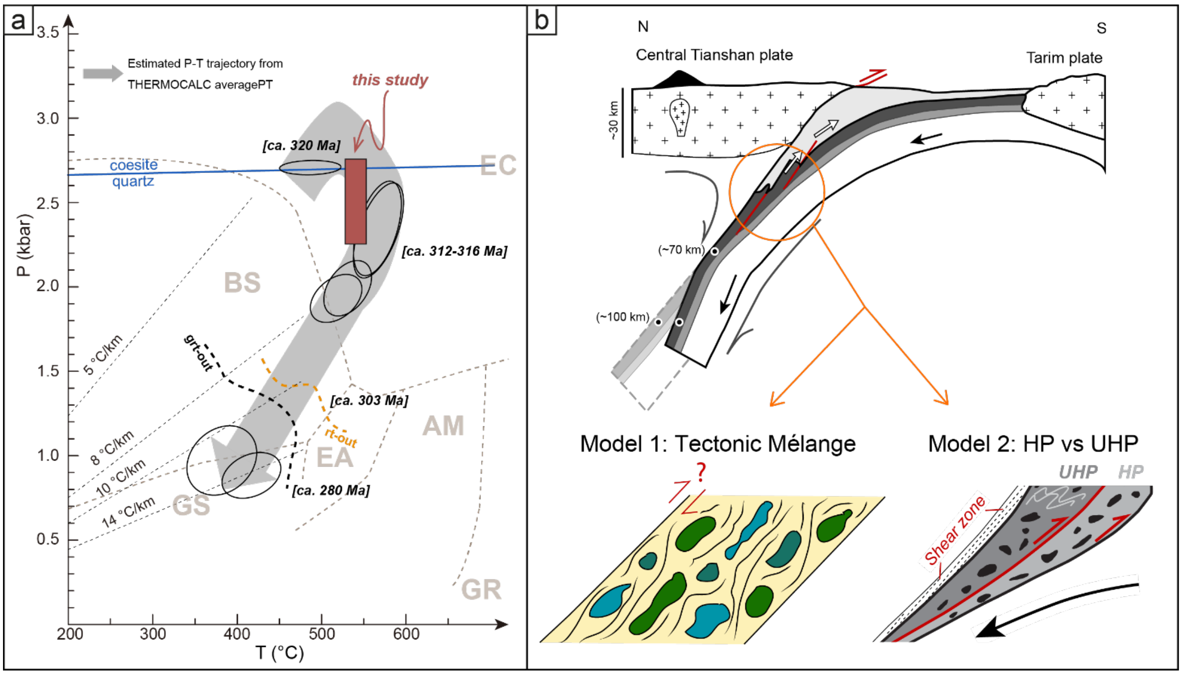

Figure 5.1: **(a)** Pressure-temperature (P-T) diagram with an estimated P-T-time path for the rocks of the southern Tianshan metamorphic belt (STMB), modified after Tan et al. (2017); peak P-T conditions estimated in this study are reported on the figure. (b) previous geodynamic interpretations for the STMB: tectonic mélange (bottom left; modified after Klemd et al., 2011) or sub-belt model, with a high-pressure (HP) unit versus ultra-high-pressure (UHP) unit (bottom right; modified after Lü et al. (2009).

5.3 Geological overview

The Tianshan orogenic belt formed by the collision of the Tarim, Yili-Kazakh and Junggar plates during the Paleozoic (Gao et al., 2009; Han et al., 2011; Long et al., 2011; Xiao et al., 2009) and extends east-west for ~2500 km in central Asia. This orogen is part of the southwestern Central Asian Orogenic Belt (CAOB) (e.g., Jahn et al., 2000; Fig. 5.2a). The CAOB is referred to as a “tectonic collage” of several subduction zones. In the southwestern Tianshan, the suture between the Yili-Tianshan and Tarim plates exposes a metamorphic belt over ~1500 km from NW China to Tajikistan (Gao et al., 1998, 1995; Hegner et al., 2010; Volkova and Budanov, 1999; Fig. 5.2b). The subduction polarity associated with this metamorphic belt is still debated, with some studies suggesting a northward polarity, i.e. underneath the Yili plate (e.g., Charvet et al., 2011; Wang et al., 2011), while others argue for a southward polarity, i.e. underneath the Tarim plate (e.g., Gao et al., 1998, 1995; Soldner et al., 2017; Xiao and Santosh, 2014).

The area studied here is located in northwestern China and is part of this metamorphic belt. It is bordered by two main structures: the south Central Tianshan Suture (SCTS) in the North and the Northern Haerkeshan Peak Fault (NHPF) in the South (Fig. 5.2c; Gao et al., 1999; van der Straaten et al., 2008). After being activated as a thrust contact, the SCTS was reactivated with a dextral strike slip movement. It separates the metamorphic belt from volcanic and volcanoclastic rocks belonging to the Yili-Tianshan plate in the North. The NHPF defines the boundary between the metamorphic belt and the marbles of the Tarim plate in the South.

The studied metamorphic belt, also called Akeyazi high-pressure metamorphic terrane (AMC, Klemd et al., 2015; Li et al., 2016; Meyer et al., 2016), is composed of a high- to ultra-high-pressure (HP-UHP)/low temperature unit in its center, bordered by a greenschist-facies unit located in the North and in the South (e.g., Gao and Klemd, 2000; this study). The HP-UHP unit mainly consists of metavolcanoclastic and metasedimentary rocks varying in composition (e.g., Gao and Klemd, 2003; this study). The southernmost parts of the Akesayi and Atantayi valleys host a large body of pillow basalts (Bayet et al., 2018; Gao et al., 1999). Available structural data is very limited at the scale of the studied area (Gao et al., 1999). Only few schistosity measurements are reported, mostly in the western part of the STMB, with a main ENE-WSW strike trend (Soldner et al., 2017; Tian and Wei, 2013).

Previous studies focused mainly on single outcrops with detailed reconstructions of pressure-temperature-time (P-T-t) paths, investigations of fluid-rock interaction processes, or recovery of the geochemical budget in the HP-UHP unit (Beinlich et al., 2010; Lü et al., 2012b; Tian and Wei, 2014; van der Straaten et al., 2008). P-T metamorphic peak conditions in the studied area have been constrained using conventional geothermobarometry based on textural equilibrium, average P-T (Thermocalc), and pseudosection modelling. The results of these studies provide very scattered estimates in the range of 330 to 650 °C at 1.4 to 3.2 GPa for peak metamorphic conditions (Gao and Klemd, 2000; Klemd et al., 2011, 2005, Lü et al., 2012b, 2009, Wei et al., 2009, 2003; Appendix B2, B3), with the most accepted value at ~530 °C and ~2.1 GPa.

Radiometric data exhibit a wide range of ages for the dynamic evolution of the belt.

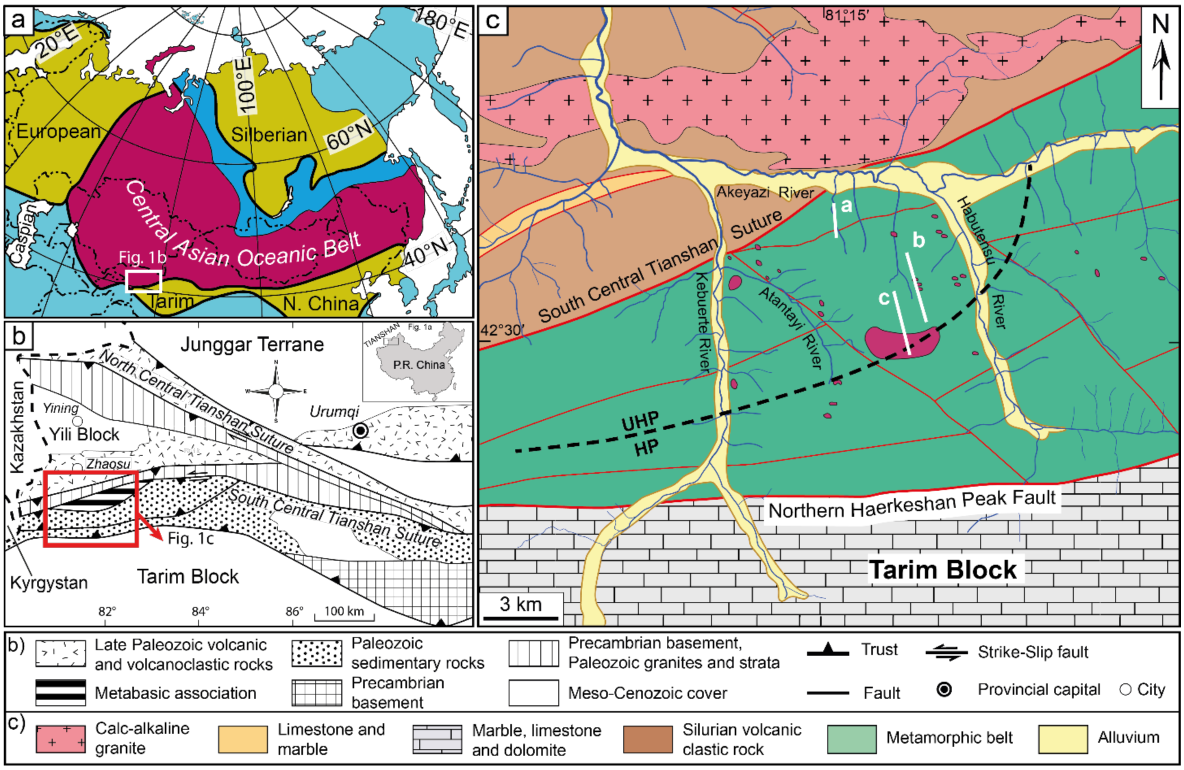

Figure 5.2: **(a)** Map of the Central Asian Orogenic Belt modified after Long et al. (2011). **(b)** Regional tectonic map of the Chinese Tianshan modified after (Gao et al., 1999). **(c)** Geological map of the high-pressure – ultra-high-pressure (HP-UHP)/ low temperature metamorphic belt in western Tianshan displaying the suggested “HP-UHP shear zone” modified after Lü et al (2012). Profiles a, b and c represent localities for field views and cross sections of figure 5.4.

Maximal burial is estimated to have occurred between ~315 Ma and ~326 Ma with a main cluster at ~319 Ma, based on Lu-Hf and Sm-Nd dating of garnet and U-Pb zircon and rutile ages (e.g., Klemd et al., 2011; Liu et al., 2014; Soldner et al., 2017; Tan et al., 2017; Fig. 5.1a). Exhumation is less well constrained, with presumably blueschist-facies to greenschist-facies conditions around ~311 Ma, based on Rb-Sr and Ar-Ar dating of white mica (Klemd et al., 2005).

5.4 Field observations: lithologies and structural data

Structural and lithostratigraphic data are illustrated in figures 5.3 to 5.5 by outcrop-scale observations of the different lithologies (Fig. 5.3), panoramic views of the Muzetekezie and Akesayi valleys (Fig. 5.4) and synthetic maps and cross-section (Fig. 5.5).

5.4.1 Lithologies

The STMB is divided in two sub-units: the high- to ultra-high-pressure (HP-UHP) unit in the central part, bordered in the North and in the South by a greenschist-facies (GS) unit (Figs. 5.4a & 3.5a). The GS and HP-UHP units are separated by a large-scale tectonic contact extending from west to east for ~13 km, namely the greenschist/high-pressure detachment (GHPD; Figs. 5.4a, 3.5a, d). The GHPD is marked by a ~50-100 m zone of intense deformation (Fig. 5.4a) and has been relocated northward with respect to its former location (Fig. 5.5c). While the contact is conspicuous in the western and central parts, it is more diffuse in the east due to the intermingling of greenschists with higher-grade metamorphic rocks close to the contact (Fig. 5.5c).

The GS unit in the North of the studied area is chiefly composed of metapelites containing chlorite-albite-actinolite ± white mica and lacking garnet (Fig. 5.3a). The GS unit extends from west to east over ca.10 km (Fig. 5.5a). Schistosity measurements reveal in the GS unit a gentle synclinal fold in the central part vanishing towards the east (In the central part, the GS unit is unconformably overlain by a ~1 km² large basin (Figs. 5.4a, 5.5a) comprising unmetamorphosed micro-conglomerates and silts (Fig. 5.3b).

The HP-UHP unit consists of a ~4-5 km-thick sequence with great lithological variability: (i) interlayered ‘purely’ mafic and metapelitic layers (Fig. 5.3c), (ii) mafic lenses and boudins embedded in more pelitic layers, (iii) layers of mixed mafic-pelitic composition and (iv) carbonates and marbles present as veins (cm-dm), layers and bodies intercalated with mafic micaschists (Fig. 5.3d).

To evaluate lithological variations within the HP-UHP unit, we classified lithologies according to the proportion of mafic and pelitic components, ranging from a 'purely' mafic rock (M-type) to a 'pure' micaschist (S-type), with intermediate mafic-micaschist compositions (MS). Mafic-micaschists, for example, contain a high proportion of white mica and lesser amounts of amphibole and/or clinopyroxene.

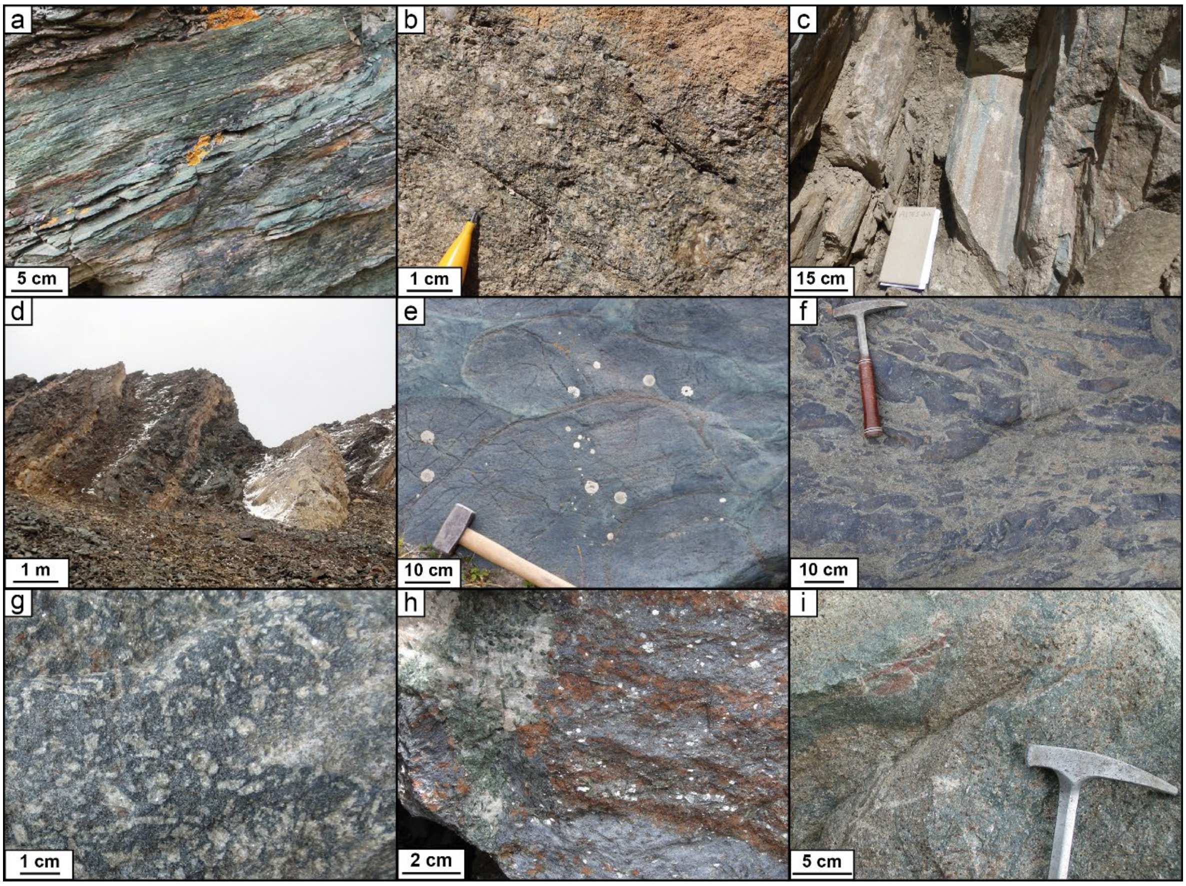

Figure 5.3: Field photographs illustrating the diverse lithologies found in the metamorphic belt. **(a)** Greenschist-facies rock from the northern part of the metamorphic belt, composed of chlorite, albite, green amphibole and lacking high-pressure indicator. **(b)** Unmetamorphosed micro-conglomerate belonging to a small sedimentary basin overlying the greenschist/high-pressure-detachment of the Muzetekexie valley (see Fig. 5.4a). **(c)** Interlayering of metasedimentary and mafic layers (omphacite, garnet and glaucophane layers) **(d)** Interlayering of meter-thick carbonate and mafic-micaschist layers. **(e)** Pillow basalt, which experienced blueschist facies-metamorphism, with eclogite-facies pillow rims. **(f)** Blueschist-facies pillow breccias filled with carbonates, located in the south-eastern part of Akesayi. **(g)** Blueschist-facies rock with blue amphibole and pseudomorphs after lawsonite. **(h)** Glaucophanite composed of white mica and ankerite in a glaucophane matrix (note the presence of an omphacite-quartz vein to the left). **(i)** Eclogite (ss) composed of omphacite, garnet and quartz.

Metapelites dominate in the North, with a small proportion of mafic components and mafic rocks, only present as thin layers or small boudins (Fig. 5.4b; topmost part of section: Fig. 5.5b). At the map scale, the lithology varies gradually from more pelitic in the North to more mafic in the South (Figs. 5.5a,b). The mafic component increases southward through the presence of large-scale lenses and m- to km-thick continuous mafic horizons, which can be mapped for up to a few kilometers (Figs. 5.5a,d). The southernmost accessible part of the HP-UHP unit consists of a large body, trending E-W over 3-4 km, of pillow basalts (Fig. 5.3e) and pillow breccias interlayered with radiolarian cherts (Fig. 5.3f). Due to the presence of glaciers and very difficult access further south, its southern extension remains unknown.

Rocks in the HP-UHP unit underwent blueschist- to eclogite-facies metamorphism, as indicated by the occurrence of index HP and UHP minerals (e.g., omphacite, glaucophane, garnet, coesite), the presence of formerly lawsonite-bearing blueschist (Fig. 5.3g), glaucophanite (Fig. 5.3h) and eclogite s.s. (Fig. 5.3i). Occasional greenschist-facies overprint can be found in the HP-UHP unit.

5.4.2 Deformation patterns in the HP-UHP unit

Both units underwent intense deformation, as evidenced by penetrative schistosity, folding and boudinage (Figs. 5.4b, 5.5d). At the km-scale, the main schistosity, S_n, appears relatively homogeneous in the HP-UHP unit (Figs. 5.4, 5.5c), with pole contours clustering around N085 30 NW (Fig. 5.5e). Several km-scale shear zones locally deflect the schistosity and allow, together with the aforementioned contrast in lithology, to divide the area in five sub-units (Figs. 5.5c,d). From north to south, sub-units 1 to 4 are characterized by thick metasedimentary to meta-mafic sequences while sub-unit 5, in the southernmost part of the sequence, corresponds to a large, km-scale body of pillow basalts and radiolarian cherts (Fig. 5.5d).

These large-scale shear zones represent highly deformed, meter to several meter wide contact zones outlined by an increase in the density of shear bands and/or overprinting crenulation. Shearing is marked at all scales by S/C fabrics and fish structures (Fig. 5.6). As an example, the shear zone bounding units 1 and 2 consists of a ~1 m mylonitic shear band with S/C structures developing in metapelitic rocks and boudinage of mafic rocks (Fig. 5.6g). Shear planes strike ~N060 on average throughout the area (Fig. 5.5e), with consistent top-to-the-north shear senses (Figs. 5.5c,d) and ubiquitous glaucophane lineations and recrystallizations (Fig. 5.6b). Some of the smaller shear zones display greenschist-facies lineations with more randomly dispersed directions.

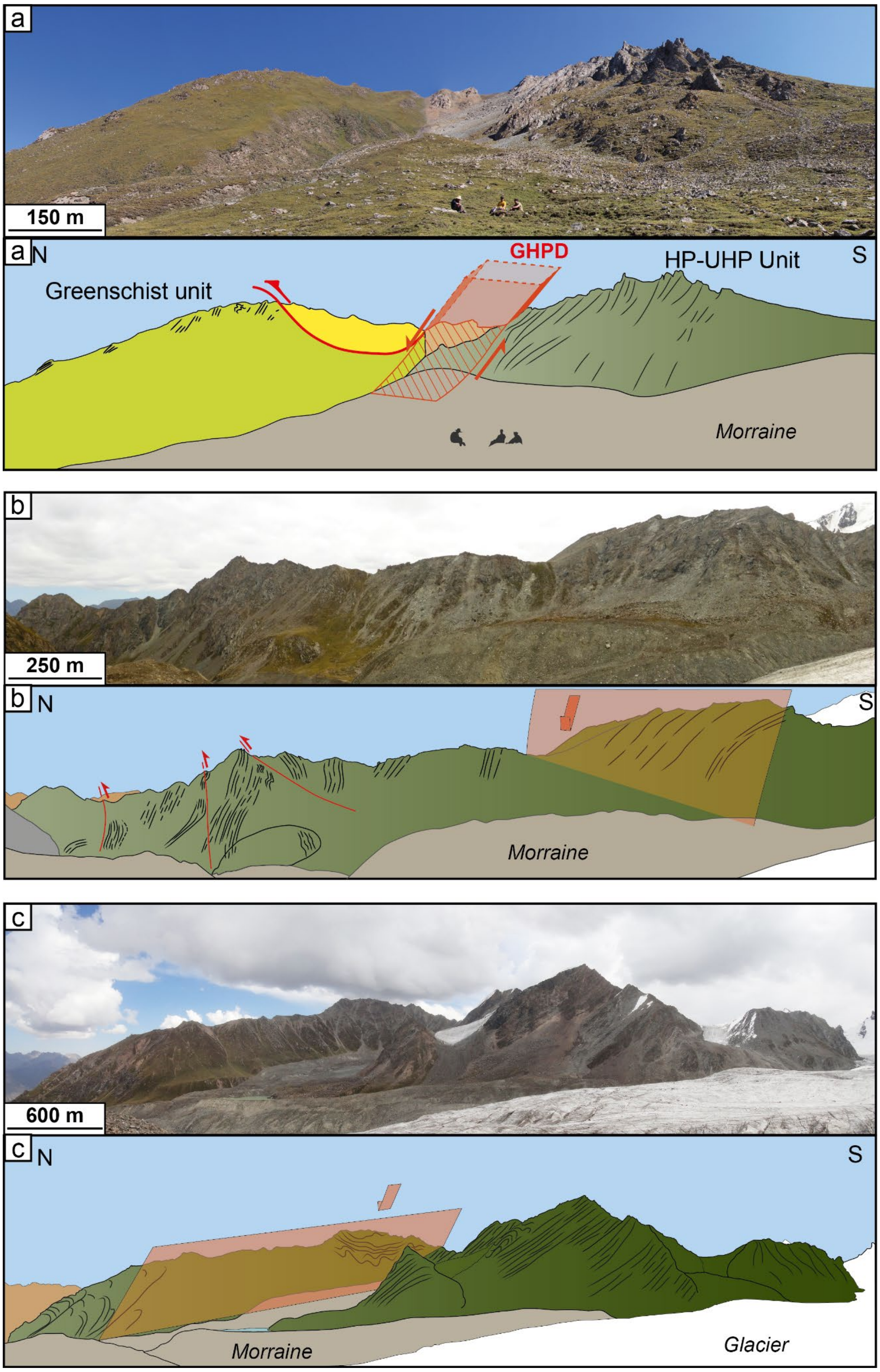

Figure 5.4: Field views of **(a)** the Muzetekexie valley and **(b)** the south-west and **(c)** central-eastern parts of the Akesayi valley. **(a)** Large detachment fault with an area of ~ 50 m of deformation – namely the greenschist/high-pressure-detachment (GHPD) – between the HP-UHP unit south of the folded greenschist, local unmetamorphosed basin unconformably overlying the greenschist-unit. **(b), (c)** Clear E-W striking, north dipping schistosity (black), and km-scale shear zones (red planes). **(b)** Smaller shear zones with different orientation are observed in addition to the km-scale shear zone. **(c)** Pluridecametric fold near the shear zone.

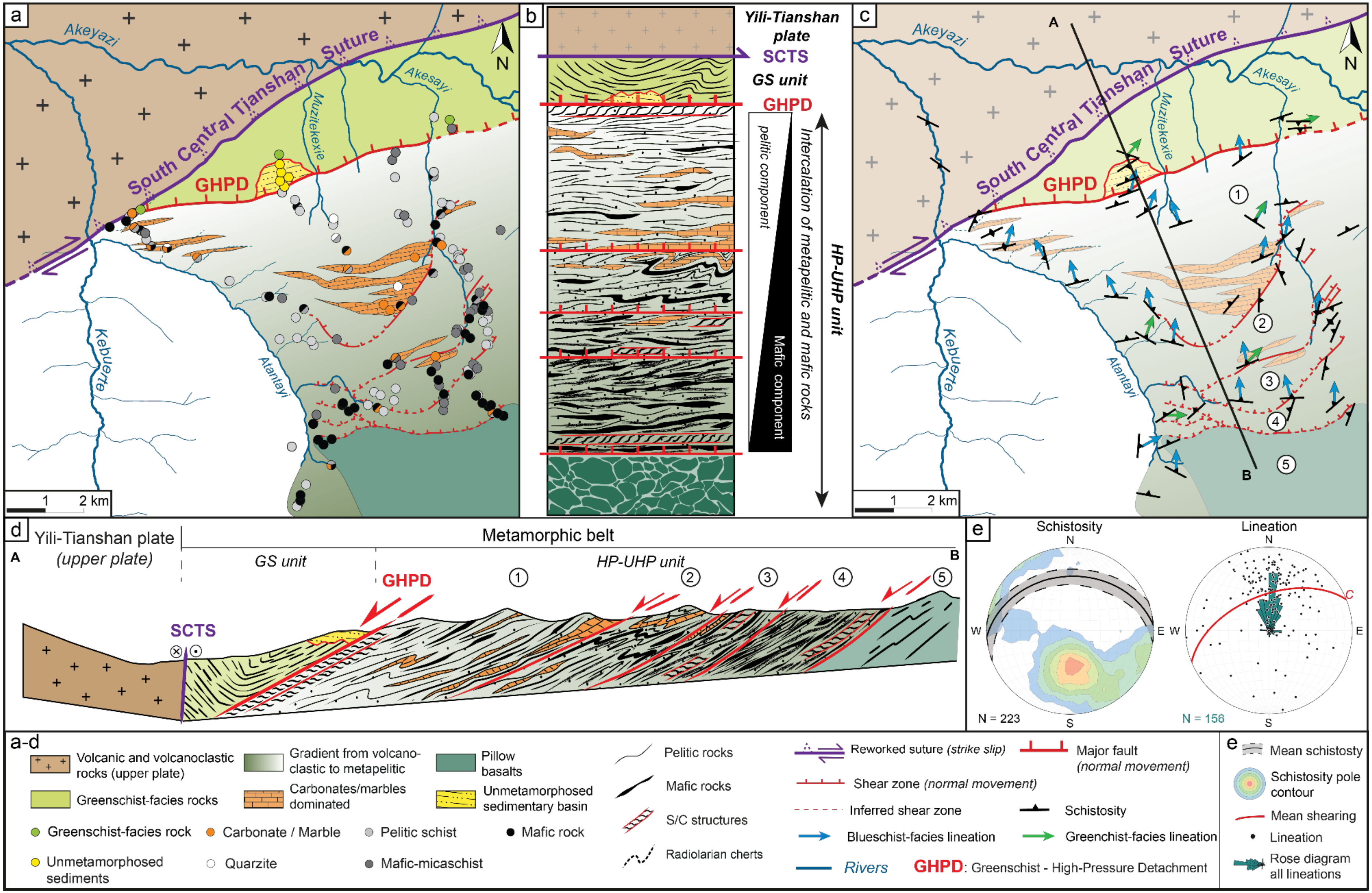
a
Akeyazi
Akesayi
Muzitekexie
Kebuerte
Atantayi
South Central Tianshan Suture
GHPD
N
1 2 km
b
Yili-Tianshan plate
SCTS
GS unit
GHPD
pelitic component
Mafic component
Intercalation of metapelitic and mafic rocks
HP-UHP unit
c
A
B
1
2
3
4
5
d
Yili-Tianshan plate
(upper plate)
Metamorphic belt
GS unit
HP-UHP unit
SCTS
e
Schistosity
Lineation
N
S
W
E
C
N = 223
N = 156
a-d
Volcanic and volcanoclastic rocks (upper plate)
Greenschist-facies rocks
Gradient from volcano-clastic to metapelitic
Carbonates/marbles dominated
Pillow basalts
Unmetamorphosed sedimentary basin
Greenschist-facies rock
Carbonate / Marble
Pelitic schist
Mafic rock
Unmetamorphosed sediments
Quartzite
Mafic-micaschist
Pelitic rocks
Mafic rocks
S/C structures
Radiolarian cherts
Reworked suture (strike slip)
Major fault (normal movement)
Shear zone (normal movement)
Inferred shear zone
Schistosity
Blueschist-facies lineation
Greenschist-facies lineation
Rivers
GHPD: Greenschist - High-Pressure Detachment
Mean schistosty
Schistosity pole contour
Mean shearing
Lineation
Rose diagram all lineations

Figure 5.5: Field data synthesis. **(a)** Lithological map, based on field observations and lithological data points (dots); **(b)** Synthetic and schematic lithological profile from north (top) to south (bottom): 1) volcanics of the Yili-Junggar plates, 2) northern folded greenschist-unit, overlain by a small unmetamorphosed sedimentary basin 3) thick metavolcano-clastic sequence showing a gradient from pelitic to mafic, with occasional carbonate intercalations, 4) pillow basalts and breccias under blueschist- and eclogite-facies conditions. **(c)** Simplified structural map of the studied area showing a ca. E-W striking north dipping schistosity (black), shearing (red lines) with a top-to-the-north sense of shearing as indicated by blueschist- (blue arrows) and greenschist-facies lineation (green arrows), separating structural sub-units (labelled 1 to 5). **(d)** Synthetic N-S cross section highlighting a lithological gradient, the presence of strongly deformed sedimentary horizons and pervasive deformation. **(e)** Stereoplot showing poles, contours, and average measurements (gray area) of the schistosity, i.e. with an E-W strike and dipping north (left). The rose diagram shows the clustering of lineation values around a N-S orientation with top-to-the-north shear senses (C, red). N represents the number of measurements.

Folding is visible at the cm- to km-scale. Large-scale folds, most obvious for meta-carbonate horizons, striking N080 on average (Fig. 5.5c). Most recumbent folds with axial planes parallel to the main schistosity rework eclogite-facies parageneses. Sheath folds, whenever observed, are accompanied by blue amphibole overgrowths **(**Fig. 5.6c).

A ubiquitous crenulation schistosity (Sc) is observed across the area (e.g., Fig. 5.6d). As for S_n, Sc strikes ENE-WSW but with a higher dip angle, and may fully overprint the main schistosity in strongly deformed areas or along shear bands (e.g., Fig. 5.6e). This deformation stage is identified as Dn+1 in the following. Distributed shearing marked by C planes reworking both Sn, Sc and recumbent folds defines a later (blueschist facies) Dn+2 deformation stage (e.g., Fig. 5.6h). Finally, meter-scale C' structures oblique to C planes, dominantly associated with chlorite overgrowths, mark the transition from blueschist- to greenschist-facies conditions (Fig. 5.6h). This episode is noted Dn+3.

5.4.3 Meter to micrometer scale structures

Boudinage, crenulation schistosity, and C' structures reworking the main schistosity, and minerals associated to these successive deformation steps, are best observed in the HP-UHP unit at the outcrop scale or in thin-section. Figure 5.6a shows features characteristic of successive deformation events.

Mafic lithologies tend to form boudins wrapped into more pelitic lithologies (Fig. 5.7a). Some of these mafic rocks show little internal deformation, even at a smaller scale (cm to mm), particularly when surrounded by metasediments: most minerals are euhedral and there is no foliation (Fig. 5.7a).

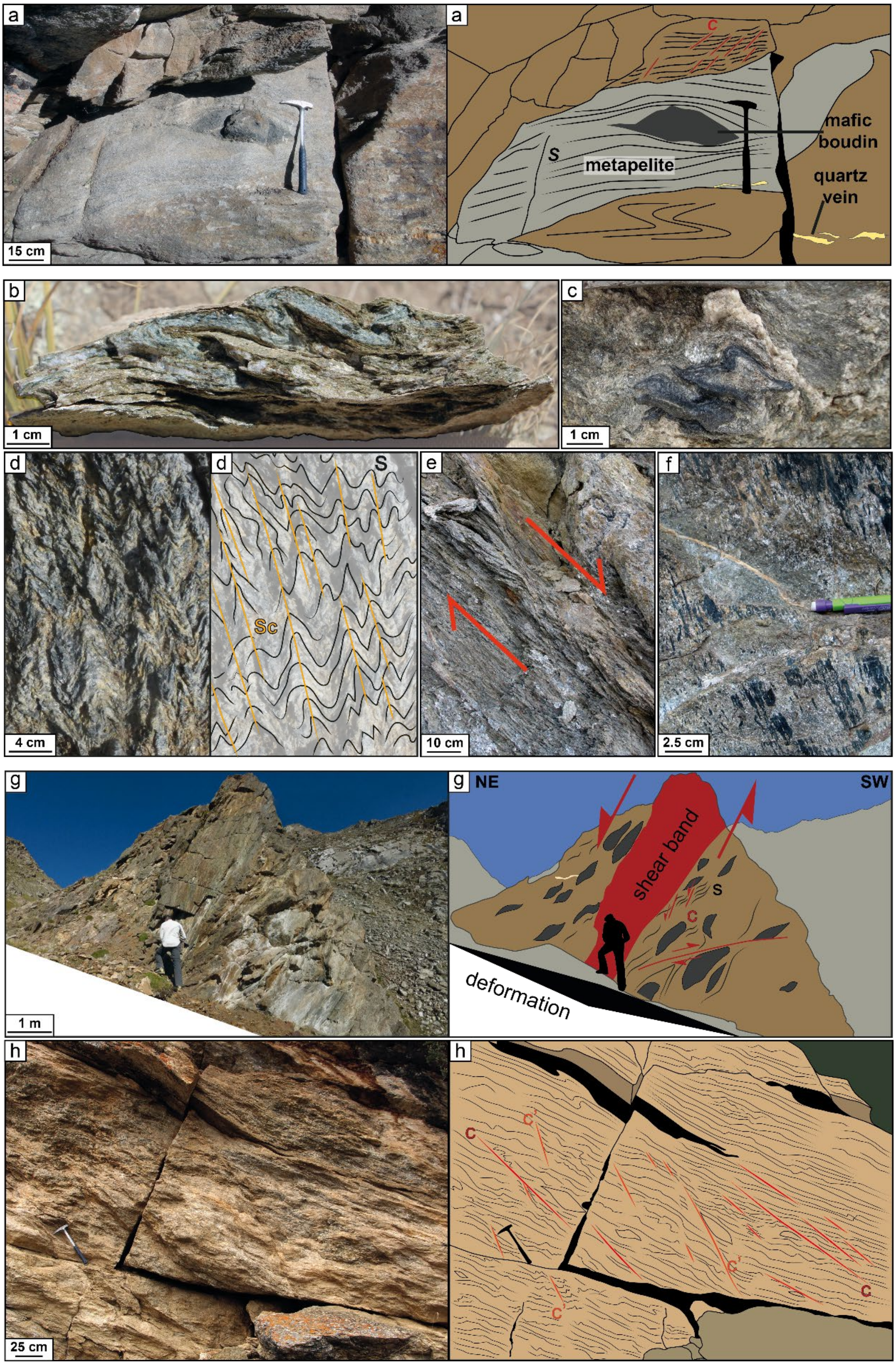
a
15 cm
a
c
mafic
boudin
s
metapelite
quartz
vein
b
1 cm
c
1 cm
d
4 cm
d
S
Sc
e
10 cm
f
2.5 cm
g
1 m
g
NE
SW
shear band
s
c
deformation
h
25 cm
h
c
c'
c'
c'
c

Figure 5.6: Photographs of the different deformation features at cm to m scale. **(a)** Mafic boudin wrapped in metasedimentary layers, displaying schistosity (S), shearing and folding features. Normal **(b)** and disharmonic **(c)** folds (blueschist- to eclogite-metamorphism). **(d)** Crenulation schistosity (Sc, orange). **(e)** Shearing (C) affecting both S and Sc, (blueschist-facies conditions, as indicated by ubiquitous glaucophane lineation) **(f)**. **(g)** Shear band depicting mylonitisation in its center with decreasing deformation outwards; **(h)** Development of C’ structures, oblique to C, with pervasive schistosity in a greenschist-facies metasedimentary rock.

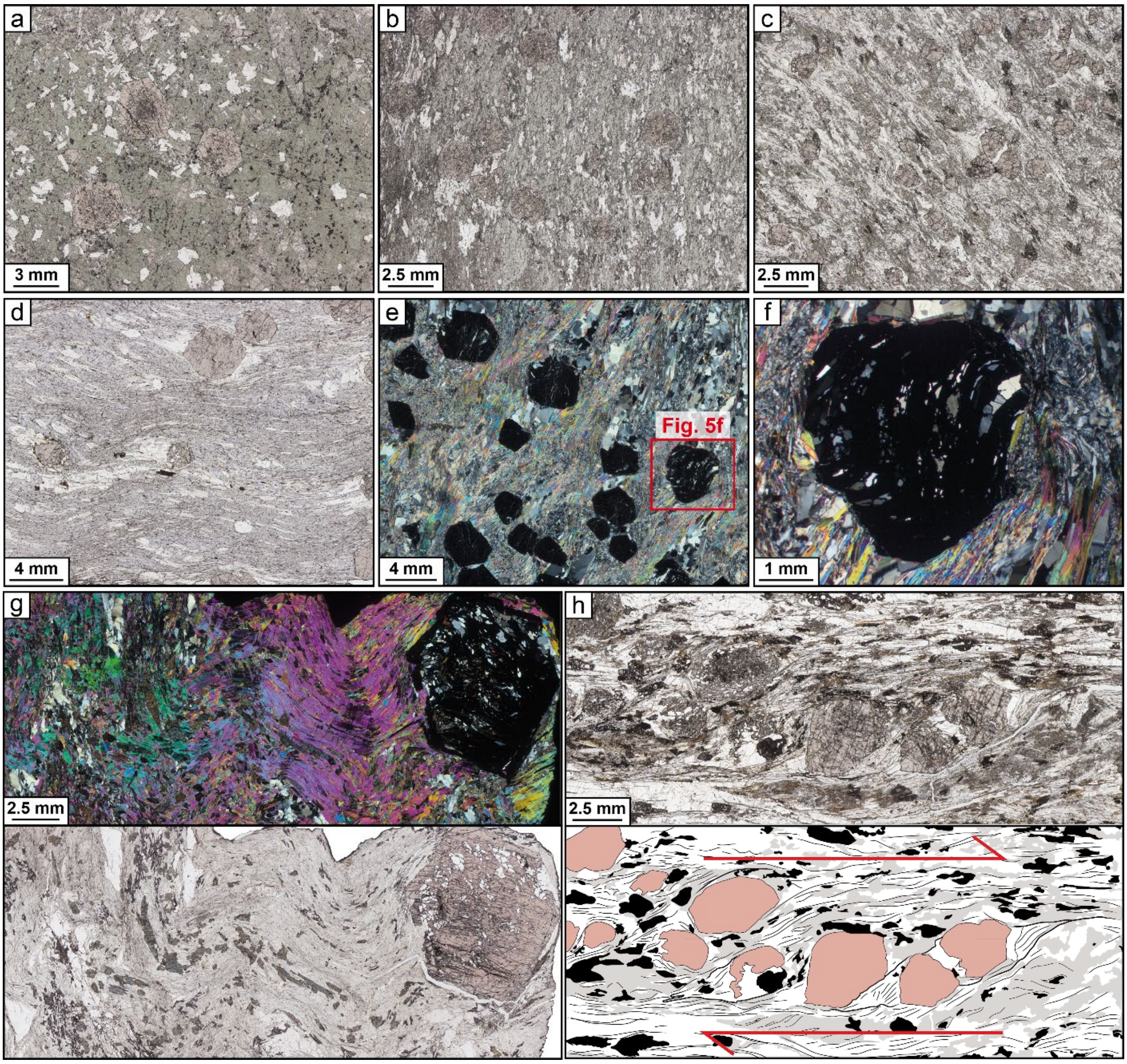

Figure 5.7: Photographs of typical microstructures: **(a)** eclogite-facies rocks showing little to no deformation (when ‘purely’ mafic). **(b)**, **(c)** Increasing deformation related to increase of the white mica content**. (d)** Deformed blueschist-facies rocks associated with the presence of white mica. **(e)** Micaschist presenting a pervasive schistosity, with quartz inclusion in a garnet host, displaying a former schistosity. **(g)** Crenulation schistosity in a mafic-micaschist. **(h)** Shearing in a garnet-bearing metapelite, represented by garnet porphyroblast rotation, development of quartz shadow pressure around garnets and pervasive white micas schistosity.

Deformation intensifies together with an increasing white mica proportion in mafic rocks, both at eclogite- (Fig. 5.7b, c) and blueschist-facies conditions (Fig. 5.7d). Omphacite-bearing mafic rocks show much less deformation than amphibole-bearing mafic rocks.

Deformation is more intense in rocks with a higher pelitic fraction, and strain tends to localize in these more pelitic horizons (Fig. 5.6a). At the hand specimen scale, deformation is accommodated by the development of a schistosity composed of white mica, quartz ± acicular amphibole. Pressure shadows develop around rotating garnet (Figs. 5.7e,f). In the most deformed samples, quartz presents undulose extinction and dynamic recrystallization (Fig. 5.7e). In addition to deformation stages recognized in the field, a former deformation stage D_{n-1} can be identified in these garnets (Figs. 5.7g,h): quartz inclusions in garnet define an older schistosity, S_{n-1}, rotated as garnet grows and commonly at an angle with S_n (Fig. 5.7f). The crenulation schistosity (Sc) develops in both MS- and S-type rocks (Fig. 5.7g). Shearing is marked by S/C structures, quartz pressure shadows around garnet, foliation fishes, boudinage and rotation of garnets in shear bands (Fig. 5.7h).

5.5 Methodology and analytical techniques

To assess metamorphic conditions of the area and reconstruct the tectono-metamorphic history, we estimated peak pressure-temperature conditions (P-T) of samples evenly distributed across the area using four different methods: 1) the Raman spectroscopy on carbonaceous material (RSCM) thermometry and 2) the Zr-in-rutile thermometry, 3) the quartz-in-garnet (QuiG) barometry, 4) phengite barometry.

The RSCM method (T_C) is based on the temperature dependent crystallinity of carbonaceous material (*CM*), which irreversibly increases with increasing temperature. RSCM thermometry thus allows to estimate peak temperatures and was calibrated over the 330-650 °C range (e.g., Beyssac et al., 2002). The Zr-in-rutile thermometry (TZr) is based on the Zr content in rutile and measured using the electron microprobe. With increasing temperature, rutile can incorporate more Zr into its structure, independently from rock composition. When quartz and zircon buffer the system the corresponding temperature can be calculated purely based on Zr-content in rutile (Zack et al., 2004). The Zr in rutile thermometer allows broad applications on various rock types over a large temperature range (430-1100 °C). We used the calibration of Ferry and Watson (2007). All measured rutiles have zircon in their close vicinity, to buffer the Zr system and were carefully checked via SEM for any possible zircon exsolution or inclusions, which may bias the calculated temperatures (Meyer et al., 2011). Both thermometers are restricted by an absolute uncertainty of about ± 50 °C due to the use of natural samples. Their precision, however, is estimated to be ± 10 °C, which reflects their high reproducibility (Beyssac et al., 2002; Zack et al., 2004).

Minimum peak pressures (P_R) were estimated using quartz-in-garnet (QuiG) barometry following the method of Enami et al. (2007) and Ashley et al. (2014b). This method is based on the different elastic moduli of garnet and quartz, resulting in less compression of the garnet lattice with increasing pressure compared to the quartz lattice. Pressure at the time of formation of the minerals is stored as residual stress in the quartz lattice enclosed by the stiff garnet container, which can be quantified using Raman spectroscopy. The stressed quartz lattice results in a shift of the 464 peak of quartz (Δ 464), reflecting the residual confining pressure (Ashley et al., 2016). However, change in garnet composition induces a modification of its elasticity, leading to subsidiary quartz lattice relaxation (Rosenfeld, 1969). Accordingly, we measured garnet compositions near all inclusions. Pressures (P_R) were then determined using the QuiBCalc program (Ashley et al., 2014b), with the equation of state of Van der Molen and Van Roermund (1986). The program requires three input parameters: 1) the quartz Raman shift (Δ 464), 2) the garnet composition, and 3) the temperature of entrapment. Garnet composition was determined by single spot EMPA at the location of the inclusion or by extrapolation from chemical maps together with line scans from EMPA. The individual entrapment temperatures for the inclusions have been carefully calculated by: 1) determining the temperature of the initial stage of garnet growth using pseudosection modeling (Perple_X 6.7.3; Connolly, 2005, 1990); 2) considering the previously determined peak temperature of each sample for garnet rim growth (TC and TZr) and 3) evaluating the distance of each inclusion from the garnet core and interpolating the temperature linearly from core to rim. The distance to the garnet core of each inclusion was determined using element distribution maps. Quartz inclusions should be small in comparison to the thin section thickness (< 1/3) and not exposed to the surface or at the bottom of the thin section to ensure good confinement conditions. Only maximum estimates of P_R were considered, as this value may have been decreased by elastic and viscous relaxation.

Peak pressures were also estimated using the phengite barometry based on the assemblage garnet–clinopyroxene–phengite (P_{GOP}), using the equilibrium described in (Waters and Martin, 1996):

6 diopside (Di) + 3 muscovite (Ms) = pyrope (Py) + 2 grossular (Grs) +3 celadonite (Cel) (1)

Equilibrium conditions are estimated following the activity models and method of Ravna and Terry (2004), based on transfer reactions between the different end-members. Temperatures estimated through this method, however, essentially rely on Fe-Mg equilibrium (e.g., Ellis and Green, 1979; Ravna, 2000), which is known to overestimate temperatures by about 50 °C, and standard deviations are large (±82 °C and ±65 °C in the quartz and coesite stability fields, respectively), in part due to the unreliable estimation of the Fe^{3+}/Fe_{tot} by charge balance. To circumvent these problems, the peak pressure was herein calculated from independent Zr-in-rutile and RSCM thermometry, since reaction (1) above can be used independently as a phengite geobarometer for a given temperature. To estimate the peak recorded pressure (PGOP), garnet with maximum $(a_{grs}^{grt})^2 a_{py}^{grt}$, omphacite with minimum a_{di}^{cpx} (and correspondingly maximum XJd) and phengite with maximum a_{Al-cel}^{phe} (maximum Si-content) were considered (Carswell et al., 2000; Ravna and Terry, 2004).

5.5.1 Electron microprobe analyses (EMPA)

Concentration of Zr in rutile was determined by EPMA performed on a JEOL JXA 8900 Superprobe electron microprobe at the Institute for Mineralogy at the Westfälische Wilhelms-Universität Münster. Operating conditions were 15 kV accelerating voltage, 120 nA beam current and a beam diameter of 3 µm. To achieve low detection limits (35 ppm) of Zr, peak counting rates were 30 s and 15 s for background for Si, Nb and Zr with 5 accumulations. To avoid boundary effects, we measured rutiles >10 µm. We used the quality control after Zack et al. (2004), by measuring the Si concentration, ensuring a maximum limit for the Si content of 250 ppm.

We performed EMPA to determine the mineral chemistry and chemical zoning of key minerals. Most of the EMPA were performed on a JEOL JXA 8200 Superprobe electron microprobe, equipped with five wavelength-dispersive spectrometers (WDS), at the Freie Universität Berlin, Germany. Some of the analyses were performed on a Cameca SX100 at Camparis in Université Paris 6. Operating conditions were 15 kV accelerating voltage, 20 nA beam current and a beam diameter of 5 µm for white micas, amphiboles and epidotes, and of 1 µm for all other minerals. Both natural and synthetic standards have been used. The raw data were corrected with the ZAF procedure. The relative analytical error for major-elements is less than 1%. Peak counting times are 10 s for Na, Mg, Al, Si, Ca, K, Ti, and Ba, 30 s for Mn and Fe, and we used half of the peak time for background counting. Element distribution maps were measured in WDS (Si, Al, Ca, Fe, Mn, Mg, Cr, Ti, Na, K) and energy-dispersive spectrometer mode with an acceleration voltage of 15 kV, a beam current of 20 nA. We used different pixel size (1-10 µm) and dwell time (70-100 ms) depending on the mapped area.

5.5.2 Raman spectroscopy (RS)

Raman spectroscopy (RS) has been performed to estimate both pressure and temperature independently. Pressure estimates on Qtz inclusions enclosed by garnet were performed at Freie Universität Berlin, Germany using a Horiba ISA Dilor Labram confocal Raman spectrometer, equipped with a Nd-YAG laser (532 nm wavelength) and temperatures on carbonaceous material at École Normale Supérieure, Paris, France using a Renishaw *in Via* equipped with an Ar ion laser (514.5 nm wavelength). Both Raman spectrometers were equipped with a CCD detector and laser spot size was focused to 1 µm through a microscope (x100 objective) on the material of interest. With a 1800 grooves/mm and 100 µm slit width the spectral resolution near 464 cm^{-1} was around 4 cm^{-1} for quartz measurements. Calibration was done on a Si standard with a 520.7 cm^{-1} peak in both cases. To ensure good determination of the quartz peak, the 464 cm^{-1} band of an additional quartz standard was used. Both standards were measured several times during the measuring period to correct for potential peak shifts with time. To avoid any heating effects on the carbonaceous material due to the laser, the laser energy on the sample surface was reduced to half of its full power by introducing adequate filters. To account for structural heterogeneity of the CM, 15-20 spectra were measured for each sample. The fitting of the spectra obtained with RS was processed using the program PeakFit 3.0 (Jandel Scientific) using a Voigt function.

5.6 Petrology and Peak P-T conditions

5.6.1 Petrography

We investigated 137 representative samples, among which ~30 were selected for analysis, from the GS unit, the HP-UHP unit with both metasedimentary, mafic, and intermediate composition rocks (sub-units 1-4), and the pillow-bearing unit (sub-unit 5). We particularly focused on blueschist- to eclogite-facies rocks to assess peak metamorphic conditions of the studied area.

5.6.1.1 Greenschist-facies unit

In the GS unit, the mineral assemblage is composed of albite + white mica + green amphibole + chlorite + epidote + quartz (Fig. 5.8a). Titanite, carbonate and iron oxides are present as minor to accessory phases. Albite and white mica present a poikilitic texture and are elongated parallel to the schistosity. Epidote, chlorite, and green amphibole make up the matrix as patchy small grains. Quartz is present as porphyroblasts in the matrix. Omphacite, blue amphibole, rutile, and garnet are systematically absent, suggesting peak metamorphism at greenschist-facies conditions. The same mineral assemblage has been determined for samples belonging to the greenschist-facies unit in the south of the belt.

5.6.1.2 Prograde blueschists

Prograde blueschists consist of blue glaucophane (up to 70 vol. %) + garnet ± white mica ± epidote ± quartz (Fig. 5.8b). Garnet porphyroblasts (0.5-1 cm) are euhedral to subhedral. Garnet contains variable amount of inclusions of quartz ± epidote ± omphacite ± amphibole ± chlorite ± carbonate and numerous small Ti-phases. Glaucophane compose the matrix as elongated crystals. The Ti-phase is mainly rutile and occasionally titanite. Some samples contain carbonate. Apatite, zircon, and iron oxide represent the accessory minerals.

5.6.1.3 Eclogites

The mineral assemblage of eclogites consists of omphacite (up to 80 vol. %) + garnet ± amphibole ± white mica ± epidote (Figs. 5.7a, 5.8c). Garnet occurs as euhedral to subhedral porphyroblasts of 0.5 mm to 3-5 cm size and contains similar inclusions to garnets in blueschists (Fig. 5.8d). Epidote and chlorite are commonly found in the core to mantle while omphacite is mainly found in the mantle of garnet, suggesting prograde garnet growth. Garnet has often inclusion-free rims (Fig. 5.8d). Matrix omphacite is anhedral and forms patchy and fibrous grains. When present, matrix amphibole is sub- to euhedral with a prismatic to needle shape. White mica is present as euhedral lamellae. Euhedral rutile occurs as inclusion in garnet, amphibole, white mica, epidote and in the matrix (up to 5%) and is in places rimmed by titanite, when found in the matrix assemblage. Some samples contain carbonate as a minor phase. Accessory minerals include apatite, pyrite, zircon, and iron oxide.

5.6.1.4 Retrograde blueschist-facies to greenschist-facies rocks

Blueschist-facies retrogression is indicated by the replacement of omphacite and/or glaucophane by blue-green amphiboles (Fig. 5.8e), with rare relicts of glaucophane in amphibole cores. Retrogression is also indicated by the presence of albite porphyroblasts (Fig. 5.8e) and titanite as the main Ti-phase although few rutile grains remain in some samples. The greenschist-facies retrogression is marked by further chloritisation of various Mg-Fe-rich minerals such as amphibole, omphacite, and garnet (Fig. 5.8f).

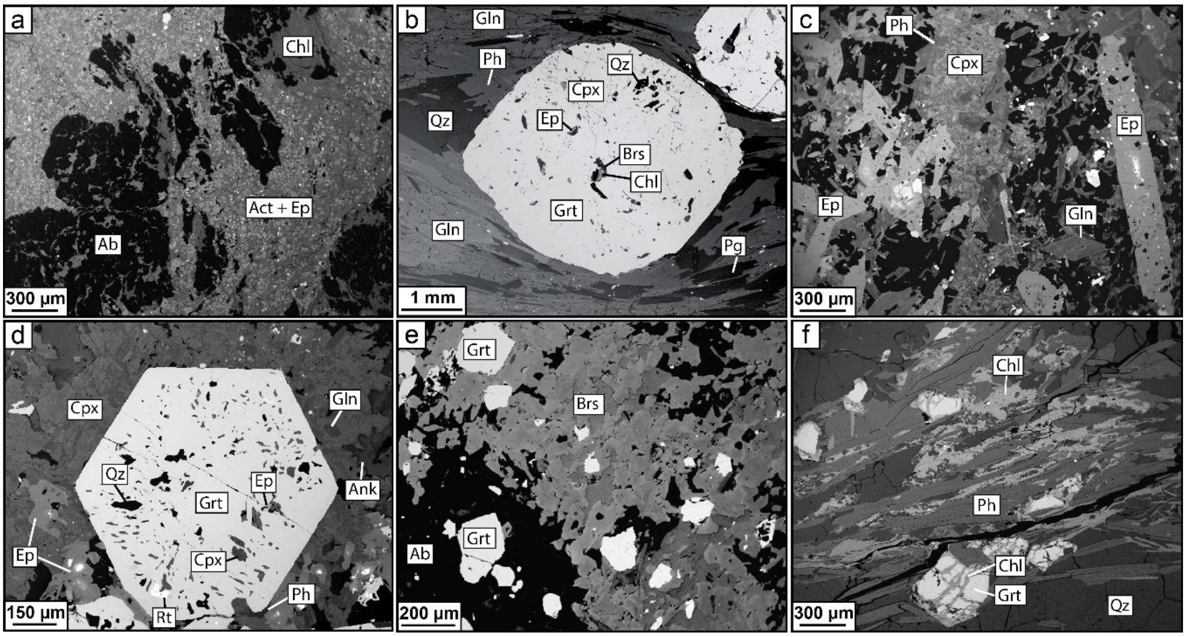

Figure 5.8: Backscattered electron (BSE) images: **(a)** greenschist-facies samples (from the greenschist-unit), with a paragenesis of Ab-Ep-Chl-Act. **(b)** Blueschist-facies sample composed of a glaucophane-phengite-paragonite matrix with quartz phenocrysts and garnet porphyroblasts. **(c) (c)** Eclogite-facies samples, with clinopyroxene matrix and euhedral phenocrysts of epidote, glaucophane, quartz and phengite. **(d)** Eclogite-facies samples with euhedral garnets hosting numerous inclusions, in a clinopyroxene matrix with euhedral epidote, phengite, glaucophane and additional ankerite. **(e)** Sample with indications for retrogressed blueschist-facies conditions, with undeformed barroisite, an albite matrix, and with small euhedral inclusion-free garnets. **(f)** Greenschist-facies retrogression in a metapelite, indicated by chloritisation of garnets, and numerous chlorite patches.

5.6.1.5 Micaschist-felsic rocks

Many rocks are characterized as garnet-bearing micaschist-felsic rocks with a mineral assemblage of white mica + garnet + quartz + albite. The presence of omphacite, amphibole, or epidote shows that these rocks are impure pelites with a variable psammitic and/or mafic fraction.

Garnet size and shape vary significantly among samples, from euhedral to anhedral. The small garnet crystals (0.1-1 mm in size) are mostly inclusion free, while the larger porphyroblasts (0.5-1 cm size) show the same inclusion pattern as the more mafic rocks. Given the intense deformation in the entire area, micaschists always present a strong schistosity (S_n), mainly marked by elongated beds of mica, quartz, and albite. Albite always presents a poikilitic texture.

5.6.2 Mineral chemistry

Representative analyses of major element composition of minerals are plotted on Fig. 5.9 and given in Table 5.1. Mineral abbreviations are after Whitney and Evans (2010).

5.6.2.1 Garnet

Most garnet porphyroblasts show a typical prograde chemical growth zoning, characterized by almandine (Fe) and spessartine (Mn) components decreasing from core to rim, while the pyrope (Mn) and grossular (Ca) components are increasing (Table 5.1; Fig. 5.9a). Some samples nevertheless exhibit garnet with different zoning patterns, such as oscillatory zoning, two step growth, or embayment due to corrosion followed by a phase of new garnet growth. Garnets in eclogite-facies MS, blueschist-facies MS, and micaschists samples have an average composition of Alm_{55-82}–Pyr_{1-15}–Grs_{14-41} (expect sample FTS 2-7: Alm_{52-63}–Pyr_{14-25}–Grs_{22-25}), Alm_{62-84}–Pyr_{4-15}–Grs_{7-26} and Alm_{60-82}–Pyr_{4-19}–Grs_{6-28}, respectively (Fig. 5.9a; Table 5.1).

5.6.2.2 White mica

White mica occurs as paragonite and/or phengite. They form single euhedral crystals of paragonite and phengite (or an intergrowth) in mafic eclogite- to blueschist-facies samples. In pelitic rocks, white mica align along the schistosity and form the matrix. Paragonite and phengite present Na (Na/(K+Na)) values of 0.8-1 and 0.1-0.3, respectively. Phengites show Fe+Mg (pfu) values ranging from 0.37 to 0.67 and a Si (pfu) content of 3.25 to 3.70 (Fig. 5.9b). Offset from the tschermak 1:1 line (Fig. 5.9b) is due to a high Fe^{3+} content. Paragonite displays a Fe (pfu) content ≤ 0.025.

5.6.2.3 Clinopyroxene

Clinopyroxene is classified according to the nomenclature of Morimoto (1988). The estimation of the ferric iron content is based on the method described in Droop T.,R. (1987). Most of the clinopyroxene minerals are omphacite (Jd_{24-58}–Ae_{0-32}–$Di\text{-}Hd_{30-62}$), except two samples, which are partly in the field of aegerine-augite (Jd_{21-34}–Ae_{30-36}–$Di\text{-}Hd_{33-47}$) (Fig. 5.9c; Table 5.1). Omphacites form a matrix of intergrown patchy grains, due to variation of jadeite and aegerine composition. Omphacite occurring as inclusion in garnet and within the matrix display the same compositional range, although inclusions tend to be closer to the aegirine-augite field.

5.6.2.4 Amphibole

Amphibole is classified according to the nomenclature of Leake et al. (1997) (Fig. 5.9d) and structural formulae are calculated after the procedure outlined by J. Schumacher (in Leake et al., 1997). Amphiboles are mainly glaucophane and barroisite in composition, with minor occurrences of winchite, richterite, Mg-hornblende, crossite and rare actinolite (Table 5.1). They occur as prismatic and acicular euhedral crystals, or prisms elongated parallel to schistosity. They form porphyroblasts floating in the matrix, as matrix minerals, or as inclusion in other minerals such as garnet. Amphibole retrogression is marked by thin barroisitic or crossitic rims surrounding glaucophane porphyroblasts. Amphibole inclusions in garnet have compositions similar to the matrix minerals.

5.6.2.5 Epidote mineral

Epidote-group minerals occur as prismatic and acicular shape porphyroblasts of various sizes in the matrix or as inclusions in garnet. Some samples contain large poikilitic crystals. Most matrix epidote-group minerals present a core to rim zoning varying from allanitic or epidotic (LREE- or Fe^{3+}-rich) to clinozoisite (Al^{3+}-rich). In the greenschist-facies sample, their composition is closer to the clinozoisite end-member, with XAl=0.7-0.9 (Table 5.1).

5.6.2.6 Chlorite

Chlorite, when present, is commonly associated with garnet and appears in garnet core regions as inclusion, or filling fractures across garnet, or replacing garnet at garnet rims. In retrogressed samples, chlorite is present in the matrix as elongated or patchy crystal. Their XMg varies between 0.2 and 0.6 in the HP-UHP unit, while chlorite in the greenschist unit has an XMg=0.64-0.67 (Table 5.1).

Table 5.1: Representative major element composition of minerals of Tianshan metamorphic rocks

Sample	AK 14.19	AK 14.19	AK 14.33	AK 14.33	AK 15.04	AK 15.04	AK 15.04	FTS 2-7	AK 14.35	AK 14.35	AK 14.19	AK 14.19	FTS 2-7
Type	*BS*	*BS*	*Ecl*	*Ecl*	*Ecl*	*Ecl*	*Ecl*	*Ecl*	*BS*	*BS*	*BS*	*BS*	*Ecl*
Mineral	Gt rim	Gt core	Gt rim	Gt core	Cpx - incl	Cpx - mat	Cpx - mat	Cpx - incl	Phg	Pg	Bar	Gln	Cross
SiO2	38.23	36.95	37.20	37.23	54.11	55.10	56.47	54.33	53.28	50.05	49.93	58.35	53.83
TiO2	0.03	0.05	0.04	0.08	0.11	0.01	0.01	0.04	0.22	0.08	0.26	0.01	0.10
Al2O3	21.64	20.74	21.90	21.21	6.71	7.56	10.69	6.81	26.63	38.62	10.48	12.22	9.62
Cr2O3	n.d.	n.d.	n.d.	n.d.	0.10	0.09	0.08	0.00	n.d.	n.d.	0.03	0.03	0.00
FeO	28.85	34.60	26.61	29.71	12.42	11.06	6.05	16.98	2.50	0.46	13.49	9.30	15.73
Fe2O3	n.d.	n.d.	n.d.	n.d.	n.d.	n.d.	n.d.	n.d.	n.d.	n.d.	n.d.	n.d.	n.d.
MnO	0.21	2.48	0.73	1.72	0.04	0.04	0.03	0.08	0.00	0.02	0.10	0.00	0.00
MgO	3.39	2.18	2.00	1.58	6.16	6.10	6.92	3.51	3.49	0.13	11.36	10.21	8.79
CaO	8.03	2.63	11.36	8.09	13.56	12.62	12.04	8.35	0.00	0.09	7.42	0.44	2.45
Na2O	0.02	0.08	0.03	0.00	6.55	7.07	7.46	9.06	0.51	6.89	3.66	6.91	6.08
K2O	0.00	0.01	0.01	0.01	0.00	0.00	0.01	0.01	9.93	0.56	0.24	0.03	0.13
Total	*100.40*	*99.68*	*99.88*	*99.63*	*99.75*	*99.63*	*99.77*	*99.16*	*96.55*	*96.90*	*96.97*	*97.52*	*96.73*
Si	6.01	5.99	5.90	5.98	1.99	2.01	2.02	0.00	3.49	3.12	7.15	7.92	7.65
Ti	0.00	0.01	0.01	0.01	0.00	0.00	0.00	0.31	0.01	0.00	0.03	0.00	0.01
Al	4.01	3.96	4.10	4.02	0.29	0.33	0.45	0.00	2.05	2.84	1.77	1.96	1.61
Cr	0.00	0.00	0.00	0.00	0.00	0.00	0.00	0.54	n.c.	n.c.	0.00	0.00	0.00
Fe_{tot}	3.79	4.69	3.53	3.99	0.38	0.34	0.18	0.20	0.14	0.02	1.62	1.06	1.87
Fe^{2+}	3.79	4.69	3.53	3.99	0.19	0.19	0.15	0.00	n.c.	n.c.	1.08	0.81	1.24
Fe^{3+}	0.00	0.00	0.00	0.01	0.19	0.15	0.03	0.20	n.c.	n.c.	0.54	0.25	0.63
Mn	0.03	0.34	0.10	0.24	0.00	0.00	0.00	0.34	0.00	0.00	0.01	0.00	0.00
Mg	0.79	0.53	0.47	0.38	0.34	0.33	0.37	0.67	0.34	0.01	2.42	2.07	1.86
Ca	1.35	0.46	1.93	1.39	0.53	0.49	0.46	0.00	0.00	0.01	1.14	0.06	0.37
Na	0.01	0.03	0.01	0.00	0.47	0.50	0.52	0.27	0.06	0.83	1.02	1.82	1.67
K	0.00	0.00	0.00	0.00	0.00	0.00	0.00	0.00	0.83	0.05	0.04	0.01	0.02
XMg	0.17	0.10	0.12	0.09	0.47	0.49	0.67	0.00	0.71	n.c.	0.60	0.66	0.50
Alm	63.56	77.97	58.51	66.52									
Pyr	13.30	8.77	7.85	6.33									
Grs	22.67	7.60	31.99	23.12									
Sps	0.48	5.66	1.63	3.91									
And	0.00	0.00	0.02	0.12									
Dio					0.34	0.33	0.35	75.00					
Hed					0.19	0.18	0.14	0.17					
Jad					0.26	0.34	0.48	0.17					
Acm					0.19	0.16	0.03	0.31					
(Ca+Na) (B)											2.00	1.88	2.00
Na (B)											0.86	1.82	1.63
$Fe^{3+}/(Fe^{3+}+Al^{VI})$											0.37	0.12	0.33

XMg=Fe2+/(Fe2+/Mg); Alm: almandine, Grs: grossular, Prp: pyrope, Sps: spessartine, And: andradite, dio: diopside, hed: hedenbergite, Jad: jadeite, acm: acmite. Fe3+ was calculated assuming stoichiometric mineral compositions

Table 5.1: following

Sample	FTS 2-7	FTS 2-7	M 14.8	M 14.8	AK 14.33	FTS 2-7	FTS 2-7	M 14.8	AK 14.19-2	AK 14.33	FTS 2-7	AK 15.04
Type	*Ecl*	*Ecl*	*GS*	*GS*	*Ecl*	*Ecl*	*Ecl*	*GS*	*BS*	*Ecl*	*Ecl*	*Ecl*
Mineral	Bar	Fe-Gln	act	Ep - mat	Ep - mat	Ep - mat	Ep - inc	Chl	Chl	Ab	Cc	Ank
SiO2	48.47	53.91	54.55	36.87	39.59	38.47	38.18	25.71	27.00	68.62	0.00	0.02
TiO2	0.27	0.12	0.00	0.41	0.09	0.07	0.01	0.04	0.05	0.03	0.01	0.00
Al2O3	10.16	9.77	0.88	28.35	32.25	24.71	21.41	19.26	19.99	19.53	0.01	0.00
Cr2O3	0.00	0.00	0.00	n.d.	n.d.	n.d.	n.d.	0.00	0.01	n.d.	0.00	11.01
FeO	19.07	15.61	9.25	0.00	0.00	0.00	0.00	18.89	22.56	0.13	0.11	0.05
Fe2O3	n.d.	n.d.	n.d.	5.18	1.60	11.20	14.78	n.d.	n.d.	n.d.	n.d.	n.d.
MnO	0.08	0.03	0.11	0.07	0.00	0.01	0.27	0.16	0.08	0.04	0.04	0.09
MgO	7.98	8.35	17.38	0.04	0.02	0.11	0.02	19.60	17.76	0.00	0.01	14.48
CaO	5.70	2.32	13.14	24.73	24.72	23.44	23.31	0.15	0.01	0.15	54.23	27.80
Na2O	4.81	6.46	0.19	0.01	0.07	0.00	0.00	0.00	0.01	11.27	0.00	0.04
K2O	0.31	0.11	0.03	0.00	0.00	0.00	0.00	0.01	0.01	0.02	0.00	0.00
Total	*96.86*	*96.66*	*95.52*	*95.66*	*98.33*	*98.01*	*97.97*	*83.82*	*87.48*	*99.78*	*54.40*	*53.49*
Si	7.11	7.70	7.91	2.92	3.01	3.03	3.06	2.75	2.80	3.00		
Ti	0.03	0.01	0.00	0.02	0.01	0.00	0.00	0.00	0.00	0.00		
Al	1.76	1.64	0.15	2.65	2.88	2.29	2.02	2.43	2.45	1.01		
Cr	0.00	0.00	0.00	0.00	0.00	0.00	0.00	n.c.	n.c.	0.00		
Fe$_{tot}$	2.34	1.86	1.12	0.34	0.09	0.66	0.89	1.69	1.96	0.01		
Fe^{2+}	1.61	1.45	1.12	n.c.	n.c.	n.c.	n.c.	n.c.	n.c.	n.c.		
Fe^{3+}	0.73	0.41	0.00	n.c.	n.c.	n.c.	n.c.	n.c.	n.c.	n.c.		
Mn	0.01	0.00	0.01	0.00	0.00	0.00	0.02	0.02	0.01	0.00		
Mg	1.75	1.78	3.76	0.00	0.00	0.01	0.00	3.13	2.75	0.00		
Ca	0.90	0.36	2.04	2.10	2.01	1.98	2.00	0.02	0.00	0.01		
Na	1.37	1.79	0.05	0.00	0.01	0.00	0.00	0.00	0.00	0.96		
K	0.06	0.02	0.01	0.00	0.00	0.00	0.00	0.00	0.00	0.00		
XMg	0.43	0.49	0.77	0.01	0.02	0.02	0.00	0.65	0.58	n.c.		
Alm												
Pyr												
Grs												
Sps												
And												
Dio												
Hed												
Jad												
Acm												
(Ca+Na) (B)	2.00	2.00	2.04									
Na (B)	1.10	1.65	0.00									
Fe^{3+}/(Fe^{3+}+Al^{VI})	0.46	0.24	0.00									

XMg=Fe2+/(Fe2+/Mg); Alm: almandine, Grs: grossular, Prp: pyrope, Sps: spessartine, And: andradite, dio: diopside, hed: hedenbergite, Jad: jadeite, acm: acmite. Fe3+ was calculated assuming stoichiometric mineral compositions

5.6.2.7 Rutile/Titanite

In fresh high-pressure rocks, the main phase is rutile occurring in the matrix and as inclusion in garnet, white mica, amphibole, and epidote. Matrix rutiles may develop a titanite rim when retrogression affected the rock.

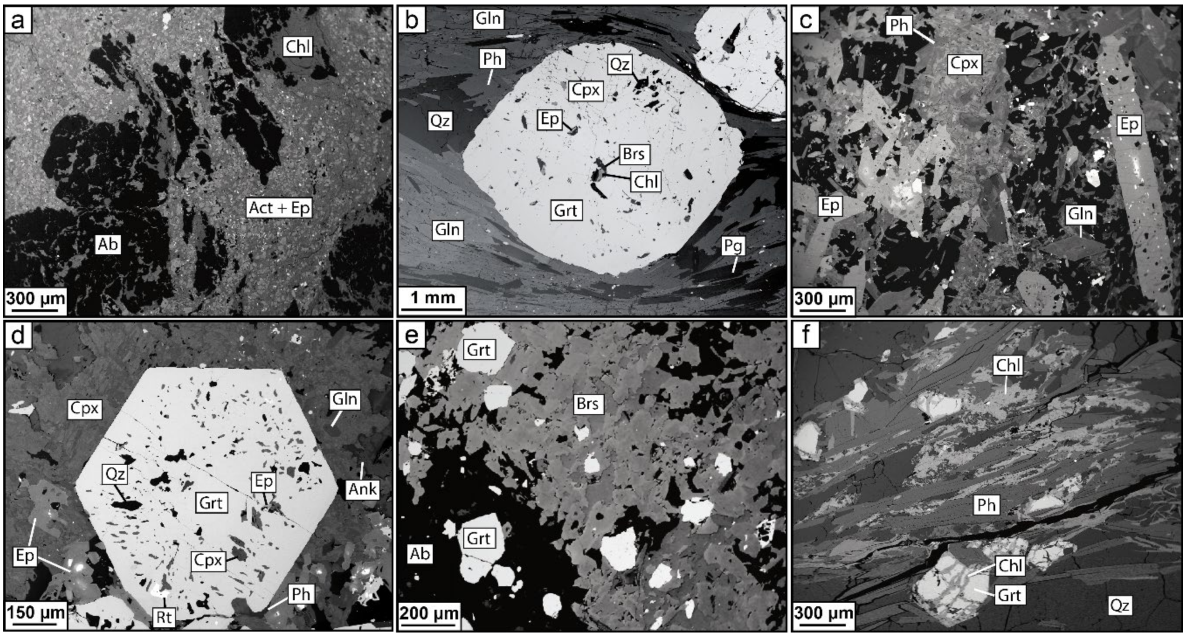

Figure 5.9: Chemical composition of garnet, phengite, amphibole and clinopyroxene, electron microprobe data). **(a)** Garnet ternary diagram presenting a high almandine-component. Eclogite samples (green field) present a higher grossular (Ca) component while blueschist-facies samples (blue field) are closer to the almandine (Fe) end-member (left). Micaschists (yellow field) present more variability, with however a tendency towards higher pyrope (Mg) content (right); **(b)** Phengite composition in the Fe+Mg vs Si p.f.u. diagram, the 1:1 black line represents the tschermak substitution ; (c) Composition of clinopyroxene in a ternary Di-Hd/Jd/Ae diagram after Morimoto (1988). Most clinopyroxene falls into the omphacite field, with few outlier compositions in the Aeg-Aug field. Different colors refer to pyroxene inclusions (orange field) and matrix pyroxene (blue field). Abbreviations after Whitney and Evans (2010); (d) Composition of amphibole, classified as glaucophane, barroisite, magnesio-hornblende, winchite or richterite and actinolite after Leake et al. (1997) (left); blue amphibole is mostly glaucophane, with a few occurrences of crossite (right).

5.6.2.8 Other minerals

Carbonates have compositions between ankerite and calcite (Table 5.1). Carbonate occurs as vein filling, single crystal in the matrix or as inclusions. Albite ($X_{Ab} > 0.98$, Table 5.1) formed during retrogression and is mostly found in metasedimentary-rich samples and occasionally in more mafic ones. Pyrite crystals occur as matrix mineral as well as inclusion in various minerals. Apatite is mostly present in the matrix as rounded grains. Zircon is present as rare small grains (few µm).

5.6.3 Peak P-T conditions

5.6.3.1 Peak temperature estimates

The thermometer based on graphitization of the carbonaceous material (T_C) was used for 24 samples in the HP-UHP unit, with a proportion of carbonaceous material (CM) varying between a few percent to up to 10-20 % of the mineral assemblage (Gt + CM + Wm + Qz ± Fd ± Amp), and for one sample north of the GHPD (M 14.10; to verify its peak metamorphic condition). The thermometer based on Zr content in rutile (T_{Zr}) was applied on 10 samples. This allows comparison of both thermometers and a temperature estimate for samples lacking carbonaceous material.

Estimated T_C values range between 525 °C and 553 °C (15 to 32 °C intra-sample error) with an average of 539 ± 13 °C (Fig. 5.10a). Two samples exhibit slightly off range T_C estimates of 509 ± 20 °C (AT 14.30) and 573 ± 29 °C (AK 14.10-1), although remaining in the range within error of the method. T_{Zr} estimates display slightly lower values: this is evidenced both by intra-sample comparison (Fig. 5.10b) and at the scale of the unit (Fig. 5.10a). T_{Zr} estimates range from 520 °C to 543 °C (14 to 22 °C intra-sample error), with 530 ± 7 °C on average (Fig. 5.10a). The combination of both thermometers results in an average temperature of 538 ± 12 °C for the entire HP-UHP unit with a rather homogeneous distribution throughout the studied area (Fig. 5.10g). No significant difference is observed between samples with distinct lithologies (blueschists, eclogites, metasediments; Fig. 5.10c). Sample M 14.10 exhibits a T_C value of 180 ± 35 °C with a maximum of 235 °C, consistent with maximum low-grade greenschist-facies conditions.

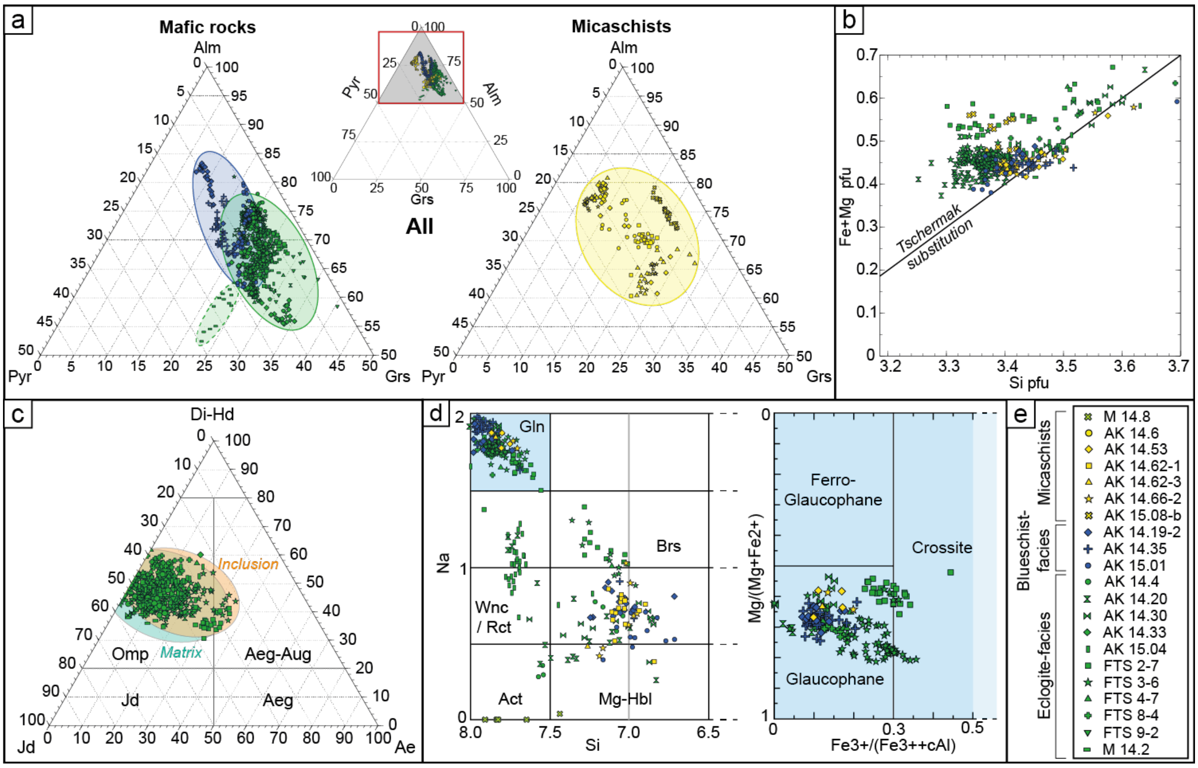

Figure 5.10: Estimates of peak P-T conditions. **(a)** Histogram of average T_C (obtained with Raman spectroscopy of carbonaceous material; red) and T_{Zr} (obtained with Zr in rutile; blue) for all samples, with an average value of ca. 535 °C. **(b)** Comparison of T_C vs T_{Zr} on samples for which both thermometers were applied. The 1:1 line (black) and method uncertainty (grey area) are indicated. **(c)** Comparison of peak temperature using the Zr-in-rutile thermometer for blueschist (left) blueschist-eclogite- (middle) and eclogite- facies conditions (right). **(d), (e)** Example of peak pressure estimates in a garnet (sample AK14.35-1); **(d)** Mn chemical map of the garnet taken for the QuiG analysis, displaying prograde continuous zoning from core to rim; location of each quartz inclusion (white crosses) and contours and labels (1-5, core, mantle, rim) of the different zones (white lines), **(e)** Raman shift (Δ 464) for each quartz inclusion (orange, left axis) and corresponding calculated pressure (black, right axis) for the different garnet zones. **(f)** Coesite Raman spectra of all coesite samples reported in this study. Distribution maps of **(g)** averaged estimated peak temperature T_C (red numbers) and T_{Zr} (blue numbers), and **(h)** pressure inferred from coesite and estimated via the QuiG and phengite barometry (black numbers; see text for details). Coesite findings are reported as stars on each map.

5.6.3.2 Minimum peak pressure estimates

The QuiG barometry was applied on 18 samples to estimate minimum values of the peak pressure (P_R) in the HP-UHP unit. Garnets used for QuiG barometry have an average composition of $Alm_{67.8}$-$Sps_{2.4}$-$Pyr_{9.0}$-$Grs_{20.5}$, with core to rim variations between $Alm_{14.9}$-$Sps_{7.8}$-$Pyr_{13.2}$-$Grs_{11.4}$ and $Alm_{4.6}$-$Sps_{1.9}$-$Pyr_{3.0}$-$Grs_{4.8}$. Most garnets present a prograde growth zoning, allowing to correlate the temperature linearly from core to rim for each mineral inclusion (Figs. 5.10d,e). The Δν464 shift (hence pressure) increases from garnet core to garnet mantle, with a slight decrease towards the garnet rim (Fig. 5.10e). Estimated values of P_R vary from 1.48 to 2.81 GPa with an error of 0.20 GPa.

5.6.3.3 Phengite barometry

For comparison and for samples lacking suitable quartz inclusions for the QuiG barometry, we applied the phengite barometry (P_{GOP}) on 6 samples in the HP-UH unit. We only considered maximum values to estimate the peak pressure, as tschermak substitution in phengite may have been lowered by later retrogression. P_{GOP} values obtained ranges from 2.33 to 2.98 GPa, with 3 samples exhibiting values above the quartz-coesite transition (>2.7GPa).

5.6.3.4 Coesite occurrences

Coesite inclusions in garnet were identified by Raman spectroscopy by their main bands at 521 cm^{-1} and are mainly found in the mantle zone of garnet (Fig. 5.10f). The presence of coesite implies a minimum pressure of 2.7 GPa for the determined regional temperature of ~540 °C. We considered a minimum peak pressure of 2.7 GPa for coesite-bearing samples, when the estimated pressure with QuiG (P_R) and/or phengite barometry (P_{GOP}) was < 2.7 GPa. This provides a new range of pressures of 2.06 to 2.98 GPa, with an average of 2.52 ± 0.25 GPa, which reveals a rather homogeneous distribution throughout the sampled area (Fig. 5.10h). No variations in pressure are observed across the observed km-scale shear zones.

5.7 Discussion

5.7.1 Peak metamorphic conditions across the HP-UHP unit

Peak P-T conditions in the HP-UHP unit were investigated using various high precision independent methods on evenly distributed samples.

Peak temperatures estimated by RSCM spectroscopy, T_C, yielded a tight cluster at ~540 °C (Figs. 5.10a,c). Only two samples depart significantly from this average value (AT 14.30, T_C=509 °C and AK 14.10-1, T_C=573 °C) and may record local temperature deviations, possibly as a result of fluid-rock interactions. T_{Zr} yields slightly lower values than T_C, although overlapping within error (Figs. 5.10a1,a2). Minor Zr diffusion out of rutile grains during cooling may have lowered T_{Zr} estimates (Cherniak, 2000; Zack et al., 2004), which seems supported by the observation of local zircon or baddeleyite exsolutions within rutile. Interestingly, T_{Zr} displays no difference in temperature for eclogites or blueschists. This confirms that the distinct mineral assemblages of these rocks reflect individual bulk composition rather than different P-T conditions (e.g., Beinlich et al., 2010; Tian and Wei, 2014).

Estimated pressures, P_R and P_{GOP}, range from 1.48 GPa to 2.81 GPa and 2.31 GPa to 2.98 GPa, respectively. It should be recalled that P_R values determined through the QuiG barometry correspond to minimum estimates of Pmax, since estimated pressures only reflect the residual pressure preserved by the quartz inclusion, whose relaxation in turn depends on the elasticity of its host (Enami, 2012). The discrepancy, in some samples and in the same garnets (e.g., AK 14.66; Fig. 5.10b2), between very low P_R estimates around 1.5 GPa and the presence of coesite inclusions implying P > 2.7 GPa, could therefore result from cracks in the vicinity of the measured quartz inclusions (thereby altering quartz relaxation; Ashley et al., 2014a) or inclusions being located too close to the thin section edge. In particular, the dilatant transformation of coesite inclusions to quartz can fracture garnet (Chopin, 1984; Gillet et al., 1984; Van der Molen and Van Roermund, 1986), leading to partial decompression of quartz inclusions. Interestingly, the quartz maximum shift, peak P_R and coesite findings are mainly located in the garnet mantle zone, followed by a slight P_R decrease towards the rim.

Pressures estimated using the phengite barometry (P_{GOP}) are calculated based on textural equilibrium between phengite-omphacite-garnet minerals (using only euhedral garnet devoid of rim corrosion to ensure equilibrium between the last growth stage and the matrix minerals). Two of the samples recording PGOP >2.7 GPa contain coesite, suggesting that one may rely on this method to estimate pressure conditions if the minerals chosen really grew in equilibrium at peak conditions.

Combining T_{Zr} and T_C yields a regional average of ca. 540 °C for the HP-UHP unit, with no significant variations in temperature along and across the area (Fig. 5.10c1). This indicates that both thermometers record peak temperatures and are not affected by retrogression (e.g., Beyssac et al., 2002), whatever the lithology (eclogite, blueschist, micaschist) and effective bulk composition (Beinlich et al., 2010).

The distribution of global effective pressure P_{eff}, taken as the maximum value of pressure estimates (i.e., out of QuiG barometry, phengite barometry and coesite occurrence), is rather uniform though less homogeneous, ranging from 2.06 GPa to 2.98 GPa, with an average of 2.52 GPa (Fig. 5.10c2). The regional average of ca. 2.5 GPa for the given peak temperatures of ca. 540 °C suggests that the whole area had been at a depth close to or at the quartz-coesite transition zone, a conclusion supported by the many coesite findings (e.g., Lü et al., 2009; Lü and Zhang, 2012, this study). The values around 2.5-2.8 GPa are also in agreement with recent pseudosection modelling in the STMB (Lü et al., 2009, 2012a; Soldner et al., 2017; Tan et al., 2017). This pressure average around 2.5-2.7 GPa is supporting the existence of a critical point at ca. 80 km depth (Agard et al., 2009) and of coupling/decoupling level from numerical models (e.g., Syracuse et al., 2010; Wada and Wang, 2009).

These results demonstrate that the metavolcanoclastic sub-units of the HP-UHP sequence were subducted and detached from the downgoing slab to form a single nappe stack near peak burial UHP conditions (Fig. 5.11a). The continuous temperature increase from garnet core to garnet rim, and slight pressure decrease from garnet mantle to garnet rim, indicates partial exhumation of this unit at a slightly higher level, while heating up to 540 °C.

5.7.2 Tectonic implications at the scale of the area

5.7.2.1 Nature and origin of the lithologies

Detailed mapping reveals that the HP-UHP unit is composed of a ~4–5 km-thick metasedimentary and metavolcanoclastic sequence grading southward from more pelitic to more mafic (Fig. 5.5b). The N-MORB, E-MORB, OIB and/or arc geochemical signatures of the mafic rocks (Gao et al., 1995; Gao and Klemd, 2003; Liu et al., 2014; van der Straaten et al., 2012) testify to a complex oceanic crust (i.e., with seamount-like heterogeneities and/or subduction related arc-volcanism), while metasedimentary components (carbonates and micaschists) may correspond to the sedimentary cover of the subducting oceanic crust and/or trench or fore-arc basin sediments (Ai et al., 2006; Gao et al., 1995; Liu et al., 2014; Meyer et al., 2016).

Intercalated radiolarian cherts, pillow basalts and pillow breccias (with N-MORB to E-MORB signature; Gao et al., 1995) of the southernmost and last accreted unit (sub-unit 5) represent the upper portion of the oceanic slab. By contrast, we suggest that the north to south lithological and compositional gradient documented here (in sub-units 1 to 4; Fig. 5.5) reflects the incorporation of increasing amounts of trench material of volcanoclastic origin (likely upper plate derived, for example as a result of large volcanic eruptions; Kutterolf et al., 2008a, 2008b; Scudder et al., 2009) as the subduction system evolves.

This increasing input of volcanoclastic material may also reflect a change from subduction accretion (with only thin veneers of deep-sea sediments, as in sub-unit 1, making their way into subduction) to subduction erosion: the more psammitic and mafic components would correspond to large pieces of the accretionary prism and arc-derived material shoveled into subduction. Such an evolution was suggested for the Apennines to explain the change in slope basin deposits and the removal of the toe of the Ligurian accretionary prism (Remitti et al., 2011) and subduction erosion was previously proposed for the STMB (Ai et al., 2006; Liu et al., 2014).

5.7.2.2 Mélange

Two contradictory concepts were so far proposed for the structural evolution of the southern Chinese Tianshan metamorphic belt (STMB; Fig. 5.1b).

On the one hand, the STMB was regarded as a block in matrix tectonic mélange, assuming eclogite boudins and bodies are embedded in “country rock” metapelites (Klemd et al., 2015, 2011; Li et al., 2016; Meyer et al., 2016). Our findings conflict with such a mélange structure, as mapping reveals km-scale lateral continuities and interlayering of mafic and sedimentary rocks (Figs. 5.5a,d; see also Gao and Klemd, 2003; Liu et al., 2014). Some rocks nevertheless show a complex and even poly-cyclic metamorphic evolution (e.g., Li et al., 2016). One possible interpretation is that these rocks, in fact loose blocks or boulders sampled along river beds, were incorporated into the sequence in between the slices, i.e., along major shear zones of the nappe stack.

On the other hand, the STMB was described as consisting of two units: a UHP unit to the North, separated from a HP unit in the South by a ~10-15 km shear zone (Lü et al., 2012a; Tian and Wei, 2014). The lack of pressure gradient across the area (Fig. 5.11a), and across a particular contact, does not support the existence of this boundary (which was progressively shifted on the maps, as more and more coesite was discovered in the area; Lü et al., 2012a; Tian and Wei, 2014 and references therein).

Overall, the intimate layering, homogeneous peak P-T estimates (irrespective of sedimentary or mafic protoliths) and almost ubiquitous coesite occurrences throughout the entire study area stand in contradiction with both concepts. Large-scale shear zones do not separate units from various depths (Fig. 5.11a), contrary to earlier suggestions (e.g., Klemd et al., 2011), but rather accommodate deep stacking and minor later offsets during exhumation.

5.7.2.3 Succession and significance of deformation stages

Five stages of deformation were identified (Table 5.2), the first one being only identified in thin section (D_{n-1}) as quartz inclusion trails in garnet. The pervasive, dominant schistosity S_n (stage D_n) strikes approximately E-W. A similar ~ENE-WSW trend was reported from a few scattered schistosity measurements in the study of Tian and Wei (2013). Soldner et al. (2017) recently reported foliation and schistosity measurements with (i) a chaotic ENE-WSW trend in Atantayi, (ii) an E-W striking trend north of Kebuerte turning into (iii) a NW-SE trend towards the South.

Later D_{n+1} to D_{n+3} fabrics show very homogeneous N-S trending lineations with top to the north shear senses. These fabrics (Fig. 5.11a) are consistent with expected exhumation dynamics following northward subduction (Scheltens et al., 2015; Soldner et al., 2017). D_n and D_{n+1} likely occurred at eclogite-facies conditions, prior to blueschist-facies conditions. D_{n+2} reflects exhumation at blueschist-facies conditions, as shown by the ubiquitous glaucophane lineations along (mm- to km-scale) shear planes. Blue- and green-amphibole lineations associated to C' planes (i.e., extensional crenulation cleavage; D_{n+3}) suggest exhumation from blueschist- to greenschist-facies conditions. Burial, by contrast, is recorded in garnets enclosing S_{n-1}, which exhibit prograde growth zoning and preserve increasing pressures from core to rim (P_R ; Fig. 5.10).

5.7.2.4 Juxtaposition of the HP-UHP unit with other units

The greenschist-facies (GS) unit is bound in the North by the SCTS (e.g., Gao et al., 1999) and in the South by the greenschist/high-pressure detachment (GHPD; this study). This study reappraises the location of the GHPD slightly further to the North with respect to former ones.

While the distinction between the HP-UHP unit and the GS unit is sharp in the West, it is less clear in the East, as samples close and on either side of the contact may contain garnet. We propose that the GHPD is more diffuse in the East because it branches into several fault strands. The eclogite sample located immediately north of the GHPD (AK 15.20), with T_C ~544°C, would thus represent a tectonic sliver sheared off the HP-UHP unit along the contact during the juxtaposition of the two units. Contrary to Gao et al. (1999), describing greenschist-facies rocks as "country rocks" containing garnet and muscovite and possibly retrogressed from higher pressure conditions, only typical low-grade mineral assemblages and peak temperatures < 250°C were indeed found in this study.

In the central part of the GS unit, a small, unmetamorphosed and mostly undeformed sedimentary basin unconformably overlains and postdates the GHPD. No age constraints could be obtained, unfortunately, for this small molasse-type continental basin.

5.7.3 Geodynamic evolution of the southern Chinese Tianshan metamorphic belt

Using the above petrological and structural constraints, we tentatively reappraise the geodynamic evolution of the southern Chinese Tianshan metamorphic belt (Figs. 5.11b,d).

5.7.3.1 Initial stage: ongoing subduction

During subduction, the trench is filled with pelitic and carbonate sediments and a accretionary prism may develop. With time, increasing amounts of volcanic arc material (and greywackes) are supplied to the trench, resulting in a progressive increase of the volcano-clastic component with respect to its metapelitic counterpart. As the subduction system further evolves, pieces of the accretionary prism and trench infill are scraped off by the descending slab and dragged down along the subduction plate interface (Fig. 5.11a).

5.7.3.2 Detachment and accretion

Pieces dragged down into subduction get sequentially detached and stacked at high-pressure eclogite-facies HP-UHP conditions (Fig. 5.11b). The first slice comprises more metapelitic trench infill material, possibly from a still sediment-dominated margin. Slices successively detached reflect the continuous incorporation of an increasing volcano-clastic component into the trench, as a result of subduction erosion and/or increased volcanic activity (see discussion in § 6.2.1). The detachment of each slice is associated with thrust contacts now bounding the structural sub-units observed in the field (Figs. 5.11a,b). Although residing at ca. 80 km depth, temperatures were buffered and the HP-UHP unit remained relatively cool. This absence of significant heating after peak burial, might be explained by shielding of the STMB from heat transfer from the overlying mantle (e.g., fluid circulation along the plate interface or presence of a mantle wedge “cold nose”; Abers et al., 2006; Bayet et al., 2018; van der Straaten et al., 2008).

Detachment and stacking of the last tectonic slice with abundant pillow basalts (i.e., sub-unit 5; Fig. 5.5) remains enigmatic, as no peak pressure could be estimated for these rocks (Fig.

5.10c): this tectonic slice was either detached from the slab at UHP conditions, or later accreted to the rest of the sequence at eclogitic yet not UHP conditions.

Juxtaposition between the HP-UHP and GS units occurred late or even postdated the subduction history. Despite the lithological homogeneity of the GS unit and the fact that it is only underlain by subducted material, its paleogeographic significance is still unclear.

5.7.3.3 Exhumation

Exhumation and pervasive thinning of the HP-UHP sequence occurred at blueschist-facies conditions, as indicated by ubiquitous glaucophane lineations, most likely through the reactivation of the former thrusts as shear zones (Fig. 5.11c). From that stage onwards the nappe stack behaved as a single unit, which is supported by the homogeneous distribution of the peak P-T values throughout the entire area (Fig. 5.11a). Sub-unit 5, if not yet part of the nappe stack (see above), must have been detached by then from the descending slab, welded and exhumed together with the HP-UHP sequence.

5.7.3.4 Present day configuration

The greenschist unit was either exhumed to the surface prior to exhumation of the HP-UHP unit or coevally, in a single tectonic event yet during ongoing subduction. In both cases, the STMB finally developed a dome-like structure with the GS unit on top of the HP-UHP unit and 'detachment' faults on each side. This metamorphic dome may have formed while the UHP unit was exhumed throughout the greenschist unit, as in metamorphic core-complexes (REFS), or may represent later folding of previously exhumed units. Owing to the lack of diagnostic shape for the exhumation P-T path in support of the first hypothesis, folding is most likely postdating much of the exhumation. Both units were later tilted and subsequently eroded. A small molasse basin formed on top of the GHPD after all metamorphic units had reached the surface, and was later squeezed during (Cenozoic?) compression.

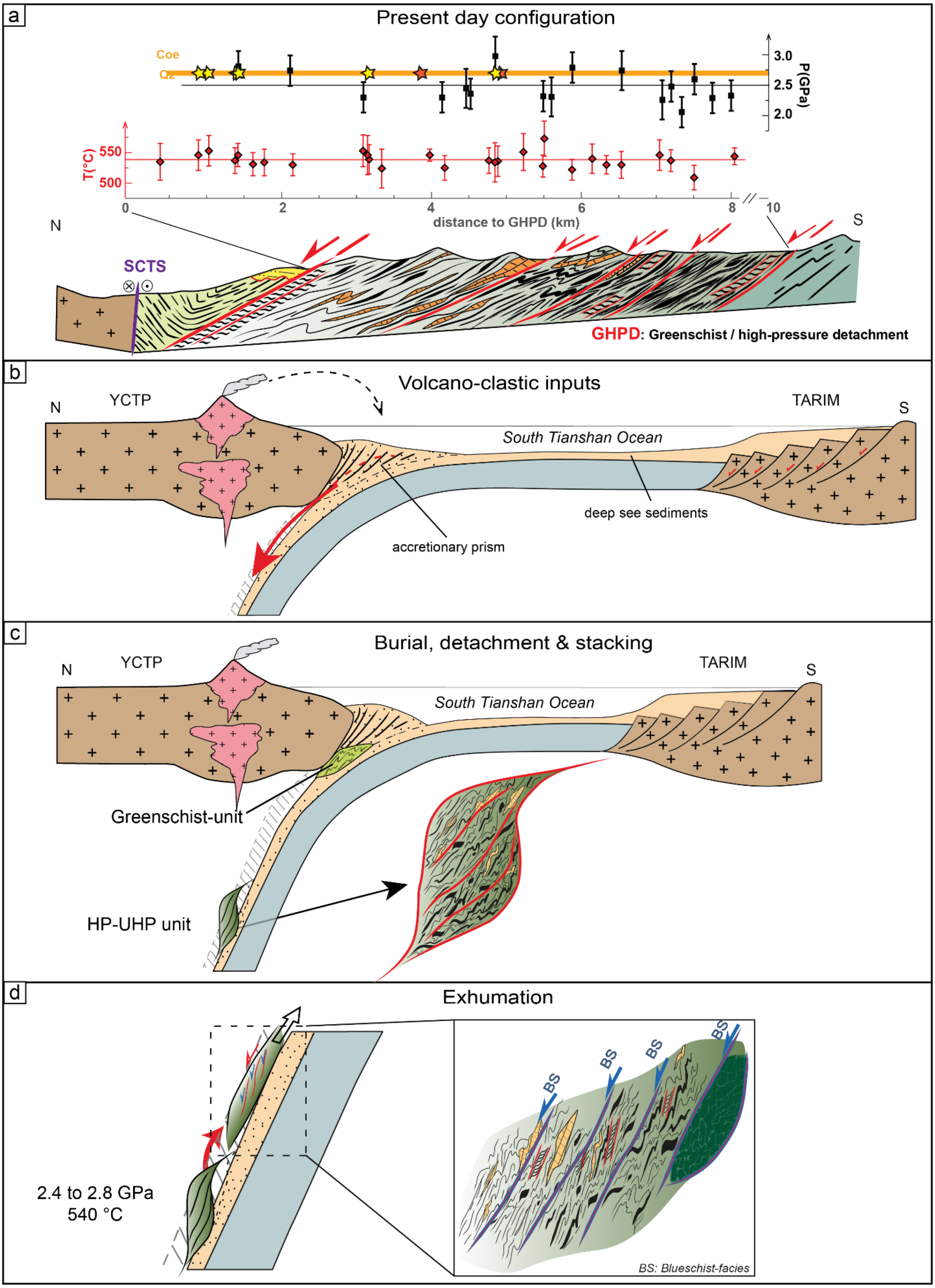
a
Present day configuration
Coe
Qz
3.0
2.5
2.0
P(GPa)
T(°C)
550
500
0
2
4
6
8
10
distance to GHPD (km)
N
S
SCTS
GHPD: Greenschist / high-pressure detachment
b
Volcano-clastic inputs
N
YCTP
TARIM
S
South Tianshan Ocean
deep see sediments
accretionary prism
c
Burial, detachment & stacking
N
YCTP
TARIM
S
South Tianshan Ocean
Greenschist-unit
HP-UHP unit
d
Exhumation
2.4 to 2.8 GPa
540 °C
BS
BS
BS
BS
BS: Blueschist-facies

Figure 5.11: Schematic geodynamic evolution model of the southern Chinese Tianshan metamorphic belt. **(a)** Present day configuration: pervasive deformation and detachment between the greenschist-unit and the HP-UHP sequence. Peak pressure-temperature estimates reported above the transect show that no gap in pressure and temperature exists between the slices. **(b)** Volcanoclastic inputs; scrapping off pieces from the accretionary prism and deposition of volcano-clastic material in the trench, further dragged down the subduction zone. **(c)** Burial, detachment and stacking at greenschist- and UHP- conditions; the UHP sequence consists of the successive accretion of several slices – separated by thrusts contacts – of material dragged down on top of the oceanic plate. **(d)** Exhumation and dismembering of the HP-UHP unit at blueschist conditions, with reactivation of the previous thrusts as blueschist-facies shear zones.

5.8 Conclusions

The systematic study of structural and lithological relationships tied to peak P-T estimates across the whole STMB allows to draw the following conclusions:

1. The lithology in the HP-UHP unit exhibits a north to south gradient, from more pelitic to more mafic. This is thought to reflect an increasing amount of volcanoclastic component in subducted material and/or a shift to subduction erosion mode through time. The studied area does not represent a block-in-matrix tectonic mélange, as continuous layers of mafic rocks are intimately interlayered with metapelitic layers.
2. The HP-UHP unit underwent rather homogeneous peak P-T conditions around ~2.5 GPa and ~540 °C and reached uniform UHP or near UHP conditions, as attested by the ubiquitous presence of coesite. Subducted trench infill was thus detached at HP-UHP conditions and stacked as several individual tectonic slices (sub-units 1-5) to form the present-day nappe stack.
3. Pervasive deformation occurs in the HP-UHP unit through five deformation stages: (i) Dn-1 records burial and is only visible at mm-scale as inclusion trails in garnet; (ii) Dn is represented by the penetrative north dipping schistosity striking ~ENE-WSW and most likely coincides with the nappe stacking of the sub-units recognized in this study (i.e., initial thrust contacts); (iii) Dn+1, corresponds to the eclogite to blueschist-facies crenulation and folding of the schistosity; (iv) Dn+2 is marked by distributed blueschist-facies shearing during exhumation and is reworking earlier, large-scale shear zones as extensional structures; (v) Dn+3 is characterized by ductile to brittle C’ structures locally cutting across all previous structures.
4. No gap in peak pressure or temperature is observed across the large-scale shear zones operating during BS-facies conditions. This observation suggest that they separate sub-

units stacked at similar depths and accommodate only minor offsets during later exhumation.

5. Progressive deformation patterns in the area are consistent with top-to-the-north subduction dynamics. The HP-UHP sequence was exhumed close to the surface and juxtaposed to the greenschist facies unit during or after its exhumation.

5.9 Acknowledgements

We thank Laura Airaghi for helpful comments and acknowledge Ralf Milke, Anja Maria Schleicher and Jasper Berndt-Gerdes for electron microprobe, XRF analyses and Raman spectroscopy. This research received funding from the People Programme (Marie Curie Actions) of the European Union’s Seventh Framework Programme FP7/2017–2013/under REA grant agreement no. 604713, ‘Zooming in between Plates (ZIP)’.

Chapter 6

A Rb-Sr perspective on the timing of peak burial for the HP-UHP Akeyasi metamorphic complex (Tianshan, NW China).

6.1 Abstract

New Rb-Sr multiple mineral isochrons were determined for the Akeyasi metamorphic belt (AMC) in Tianshan (NW China). Six samples, five micaschists and a white mica-bearing eclogite were taken from spatially distributed localities. The high-pressure mineral assemblages are characterized by an interlayering of phengite and paragonite with varying proportion among samples. Petrological observations suggest that paragonite growth likely occurred at prograde and retrograde stages of the metamorphic evolution. Additional pseudosection calculations indicate that they crystallize only at low pressure (<2.2 GPa) and are absent near peak metamorphic conditions. Three samples located in the north, center, and southern part of the AMC yield coherent Rb-Sr ages of 321.1 ± 1.7 Ma, 321.0 ± 1.9 Ma and 322.7 ± 1.9 Ma, in agreement with the previously determined timing of the peak metamorphism. Two samples exhibit isochrons suggesting younger ages of 315.9 ± 1.8 Ma and 310.0 ± 2.5 Ma, with the latter interpreted as reflecting a post-peak equilibration phase recorded in the AMC. One sample only results in a non-satisfying errorchron. Scattered results show that the interlayering of phengite and paragonite in our samples played an important role on determined age values and their significance for dating geological processes. Data from literature and this study demonstrate that: 1) near peak burial conditions occurred near 320.5 ± 6.6 Ma (2σ), followed by post-peak exhumation around 311 Ma; 2) different radiometric methods are required to interpret the obtained age values; and 3) there is a need to apply combined radiochronometric methods on spatially well distributed samples in a systematic way to unravel the geodynamic evolution of the AMC.

6.2 Introduction

Deciphering the geodynamic evolution of paleo-subduction systems is based on the accessible rock record and the knowledge of its geological context. In terms of high-pressure units it therefore requires extracting how the rocks have been buried and exhumed along, with the information of how they got juxtaposed to each other. The Akeyasi metamorphic belt (AMC), located in the Tianshan orogen (NW China), represents an example of such a high-pressure (HP) to ultra-high-pressure (UHP) complex. The geodynamic evolution of this belt is debated with contradictory geodynamic models. On one hand, the HP-UHP unit is described as being composed of mafic blocks in a metasedimentary matrix, interpreted as a tectonic mélange with rocks derived from various depths (e.g., Klemd et al. 2011). The rock record of such a mélange would display significant scatter of the peak pressure and temperature values and metamorphic ages found in the individual blocks and the matrix (e.g., Festa et al., 2010). On the other hand, Bayet et al. (2018) showed that the entire HP-UHP unit experienced very similar peak P-T conditions of ca. 540 °C and 2.5 GPa throughout its exposure, with widespread coesite findings, and a lithological sequence with continuous layers rather than blocks in matrix. They interpreted this rock record as being indicative for stacking of individual slices at great depth and an exhumation of the entire unit in a single process. Such a model implies coherent metamorphic ages for all high-pressure lithologies with no significant variations.

Previous studies attempting to constrain the timing of peak and post-peak metamorphic conditions in the AMC yielded scattered results applying Lu-Hf and Sm-Nd on garnet, U-Pb on zircon and rutile, and Rb-Sr on white mica geochronology. Peak metamorphic conditions were estimated to have occurred around 320.5 ± 6.6 Ma (e.g.Klemd et al. 2011; Liu et al., 2014; Soldner et al., 2017; Tan et al., 2017), while post-peak exhumation is less well constrained, with only a few studies clustering around 311 Ma (Klemd et al., 2005). Since none of the studies has been focused on samples from various and spatially widespread localities, this scatter in ages might be caused by the use of different methods, rock types, and analytical procedures.

The application of the Rb-Sr system on phengites turned out to be of particular use to date high-pressure events as phengite is a high-pressure phase and very prone to equilibrate with high-pressure mineral assemblage (e.g., di Vincenzo et al., 2006; Glodny et al., 2002). Still, the ability of the Rb-Sr phengite geochronology to date precisely the maximum P-T conditions might be biased by potential disequilibrium, re-equilibration, and closure temperature issues (Glodny et al., 2005; Kagami et al., 2003; Yong et al., 2013). However, Glodny et al. (2005) showed that metamorphic Rb-Sr white mica ages are related to crystallization or recrystallization of phengite, thus, to the last equilibration stage and not to cooling. Accordingly, to determine the significance of Rb-Sr ages it is of importance to combine dating with detailed petrological investigations.

In this study, we apply the Rb-Sr system to date phengite, given that phengite is a high-pressure mineral and that most of the rocks of the AMC are metasediments and white-mica bearing rocks (Gao and Klemd, 2003; Meyer et al., 2016; Wei et al., 2009). We report new Rb-Sr phengite ages from six samples well distributed over the entire AMC. Previously determined Rb-Sr data were recalculated using the new decay calibration λ^{87}Rb = 1.3972 ± 0.0045 × 10^{-11} yr^{-1} (Villa et al., 2015). We present a combined petrological and geochemical study and discuss the significance of our Rb-Sr regression ages in the context of the geodynamic evolution of the AMC.

6.3 Geological setting

The Tianshan orogen formed through the Paleozoic collision between the Tarim, Yili-Kazakh and Junggar plates and is part of the Central Asian Orogenic Belt (CAOB; e.g., Gao et al., 2009; Jahn et al., 2000; Kröner et al., 2014; Long et al., 2011). The Akeyasi metamorphic complex (AMC) is exposed in the southwestern Tianshan (NW-China; Gao et al., 1999, 1995; Fig. 6.1a). The AMC is delimited by the south Central Tianshan Suture (SCTS) in the north and the Northern Haerkeshan Peak Fault in the south, and contains a high-pressure to ultra-high-pressure (HP-UHP) unit in its central part (Bayet et al., 2018; Gao and Klemd, 2000; Fig. 6.1b).

The HP-UHP unit consists of interlayered metavolcanoclastic and metapelitic rocks with a gradient from more pelitic in the north to more mafic in the south (e.g., Bayet et al., 2018; Gao and Klemd, 2000). Rocks of the HP-UHP unit underwent eclogite-facies metamorphism with widespread numerous coesite occurrences (Bayet et al., 2018; Lü and Zhang, 2012). The AMC area exhibits pervasive deformation illustrated by penetrative schistosity, folding and shearing at various scales. Locally, km-scale shear zone separate structural sub-units developed during exhumation. Yet, the sub-units do not originate from various depths, as attested by spatially well-distributed rather homogeneous peak pressure (P) and temperature (T) conditions of ~2.5 GPa and ~ 540 °C for the entire HP-UHP unit (Bayet et al., 2018).

Based on various dating methods, including U-Pb on zircon and rutile, Lu-Hf and Sm-Nd on garnet, and Rb-Sr on white mica, the subduction events exhibited a wide range of age estimates, with ages for the peak burial varying between ~ 315 Ma and ~ 326 Ma. All together, they cluster around 320 Ma (e.g., Klemd et al. 2011; Li et al., 2011; Liu et al., 2014; Soldner et al., 2017; Tan et al., 2017; Yang et al., 2013; Fig. 6.1b). Exhumation is poorly constrained, with an estimation of ca. 311 Ma, mainly based on Rb-Sr, Ar-Ar, and K-Ar white mica ages (Klemd et al., 2005).

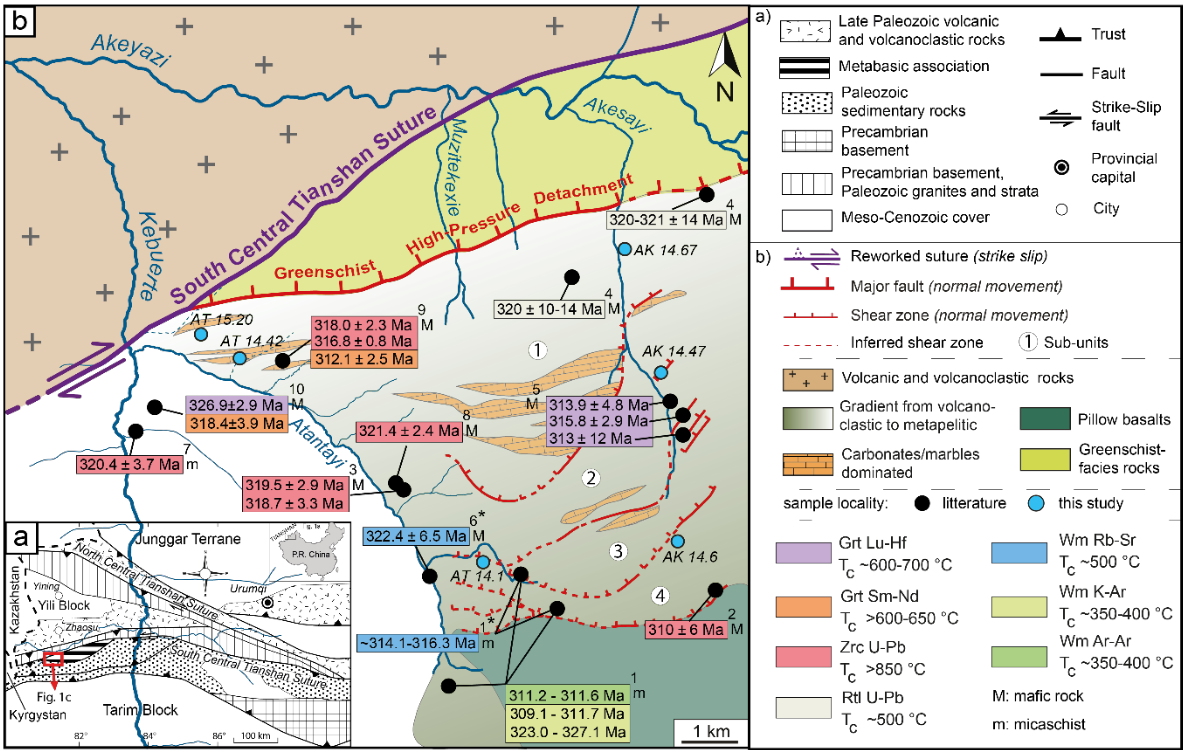

Figure 6.1: Geological overview maps of **(a)** the western Chinese Tianshan (Gao et al., 1999), **(b)** the Akeyazi metamorphic belt (AMC) modified after Bayet et al. (2018). The HP-UHP unit is located south to the Greenschist High-Pressure Detachment with labelled structural subunits 1 to 4. The literature coresponding to the displayed ages is indicated by the number on the upper-right corner of the boxes as listed in Appendix C1: #1: Klemd et al. 2005; #2: Zhang et al., 2007; #3: Su et al., 2010; #4: Klemd et al., 2011; #5: Li et al., 2011; #6: John et al., 2012; #7: Yang et al., 2013; #8: Liu et al., 2014; #9: Soldner et al., 2017; #10: Tan et al., 2017. Rb-Sr ages from John et al., 2012 and Klemd et al., 2005 were recalculated using the new decay constant of Villa (2015) as indicated by an asterix next to the number. Abbreviations: T_C: closure temperature; Gt: garnet; Zrc: zircon; Rtl: rutile; Wm: white mica.

6.4 Analytical methods

To determine the mineral chemistry and investigate the chemical zoning and the potential intergrowth of some minerals, electron microprobe analyses (EMPA) were carried out. EMPA were performed on a JEOL JXA 8200 Superprobe electron microprobe equipped with five wavelength-dispersive spectrometers (WDS) at the Freie Universität Berlin, Germany. Mineral analyses were performed using 15 kV accelerating voltage, a beam current 20 nA, and a beam diameter of 5 µm for white micas and amphiboles, and of 1 µm for all other minerals. Synthetic and natural standards were used. We applied the method described in Morimoto (1988) to estimate the ferric iron content of clinopyroxenes. Structural formulae of amphiboles and omphacite were calculated after the method of J. Schumacher (in Leake et al., 1997) and Droop T.,R., (1987), respectively. Minerals are abbreviated as suggested by Whitney and Evans (2010). Element distribution maps were measured in WDS and EDS (energy-dispersive spectrometer) mode with an acceleration voltage of 15 kV, a beam current of 100 nA.

We conducted Rb-Sr isotope analyses on mineral separates solely, to avoid potential disequilibrium of bulk rock analysis. We aimed for using three fractions of white mica and to establish the low intercept of the isochrons using additional apatite, amphibole, or omphacite fraction, depending on samples. All samples were crushed, sieved (100 µm, 280 µm and 500 µm), and subsequently cleaned with deionized water. Rb-Sr isotopic analysis were carried out at the Freie Universität Berlin, Germany. We spiked white micas (~5 mg), amphibole and omphacite (~10 mg), and apatite (~1 mg) with enriched ^{87}Rb and ^{84}Sr tracers prior to dissolution in a HF-HNO_3 mixture in Teflon bombs. Separation and purification of Rb and Sr were conducted in a silica-column filled with AG50W-X8 ion exchange resin. Isotopic ratios of Rb and Sr were determined in static multi-collection on a Thermo-Finnigan TRITON thermal ionization mass spectrometer (TIMS). Procedural blanks were lower than 100 pg for Rb and Sr. Measured ^{87}Sr/^{86}Sr ratios were corrected for mass-fractionation using ^{86}Sr/^{88}Sr = 0.1194 and using corrected NBS-987 Sr and an in-house Rb common solution as external standard. Standard NBS-987 Sr was measured at ^{87}Sr/^{86}Sr = 0.709879 ± 0.00044210 (2σ, n=32). The errors of element concentrations were less than 0.5% (2σ). We applied an error of 1% for ^{87}Rb/^{86}Sr and of 0.005% for ^{87}Sr/^{86}Sr. Isochron parameters were calculated using the Isoplot software (version 4.15; Ludwig, 2012).

6.5.5 Samples petrography and texture

6.5.1 Samples strategy and characterization

We conducted Rb–Sr geochronology on six samples spatially well-distributed over the entire HP-UHP unit (Fig. 6.1b). Samples were taken from different ‘subunits’ from north to south in the Akesayi and Atantayi valleys, to cross-check potential lateral variations in metamorphic ages.

Table 6.1. Whole rock major elements (in weight %) and trace elements (in ppm) composition

Sample	**AK 14.6-1**	**AT 14.47-1**	**AK 14.67-3**	**AT 14.1-3**	**AT 14.42-11**	**AT 15.20-B**
Rock type	**Mafic-micaschist**	**Mafic-micaschist**	**Micaschist**	**Micaschist**	**Wm-bearing eclogite**	**Micaschist**
SiO_2	61.70	62.89	66.96	70.37	45.02	64.45
TiO_2	0.79	0.79	0.31	0.38	1.09	0.68
Al_2O_3	16.94	15.90	14.75	12.51	14.07	15.02
Fe_2O_3	7.05	6.08	4.33	5.89	10.48	6.52
MnO	0.10	0.09	0.07	0.12	0.15	0.12
MgO	3.70	2.74	1.92	2.27	7.51	2.96
CaO	1.38	1.63	3.67	1.48	12.59	1.36
Na_2O	2.94	2.37	2.52	1.96	2.93	1.60
K_2O	2.09	2.81	1.02	2.02	0.19	3.11
P_2O_5	0.15	0.12	0.07	0.13	0.13	0.17
H_2O	2.68	2.60	2.02	2.15	1.89	3.11
CO_2	0.23	1.61	2.06	0.49	3.50	0.61
Sum	99.76	99.63	99.70	99.77	99.55	99.71
Ba	443	807	499	460	456	770
Cr	102	97	28	15	583	95
Ga	20	20	15	15	15	17
Nb	12	14	<10	<10	<10	12
Ni	55	46	<10	<10	160	44
Rb	93	117	25	49	<10	139
Sr	218	167	222	94	121	82
V	119	106	58	48	291	107
Y	30	32	14	19	29	30
Zn	80	81	60	103	94	97
Zr	184	232	77	75	61	182

XRF data (GFZ Potsdam). Wm, white-mica.

AK14.67-3 (GPS: 42°33'05" N, 81°18'03" E), AK 14.47-1(GPS: 42°31'46" N, 81°18'34" E) and AK 14.6-1 (GPS: 42°29'57" N, 81°18'49" E) belong to units 1, 2 and 4 from the Akesayi valley, respectively. AT 14.42-11 (GPS: 42°31'455' N, 81°12'27" E) and AT 14.1-3 (GPS: 42°29'44" N, 81°15'59" E) are located in units 1 and 4 from the Atantayi valley, respectively. Sample AT 15.20-b (GPS: 42°32'11" N, 81°11'54" E), located close to sample AT 14.42-11, was additionally analyzed.

Whole rock major- and trace-element compositions are presented in Table 6.1. Besides sample AT 14.42-11, all samples display similar silica rich compositions (61.7 to 70.4 %) and are classified as micaschists. Their Rb and Sr concentrations vary between 25 and 139 ppm and between 82 and 222 ppm, respectively. Sample AT 14.42-11 is described as a white mica-bearing eclogite with a low silica content (45.0 %) and concentrations of Rb and Sr <10 ppm and of 121 ppm, respectively.

All samples underwent similar peak temperature conditions near 540 °C. Their minimum peak pressure has been estimated at ca. 2.7 GPa, with the exception of sample AK 14.6-1, which lacks any pressure estimate.

6.5.2 Mineral chemistry

Representative analyses of the major element composition of minerals are given in Table 6.1 and plotted on Fig. 6.2.

6.5.2.1 Clinopyroxene and amphibole

Clinopyroxene is classified as omphacite and forms a matrix of intergrown patchy grains related to variations in jadeite and acmite contents. Amphibole is mainly glaucophane, with rare barroisite or actinolite occurrence, and occurs as phenocrysts floating in the matrix, as matrix mineral, or as inclusion in other minerals such as garnet. Amphibole is either prismatic or acicular euhedral crystal, or prism elongate parallel to schistosity.

6.5.2.2 White mica

White mica occurs as both phengite and paragonite (Fig. 6.2). Iron values (pfu) range from 0.06 to 0.18 for phengite and are <0.03 for paragonite. X_{Fe} values of phengite vary between 0.34 and 0.64. Silica contents of phengite range from 3.25 to 3.64 pfu.

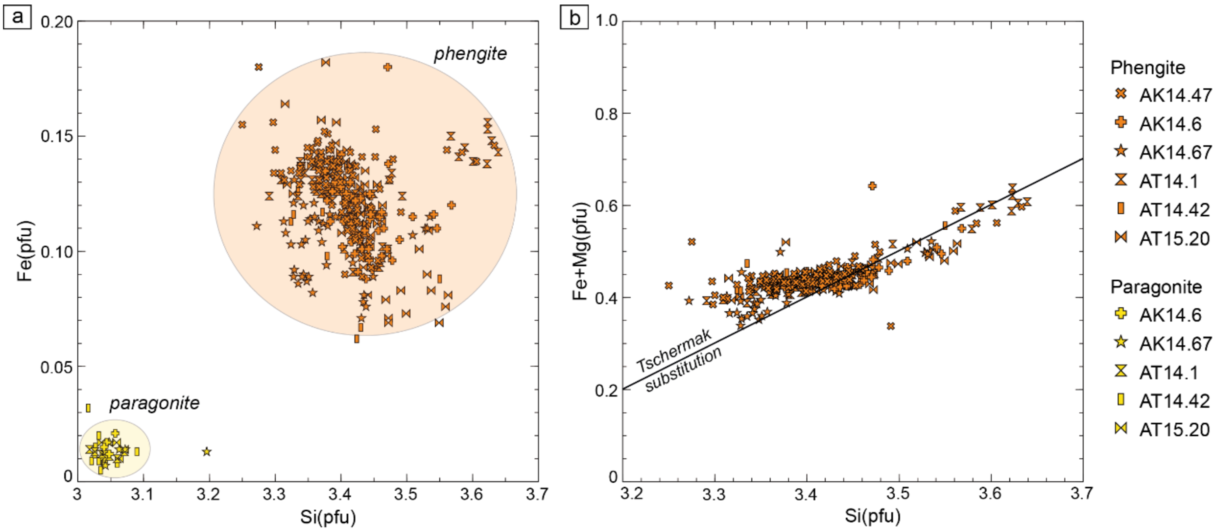

Figure 6.2: Chemical composition plot of white micas for this study. **(a)** Fe content in white mica against Si (pfu). Paragonites (yellow symbols) contain very low Fe content and Si <3.1 while phengite (orange symbols) Si and Fe content are higher. **(b)** Fe+Mg (pfu) relative to Si (pfu) content in phengite. Phengites exhibit an increase of Fe+Mg (pfu) with increasing Si (pfu). Most analysis plot above the tschermak substitution, as ‘true’ phengites.

6.5.3 Petrography

Mineral assemblages vary among the samples with white mica, quartz, and garnet being present in all samples. Apatite was found as accessory mineral in all samples with the exception of sample AT 14.42-11. The white mica fraction consists of phengite and paragonite, which can be easily distinguished on backscattered electron images (BSE) with the SEM and on chemical maps. Phengite exhibits a light grey color on BSE image and high K concentrations, while paragonite displays a dark color on BSE images and high Na concentrations (Fig. 6.3). Phengite and paragonite are often interlayered, strongly deformed and define the schistosity (Figs. 6.3a, b, c). Some paragonite formed prograde, as indicated by a rim consisting of phengite and an increase of K into the crystal interior (Fig. 6.3d). On the contrary, it is evident that euhedral paragonite crystals formed post-kinematic, as they float in the matrix with an orientation different to the schistosity or surround prograde phengite (Fig. 6.3e). Finally, paragonite and phengite can be found intergrown with other minerals, such as amphibole (Fig. 6.3f). Albite present in the various samples is systematically retrograde and present a poikilitic texture, with numerous inclusions.

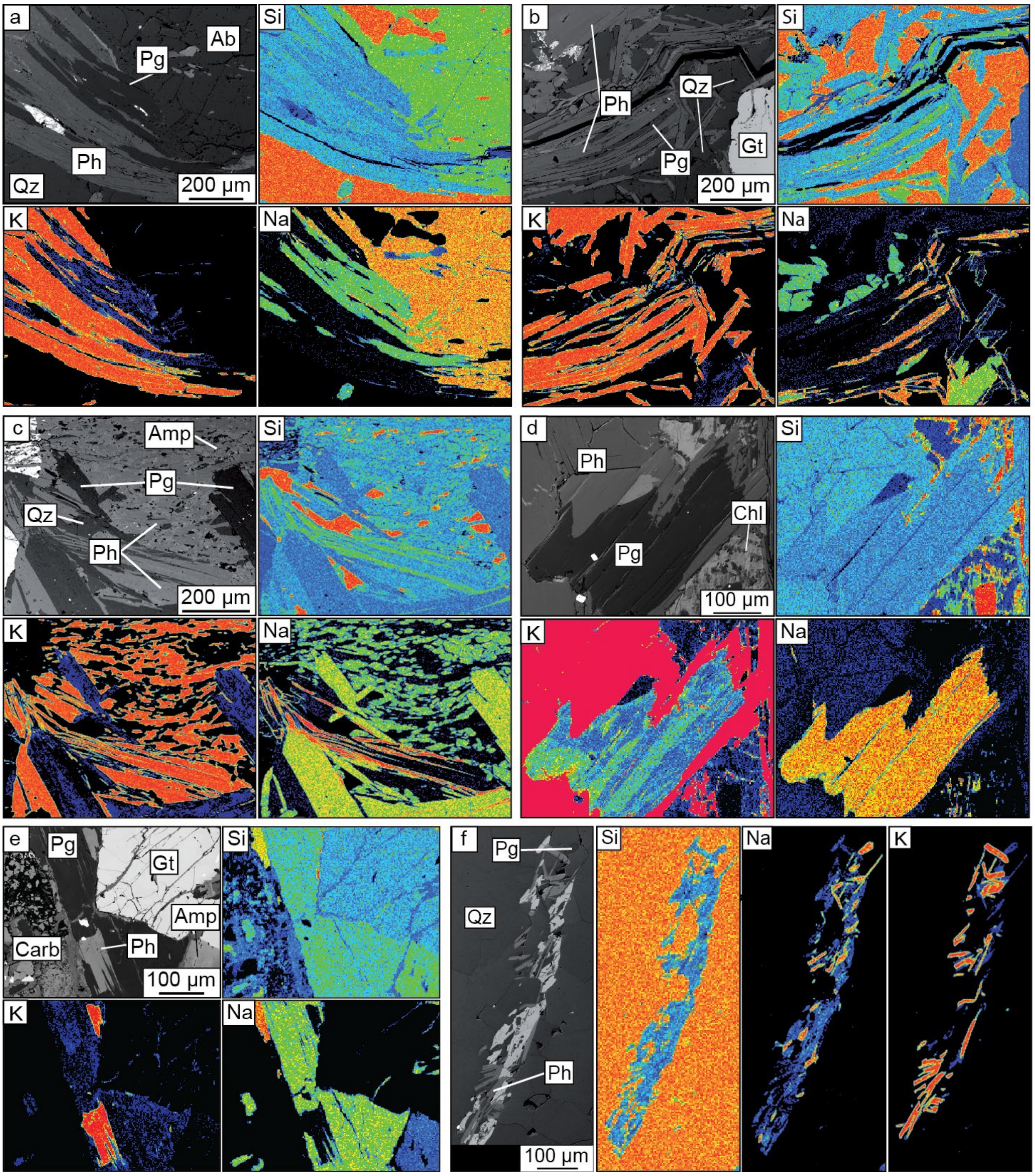

Figure 6.3: BSE images and Si, K, and Na chemical maps of white micas. **(a)** Interlayered and schistosed phengite and paragonite in a quartz an albite matrix. **(b)** Highly deformed interlayered phengite and paragonite surrounded by quartz and garnet. **(c)** Elongated phengite and euhedral paragonite which developed in an orientation differently to the phengite, both in an amphibole-rich matrix. **(d)** Prograde paragonite embedded in phengite, presenting corroded rims and in increase of K towards the crystal interior. **(e)** Assemblage of garnet, amphibole, carbonate, paragonite and phengite, with phengite is overgrown by prograde paragonite. **(f)** Phengite, paragonite and amphibole assemblage in a quartz matrix.

6.5.3.1 Sample AK 14.6-1

Sample AK 14.6-1 is a mafic, garnet-bearing micaschist consisting of white mica – quartz – garnet – amphibole – titanite ± chlorite and organic matter. The matrix defining the schistosity consists of elongated phengite, paragonite, and glaucophane crystals. Subhedral to rounded garnet porphyroblasts (1-2 mm in size) are fractured and float in the matrix. They are mostly inclusion free with the exception that some contain quartz and small rutile inclusions. Some of the white micas are orientated differently to the matrix and occur as 1-2 mm long lamellae, which formed post-kinematically. Quartz bands show little deformation. Relict titanite crystals contain many amphibole inclusions.

6.5.3.2 Sample AK 14.47-1

Sample AK 14.47-1 is a garnet-bearing, albite-rich micaschist. Mineral assemblage consists of quartz – white mica – garnet – albite – amphibole ± titanite ± chlorite ± carbonates with minor apatite (>100 µm), epidote, titanite and oxides. The sample underwent strong deformation with a well-developed schistosity, shearing and garnet rotation. The matrix is composed of white mica, quartz, albite, and some amphibole. Garnet occurs as subhedral-fractured porphyroblasts of 1 to 2 mm in diameter and contains large quartz and small rutile inclusions. White mica is mainly phengite, occasionally interlayered with paragonite. Retrograde albite exhibits large crystals (0.5-1.5 mm) with a poikilitic texture overgrowing white mica, glaucophane, quartz, garnet, and rutile crystals. Titanite also occurs as poikilitic grains.

6.5.3.3 Sample AK 14.67-3

Sample AK 14.67-3 is a garnet-bearing quartz-rich micaschist. The mineral assemblage comprises quartz – white mica – garnet – carbonates ± amphibole ± epidote ± omphacite ± chlorite with apatite, oxides, albite, epidote, and titanite as accessory minerals. Quartz and white mica matrix minerals form the schistosity. Garnet occurs as a few large (~3-5 mm) anhedral poikilitic porphyroblasts, highly deformed and fractured. Garnet hosts many inclusions comprising of large quartz, and smaller epidote, albite, paragonite, and phengite grains. White mica occurs as phengite and paragonite, both elongated, and define the schistosity. Some of the paragonite is oblique orientated to the main schistosity. Quartz occurs as polycrystalline aggregates. Chlorite and carbonate (ankerite and calcite) occur randomly distributed within the matrix. Few albite is present in the sample, with white mica, rutile, amphibole, and quartz inclusions.

6.5.3.4 Sample AT 14.1-3

Sample AT 14.3-1 is a garnet-bearing, albite-rich micaschist. Quartz – albite – white mica – garnet – amphibole– chlorite ± titanite compose the main mineral assemblage. The foliated matrix consists of quartz, white mica, and albite beds. Contrary to previous samples, garnet occurs as numerous small euhedral undeformed grains (~100-200 µm). They are mostly inclusion free, with rare small rutile inclusions. White mica occurs as thin elongated flakes. Quartz displays polycrystalline recrystallization and undulosed extinction. Amphibole is present as small grains in the matrix. Albite displays again large retrograde poikilitic porphyroblasts (~2-5 mm) containing garnet, white mica and rutile inclusions.

6.5.3.5 Sample AT 15.20-b

AT 15.20-b is a quartz-rich garnet-bearing micaschist composed of quartz – white mica – garnet – titanite ± albite ± chlorite and minor calcite and rutile. The sample is highly deformed with the schistosity defined by micas and quartz, being reworked by shearing. Garnet is highly fractured and subhedral with large quartz and small rutile inclusions. White mica mainly forms thin elongated crystals (~1-2 mm) with some smaller and thicker crystals orientated differently to the schistosity. Quartz present undulosed extinction and polycrystalline recrystallization. Albite present a poikilitic texture, and hosts rutile, mica, quartz, garnet, carbonate, and few zircon grains.

6.5.3.6 Sample AT 14. 42-11

Sample AT 14.42-11 is a white-mica-bearing eclogite composed of omphacite – garnet – white mica – amphibole – quartz as main minerals. The sample is slightly deformed with a patchy omphacitic matrix. Garnet occurs as large subhedral porphyroblasts (1-3 mm). They are highly fractured and strongly deformed with numerous quartz, chlorite, and amphibole inclusions. White mica forms large elongated lamellae (~1-2 mm long). Quartz mainly forms at the tail of garnets and presents only ca. 5% of the mineral assemblage. It likely developed by polycrystalline recrystallization and exhibits undulosed extinction. . Relict amphibole contains numerous inclusions and is chemically zoned as indicated by a variation in birefringence from core to rim.

6.6 Rb-Sr isotope analyses

Analytical data and calculated isochrons are reported in Table. 6.2 and Fig. 6.4, respectively. Some samples yield errorchrons with large MSWD (>2.5) and errors, when using all analyzed mineral separates (Appendix Table C3, Fig. C4). However, if only mineral separates with satisfying analytical results were taken (e.g., phengite Rb and Sr concentrations > 100 and < 250 ppm, respectively, and low 2σ errors on $^{87}Sr/^{86}Sr$ ratios), then reliable isochrons for five of the six samples could be derived (MSWD >0.3 to <2.5; cf. Kullerud, 1991). Sample AK 14.6-1 required a second stage of mineral separation and analysis, as the first trial yielded errorchon ages. Sample AT 15.20-b produced an errorchron with a high MSWD (417) and a regression age of 316 ± 38 Ma. Samples AK 14.47-1, AK 14.67-3 and AT 14.1-3 are indistinguishable in age within error, with a mean age of 321.6 Ma ± 1.9 Ma (2σ).

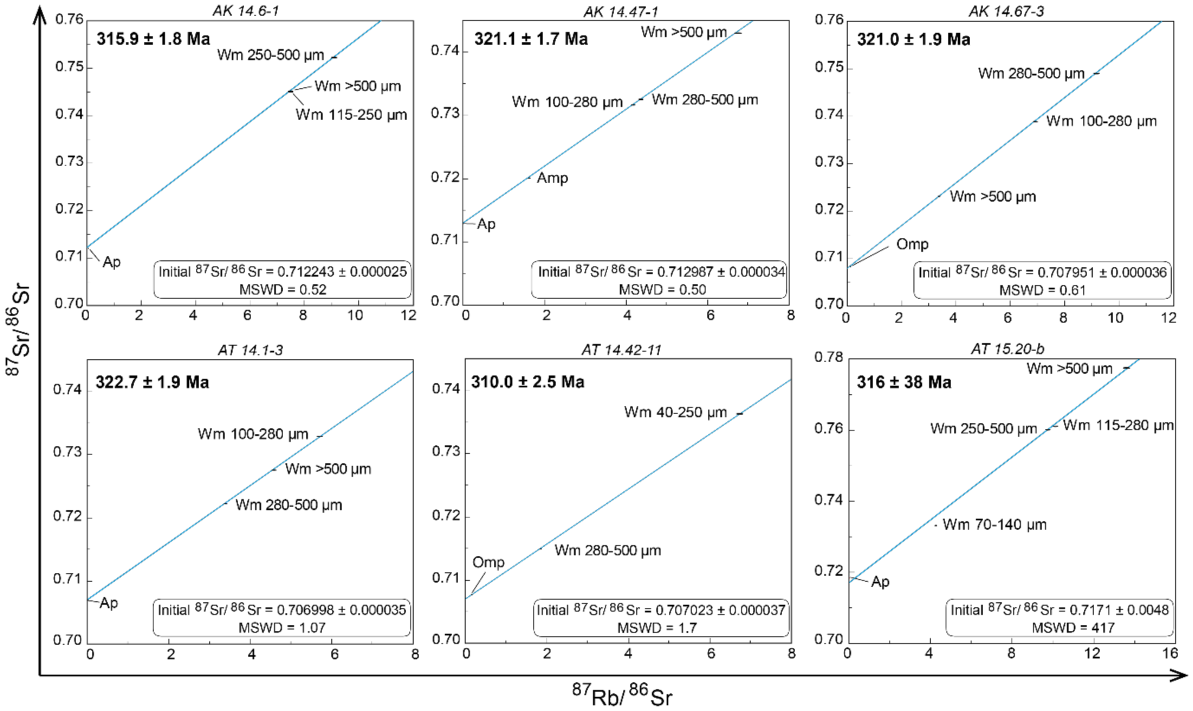

Figure 6.4: Rb-Sr regression calculations of the samples from the AMC (Tianshan). Analytical data: see Table 6.2 and Appendix Table C3. Abbreviations: Wm: white mica; Ap: apatite; Amp: amphibole; Omp: omphacite. White mica Fraction size is indicated for each diagram.

Samples AK 14.6-1 and AT 14.42-11 display younger regression ages of 315.9 ± 1.8 Ma and 310.0 ± 2.5 Ma, respectively.

Table 6.2. Rb-Sr Isotope Data for Rocks from the Western Tianshan

Sample **Mineral -fraction**	**Analysis number**	**Rb** *(ppm)*	**Sr** *(ppm)*	**^{87}Rb/^{86}Sr**	**^{87}Sr/^{86}Sr** *(± 2σ)*	**Ages** *(Ma ± 2σ)*
AK 14.6-1						
Wm 115-250 µm	2277	361.5	140.7	7.460666	0.745139 (10)	315.9 ± 1.8
Wm 250-500 µm	2278	410.8	131.6	9.071209	0.752331 (11)	
Wm >500 µm	2279	384.4	149.6	7.463018	0.745384 (13)	
Ap 100-280 µm	2258	9.5	2357.9	0.011600	0.712290 (11)	
AK 14.47-1						
Wm 100-280 µm	2234	316.1	220.1	4.164987	0.731738 (11)	321.1 ± 1.7
Wm 280-500 µm	2235	316.5	210.8	4.355155	0.732649 (7)	
Wm >500 µm	2236	347.5	150.0	6.728512	0.743141 (9)	
Ap 100-500 µm	2260	1.1	1971.5	0.001600	0.712996 (36)	
Amp 100-280 µm	2243	23.9	42.8	1.619959	0.720246 (13)	
AK 14.67-3						
Wm 100-280 µm	2237	195.7	82.1	6.924690	0.738965 (36)	321.0 ± 1.9
Wm 280-500 µm	2238	204.1	64.7	9.168297	0.749138 (11)	
Wm >500 µm	2239	177.7	152.4	3.379840	0.723208 (12)	
Omp 100-280 µm	2244	5.5	135.0	0.118071	0.708480 (4)	
AT 14.1-3						
Wm 100-280 µm	2224	189.8	96.6	5.701735	0.732869 (11)	322.7 ± 1.9
Wm 280-500 µm	2225	174.7	149.7	3.382655	0.722311 (8)	
Wm >500 µm	2226	193.2	122.3	4.582193	0.727582 (12)	
Ap 0-280 µm	2258	2.0	2485.3	0.002300	0.707009 (24)	
AT 14.42-11						
Wm 40-250 µm	2255	145.0	62.5	6.733406	0.736372 (9)	310.0 ± 2.5
Wm 280-500 µm	2228	105.0	164.7	1.846378	0.714995 (12)	
Omp 100-280 µm	2242	1.5	27.5	0.153514	0.707695 (23)	
AT 15.20-b						
Wm 70-140 µm	2270-71	100.7	69.0	4.235254	0,733329 (16)	316 ± 38
Wm 115-280 µm	2272	284.3	82.0	10.080637	0,761339 (8)	
Wm 250-500 µm	2273	271.7	81.2	9.732531	0,760465 (10)	
Wm >500 µm	2274	375.4	80.5	13.581951	0,777912 (12)	
Ap 140-280 µm	2280	1.7	1615.5	0.003000	0,718793 (24)	

Based on repeated measurements, the 87Rb/86Sr ratios were assigned an uncertainty of 1%. In the course of this study, repeated runs of NBS standard 987 gave an average 87Sr/86Sr ratio of 0.710278 ± 0.000024 (± 2σ, n= 35). Total procedural blanks were less than 0.1 ng for Rb and 0.24 ng for Sr. Wm: white mica; Ap: apatite; Amp: amphibole; Omp: omphacite

6.7 Discussion

6.7.1 Rb-Sr age interpretation

The Rb-Sr method might be affected by potential disequilibrium, late stage re-equilibration, and closure temperature effects that all may influence the age estimate (Glodny et al., 2005; Kagami et al., 2003; Yong et al., 2013). However, the combination of Rb-Sr dating with a petrological study and pseudosection calculation allows interpreting these ages. We only considered isochrons being fully reliable with a MSWD between 0.3 and 2.5 (Kullerud, 1991). Data for which the ^{85}Rb/^{87}Rb ratio measured by the TIMS was very close to the natural abundance ratio (e.g., amphibole of sample AK 14.6-1) have been excluded from the calculation. These values resulted from a miscalculation of the weighing and spiking due to Rb and Sr values from literature (Beinlich et al., 2010; Klemd et al., 2005; van der Straaten et al., 2008), which were used as a starting point. Isochrons calculated with only three points or even less, lack reliability and the age interpretation should be seen skeptically. In general, values for mineral fractions plotting far off the isochron were excluded as they indicate disequilibrium to the overall system.

In order to interpret our Rb-Sr isotope data we calculated phase relations using Perple_X 6.6.8 (Connolly, 1990) to display the potential P-T path of the region in the context of white mica growth (Fig. 6.5). Separation of paragonite and phengite is possible via magnetic separations because phengite contains significantly more Fe than paragonite (Fig. 6.2a). However, beside the occurrence of individual flakes, paragonite and phengite are often finely interlayered (Figs. 6.3 a,b,c). The P-T field at which both paragonite and phengite are coexisting is well below peak conditions, with ~1.8 to 2.1 GPa at the given temperature range between 450 to 550 °C (Fig. 6.5). This indicates that there might be different generations of paragonite in the sample record and potentially several phases of phengite recrystallization. This may result in a disequilibrium between the various paragonites and phengites fractions. Furthermore, a dilution of ^{87}Rbr/^{86}Sr and ^{87}Sr/^{86}Sr ratios of the apparent phengitic white mica fractions may occur, if the intergrowth is considered (e.g., Glodny et al., 2005b). This implies potential variations in the determined age, depending on whether the white mica fractions are pure phengite or a mixture of phengite and paragonite. Fractions containing paragonite typically contain low Rb concentration (< 100 ppm) and high Sr concentration (>250 ppm) and were excluded from calculation.

Inherited mineral inclusions or parts of mineral fractions may lead to disequilibrium and older age values as demonstrated by e.g., Baxter and Scherer (2013). Although the white mica fractions were cautiously grinded to remove potential inclusions, some inherited inclusions might have remained. Similarly, some of the white mica fractions include very small grain sizes (<70 µm), potentially containing inherited grains which were difficult to separate from the white mica. Additionally, the aforementioned mixing of phengite with paragonite will further lead to disequilibrium and wrong age estimates. This is likely the case for sample AT 15.20-b, in which prograde paragonite was identified and likely induced scattered isochron relationships.

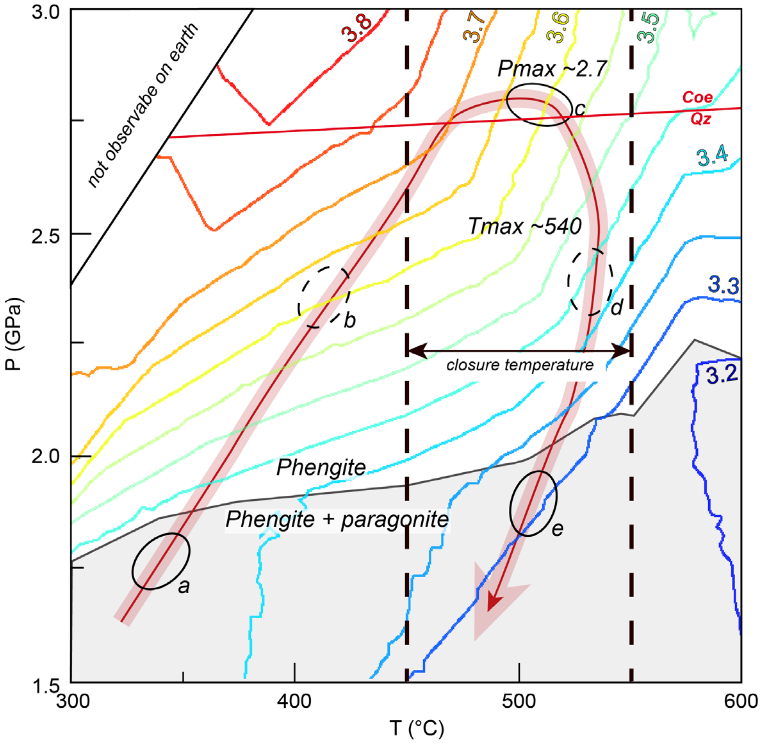

Figure 6.5: P-T pseudosection in the system NaMnKFMASHO (PERPLE_X v6.6.8; Connolly, 1990). Average bulk chemistry of the micaschists was taken for calculation. Si-isopleths of phengite are labelled and represented by colored lines. The quartz-coesite transition is illustrated (red line). Phengite and paragonite coexist in the same P-T field (grey area) at lower pressures (<1.8-2.2 GPa). The estimated closure temperature for Rb-Sr in white micas of ca 500 ± 50 °C is represented by dashed lines. Maximum pressures ~2.7 GPa and peak temperatures ~540 °C are also reported (Bayet et al. 2018). Circles (a to e) represent hypothetical stages of white mica growth showing that interlayering of phengite and paragonite may have occurred at low-pressure during prograde (a) or retrograde (e) evolution.

In contrast, post-kinematic re-equilibration or crystallization of minerals such as paragonite (e.g., sample AT 14.42-11) will lead to a younger age estimation or disequilibrium, respectively. Mineral separates with a low $^{87}Rb/^{86}Sr$ ratio, such as apatite and omphacite, are crucial to define the initial $^{87}Sr/^{86}Sr$ value and potential inheritance or re-equilibration will strongly affect the validity of the isochron. Several studies showed that the AMC underwent intensive fluid circulation (e.g., Beinlich et al., 2010; van der Straaten et al., 2008) and pervasive deformation (Bayet et al., 2018; Soldner et al., 2017). Fluids and deformation commonly induce dissolution-recrystallization processes leading to re-equilibration of some or several of the minerals (e.g., Glodny et al., 2008). Fluid sensitive minerals such as apatite (Kusebauch et al., 2015) are then re-equilibrated and the age is biased by a post peak metamorphic fluid event. This might be the case for sample AT 15.20-b, displaying a younger age estimate when the apatite is considered.

Finally, the closure temperature for Rb-Sr white micas in metamorphic systems is not well defined with an average value of 500 ± 50 °C (Jäger et al., 1967), which overlaps within error with the peak temperature of the AMC (Bayet et al., 2018; Fig. 6.6). This suggests that potential resetting might have occurred in some of the white mica from our samples and lead to younger age estimates or errorchron relationships. Alternatively, this implies that the white mica likely recorded the last equilibration event near the peak temperature.

Isochrons of sample AK 14.47-1, AK 14.67-3 and AT 14.1-3 present an age of ca. 321 Ma, in agreement with previous determinations of the timing of the peak burial (Fig. 6.1b). This implies that white mica in those samples dated the growth or equilibration of phengite near peak conditions as shown on Fig. 6.5 (circle c). In fact, the Si-in phengite isopleths are in agreement with estimated peak conditions for the area of ca. 540 °C and 2.5 to 2.7 GPa (circles b to d; Bayet et al. 2018).

6.7.2 Previous dating attempts

6.7.2.1 Rb-Sr, Ar-Ar and K-Ar dating

Recalculated Rb-Sr values, using the new recommended decay constant of $\lambda^{87}Rb = 1.3972 \times 10^{-11}\ yr^{-1}$ (Villa et al., 2015), display similar results than this study. John et al. (2012) obtained an age of ca. 322 Ma for a whole-rock mixing line of a fluid-rock interaction sample transect from the blueschist host-rock via reaction halo into the eclogite vein values. The age has been interpreted to have formed due to prograde slab dehydration near peak metamorphic conditions (Beinlich et al., 2010; John et al., 2012). Alternatively, Klemd et al., (2005) calculated ages ranging from 306.7 to 316.3 Ma based on white mica mineral separates. If only age values based on widespread isochrons and well-constrained lower intercept values are considered, then the ages range vary between 314.1 and 316.3 Ma (Fig. 6.1b), identical to our 315.9 ± 1.8 Ma age value for sample AK 14.6-1. The two distinct age values of ca. 321 Ma and ca. 315 Ma may represent different stages of metamorphism. Bayet et al (2018) reported numerous shear zones in their study, in particular in the area in which samples of the study of Klemd et al. (2011) were located. Glodny et al. (2008) demonstrated the possibility of isotopic resetting induced by recrystallization of the white mica in the western Gneiss Region (Norway). We thus interpret the younger ages of ca. 315 Ma as deriving from recrystallization during deformation, given their sample locality close to shear zones (Fig. 6.1b).

Constrains on the timing of the exhumation of the AMC is possibly provided by Ar-Ar and K-Ar dating, however, difficulties in the interpretation of Ar-Ar and K-Ar ages derive from the often observed evidences of excess of Ar (e.g., Li et al., 1994; Ruffet et al., 1997). The excess of Argon results in older age estimation complicating their interpretation significantly. Rb-Sr mica dating tends to provide robust data and likely reflects the last equilibration stage. Therefore, post-peak ages can be dated combining both Ar-Ar and Rb-Sr dating, when mineral fractions clearly indicate a post-kinematic crystallization, such as retrograde paragonite. In their paper, Klemd et al., (2005), evaluated the timing of exhumation using additional Ar-Ar and K-Ar dating on both phengite and paragonite. Ar-Ar and K-Ar on mixed phengite and paragonite minerals yield homogeneous and consistent isochrons displaying ages of ca. 311 Ma. An older age of ca. 325 Ma, in the range of our best estimate for the peak of burial, was obtained using K-Ar on phengite only.

6.7.2.2 Lu-Hf and Sm-Nd dating of garnet

The prograde path up to the maximum temperature can be dated by applying both the Lu-Hf and the Sm-Nd dating methods on garnet. During sample preparation, it is critical to separate inclusions from the garnet host, given that inherited inclusions will lead to potential disequilibria resulting in a bias of the results, and thus cause meaningless dates instead of significant ages (Baxter and Scherer, 2013; Blichert-Toft and Frei, 2001; Scherer et al., 2000; Thöni and Jagoutz, 1992).

Two studies reported Lu-Hf garnet growth ages, with distinct values of ca. 326 Ma (Soldner et al., 2017) and ca. 315 Ma (Klemd et al., 2011). This discrepancy may be due to the use of different techniques for sample preparation and analysis, on different localities and types of garnet. On the one hand, Klemd et al. (2011) collected samples close to a highly deformed zone with several shear zones (Fig. 6.1b). The studied garnets varied in size (~50 to ~200 µm) and inclusion proportion (from ca. 40 % to nearly inclusion free). Lutetium concentration profiles of the garnets from core to rim showed that the peak of Lu concentration is often located in the outer zone of the core or within the mantle zone of the garnet. This possibly results from the breakdown of a refractory REE-bearing mineral (e.g., titanite) during garnet growth (e.g., Hickmott et al., 1987; Skora et al., 2006).

Garnet was separated from its inclusions, after the method described in Lagos et al. (2007), which aims to dissolve the garnet itself, leaving refractory Hf containing inclusions intact. On the other hand, Soldner et al. (2017), applied Lu-Hf dating on a fraction of large garnet (~500 µm) containing a few inclusions only, with a clear peak in Lu concentration in the core zone of the garnet. Contrary to Klemd et al. (2011), they followed the methods of Anczkiewicz and Thirlwall (2003) to separate garnet from inclusions, by selectively dissolving them. Comparison and evaluation of the age meaning of both studies is difficult given the differences in sample location and the different sample preparation and isotope analysis techniques.

Only a few studies were conducted in the AMC using ^{147}Sm-^{143}Nd dating. Lu is predominately found in the core of garnet whereas the peak of Sm and Nd concentration are often found close to the mantle and the rim, respectively, and Hf is not incorporated in the garnet by simple Rayleigh fractionation processes (Scherer et al., 2000; Skora et al., 2006). For these reasons, Lu–Hf generally yield older ages than Sm–Nd. Accordingly, Soldner et al. (2017) performed Sm-Nd dating additionally to Lu-Hf, using the same garnet fractions, given that Lu and Sm are preferentially incorporated in garnet core and rim, respectively (Lapen et al., 2003). This resulted in a garnet growth age of 326 Ma and an estimate for the peak metamorphic event of ca. 318 Ma. Both ages are in the range of the best age estimate for the peak metamorphic stage of the AMC (Fig. 6.6). Applying the Sm-Nd method on garnet as well, Tan et al. (2017) obtained a well-defined isochron of 312.1 ± 2.4 Ma (MSWD=0.78), interpreted as dating post peak eclogite-facies deformation.

6.7.2.3 U-Pb dating of accessory phases

Age determination by U-Pb dating of zircon may record various stages of zircon growth, thus it is difficult to associate the age values with specific metamorphic events (Rubatto, 2002). Yet, most of U-Pb dating in the AMC, interpreted as providing the age of peak metamorphism, revealed similar ages of ca. 320 Ma (e.g., Su et al., 2010; Tan et al., 2017; Yang et al., 2013; Fig. 6.6) to those obtained by methods that clearly determined the ages of metamorphic minerals. We excluded the ages of Zhang et al. (2007) and Du et al. (2014) from this evaluation, as they are not in agreement with most of the ages in this region and are based on poorly constrained isochron relationships yielding a rather low spread.

U-Pb rutile dating, however, dates rutile growth that might have been affected by recrystallization during fluid-circulation, at near or post peak conditions, or being affected by Pb

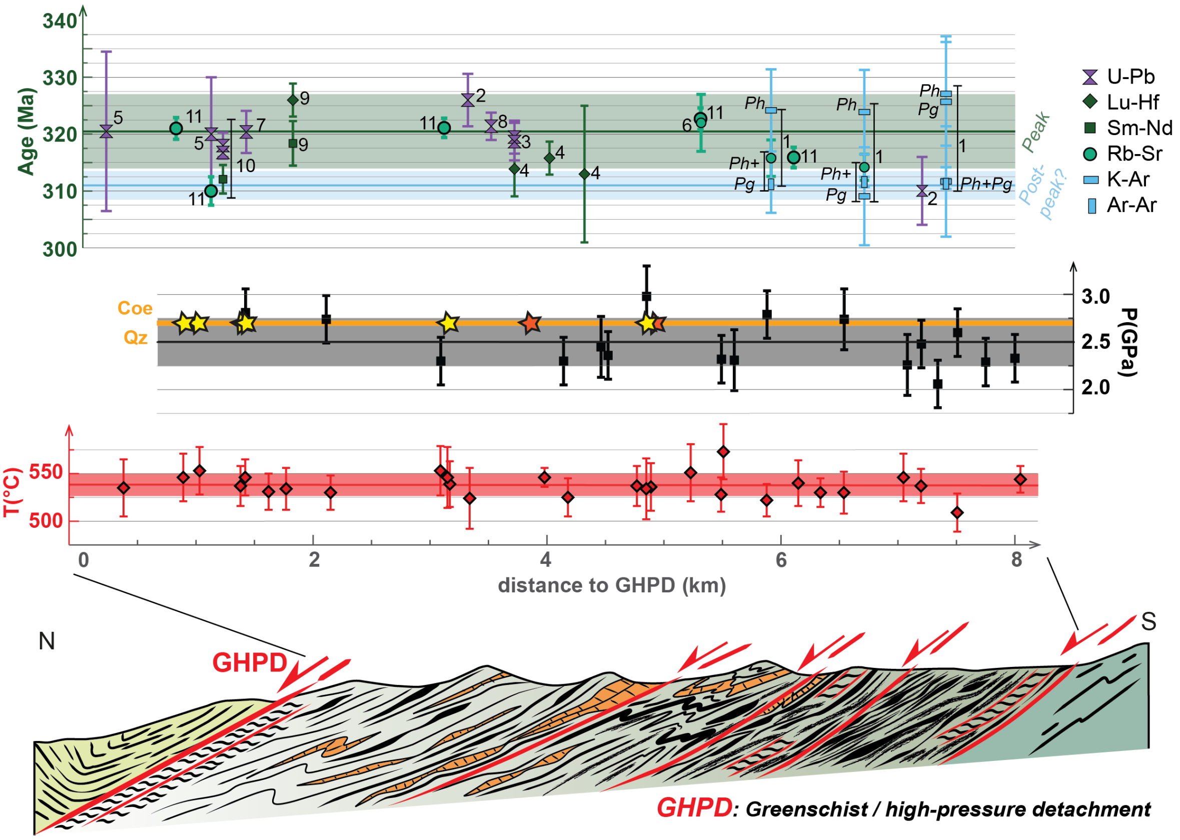

Figure 6.6: Cross-section of the AMC from N to S modified after Bayet et al. (2018). Subunits 1 to 4, divided by km-scale shear zones, are reported on the section. Peak temperature (red lozenge, bellow) cluster around 538 °C (red line) with en error of ±12 °C (stdv, red band). Peak pressure (black squares, middle) and coesite occurrence (stars) with the quartz-coesite transition (orange line) exhibit a wider range of determined pressures with an average of 2.5 GPa (black line) with an error of ±0.25 GPa (black band). Metamorphic ages reported for the AMC in previous literature (numbers 1 to 10) correspond to Fig. 6.1b and Appendix Table C1. Data from this study (number 11) correspond to blue-green bigger circles. The timing of the PT conditions close peak burial is represented by the average (green line) at 320.5 Ma and error of ±6.5 (2σ, green band). The timing of post-peak conditions is estimated to have occurred around 311.1 Ma (blue line) with an error of ca. ±2.2 Ma (2σ, blue band). Ar-Ar dating on white mica is plotted separately according to dating on phengite only (Ph), paragonite only (Pg) or a combination of both (Ph+Pg).

loss during cooling based on the closure temperature effects (e.g., Li et al., 2011; Mezger et al., 1989; Zack et al., 2011). Su et al. (2010) attempted to constrain the age of peak metamorphic conditions using U-Pb on rutile from dehydration veins and from rutile equilibrated with eclogite-facies matrix minerals (Fig. 6.1b). Although remaining in the same range for the best estimate of peak metamorphism, the large error of 10 Ma prevents from using this result as a robust value (Fig. 6.6). Many samples contain rutile in the AMC, some of which were used to estimate peak temperature using the Zr in rutile thermometer (Bayet et al., 2018; Lü et al., 2012b). As underlined in Zack et al. (2011), combining U-Pb dating on rutile and the Zr in rutile thermometer provides a great potential to date near peak metamorphic conditions, as rutile is occurring at high pressure conditions only (e.g., John et al., 2011).

6.8 Geodynamic implications and conclusions

Even though age estimates of ca. 320 Ma for peak-metamorphic conditions are clustering around the mean value, they remain coherent within the frame of a few million years. In the case of a tectonic mélange, variations in ages are expected (Festa et al., 2010). However, some studies demonstrated that the evaluation of the age of block and matrix is difficult to estimate, and might actually result in a similar age (e.g., Bröcker and Keasling, 2006; Bulle et al., 2010; Wakabayashi, 2015). Instead, an overall peak metamorphism age of ca. 320 Ma and homogeneous P-T conditions between mafic and metasedimentary rocks seem to be in agreement with the hypothesis of a coherent slab stacking at ca. 80 km depth (Bayet et al., 2018), rather than a tectonic mélange.

To conclude, the new Rb-Sr phengite dating resulted in distinct age populations. Three of the samples cluster around ca. 321 Ma, in agreement with previous age estimates for the peak metamorphic conditions. One of the sample overlaps within error with the range of ages for peak burial, although displaying a slightly younger age of ca. 315 Ma. The youngest age value of ca. 310 Ma is likely correlated to post peak exhumation processes, in agreement with results from Ar-Ar dating on paragonite and some U-Pb zircon rim data.

Various methods, such as Sm-Nd and Lu-Hf dating of garnet, U-Pb on zircon and Rb-Sr on white micas and whole rock, resulted in the same age range of 320 ± 6 Ma for the conditions of peak burial. Although all the methods provided ages that are in good agreement with each other, any age variations smaller than ca. ± 6 Ma, 2σ, are not resolvable. This still allows a rather large spread of ages within the metasediments and the metavolcanoclastic rock record. From this perspective, the concept of the AMC representing a mélange cannot be fully ruled out. Thus, it is important to apply various geochronological methods and isotopic systems on spatially well-distributed samples in a systematic way. This would allow age comparison within and between samples, and eventually lead to a better characterization of the geodynamic evolution of the AMC.

6.9 Acknowledgements

We are grateful to Monika Feth for helpful technical support during sample preparation and TIMS analytical work. We thank Anja Maria Schleicher (GFZ, Potsdam) for XRF sample preparation and analysis. We acknowledge Johannes Glodny for helpful comments on Rb-Sr system and sample preparation. This research received funding from the People Programme (Marie Curie Actions) of the European Union’s Seventh Framework Programme FP7/2017–2013/under REA grant agreement no. 604713, ‘Zooming in between Plates (ZIP).

Chapter 7

Conclusions and outlook

7.1 Conclusions

1. The AMC is composed of two main units: the greenschist-facies (GS) unit, located north and south, and the HP-UHP unit in the central part. In the North, the GS and HP-UHP units are separated by a large detachment, the Greenschist High Pressure Detachment (GHPD), forming a strongly deformed area. The GS unit consists of metapelites with main mineral assemblage of green amphibole, chlorite, and albite.

2. The HP-UHP unit is composed of mixed and interlayered metapelites and volcano-clastic rocks intercalated with carbonate lenses, bodies, and layers. Mafic rocks appear mainly as layers intercalated between metapelitic rocks but also occur as boudins and lenses. The lithology in the HP-UHP unit gradually evolves from pelitic-rich (north) to mafic-rich (south). Although varying in composition, garnet is ubiquitous in the HP-UHP unit.

3. The AMC experienced intensive deformation, with pervasive schistosity throughout the entire area. In the HP-UHP unit, the main schistosity, striking roughly E-W and dipping north, is reworked by folding and crenulation schistosity. Shearing occurs at various scales down to cm-scale and reworks schistosity and folding. The shearing strikes approximately NE-SW with a top-to-the-north sense of shearing indicated by pervasive glaucophane lineation. The HP-UHP unit is subdivided in five structural sub-units by km-scale shear zones. Field data indicate a top-to-the-north subduction polarity, in agreement with the literature.

4. The HP-UHP unit displays rather homogeneous P-T conditions of 538 ± 12°C and 2.5 ± 0.25 GPa, with numerous coesite findings throughout the HP-UHP unit. This implies that the sequence south of the GHPD reached UHP conditions or close to UHP conditions, and was stacked at similar levels. The homogeneity of the peak P-T conditions involves that the observed km-scale shear zones do not divide units originating from various depths.

5. Rb-Sr white mica dating provides new data on peak metamorphic conditions as well as an insight in the post-peak conditions in the HP-UHP unit. A review of the previous age estimates in the AMC revealed that peak metamorphic conditions occurred at 320.5 ± 6.6 Ma (2σ) and post-peak conditions at ca. 311 Ma. In this study, three samples located in the northeast, central-east and southwestern part of the HP-UHP unit yield similar ages of 321.6 ± 1.9 Ma. These Rb-Sr ages are in good agreement with proposed peak metamorphic ages in the literature. A sample located in the central-east part shows a slightly younger age of 315.9 ±

1.8 Ma. This is however, still in the range of the metamorphic peak conditions. Finally, a last sample displays a weak isochron with an age of 310.0 ± 2.5 Ma that has been interpreted as a post-peak metamorphic conditions age.

6. The rather homogeneous peak P-T conditions and peak metamorphic ages throughout the various lithologies and structures in the HP-UHP unit are not in agreement with the previous model of a tectonic mélange. Furthermore, the concept of the AMC subdivided in two sub-units (HP and UHP) does not fit with our findings, since coesite has been found further south than previously described. However, none of the proposed models can be fully ruled out, given the lack of information on P-T-t constraints in some parts of the AMC.
7. Our findings lead to the conceptualization of a new geodynamic model for the AMC. We interpret the north to south lithological gradient as deriving from trench infill. As the subduction system evolves, ashes from arc volcanism are increasingly incorporated and finely interlayered to the carbonates of the oceanic plate cover and metasediments provided by the eroding accretionary prism. The material is dragged down the plate interface on top of the downgoing plate. In an early stage, some of the metasediments are stacked near greenschist-facies conditions level. The rest of the material is buried, detached, and subsequently underplated at ca. 80 km depth (ca. 2.5-2.6 GPa). The observed HP-UHP sequence results from the stacking of several volcano-clastic slices thrusted on top of each other. Subsequent exhumation reworked the former thrusts in top-to-the-north extensional blueschist-facies shear zones. The last pillow basalt slice was either stacked to the sequence at UHP conditions, or during exhumation of the sequence through HP conditions. Finally, the GS unit was exhumed to the surface prior or simultaneously with the HP-UHP unit.

7.2 Implications for subduction zones

The AMC represents the first record of a thick volcano-clastic sequence stacked for a few million years at a depth of ca. 80km. This depth corresponds to a key coupling-decoupling transition, predicted by numerical models and supported by geophysical studies (e.g., Abers et al., 2006, Wada and Wang, 2009). This unusual thick buoyant sequence contradicts with predicted formation of diapirs at such depths (e.g., Behn et al., 2011). Instead, diapirs may only form deeper down and/or farther away from the plate interface. The temperatures remained rather cold (~540 °C), indicating for mechanisms buffering the temperature such as the presence of a mantle wedge "cold nose"; (Abers et al., 2006), a thickened overriding plate (e.g., Ruh et al., 2015), or efficient fluid circulation along the plate interface (e.g., van der Straaten, 2008).

The observed lithological gradient in the AMC is inferred to result from the transition of a subduction system from accretionary to erosive, with the formation of a thick accretionary prism, later destroyed by frontal erosion. Trench infill, composed of volcanic arc ashes deposits and parts of an erosive accretionary prism, provided significant amounts of volcano-clastic material in the subduction zone. The thickness of each slice of the sequence during stacking, and subsequent shearing and thinning of the 4-5 km thick sequence, support a thickness of ca. 5 km for the plate interface, previously deduced from geophysical observations (Abers, 2005).

7.3 Outlook

This study demonstrated that the AMC is a promising area to study mechanisms occurring at depths of ca. 80 km. The access and field conditions did not permit the mapping of some areas. The center of the HP-UHP unit and the southern part that contains the pillow basalts, lack structural data and require further investigation, e.g., to shed light on the geodynamic of the lower plate and mechanisms of detachment and exhumation of the pillow basalts.

The well-preserved eclogite, blueschist, and metasedimentary rocks contain mineral assemblages with abundant garnets, phengite, rutile, and zircon, ideal to combine geothermobarometry and geochronology (Fig. 7). Garnet is a key mineral, as it records different metamorphic stages and hosts inclusions during growth on the burial path. Depending on garnet zoning, inclusions and chemistry, information on the P- T conditions during burial (Fig. 7a), minimum peak pressure (QuiG barometry; Fig. 7b) and Lu-Hf and Sm-Nd ages can be determined (Fig. 7a). Additional pressure can be estimated using phengite barometry when garnet is in textural equilibrium with omphacite and phengite (Fig. 7c).

As shown in chapter 3, combined with a careful and robust petrological study, different metamorphic stages can be dated using Rb-Sr dating on phengite (Fig. 7d). Although many studies focused on U-Pb zircon dating (Fig. 7e), one single study used U-Pb rutile dating (Fig. 7f). Zirconium in rutile thermometry could be applied on more samples and combined with U-Pb rutile dating, as rutile reflects near peak-conditions or is related to fluid-events.

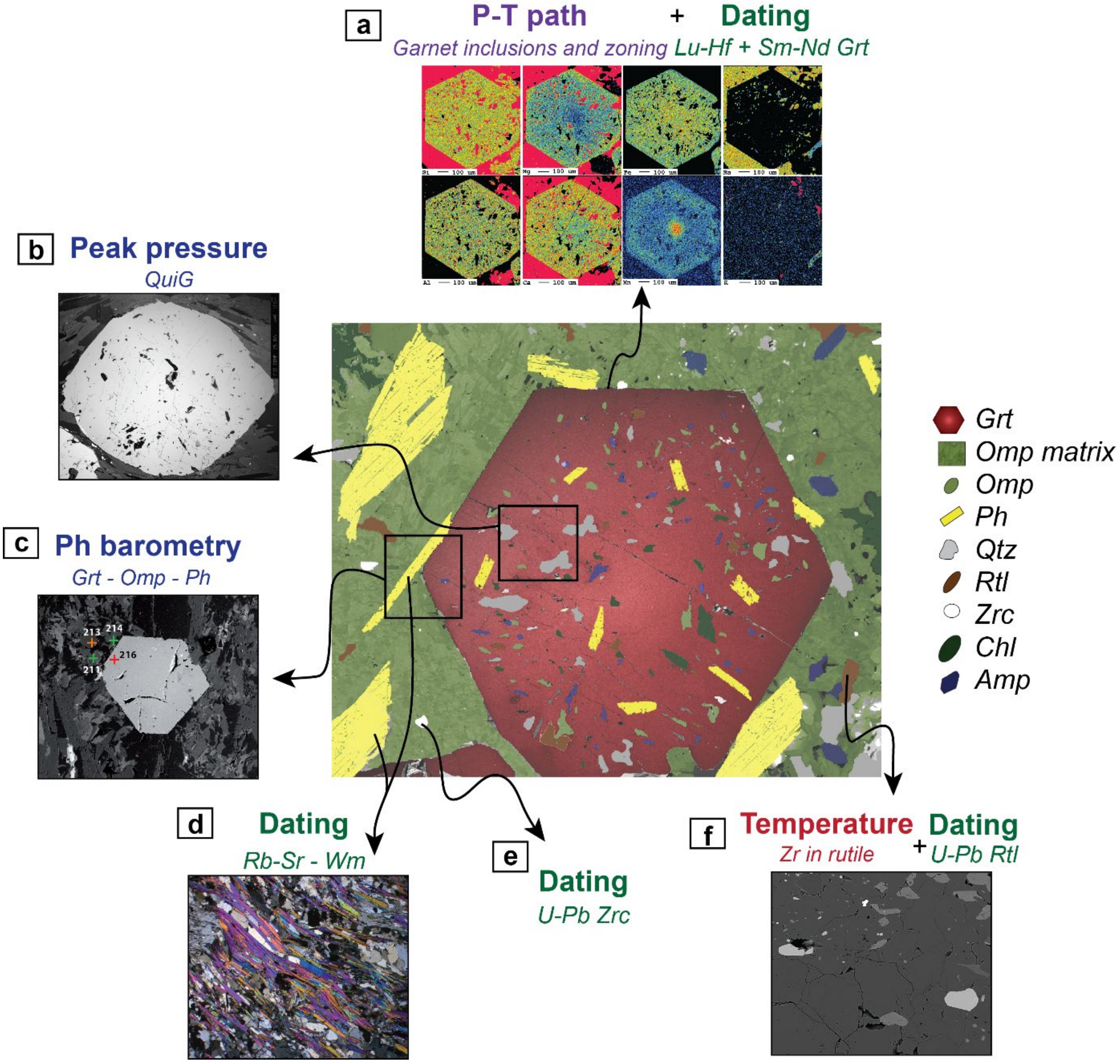

Figure 7: Schematic mineral assemblage of rocks in the AMC. **(a)** Compositional maps of Si, Mg, Fe, Na, Al, Ca, Mn and K of a garnet, presenting numerous inclusions and prograde zoning, for potential use to constrain pressure-temperature (P-T) path and age (Lu-H and Sm-Nd dating). **(b)** Garnet containing quartz inclusions used for minimum peak pressure estimates via QuiG barometry (see chapters 2 and 3). **(c)** Garnet, omphacite and phengite in textural equilibrium, used to apply phengite barometry. **(d)** Matrix phengite for Rb-Sr dating. **(e)** Possibility to use zircon for U-Pb dating. **(f)** Presence of rutile, compatible for Zr in rutile thermometry and U-Pb dating. Abbreviations: Grt: garnet; Omp: omphacite; Ph: Phengite ; Qtz: quartz; Rtl: rutile; Zrc: zircon; Chl: chlorite; Amp: amphibole.

Using the aforementioned techniques in a systematic way on widely distributed samples would help refining our geodynamic model.

Additionally, using geochemistry to conduct stable isotope and trace elements studies would improve to determine the origin of carbonates and sediments.

Finally, a collaboration has been initiated with Jonas Ruh, as part of the ZIP project, to realize numerical models on burial and exhumation of metasedimentary material. The information collected during this study can be implemented in a numerical model to test our hypothesis on the geodynamic evolution of the AMC.

Acknowledgements

I want to thank my advisors, Timm John and Philippe Agard, who initiated this project and trusted me to lead it to the end. In particular, thank you Philippe for leading/managing the ZIP project, in which I learnt and developed many skills. Timm, even with our different cultures and advising between France and Germany, we learnt with time to work efficiently together and walk the same way. You provided many wise advises and I could discuss of my research with you with great interest. You believed in me, pushed me, and supported me, especially towards the end. Philippe, I am glad of our collaboration and that you were my second advisor. I have learned a lot from you and you took time for me when I would come to work with you in Paris, for discussions (even though we might not have always agree) and helped me to have a broader view on my research. Both of you brought me your knowledge and experience in distinct fields, helped me and supported me for my work.

I am fortunate to have been part of the ZIP project, who provided financial support for my salary and research (Marie Curie action). This funding allowed me to lead my research in this wonderful (mainly in summer) city, which is Berlin, and to obtain full support for research. Since last March, I am grateful to have received financial support from the Agentur für Arbeit, and the last months from my family.

Thanks to the ZIP project, I had the opportunity to go two times to my fieldwork area in China, to go often to Paris for about a third of my PhD to work with Philippe, and to travel through the world. Most of all, I met all the amazing ZIPPIES students, who became my friends, and with whom I will always have a special bond.

I want to acknowledge my Chinese colleagues, Tan Zhou, Ji-Li Li and Jun Gao who were of a considerable help for field work in China. They took care of everything and this fieldwork would not have been possible without them. And of course, Lowen Morritz, who helped me during his master for fieldwork and did analysis for the pressure in garnet in the Atantayi, used in this work.

During my PhD, I had the pleasure to work with my dear colleagues from the Mineralogy-Petrology, Geochemistry, and tectonic groups. They were always there whenever I needed them for work, breaks and, of course, beers!

Great gratitude goes to Christiane Behr, Ralf Milke, Martina Menneken, Jasper Bernt-Gerdes, Elis Hoffmann and Damien Deldicque for help during sample preparation and analytical work at the microprobe, Raman spectroscopy and TIMS. Vielen Dank Frau Feth für alle Ihre Geduld und Hilfe. Ohne Sie könnte ich leider kein Geochemie machen. Sie haben mir viele Hilfe gebrochen wärend alle Schritte meiner Rb-Sr Arbeit. Great thanks to Esther Schwarzenbach as a friend and for help during my research, and to Hans Vrijmoed, Elis Hoffmann, Harry Becker and Johannes Glodny for discussions, from which I greatly benefited to improve, see with more clarity and have an external look on my research.

Thank you to Sarah Incel and Daniel Peters who helped me translating my abstract in German, as my level was not sufficient (Zippies power!). And thanks to Moritz Liesegang and Robbin Visser for corrections of parts of my thesis.

Last, but not least, warm thanks to all my friends for moral support. The list is long, but I am very fortunate to have you in my life. In particular, three friends who constantly supported me and were there during the good and especially the bad moments: ευχαριστώ πολύ Io Ioannidi, Merci mille fois Manon Bouvard and Vielen Dank Kathrin Schneider! Also, I want to particularly thank Timothée Boï, who was present and gave full support during the first and last year of the PhD. Thank you for your kindness, patience and strength you gave me. Many thanks to my friends from Paris, who supported me from far or close when visiting me. Merci Audrey, Lulu, Vivie, Sandra, Zineb, Lorella, Marianne, Sarah … et bien d’autres.

And of course to my family who never doubted and always believed in me: Merci Célia pour être une soeur exceptionnelle, Maman, Papa et Vé pour avoir toujours été là et pour votre amour incommensurable. To my grandparents who were proud of me during my PhD, but unfortunately left us both last year...

References

Abers, G.A., 2005. Seismic low-velocity layer at the top of subducting slabs: Observations, predictions, and systematics. Phys. Earth Planet. Inter. 149, 7–29. https://doi.org/10.1016/j.pepi.2004.10.002

Abers, G.A., 2000. Hydrated subducted crust at 100-250 km depth. Earth Planet. Sci. Lett. 176, 323–330.

Abers, G.A., van Keken, P.E., Hacker, B.R., 2017. The cold and relatively dry nature of mantle forearc in subduction zones. Nature 10, 333–337. https://doi.org/10.1038/ngeo2922

Abers, G.A., van Keken, P.E., Kneller, E.A., Ferris, A., Stachnik, J.C., 2006. The thermal structure of subduction zones constrained by seismic imaging: Implications for slab dehydration and wedge flow. Earth Planet. Sci. Lett. 241, 387–397. https://doi.org/10.1016/j.epsl.2005.11.055

Agard, P., Lemoine, M., 2005. Faces of the Alps: structure and geodynamic evolution. Comm. Geol. Map World.

Agard, P., Plunder, A., Angiboust, S., Bonnet, G., Ruh, J., 2018. The subduction plate interface : rock record and mechanical coupling (from long to short timescales). LITHOS 321, 537–561.

Agard, P., Vitale-Brovarone, A., 2013. Thermal regime of continental subduction: The record from exhumed HP-LT terranes (New Caledonia, Oman, Corsica). Tectonophysics 601, 206–215. https://doi.org/10.1016/j.tecto.2013.05.011

Agard, P., Yamato, P., Jolivet, L., Burov, E., 2009. Exhumation of oceanic blueschists and eclogites in subduction zones: Timing and mechanisms. Earth-Science Rev. 92, 53–79. https://doi.org/10.1016/j.earscirev.2008.11.002

Ai, Y., Zhang, L., Li, X., Qu, J., 2006. Geochemical characteristics and tectonic implications of HP-UHP eclogites and blueschists in Southwestern Tianshan, China. Prog. Nat. Sci. 16, 624–632. https://doi.org/10.1080/10020070612330044

Allen, J.L., 2005. A multi-kilometer pseudotachylyte system as an exhumed record of earthquake rupture geometry at hypocentral depths (Colorado , USA). Tectonophysics 402, 37–54. https://doi.org/10.1016/j.tecto.2004.10.017

Allen, M.B., Windley, B.F., Zhang, C., 1993. Paleoizoic collisional tectonics and magmatism of the Chinese Tien Shan, central Asia. Tectonophysics 220, 89–115.

Anczkiewicz, R., Thirlwall, M.F., 2003. Improving precision of Sm-Nd garnet dating by H_2SO_4 leaching: a simple solution to the phosphate inclusion problem. Geol. Soc. London, Spec. Publ. 220, 83–91. https://doi.org/10.1144/GSL.SP.2003.220.01.05

Angiboust, S., Agard, P., 2010. Initial water budget: The key to detaching large volumes of eclogitized oceanic crust along the subduction channel? Lithos 120, 453–474. https://doi.org/10.1016/j.lithos.2010.09.007

Angiboust, S., Agard, P., Jolivet, L., Beyssac, O., 2009. The Zermatt-Saas ophiolite: The largest (60-km wide) and deepest (c. 70-80km) continuous slice of oceanic lithosphere detached from a subduction zone? Terra Nov. 21, 171–180. https://doi.org/10.1111/j.1365-

3121.2009.00870.x

Angiboust, S., Agard, P., Yamato, P., Raimbourg, H., 2012a. Eclogite breccias in a subducted ophiolite : A record of intermediate- depth earthquakes ? Geology 40, 707–710. https://doi.org/10.1130/G32925.1

Angiboust, S., Wolf, S., Burov, E., Agard, P., Yamato, P., 2012b. Effect of fluid circulation on subduction interface tectonic processes : Insights from thermo-mechanical numerical modelling. Earth Planet. Sci. Lett. 357–358, 238–248. https://doi.org/10.1016/j.epsl.2012.09.012

Aoya, M., Kouketsu, Y., Endo, S., Shimizu, H., Mizukami, T., Nakamura, D., Wallis, S., 2010. Extending the applicability of the Raman carbonaceous-material geothermometer using data from contact metamorphic rocks. J. Metamorph. Geol. 28, 895–914. https://doi.org/10.1111/j.1525-1314.2010.00896.x

Arcay, D., Tric, E., Doin, M.P., 2005. Numerical simulations of subduction zones. Effect of slab deghydration on the mantle wedge dynamics. Phys. Earth Planet. Inter. 149, 133–153. https://doi.org/10.1016/j.pepi.2004.08.020

Ashley, K.T., Caddick, M.J., Steele-MacInnis, M.J., Bodnar, R.J., Dragovic, B., 2014a. Geothermobarometric history of subduction recorded by quartz inclusions in garnet. Geochemistry, Geophys. Geosystems 15, 350–360. https://doi.org/10.1002/2013GC005106

Ashley, K.T., Steele-MacInnis, M., Bodnar, R.J., Darling, R.S., 2016. Quartz-in-garnet inclusion barometry under fire: Reducing uncertainty from model estimates. Geology 44, 699–702. https://doi.org/10.1130/G38211.1

Ashley, K.T., Steele-MacInnis, M., Caddick, M.J., 2014b. QuIB Calc: A MATLAB®script for geobarometry based on Raman spectroscopy and elastic modeling of quartz inclusions in garnet. Comput. Geosci. 66, 155–157. https://doi.org/10.1016/j.cageo.2014.01.005

Audet, P., Bostock, M.G., Christensen, N.I., Peacock, S.M., 2009. Seismic evidence for overpressured subducted oceanic crust and megathrust fault sealing. Nature 457, 76–78. https://doi.org/10.1038/nature07650

Austrheim, H., Andersen, T.B., 2004. Pseudotachylytes from Corsica : fossil earthquakes from a subduction complex. Terra Nov. 16, 193–197. https://doi.org/10.1111/j.1365-3121.2004.00551.x

Aygül, M., Oberhänsli, R., 2017. Tectonic Stacking of HP/LT Metamorphic Rocks in Accretionary Wedges and the Role of Shallowing Slab-Mantle Decoupling. Tectonics 36, 2332–2346. https://doi.org/10.1002/2017TC004689

Baxter, E.F., Scherer, E.E., 2013. Garnet geochronology: Timekeeper of tectonometamorphic processes. Elements 9, 433–438. https://doi.org/10.2113/gselements.9.6.433

Bayet, L., John, T., Agard, P., Gao, J., Li, J., 2018. Massive sediment accretion at ~ 80 km depth along the subduction interface : Evidence from the southern Chinese Tianshan. https://doi.org/https://doi.org/10.1130/G40201.1

Bebout, G.E., 2007. Metamorphic chemical geodynamics of subduction zones. Earth Planet. Sci. Lett. 260, 373–393. https://doi.org/10.1016/j.epsl.2007.05.050

Bebout, G.E., Penniston-Dorland, S.C., 2016. Fluid and mass transfer at subduction interfaces-The field metamorphic record. Lithos 240–243, 228–258. https://doi.org/10.1016/j.lithos.2015.10.007

Behn, M.D., Kelemen, P.B., Hirth, G., Hacker, B.R., Massonne, H.J., 2011. Diapirs as the source of the sediment signature in arc lavas. Nat. Geosci. 4, 641–646. https://doi.org/10.1038/ngeo1214

Beinlich, A., Klemd, R., John, T., Gao, J., 2010. Trace-element mobilization during Ca-metasomatism along a major fluid conduit: Eclogitization of blueschist as a consequence of fluid-rock interaction. Geochim. Cosmochim. Acta 74, 1892–1922.

Benioff, H., 1949. Seismic evidence for the fault origin of oceanic deeps. Bull. Geol. Soc. Am. 60, 1837–1856. https://doi.org/10.1130/0016-7606(1949)60[1837:GROTIO]2.0.CO;2

Beyssac, O., Bollinger, L., Avouac, J.P., Goffé, B., 2004. Thermal metamorphism in the lesser Himalaya of Nepal determined from Raman spectroscopy of carbonaceous material. Earth Planet. Sci. Lett. 225, 233–241. https://doi.org/10.1016/j.epsl.2004.05.023

Beyssac, O., Goffé, B., Chopin, C., Rouzaud, J.N., 2002. Raman spectra of carbonaceous material in metasediments: A new geothermometer. J. Metamorph. Geol. 20, 859–871. https://doi.org/10.1046/j.1525-1314.2002.00408.x

Bjørnerud, M.G., 2002. Processes leading to eclogitization (densification) of subducted and tectonically buried crust. J. Geophys. Res. 107. https://doi.org/10.1029/2001JB000527

Blichert-Toft, J., Frei, R., 2001. Complex Sm-Nd and Lu-Hf isotope systematics in metamorphic garnets from the Isua supracrustal belt, West Greenland. Geochim. Cosmochim. Acta 65, 3177–3189. https://doi.org/10.1016/S0016-7037(01)00680-9

Bond, G.C., Kominz, M.A., 1984. Construction of tectonic subsidence curves for the early Paleozoic miogeocline, southern Canadian Rocky Mountains: implications for subsidence mechanisms, age of breakup, and crustal thinning (Canada). Geol. Soc. Am. Bull. 95, 155–173. https://doi.org/10.1130/0016-7606(1984)95<155:COTSCF>2.0.CO;2

Bostock, M.G., Hyndman, R.D., Rondenay, S., Peacock, S.M., 2002. An inverted continental Moho and serpentinization of the forearc mantle. Nature 417, 536–538.

Bröcker, M., Keasling, A., 2006. Ionprobe U-Pb zircon ages from the high-pressure/low-temperature mélange of Syros, Greece: Age diversity and the importance of pre-Eocene subduction. J. Metamorph. Geol. 24, 615–631. https://doi.org/10.1111/j.1525-1314.2006.00658.x

Brun, J., Faccenna, C., 2008. Exhumation of high-pressure rocks driven by slab rollback. Earth Planet. Sci. Lett. 272, 1–7.

Bulle, F., Bröcker, M., Gärtner, C., Keasling, A., 2010. Geochemistry and geochronology of HP mélanges from Tinos and Andros, cycladic blueschist belt, Greece. Lithos 117, 61–81. https://doi.org/10.1016/j.lithos.2010.02.004

Burchfiel, B.C., Brown, E.T., Qidong, D., Xianyue, F., Jun, L., Molnar, P., Jianbang, S., Zhangming, W., Huichuan, Y., 1999. Crustal Shortening on the Margins of the Tien Shan, Xinjiang, China. Int. Geol. Rev. 41, 665–700.

Burov, E.B., 2011. Rheology and strength of the lithosphere. Mar. Pet. Geol. 28, 1402–1443. https://doi.org/10.1016/j.marpetgeo.2011.05.008

Byerlee, J., 1993. Model for episodic flow of high-pressure water in fault zones before earthquakes. Geology. https://doi.org/10.1130/0091-7613(1993)021<0303:MFEFOH>2.3.CO

Calahorrano, A., Sallarès, V., Collot, J., Sage, F., Ranero, C.R., 2008. Nonlinear variations of the physical properties along the southern Ecuador subduction channel : Results from depth-migrated seismic data. Earth Planet. Sci. Lett. 267, 453–467. https://doi.org/10.1016/j.epsl.2007.11.061

Calvert, A.J., 2004. Seismic reflection imaging of two megathrust shear zones in the northern Cascadia subduction zone. Nature 428, 163–167. https://doi.org/10.1038/nature02346.1.

Cannat, M., Mével, C., Maia, M., Deplus, C., Durand, C., Gente, P., Agrinier, P., Belarouchi, A., Dubuisson, G., Humler, E., Reynolds, J., 1995. Thin crust , ultramafic exposures , and rugged faulting patterns at the Mid-Atlantic Ridge (22 ° – 24 ° N). Geology 23, 49–52.

Carroll, A.R., Graham, S.A., Hendrix, M.S., Ying, D., Zhou, D., 1995. Late Paleozoic tectonic amalgamation of northwestern China: sedimentary record of the northern Tarim, northwestern Turpan, and southern Junggar basins. Geol. Soc. Am. Bull. 107, 571–594.

Carswell, D.A., Wilson, R.N., Zhai, M., 2000. Metamorphic evolution, mineral chemistry and thermobarometry of schists and orthogneisses hosting ultra-high pressure eclogites in the Dabieshan of central China. Lithos 52, 121–155. https://doi.org/10.1016/S0024-4937(99)00088-2

Castro, A., Gerya, T., García-Casco, A., Fernández, C., Díaz-Alvarado, J., Moreno-Ventas, I., Löw, I., 2010. Melting relations of MORB-sediment mélanges in underplated mantle wedge plumes; Implications for the origin of Cordilleran-type batholiths. J. Petrol. 51, 1267–1295. https://doi.org/10.1093/petrology/egq019

Charvet, J., Shu, L., Laurent-Charvet, S., Wang, B., Faure, M., Cluzel, D., Chen, Y., De Jong, K., 2011. Palaeozoic tectonic evolution of the Tianshan belt, NW China. Sci. China Earth Sci. 54, 166–184.

Charvet, J., Shu, L.S., Laurent-Charvet, S., others, 2007. Paleozoic structural and geodynamic evolution of eastern Tianshan (NW China): welding of the Tarim and Junggar plates. Episodes 30, 162–186.

Chen, K., Gumiaux, C., Augier, R., Chen, Y., Wang, Q., Lin, W., Wang, S., 2011. The Mesozoic palaeorelief of the northern Tian Shan (China). Terra Nov. 23, 195–205.

Cherniak, D.J., 2000. Pb diffusion in rutile. Contrib. to Mineral. Petrol. 139, 198–207. https://doi.org/10.1007/PL00007671

Chopin, C., 2003. Ultrahigh-pressure metamorphism: Tracing continental crust into the mantle. Earth Planet. Sci. Lett. 212, 1–14. https://doi.org/10.1016/S0012-821X(03)00261-9

Chopin, C., 1984. Coesite and pure pyrope in high-grade blueschists of the Western Alps: a first record and some consequences. Contrib. to Mineral. Petrol. 86, 107–118. https://doi.org/10.1007/BF00381838

Chorowicz, J., 2005. The East African rift system. J. African Earth Sci. 43, 379–410. https://doi.org/10.1016/j.jafrearsci.2005.07.019

Chuang, L., Bostock, M., Wech, A., Plourde, A., 2017. Plateau subduction , intraslab seismicity , and the Denali (Alaska) volcanic gap. Geology 45, 1–4. https://doi.org/10.1130/G38867.1

Clift, P., Vannucchi, P., 2004. Controls on tectonic accretion versus erosion in subduction zones: Implications for the origin and recycling of the continental crust. Rev. Geophys. 42. https://doi.org/10.1029/2003RG000127

Cloos, M., Shreve, R.L., 1996. Shear-zone thickness and the seismicity of Chilean- and Marianas-type subduction zones. Geology 24, 107–110. https://doi.org/10.1130/0091-7613(1996)024<0107:SZTATS>2.3.CO;2

Cloos, M., Shreve, R.L., 1988a. Subduction-Channel Model of Prism Accretion, Melange Formation, Sediment Subduction, and Subduction Erosion at Convergent Plate Margins: 2. Implications and Discussion. Pure Appl. Geophys. PAGEOPH 128, 501–545. https://doi.org/10.1007/BF00874548

Cloos, M., Shreve, R.L., 1988b. Subduction-Channel Model of Prism Accretion , Melange Formation , Sediment Subduction , and Subduction Erosion at Convergent Plate Margins : 1 . Background and Description. Pure Appl. Geophys. PAGEOPH 128, 455–500.

Coleman, R.G., 1989. Continental growth of northwest China. Tectonics 8, 621–635.

Connolly, J.A.D., 2005. Computation of phase equilibria by linear programming: A tool for geodynamic modeling and its application to subduction zone decarbonation. Earth Planet. Sci. Lett. 236, 524–541. https://doi.org/10.1016/j.epsl.2005.04.033

Connolly, J.A.D., 1990. Multivariable phase diagrams: an algorithm based on generalized thermodynamics. Am. J. Sci. 290, 666–718.

Connolly, J.A.D., Kerrick, D.M., 2002. Metamorphic controls on seismic velocity of subducted oceanic crust at 100-250 km depth. Earth Planet. Sci. Lett. 204, 61–74.

Coward, M., Dietrich, D., 1989. Alpine tectonics −− an overview. Geol. Soc. , London , Spec. Publ. 45, 1–29. https://doi.org/10.1144/GSL.SP.1989.045.01.01

Currie, C.A., Beaumont, C., Huismans, R.S., 2007. The fate of subducted sediments: A case for backarc intrusion and underplating. Geology 35, 1111–1114. https://doi.org/10.1130/G24098A.1

Dal Piaz, G. V, 2001. History of tectonic interpretations of the Alps. J. Geodyn. 32, 99–114.

Davies, J.H., von Blanckenburg, F., 1995. Slab breakoff: A model of lithosphere detachment and its test in the magmatism and deformation of collisional orogens. Earth Planet. Sci. Lett. 129, 85–102.

di Vincenzo, G., Tonarini, S., Lombardo, B., Castelli, D., Ottolini, L., 2006. Comparison of 40Ar-39Ar and Rb-Sr data on phengites from the UHP Brossasco-Isasca unit (Dora Maira Massif, Italy): Implications for dating white Mica. J. Petrol. 47, 1439–1465. https://doi.org/10.1093/petrology/egl018

Dickinson, W.R., 1974. Plate tectonics and sedimentation.

Droop, G.T.R., 1987. A General Equation for Estimating Fe3+ Concentrations in Ferromagnesian Silicates and Oxides from Microprobe Analyses, Using Stoichiometric Criteria. Mineral. Mag. 51, 431–435. https://doi.org/10.1180/minmag.1987.051.361.10

Du, J.-X., Zhang, L.-F., Shen, X.-J., Bader, T., 2014. A new P-T-t path of eclogites from Chinese southwestern Tianshan: constraints from P-T pseudosections and Sm-Nd isochron dating. Lithos 200–201, 258–272.

Duarte, C.J., Schellart, W.P., Cruden, A.R., 2013. Three-dimensional dynamic laboratorymodels of subduction with an overriding plate and variable interplate rheology. Geophys. J. Int. 195, 47–66. https://doi.org/10.1093/gji/ggt257

Ellis, D.J., Green, D.H., 1979. An experimental study of the effect of Ca upon garnet-clinopyroxene Fe-Mg exchange equilibria. Contrib. to Mineral. Petrol. 71, 13–22. https://doi.org/10.1007/BF00371878

Enami, M., 2012. Influence of garnet hosts on the Raman spectra of quartz inclusions. J. Mineral. Petrol. Sci. 107, 173–180. https://doi.org/10.2465/jmps.111216

Enami, M., Nishiyama, T., Mouri, T., 2007. Laser Raman microspectrometry of metamorphic quartz: A simple method for comparison of metamorphic pressures. Am. Mineral. 92, 1303–1315. https://doi.org/10.2138/am.2007.2438

England, P.C., Holland, T.J.B., 1979. Archimedes and the Tauern eclogites: the role of buoyancy in the preservation of exotic eclogite blocks. Earth Planet. Sci. Lett. 44, 287–294.

Ernst, W.G., Maruyama, S., Wallis, S., 1997. Buoyancy-driven , rapid exhumation of ultrahigh-pressure metamorphosed continental crust. Geology 94, 9532–9537.

Fairhead, J.D., Stuart., G.W., 1982. The seismicity of the East African rift system and comparison with other continental rifts, in: Continental and Oceanic Rifts. pp. 41–61.

Ferrand, T.P., Hilairet, N., Incel, S., Deldicque, D., Labrousse, L., Gasc, J., Renner, J., Wang, Y., Green, H.W., Schubnel, A., 2017. Dehydration-driven stress transfer triggers intermediate-depth earthquakes. Nat. Commun. 8, 1–11. https://doi.org/10.1038/ncomms15247

Ferré, E.C., Geissman, J.W., Chauvet, A., Vauchez, A., Zechmeister, M.S., 2015. Focal mechanism of prehistoric earthquakes deduced from pseudotachylyte fabric. Geology 43, 1–4. https://doi.org/10.1130/G36587.1

Ferris, A., Abers, G.A., Christensen, D.H., Veenstra, E., 2003. High resolution image of the subducted Pacific (?) plate beneath central Alaska, 50-150 km depth. Earth Planet. Sci. Lett. 214, 575–588. https://doi.org/10.1016/S0012-821X(03)00403-5

Ferry, J.M., Watson, E.B., 2007. New thermodynamic models and revised calibrations for the Ti-in-zircon and Zr-in-rutile thermometers. Contrib. to Mineral. Petrol. 154, 429–437. https://doi.org/10.1007/s00410-007-0201-0

Festa, A., Dilek, Y., Pini, G.A., Codegone, G., Ogata, K., 2012. Mechanisms and processes of stratal disruption and mixing in the development of mélanges and broken formations: Redefining and classifying mélanges. Tectonophysics 568–569, 7–24. https://doi.org/10.1016/j.tecto.2012.05.021

Festa, A., Pini, G.A., Dilek, Y., Codegone, G., 2010. Mélanges and mélange-forming processes: A historical overview and new concepts. Int. Geol. Rev. 52, 1040–1105. https://doi.org/10.1080/00206810903557704

Frey, F.A., Bryan, W.B., Thompson, G., 1974. Atlantic Ocean Floor: Geochemistry and Petrology of Basalts From Legs 2 and 3 of the Deep-Sea Drilling Project. J. Geophys. Res. 79, 5507–5527.

Furukawa, Y., 1993. Depth of the decoupling plate interface and thermal structure under arcs. J. Geophys. Res. 98, 20005–20013. https://doi.org/10.1029/93JB02020

Gallo, D.G., Fox, P.J., Macdonald, C., 1986. A Sea Beam Investigation of the Clipperton Transform Fault: The Morphotectonic Expression of a Fast Slipping Transform Boundary. J. Geophys. Res. 91, 3455–3467.

Gao, J., He, G., Li, M., Xiao, X., Tang, Y., Wang, J., Zhao, M., 1995. The mineralogy, petrology, metamorphic PTDt trajectory and exhumation mechanism of blueschists, south Tianshan, northwestern China. Tectonophysics 250, 151–168.

Gao, J., Klemd, R., 2003. Formation of HP-LT rocks and their tectonic implications in the western Tianshan Orogen, NW China: geochemical and age constraints. Lithos 66, 1–22.

Gao, J., Klemd, R., 2001. Primary fluids entrapped at blueschist to eclogite transition: evidence from the Tianshan meta-subduction complex in northwestern China. Contrib. to Mineral. Petrol. 142, 1–14.

Gao, J., Klemd, R., 2000. Eclogite Occurrences in the Southern Tianshan High-Pressure Belt, Xinjiang, Western China. Gondwana Res. 3, 33–38.

Gao, J., Li, M., Xiao, X., Tang, Y., He, G., 1998. Paleozoic tectonic evolution of the Tianshan Orogen, northwestern China. Tectonophysics 287, 213–231.

Gao, J., Long, L., Klemd, R., Qian, Q., Liu, D., Xiong, X., Su, W., Liu, W., Wang, Y., Yang, F., 2009. Tectonic evolution of the South Tianshan orogen and adjacent regions, NW China: geochemical and age constraints of granitoid rocks. Int. J. Earth Sci. 98, 1221–1238.

Gao, Klemd, Zhang, Wang, Xiao, 1999. P–T path of high-pressure/low-temperature rocks and tectonic and implications in the western Tianshan Mountains and NW China. J. Metamorph. Geol. 17, 621–636.

Gerya, T. V., Perchuk, L.L., Burg, J.P., 2008. Transient hot channels: Perpetrating and regurgitating ultrahigh-pressure, high-temperature crust-mantle associations in collision belts. Lithos 103, 236–256. https://doi.org/10.1016/j.lithos.2007.09.017

Gerya, T. V., Stöckhert, B., Perchuk, A.L., 2002. Exhumation of high-pressure metamorphic rocks in a subduction channel: A numerical simulation. Tectonics 21, 6-1-6–19. https://doi.org/10.1029/2002TC001406

Gillet, P., Ingrin, J., Chopin, C., 1984. Coesite in subducted continental crust: P-T history deduced from an elastic model. Earth Planet. Sci. Lett. 70, 426–436. https://doi.org/10.1016/0012-821X(84)90026-8

Glodny, J., Bingen, B., Austrheim, H., Molina, J.F., Rusin, A., 2002. Precise eclogitization ages deduced from Rb / Sr mineral systematics : The Maksyutov. Geochim. Cosmochim. Acta

66, 1221–1235. https://doi.org/https://doi.org/10.1016/S0016-7037(01)00842-0

Glodny, J., Kühn, A., Austrheim, H., 2008. Diffusion versus recrystallization processes in Rb-Sr geochronology: Isotopic relics in eclogite facies rocks, Western Gneiss Region, Norway. Geochim. Cosmochim. Acta 72, 506–525. https://doi.org/10.1016/j.gca.2007.10.021

Glodny, J., Ring, U., Kühn, A., Gleissner, P., Franz, G., 2005. Crystallization and very rapid exhumation of the youngest Alpine eclogites (Tauern Window, Eastern Alps) from Rb/Sr mineral assemblage analysis. Contrib. to Mineral. Petrol. 149, 699–712. https://doi.org/10.1007/s00410-005-0676-5

Green, H.W., 2007. Shearing instabilities accompanying high-pressure phase transformations and the mechanics of deep earthquakes. Proc. Natl. Acad. Sci. 104, 9133–9138. https://doi.org/10.1073/pnas.0608045104

Grigull, S., Krohe, A., Moos, C., Wassmann, S., Stöckhert, B., 2012. “Order from chaos”: A field-based estimate on bulk rheology of tectonic mélanges formed in subduction zones. Tectonophysics 568–569, 86–101. https://doi.org/10.1016/j.tecto.2011.11.004

Gucwa, P.R., 1975. Middle to Late Cretaceous sedimentary melange, Franciscan complex, northern California. Geology 105–108. https://doi.org/10.1130/0091-7613(1975)3<105

Guillot, S., Hattori, K., Agard, P., Schwartz, S., Vidal, O., 2009. Exhumation processes in oceanic and continental subduction context. Springer Berlin Heidelberg. https://doi.org/10.1007/978-3-540-87974-9

Guillot, S., Hattori, K.H., de Sigoyer, J., Nägler, T., Auzende, A., 2001. Evidence of hydration of the mantle wedge and its role in the exhumation of eclogites. Earth Planet. Sci. Lett. 193, 115–127.

Hacker, B.R., 2008. H 2 O subduction beyond arcs. Geochemistry, Geophys. Geosystems 9. https://doi.org/10.1029/2007GC001707

Hacker, B.R., Abers, G.A., Peacock, S.M., 2003a. Subduction factory 1 . Theoretical mineralogy , densities , seismic wave speeds , and H 2 O contents 108, 1–26. https://doi.org/10.1029/2001JB001127

Hacker, B.R., Kelemen, P.B., Behn, M.D., 2011. Differentiation of the continental crust by relamination. Earth Planet. Sci. Lett. 307, 501–516. https://doi.org/10.1016/j.epsl.2011.05.024

Hacker, B.R., Peacock, S.M., Abers, G.A., Holloway, S.D., 2003b. Subduction factory 2 . Are intermediate-depth earthquakes in subducting slabs linked to metamorphic dehydration reactions ? 108. https://doi.org/10.1029/2001JB001129

Halpaap, F., Rondenay, S., Ottemöller, L., 2018. Journal of Geophysical Research : Solid Earth in the Western Hellenic Subduction Zone : New Constraints From Tomography. J. Geophys. Res. Solid Earth 123, 3000–3026. https://doi.org/10.1002/2017JB015154

Han, B.-F., He, G.-Q., Wang, X.-C., Guo, Z.-J., 2011. Late Carboniferous collision between the Tarim and Kazakhstan–Yili terranes in the western segment of the South Tian Shan Orogen, Central Asia, and implications for the Northern Xinjiang, western China. Earth-Science Rev. 109, 74–93.

Han, Y., Zhao, G., 2017. Final amalgamation of the Tianshan and Junggar orogenic collage in the southwestern Central Asian Orogenic Belt: Constraints on the closure of the Paleo-Asian Ocean. Earth-Science Rev. ?, 1–24. https://doi.org/10.1016/j.earscirev.2017.09.012

Handy, M.R., Schmid, S.M., Bousquet, R., Kissling, E., Bernoulli, D., 2010. Reconciling plate-tectonic reconstructions of Alpine Tethys with the geological–geophysical record of spreading and subduction in the Alps. Earth Sci. Rev. 102, 121–158. https://doi.org/10.1016/j.earscirev.2010.06.002

Hegner, E., Klemd, R., Kröner, A., Corsini, M., Alexeiev, D. V., Iaccheri, L.M., Zack, T., Dulski, P., Xia, X., Windley, B.F., 2010. Mineral ages and p-t conditions of late paleozoic high-pressure eclogite and provenance of mélange sediments from atbashi in the south tianshan orogen of kyrgyzstan. Am. J. Sci. 310, 916–950. https://doi.org/10.2475/09.2010.07

Hermann, J., Spandler, C., Hack, A., Korsakov, A. V, 2006. Aqueous fluids and hydrous melts in high-pressure and ultra-high pressure rocks : Implications for element transfer in subduction zones. Lithos 92, 399–417. https://doi.org/10.1016/j.lithos.2006.03.055

Hickmott, D.D., Shimizu, N., Spear, F.S., Selverstone, J., 1987. Trace-element zoning in a metamorphic garnet. Geology 15, 573–576. https://doi.org/10.1130/0091-7613(1987)15<573:TZIAMG>2.0.CO;2

Holland, T.J.B., Powell, R., 1998. An internally consistent thermodynamic data set for phases of petrological interest. J. Metamorph. Geol. 16, 309–343.

Hu, A., Jahn, B.M., Zhang, G., Chen, Y., Zhang, Q., 2000. Crustal evolution and Phanerozoic crustal growth in northern Xinjiang: Nd isotopic evidence. Part I. Isotopic charaterization of basement rocks. Tectonophysics 328, 15–51. https://doi.org/10.1016/S0040-1951(00)00176-1

Huang, C.Y., Shyu, C.T., Lin, S.B., Lee, T.Q., Sheu, D.D., 1992. Marine geology in the arc-continent collision zone off southeastern Taiwan: Implications for late neogene evolution of the coastal range. Mar. Geol. 107, 183–212. https://doi.org/10.1016/0025-3227(92)90167-G

Husson, L., Brun, J., Yamato, P., Faccenna, C., 2009. Episodic slab rollback fosters exhumation of HP – UHP rocks. Geophys. J. Int. 179, 1292–1300. https://doi.org/10.1111/j.1365-246X.2009.04372.x

Hyndman, R.D., Peacock, S.M., 2003. Serpentinization of the forearc mantle. Earth Planet. Sci. Lett. 212, 417–432. https://doi.org/10.1016/S0012-821X(03)00263-2

Hyndman, R.D., Wang, K., 1993. Thermal constraints on the zone of major thrust earthquake failure: The Cascadia Subduction Zone. J. Geophys. Res. 98, 2039–2060. https://doi.org/10.1029/92JB02279

Igarashi, T., Matsuzawa, T., Umino, N., Hasegawa, A., 2001. Spatial distribution of focal mechanisms for interplate and intraplate earthquakes associated with the subducting Pacific plate beneath the northeastern Japan arc: A triple-planed deep seismic zone. J. Geophys. Res. 106, 2177–2191.

Incel, S., Hilairet, N., Labrousse, L., John, T., Deldicque, D., Ferrand, T., Wang, Y., Renner, J., Morales, L., Schubnel, A., 2017. Laboratory earthquakes triggered during eclogitization of lawsonite-bearing blueschist. Earth Planet. Sci. Lett. 459, 320–331. https://doi.org/10.1016/j.epsl.2016.11.047

Jäger, E., Niggli, E., Wenk, E., 1967. Rb-Sr Altersbestimmungen an Glimmern der Zentralalpen. Kuemmerly und Frey.

Jahn, B., Wu, F., Chen, B., 2000. Granitoids of the Central Asian Orogenic Belt and continental growth in the Phanerozoic. Trans. R. Soc. Edinb. Earth Sci. 91, 181–193.

Jestin, F., Huchon, P., Gaulier, J.M., 1994. The Somalia plate and the East African Rift System : present-day kinematics. Geophys. J. Int. 116, 637–654.

John, T., Gussone, N., Podladchikov, Y.Y., Bebout, G.E., Dohmen, R., Halama, R., Klemd, R., Magna, T., Seitz, H.M., 2012. Volcanic arcs fed by rapid pulsed fluid flow through subducting slabs. Nat. Geosci. 5, 489–492. https://doi.org/10.1038/ngeo1482

John, T., Klemd, R., Gao, J., Garbe-Schoenberg, C.-D., 2008. Trace-element mobilization in slabs due to non steady-state fluid-rock interaction: Constraints from an eclogite-facies transport vein in blueschist (Tianshan, China). Lithos 103, 1–24.

John, T., Klemd, R., Klemme, S., Pfänder, J.A., Hoffmann, J.E., Gao, J., 2011a. Nb-Ta fractionation by partial melting at the titanite-rutile transition. Contrib. to Mineral. Petrol. 161, 35–45. https://doi.org/10.1007/s00410-010-0520-4

John, T., Medvedev, S., Rüpke, L.H., Andersen, T.B., Podladchikov, Y.Y., 2009. Generation of intermediate-depth earthquakes by self-localizing thermal runaway. Nat. Geosci. 2, 137–140. https://doi.org/10.1038/ngeo419

John, T., Scambelluri, M., Frische, M., Barnes, J.D., Bach, W., 2011b. Dehydration of subducting serpentinite : Implications for halogen mobility in subduction zones and the deep halogen cycle. Earth Planet. Sci. Lett. 308, 65–76. https://doi.org/10.1016/j.epsl.2011.05.038

John, T., Schenk, V., 2006. Interrelations between intermediate-depth earthquakes and fluid flow within subducting oceanic plates : Constraints from eclogite facies pseudotachylytes. Geology 34, 557–560. https://doi.org/10.1130/G22411.1

John, T., Scherer, E.E., Schenk, V., Herms, P., Halama, R., Garbe-Schönberg, D., 2010. Subducted seamounts in an eclogite-facies ophiolite sequence: The Andean Raspas Complex, SW Ecuador. Contrib. to Mineral. Petrol. 159, 265–284. https://doi.org/10.1007/s00410-009-0427-0

Jolivet, M., Dominguez, S., Charreau, J., Chen, Y., Li, Y., Wang, Q., 2010. Mesozoic and Cenozoic tectonic history of the central Chinese Tian Shan: Reactivated tectonic structures and active deformation. Tectonics 29.

Kagami, H., Shimura, T., Yuhara, M., Owada, M., Osanai, M., Shiraishi, K., 2003. Resetting and closing condition of Rb-Sr whole-rock isochron system: some samples of metamorphic and granitic rocks from the Gondwana super-continent and Japan Arc. Polar Geosci. 16, 227--242.

Kaneko, Y., Maruyama, S., Terabayashi, M., Yamamoto, H., Ishikawa, M., Anma, R., Parkinson, C.D., Ota, T., Nakajima, Y., Katayama, I., Yamamoto, J., Yamauchi, K., 2000. Geology of the Kokchetav UHP-HP metamorphic belt, Northern Kazakhstan. Isl. Arc 9, 264–283. https://doi.org/10.1046/j.1440-1738.2000.00278.x

Karig, D.E., Sharman, G.F., 1975. Subduction and accretion in trenches. Bull. Geol. Soc. Am. 86, 377–389. https://doi.org/10.1130/0016-7606(1975)86<377:SAAIT>2.0.CO;2

Kato, N., Hirasawa, T., 1997. A numerical study on seismic coupling along subduction zones using a laboratory-derived friction law. Phys. Earth Planet. Inter. 102, 51–68.

Keken, P.E. Van, Kiefer, B., Peacock, S.M., 2002. High-resolution models of subduction zones: Implications for mineral dehydration reactions and the transport of water into the deep mantle. Geochemistry, Geophys. Geosystems 3, 1–20. https://doi.org/10.1029/2001GC000256

Kimura, G., Mukai, A., 1991. Underplated units in an accretionary complex: melange of the Shimanto Belt of eastern Shikoku, southwest Japan. Tectonics 10, 31–50.

Kincaid, C., Sacks, I.S., 1997. Thermal and dynamical evolution of the upper mantle in subduction zones. J. Geophys. Res. Solid Earth 102, 12295–12315. https://doi.org/10.1029/96JB03553

Kirby, S.H., 1983. Rheology of the Lithospere. Rev. Geophys. Sp. Phys. 21, 1458–1487. https://doi.org/10.1029/RG021i006p01458

Kirby, S.H., Stein, S., Okal, E.A., Rubie, D.C., 1996. METASTABLE MANTLE PHASE TRANSFORMATIONS AND DEEP EARTHQUAKES IN SUBDUCTING OCEANIC LITHOSPHERE. Rev. Geophys. 34, 261–306.

Klemd, R., Bröcker, M., Hacker, B.R., Gao, J., Gans, P., Wemmer, K., 2005. New Age Constraints on the Metamorphic Evolution of the High-Pressure/Low-Temperature Belt in the Western Tianshan Mountains, NW China. J. Geol. 113, 157–168. https://doi.org/10.1086/427666

Klemd, R., Gao, J., Li, J.L., Meyer, M., 2015. Metamorphic evolution of (ultra)-high-pressure subduction-related transient crust in the South Tianshan Orogen (Central Asian Orogenic Belt): Geodynamic implications. Gondwana Res. 28, 1–25. https://doi.org/10.1016/j.gr.2014.11.008

Klemd, R., John, T., Scherer, E.E., Rondenay, S., Gao, J., 2011. Changes in dip of subducted slabs at depth: Petrological and geochronological evidence from HP-UHP rocks (Tianshan, NW-China). Earth Planet. Sci. Lett. 310, 9–20.

Kopf, A.J., 2002. Significance of mud volcanism. Rev. Geophys. 40, 2-1-2–52. https://doi.org/10.1029/2000RG000093

Kopp, H., Flueh, E.R., Petersen, C.J., Weinrebe, W., Wittwer, A., Scientists, M., 2006. The Java margin revisited : Evidence for subduction erosion off Java. Earth Planet. Sci. Lett. 242, 130–142. https://doi.org/10.1016/j.epsl.2005.11.036

Kröner, A., Kovach, V., Belousova, E., Hegner, E., Armstrong, R., Dolgopolova, A., Seltmann, R., Alexeiev, D. V., Hoffmann, J.E., Wong, J., Sun, M., Cai, K., Wang, T., Tong, Y., Wilde, S.A., Degtyarev, K.E., Rytsk, E., 2014. Reassessment of continental growth during the accretionary history of the Central Asian Orogenic Belt. Gondwana Res. 25, 103–125. https://doi.org/10.1016/j.gr.2012.12.023

Kullerud, L., 1991. On the calculation of isochrons. Chem. Geol. Isot. Geosci. Sect. 87, 115–124. https://doi.org/10.1016/0168-9622(91)90045-X

Kusebauch, C., John, T., Whitehouse, M.J., Klemme, S., Putnis, A., 2015. Distribution of halogens between fluid and apatite during fluid-mediated replacement processes. Geochim. Cosmochim. Acta 170, 225–246. https://doi.org/10.1016/j.gca.2015.08.023

Kutterolf, S., Freundt, A., Peréz, W., 2008a. Pacific offshore record of plinian arc volcanism in Central America: 2. Tephra volumes and erupted masses. Geochemistry, Geophys. Geosystems 9, n/a-n/a. https://doi.org/10.1029/2007GC001791

Kutterolf, S., Freundt, A., Peréz, W., Mörz, T., Schacht, U., Wehrmann, H., Schmincke, H.-U., 2008b. Pacific offshore record of plinian arc volcanism in Central America: 1. Along-arc correlations. Geochemistry, Geophys. Geosystems 9, n/a-n/a. https://doi.org/10.1029/2007GC001631

Lagos, M., Scherer, E.E., Tomaschek, F., Münker, C., Keiter, M., Berndt, J., Ballhaus, C., 2007. High precision Lu-Hf geochronology of Eocene eclogite-facies rocks from Syros, Cyclades, Greece. Chem. Geol. 243, 16–35. https://doi.org/10.1016/j.chemgeo.2007.04.008

Lallemand, S., Le Pichon, X., 1987. Coulomb wedge model applied to the subduction of seamounts in the Japan Trench. Geology 15, 1065–1069. https://doi.org/10.1130/0091-7613(1987)15<1065:CWMATT>2.0.CO;2

Lapen, T.J., Johnson, C.M., Baumgartner, L.P., Mahlen, N.J., Beard, B.L., Amato, J.M., 2003. Burial rates during prograde metamorphism of an ultra-high-pressure terrane: An example from Lago di Cignana, western Alps, Italy. Earth Planet. Sci. Lett. 215, 57–72. https://doi.org/10.1016/S0012-821X(03)00455-2

Lash, G.G., 1987. Documentation and significance of progressive microfabric changes in Middle Ordovician trench mudstones. Geol. Soc. Am. Bull. 101, 1268–1279.

Laurent, V., Jolivet, L., Roche, V., Augier, R., Scaillet, S., Cardello, G.L., 2016. Strain localization in a fossilized subduction channel: Insights from the Cycladic Blueschist Unit (Syros, Greece). Tectonophysics 672–673, 150–169. https://doi.org/10.1016/j.tecto.2016.01.036

Lázaro, C., García-Casco, A., Rojas Agramonte, Y., Kröner, A., Neubauer, F., Iturralde-Vinent, M., 2009. Fifty-five-million-year history of oceanic subduction and exhumation at the northern edge of the Caribbean plate (Sierra del Convento mélange, Cuba). J. Metamorph. Geol. 27, 19–40. https://doi.org/10.1111/j.1525-1314.2008.00800.x

Leake, B., Woolley, A.R., Arps, C.E.S., Birch, W.D., Gilbert, C.M., Grice, J.D., Hawthorne, F.C., Kato, A., Kisch, H.J., Krivovichev, V.G., Linthout, K., Laird, J., Mandarino, J.A., Maresch, W. V., Nickel, E.H., Rock, N.M.S., Schumacher, J.C., Smith, D.C., Stephenson, N.C.N., Ungaretti, L., Whittaker, E.J.W., Youzhi, G., 1997. Nomenclature of Amphiboles: Report of the Subcommittee on Amphiboles of the International Mineralogical Association Commission on New Minerals and Mineral Names. Can. Mineral. 35, 1571–1606. https://doi.org/https://doi.org/10.1180/minmag.1997.061.405.13

Le Pichon, X., 1968. Sea-floor spreading and continental drift. J. Geophys. Res. 73, 3661–3697. https://doi.org/10.1029/JB073i012p03661

Li, J.L., Klemd, R., Gao, J., Jiang, T., Song, Y.H., 2015. A common high-pressure metamorphic evolution of interlayered eclogites and metasediments from the “ultrahigh-pressure unit” of the Tianshan metamorphic belt in China. Lithos 226, 169–182. https://doi.org/10.1016/j.lithos.2014.12.006

Li, J.L., Klemd, R., Gao, J., John, T., 2016. Poly-cyclic metamorphic evolution of eclogite: Evidence for multistage burial-exhumation cycling in a subduction channel. J. Petrol. 57, 119–146. https://doi.org/10.1093/petrology/egw002

Li, J.L., Klemd, R., Gao, J., Meyer, M., 2012. Coexisting carbonate-bearing eclogite and blueschist in SW Tianshan, China: Petrology and phase equilibria. J. Asian Earth Sci. 60, 174–187. https://doi.org/10.1016/j.jseaes.2012.08.015

Li, Q. li, Lin, W., Su, W., Li, X. hua, Shi, Y. hong, Liu, Y., Tang, G. qiang, 2011. SIMS U-Pb rutile age of low-temperature eclogites from southwestern Chinese Tianshan, NW China. Lithos 122, 76–86. https://doi.org/10.1016/j.lithos.2010.11.007

Li, S., Wang, S., Chen, Y., Liu, D., Qiu, J., Zhou, H., Zhang, Z., 1994. Excess argon in phengite from eclogite: Evidence from dating of eclogite minerals by SmNd, RbSr and40Ar39Ar methods. Chem. Geol. 112, 343–350. https://doi.org/10.1016/0009-2541(94)90033-7

Liou, J.G., Tsujimori, T., Zhang, R.Y., Katayama, I., Maruyama, S., 2004. Global UHP Metamorphism and Continental Subduction/Collision: The Himalayan Model. Int. Geol. Rev. 46, 1–27. https://doi.org/10.2747/0020-6814.46.1.1

Liu, X., Su, W., Gao, J., Li, J., Jiang, T., Zhang, X., Ge, X., 2014. Paleozoic subduction erosion involving accretionary wedge sediments in the South Tianshan Orogen: Evidence from geochronological and geochemical studies on eclogites and their host metasediments. Lithos 210, 89–110. https://doi.org/10.1016/j.lithos.2014.09.017

Lloyd, G.E., Butler, R.W.H., Casey, M., Tatham, D.J., Mainprice, D., 2011. Constraints on the seismic properties of the middle and lower continental crust. Geol. Soc. London, Spec. Publ. 360, 7–32. https://doi.org/10.1144/SP360.2

Locatelli, M., Verlaguet, A., Agard, P., Federico, L., Angiboust, S., 2018. Intermediate-depth brecciation along the subduction plate interface (Monviso eclogite, W. Alps). Lithos 320–321, 378–402.

Long, L., Gao, J., Klemd, R., Beier, C., Qian, Q., Zhang, X., Wang, J., Jiang, T., 2011. Geochemical and geochronological studies of granitoid rocks from the Western Tianshan Orogen: Implications for continental growth in the southwestern Central Asian Orogenic Belt. Lithos 126, 321–340.

Lü, Z., Bucher, K., Zhang, L., Du, J., 2012a. The Habutengsu metapelites and metagreywackes in western Tianshan, China: Metamorphic evolution and tectonic implications. J. Metamorph. Geol. 30, 907–926. https://doi.org/10.1111/j.1525-1314.2012.01002.x

Lü, Z., Zhang, L., 2012. Coesite in the eclogite and schist of the Atantayi Valley, southwestern Tianshan, China. Chinese Sci. Bull. 57, 1467–1472.

Lü, Z., Zhang, L., Du, J., Bucher, K., 2009. Petrology of coesite-bearing eclogite from Habutengsu Valley, western Tianshan, NW China and its tectonometamorphic implication. J. Metamorph. Geol. 27, 773–787.

Lü, Z., Zhang, L., Du, J., Yang, X., Tian, Z., Xia, B., 2012b. Petrology of HP metamorphic veins in coesite-bearing eclogite from western Tianshan, China: Fluid processes and elemental mobility during exhumation in a cold subduction zone. Lithos 136–139, 168–186. https://doi.org/10.1016/j.lithos.2011.10.011

Ludwig, K.R., 2012. User’s Manual for Isoplot 3.75, a geochronological toolkit for Microsoft Excel. Berkeley Geochronol. Cent. Spec. Publ. 5, 1–72.

Marschall, H.R., Schumacher, J.C., 2012. Arc magmas sourced from mélange diapirs in subduction zones. Nat. Geosci. 5, 862–867. https://doi.org/10.1038/ngeo1634

Marsh, B.D., 1977. ISLAND ARC DEVELOPMENT: SOME OBSERVATIONS , EXPERIMENTS , AND SPECULATIONS1. J. Geol. 87, 687–713.

McKenzie, D., 1972. Active tectonics of the Mediterranean region. Geophys. J. R. Astron. Soc. 30, 109–185.

McKenzie, D.P., Parker, R.L., 1967. The North Pacific: An example of tectonics on a sphere. Nature 216, 1276–1280. https://doi.org/10.1038/2161276a0

Métois, M., Socquet, A., Vigny, C., 2012. Interseismic coupling , segmentation and mechanical behavior of the central Chile subduction zone. J. Geophys. Res. 117, 1–16. https://doi.org/10.1029/2011JB008736

Métois, M., Vigny, C., Socquet, A., 2016. Interseismic Coupling , Megathrust Earthquakes and Seismic Swarms Along the Chilean Subduction Zone (38 ° – 18 ° S). Pure Appl. Geophys. 173, 1431–1449. https://doi.org/10.1007/s00024-016-1280-5

Meyer, M., John, T., Brandt, S., Klemd, R., 2011. Trace element composition of rutile and the application of Zr-in-rutile thermometry to UHT metamorphism (Epupa Complex, NW Namibia). Lithos 126, 388–401. https://doi.org/10.1016/j.lithos.2011.07.013

Meyer, M., Klemd, R., John, T., Gao, J., Menneken, M., 2016. An (in-)coherent metamorphic evolution of high-P eclogites and their host rocks in the Chinese southwest Tianshan? J. Metamorph. Geol. 34, 121–146. https://doi.org/10.1111/jmg.12175

Mezger, K., Hanson, G.N., Bohlen, S.R., 1989. High-precision UPb ages of metamorphic rutile: application to the cooling history of high-grade terranes. Earth Planet. Sci. Lett. 96, 106–118. https://doi.org/10.1016/0012-821X(89)90126-X

Molnar, P., Tapponnier, P., 1977. The collision between India and Eurasia. Sci. Am. 236, 30–41.

Molnar, P., Tapponnier, P., 1975a. Cenozoic Tectonics of Asia: Effects of a Continental Collision. Science (80-.). 189, 419–426.

Molnar, P., Tapponnier, P., 1975b. Cenozoic Tectonics of Asia: Effects of a Continental Collision. Science (80-.). 189, 419–426. https://doi.org/10.1098/rsta.1988.0089

Moreno, M., Rosenau, M., Oncken, O., 2010. 2010 Maule earthquake slip correlates with pre-seismic locking of Andean subduction zone. Nature 467, 198–202. https://doi.org/10.1038/nature09349

Morimoto, N., 1988. Nomenclature of Pyroxenes. Mineral. Petrol. 39, 55–76. https://doi.org/10.1007/BF01226262

Nielsen, S.G., Marschall, H.R., 2017. Geochemical evidence for mélange melting in global arcs. Sci. Adv. 3, 1–7. https://doi.org/10.1126/sciadv.1602402

Okubo, P.G., Aki, K., 1987. Fractal Geometry in the San Andreas Fault System. J. Geophys. Res. 92, 345–355.

Oncken, O., Chong, G., Franz, G., Giese, P., Götze, H.-J., Ramos, V.A., Strecker, M.R., Wigger, P., 2006. The Andes: Active Subduction Orogeny.

Onishi, C.T., Kimura, G., 1995. Change in fabric of melange in the Shimanto Belt, Japan: Change in relative convergence? Tectonics 14, 1273–1289.

Oxburgh, E.R., Parmentier, E.M., 1977. Compositional and density stratification in oceanic lithosphere-causes and consequences. J. Geol. Soc. London. 133, 343–355. https://doi.org/10.1144/gsjgs.133.4.0343

Pacheko, J., Sykes, L.R., Scholz, C.H., 1993. Nature of Seismic Coupling Along Simple Plate Boundaries of the Subduction Type. J. Geophys. Res. Solid Earth 98, 14133–14159.

Pawley, A.R., Holloway, J.R., 1993. Water Sources for Subduction Zone Volcanism : New Experimental Constraints. Science (80-.). 260, 664–667.

Peacock, S.M., 2001. Are the lower planes of double seismic zones caused by serpentine dehydration in subducting oceanic mantle? Geology 29, 299–302. https://doi.org/10.1130/0091-7613(1980)?8<11:APCAKM>?2.0.CO

Peacock, S.M., 1990. Fluid Processes Subduction Zones. Science (80-.). 248, 329–337.

Peacock, S.M., Christensen, N.I., Bostock, M.G., Audet, P., 2011. High pore pressures and porosity at 35 km depth in the Cascadia subduction zone. Geology 39, 471–474. https://doi.org/10.1130/G31649.1

Peacock, S.M., Hyndman, R.D., 1999. Hydrous minerals in the mantle wedge and the maximum depth of subduction thrust earthquakes. Geophys. Res. Lett. 26, 2517–2520.

Philippot, P., 1993. Fluid-melt-rock interaction in mafic eclogites and coesite- bearing metasediments : Constraints on volatile recycling during subduction. Chem. Geol. 108, 93–112.

Plank, T., Langmuir, C.H., 1998. The chemical composition of subducting sediment and its consequences for the crust and mantle. Chem. Geol. Isot. Geosci. Sect. 145, 325–394.

Plank, T., Langmuir, C.H., 1993. Tracing trace elements from sediment input to volcanic output at subduction zones. Nature 362, 739–742.

Plunder, A., Agard, P., Chopin, C., Pourteau, A., Okay, A.I., 2015. Accretion, underplating and exhumation along a subduction interface: From subduction initiation to continental subduction (Tavşanli zone, W. Turkey). Lithos 226, 233–254. https://doi.org/10.1016/j.lithos.2015.01.007

Poli, S., Schmidt, M.W., 2002. Petrology of subducted slabs. Annu. Rev. Earth Planet. Sci. 30, 207–235. https://doi.org/10.1146/annurev.earth.30.091201.140550

Poli, S., Schmidt, M.W., 1995. H20 transport and release in subduction zones : Experimental constraints on basaltic and andesitic systems. J. Geophys. Res. 100, 22299–22314.

Raimbourg, H., Jolivet, L., Leroy, Y., 2007. Consequences of progressive eclogitisation on crustal exhumation, a mechanical study. Geophys. J. Int. 168, 379–401. https://doi.org/10.1111/j.1365-246X.2006.03130.x

Ranero, C.R., Grevemeyer, I., Sahling, H., Barckhausen, U., Hensen, C., Wallmann, K., Weinrebe, W., Vannucchi, P., Von Huene, R., McIntosh, K., 2008. Hydrogeological system of erosional convergent margins and its influence on tectonics and interplate seismogenesis. Geochemistry, Geophys. Geosystems 9. https://doi.org/10.1029/2007GC001679

Ravna, E.J.K., 2000. The garnet – clinopyroxene Fe 2 + – Mg geothermometer : an updated calibration. J. Metamorph. Geol. 211–219.

Ravna, E.J.K., Terry, M.P., 2004. Geothermobarometry of UHP and HP eclogites and schists - An evaluation of equilibria among garnet-clinopyroxene-kyanite-phengite-coesite/quartz. J. Metamorph. Geol. 22, 579–592. https://doi.org/10.1111/j.1525-1314.2004.00534.x

Raymond, L.A., 1975. Tectonite and Melange — A Distinction. Geology 7–9. https://doi.org/10.1130/0091-7613(1975)3<7

Reinecke, T., 1998. Prograde high- to ultrahigh-pressure metamorphism and exhumation of oceanic sediments at Lago di Cignana, Zermatt-Saas Zone, western Alps. Lithos 42, 147–189. https://doi.org/10.1016/S0024-4937(97)00041-8

Remitti, F., Vannucchi, P., Bettelli, G., Fantoni, L., Panini, F., Vescovi, P., 2011. Tectonic and sedimentary evolution of the frontal part of an ancient subduction complex at the transition from accretion to erosion: The case of the Ligurian wedge of the Northern Apennines, Italy. Bull. Geol. Soc. Am. 123, 51–70. https://doi.org/10.1130/B30065.1

Ring, U., Glodny, J., Will, T., Thomson, S., 2010. The Hellenic Subduction System : High-Pressure Metamorphism , Exhumation , Normal Faulting , and Large-Scale Extension. Annu. Rev. Earth Planet. Sci. 38, 45–76. https://doi.org/10.1146/annurev.earth.050708.170910

Rosenfeld, J.L., 1969. Stress effects around quartz inclusions in almandine and the piezothermometry of coexisting aluminum silicates. Am. J. Sci. https://doi.org/10.2475/ajs.267.3.317

Rowe, C.D., Moore, J.C., Remitti, F., 2013. The thickness of subduction plate boundary faults from the seafloor into the seismogenic zone. Geology 41, 991–994. https://doi.org/10.1130/G34556.1

Rowe, C.D., Science, E., Santa, C., Street, H., Cruz, S., Moore, J.C., Meneghini, F., Maria, S., 2005. Large-scale pseudotachylytes and fluidized cataclasites from an ancient subduction thrust fault. Geology 33, 937–940. https://doi.org/10.1130/G21856.1

Rubatto, D., 2002. Zircon trace element geochemistry: Partitioning with garnet and the link between U-Pb ages and metamorphism. Chem. Geol. 184, 123–138. https://doi.org/10.1016/S0009-2541(01)00355-2

Ruffet, G., Gruau, G., Ballèvre, M., Féraud, G., Philippot, P., 1997. Rb-Sr and ^{40}Ar-^{39}Ar laser probe dating of high-pressure phengites from the Sesia zone (Western Alps): underscoring of excess argon and new age constraints on the high-pressure metamorphism. Chem. Geol. 141, 1–18. https://doi.org/10.1016/S0009-2541(97)00052-1

Ruh, J.B., Le Pourhiet, L., Agard, P., Burov, E., Gerya, T., 2015. Tectonic slicing of subducting oceanic crust along plate interfaces: Numerical modeling. Geochemistry, Geophys. Geosystems 16, 3505–3531. https://doi.org/10.1002/2015GC005998

Sasaki, J., Peterson, N.L., Hoshino, K., 1985. Tracer impurity diffusion in single-crystal rutile (TiO2-x). J. Phys. Chem. Solids 46, 1267–1283. https://doi.org/10.1016/0022-3697(85)90129-5

Scambelluri, M., Fiebig, J., Malaspina, N., Müntener, O., Pettke, T., 2004. Serpentinite Subduction : Implications for Fluid Processes and Trace-Element Recycling. Int. Geol. Rev. 46, 595–613.

Scambelluri, M., Pettke, T., van Roermund, H.L.M., 2008. Majoritic garnets monitor deep subduction fluid flow and mantle dynamics. Geology 36, 59–62. https://doi.org/10.1130/G24056A.1

Scambelluri, M., Philippot, P., 2001. Deep fluids in subduction zones. Lithos 55, 213–227. https://doi.org/10.1016/S0024-4937(00)00046-3

Scheltens, M., Zhang, L., Xiao, W., Zhang, J., 2015. Northward subduction-related orogenesis of the southern Altaids: Constraints from structural and metamorphic analysis of the HP/UHP accretionary complex in Chinese southwestern Tianshan, NW China. Geosci. Front. 6, 191–209. https://doi.org/10.1016/j.gsf.2014.08.002

Scherer, E.E., Cameron, K.L., Blichert-Toft, J., 2000. Lu-Hf garnet geochronology: Closure temperature relative to the Sm-Nd system and the effects of trace mineral inclusions. Geochim. Cosmochim. Acta 64, 3413–3432. https://doi.org/10.1016/S0016-7037(00)00440-3

Scholl, D.W., von Huene, R., Vallier, T.L., Howell, D.G., 1980. Sedimentary masses and concepts about tectonic processes at underthrust ocean margins (subduction). Geology 8, 564–568. https://doi.org/10.1130/0091-7613(1980)8<564:SMACAT>2.0.CO

Scholz, C.H., 1998. Earthquakes and friction laws. Nature 391, 37–42.

Scholz, C.H., Small, C., 1997. The effect of seamount subduction on seismic coupling. Geology 25, 487–490.

Schurr, B., Asch, G., Hainzl, S., Bedford, J., Hoechner, A., Palo, M., Wang, R., Moreno, M., Bartsch, M., Zhang, Y., Oncken, O., Tilmann, F., Dahm, T., Victor, P., Barrientos, S., Vilotte, J.-P., 2014. Gradual unlocking of plate boundary controlled initiation of the 2014 Iquique earthquake. Nature 512, 299–302. https://doi.org/doi:10.1038/nature13681

Scudder, R.P., Murray, R.W., Plank, T., 2009. Dispersed ash in deeply buried sediment from the northwest Pacific Ocean: An example from the Izu-Bonin arc (ODP Site 1149). Earth Planet. Sci. Lett. 284, 639–648. https://doi.org/10.1016/j.epsl.2009.05.037

Sengor, A.M.C., Natal'in, B.A., Burtman, V.S., 1993. Evolution of the Altaid tectonic collage and Palaeozoic crustal growth in Eurasia. Nature 364, 299–307.

Sengor, celal A.M., 1987. Tectonic subdivisions and evolution of Asia. Istanbul Tek. Univ. Bul. 40, 355–435.

Shreve, R.L., Cloos, M., 1986. Dynamics of Sediment Subduction, Melange Formation, and

Prism Accretion. J. Geophys. Res. 91, 10229–10245.

Sibson, R.H., 1986. Brecciation Processes in Fault Zones : Inferences from Earthquake Rupturing. Pure Appl. Geophys. 124, 159–175.

Skora, S., Baumgartner, L.P., Mahlen, N.J., Johnson, C.M., Pilet, S., Hellebrand, E., 2006. Diffusion-limited REE uptake by eclogite garnets and its consequences for Lu-Hf and Sm-Nd geochronology. Contrib. to Mineral. Petrol. 152, 703–720. https://doi.org/10.1007/s00410-006-0128-x

Smith, D.C., 1984. Coesite in clinopyroxene in the Caledonides and its implications for geodynamics. Nature 310, 641–644. https://doi.org/10.1038/310641a0

Soldner, J., Oliot, E., Schulmann, K., Štípská, P., Kusbach, V., Anczkiewicz, R., 2017. Metamorphic P–T–t–d evolution of (U)HP metabasites from the South Tianshan accretionary complex (NW China) — Implications for rock deformation during exhumation in a subduction channel. Gondwana Res. 47, 161–187. https://doi.org/10.1016/j.gr.2016.07.007

Spandler, C., Pirard, C., 2013. Element recycling from subducting slabs to arc crust: A review. Lithos 170–171, 208–223. https://doi.org/10.1016/j.lithos.2013.02.016

St. Clair, J., Holbrook, W.S., van Avendonk, H.J.A., Lizarralde, D., 2016. Along-strike structure of the Costa Rican convergent margin fromseismic a refraction/reflection survey: Evidence for underplating beneath the inner forearc. Geochemistry, Geophys. Geosystems 17, 501–520. https://doi.org/10.1002/2015GC006029.Received

Su, W., Gao, J., Klemd, R., Li, J.-L., Zhang, X., Li, X.-H., Chen, N.-S., Zhang, L., 2010. U–Pb zircon geochronology of Tianshan eclogites in NW China: implication for the collision between the Yili and Tarim blocks of the southwestern Altaids. Eur. J. Mineral. 22, 473–478. https://doi.org/10.1127/0935-1221/2010/0022-2040

Syracuse, E.M., van Keken, P.E., Abers, G.A., Suetsugu, D., Bina, C., Inoue, T., Wiens, D., Jellinek, M., 2010. The global range of subduction zone thermal models. Phys. Earth Planet. Inter. 183, 73–90. https://doi.org/10.1016/j.pepi.2010.02.004

Tan, E., Lavier, L.L., van Avendonk, H.J.A., Heuret, A., 2012. The role of frictional strength on plate coupling at the subduction interface. Geochemistry, Geophys. Geosystems 13. https://doi.org/10.1029/2012GC004214

Tan, Z., Agard, P., Gao, J., John, T., Li, J.L., Jiang, T., Bayet, L., Wang, X.S., Zhang, X., 2017. P–T–time-isotopic evolution of coesite-bearing eclogites: Implications for exhumation processes in SW Tianshan. Lithos 278–281, 1–25. https://doi.org/10.1016/j.lithos.2017.01.010

Tatsumi, Y., 1989. Migration of fluid phases and genesis of basalt magmas in subduction zones 94, 4697–4707.

Tatsumi, Y., 1986. Formation of the volcanic front in subduction zones. Geophys. Res. Lett. 13, 717–720.

Thielmann, M., Rozel, A., Kaus, B.J.P., Ricard, Y., 2015. Intermediate-depth earthquake generation and shear zone formation caused by grain size reduction and shear heating. Geology 43, 791–794. https://doi.org/10.1130/G36864.1

Thompson, J.B.J., 1955. The thermodynamic basis for the mineral facies concept. Am. J. Sci. 253, 65–103.

Thöni, M., Jagoutz, E., 1992. Some new aspects of dating eclogites in orogenic belts: Sm-Nd, Rb-Sr, and Pb-Pb isotopic results from the Austroalpine Saualpe and Koralpe type-locality (Carinthia/Styria, southeastern Austria). Geochim. Cosmochim. Acta 56, 347–368. https://doi.org/10.1016/0016-7037(92)90138-9

Tian, Z.L., Wei, C.J., 2014. Coexistence of garnet blueschist and eclogite in South Tianshan, NW China: Dependence of P-T evolution and bulk-rock composition. J. Metamorph. Geol. 32, 743–764. https://doi.org/10.1111/jmg.12089

Tian, Z.L., Wei, C.J., 2013. Metamorphism of ultrahigh-pressure eclogites from the Kebuerte Valley, South Tianshan, NW China: phase equilibria and P-T path. J. Metamorph. Geol. 31, 281–300.

Tichelaar, B.W., Ruff, L.J., 1993. Depth of seismic coupling along subduction zones. J. Geophys. Res. Solid Earth 98, 2017–2037.

Toda, S., Stein, R.S., Kirby, S.H., Bozkurt, S.B., 2008. A slab fragment wedged under Tokyo and its tectonic and seismic implications. Nat. Geosci. 1, 771–776. https://doi.org/10.1038/ngeo318

Van der Molen, I., Van Roermund, H.L.M., 1986. The pressure path of solid inclusions in minerals: the retention of coesite inclusions during uplift. Lithos 19, 317–324. https://doi.org/10.1016/0024-4937(86)90030-7

van der Straaten, F., Halama, R., John, T., Schenk, V., Hauff, F., Andersen, N., 2012. Tracing the effects of high-pressure metasomatic fluids and seawater alteration in blueschist-facies overprinted eclogites: Implications for subduction channel processes. Chem. Geol. 292–293, 69–87.

van der Straaten, F., Schenk, V., John, T., Gao, J., 2008. Blueschist-facies rehydration of eclogites (Tian Shan, NW-China): Implications for fluid-rock interaction in the subduction channel. Chem. Geol. 255, 195–219.

van Keken, P.E., Currie, C., King, S.D., Behn, M.D., Cagnioncle, A., He, J., Katz, R.F., Lin, S.C., Parmentier, E.M., Spiegelman, M., Wang, K., 2008. A community benchmark for subduction zone modeling. Phys. Earth Planet. Inter. 171, 187–197. https://doi.org/10.1016/j.pepi.2008.04.015

van Keken, P.E., Hacker, B.R., Syracuse, E.M., Abers, G.A., 2011. Subduction factory : 4 . Depth - dependent flux of H 2 O from subducting slabs worldwide. J. Geophys. Res. 116. https://doi.org/10.1029/2010JB007922

VanLaningham, S., Meigs, A., Goldfinge, C., 2006. The effects of rock uplift and rock resistance on river morphology in a subduction zone forearc, Oregon, USA Sam. Earth Surf. Process. Landforms 31, 1257–1279. https://doi.org/10.1002/esp

Vannucchi, P., Remitti, F., Bettelli, G., 2008. Geological record of fluid flow and seismogenesis along an erosive subducting plate boundary. Nature 451, 699–703. https://doi.org/10.1038/nature06486

Vannucchi, P., Sage, F., Phipps Morgan, J., Remitti, F., Collot, J.Y., 2012. Toward a dynamic concept of the subduction channel at erosive convergent margins with implications for interplate material transfer. Geochemistry, Geophys. Geosystems 13, 1–24. https://doi.org/10.1029/2011GC003846

Villa, I.M., De Bièvre, P., Holden, N.E., Renne, P.R., 2015. IUPAC-IUGS recommendation on the half life of ^{87}Rb. Geochim. Cosmochim. Acta 164, 382–385. https://doi.org/10.1016/j.gca.2015.05.025

Vine, F.J., Matthews, D.H., 1963. Magnetic anomalies over oceanic ridges. Nature 199, 947–949.

Volkova, N.I., Budanov, V.I., 1999. Geochemical discrimination of metabasalt rocks of the Fan-Karategin transitional blueschist/greenschist belt, South Tianshan, Tajikistan: seamount volcanism and accretionary tectonics. Lithos 47, 201–216.

von Huene, R., 1986. To accrete or not accrete, that is the question. Geol. Rundschau 75, 1–15. https://doi.org/10.1007/BF01770175

von Huene, R., Culotta, R., 1989. Tectonic erosion at the front of the Japan Trench convergent margin. Tectonophysics 160, 75–90. https://doi.org/10.1016/0040-1951(89)90385-5

von Huene, R., Ranero, C.R., Vannucchi, P., 2004. Generic model of subduction erosion. Geology 32, 913–916. https://doi.org/10.1130/G20563.1

von Huene, R., Scholl, D.W., 1991. Observations at convergent margins concerning sediment subduction, subduction erosion, and the growth of continental crust. Rev. Geophys. 29, 279–316. https://doi.org/10.1029/91RG00969

Wada, I., Wang, K., 2009. Common depth of slab-mantle decoupling: Reconciling diversity and uniformity of subduction zones. Geochemistry, Geophys. Geosystems 10. https://doi.org/10.1029/2009GC002570

Wada, I., Wang, K., He, J., Hyndman, R.D., 2008. Weakening of the subduction interface and its effects on surface heat flow, slab dehydration, and mantle wedge serpentinization. J. Geophys. Res. Solid Earth 113, 1–15. https://doi.org/10.1029/2007JB005190

Wadati, K., 1935. On the activity of deep-focus earthquakes in the Japan Islands and neighborhoods. Geophys. Mag. 8, 305–325.

Wakabayashi, J., 2015. Anatomy of a subduction complex: Architecture of the Franciscan Complex, California, at multiple length and time scales. Int. Geol. Rev. 57, 669–746. https://doi.org/10.1080/00206814.2014.998728

Wakita, K., Metcalfe, I., 2005. Ocean plate stratigraphy in East and Southeast Asia. J. Asian Earth Sci. 24, 679–702. https://doi.org/10.1016/j.jseaes.2004.04.004

Wallace, R.E., 1990. The San Andreas fault system, California. US Gov. Print. Off.

Wang, B., Shu, L., Faure, M., Jahn, B. ming, Cluzel, D., Charvet, J., Chung, S. lin, Meffre, S., 2011. Paleozoic tectonics of the southern Chinese Tianshan: Insights from structural, chronological and geochemical studies of the Heiyingshan ophiolitic mélange (NW China). Tectonophysics 497, 85–104. https://doi.org/10.1016/j.tecto.2010.11.004

Waters, D.J., Martin, H.N., 1996. The garnet-cpx-phengite barometer—recommended calibration and calculation method. URL http//www. earth. ox. ac. uk/~

davewa/research/eclogites/ecbarcal. html accessed 3, 14.

Watson, E.B., Wark, D.A., Thomas, J.B., 2006. Crystallization thermometers for zircon and rutile. Contrib. to Mineral. Petrol. 151, 413–433. https://doi.org/10.1007/s00410-006-0068-5

Wegener, A., 1929. Die entstehung der kontinente und ozeane.

Wegener, A., 1912. Die Entstehung der Kontinente. Geol. Rundschau 3, 276–292. https://doi.org/10.1007/BF02202896

Wei, C., Wang, W., Clarke, G.L., Zhang, L., Song, S., 2009. Metamorphism of High/ultrahigh-pressure Pelitic–Felsic Schist in the South Tianshan Orogen, NW China: Phase Equilibria and P–T Path. J. Petrol. 50, 1973–1991.

Wei, C.J., Powell, R., Zhang, L.F., 2003. Eclogites from the south Tianshan, NW China: petrological characteristic and calculated mineral equilibria in the Na2O–CaO–FeO–MgO–Al2O3–SiO2–H2O system. J. Metamorph. Geol. 21, 163–179.

White, R.S., 1984. Atlantic oceanic crust : seismic structure of a slow-spreading ridge. Geol. Soc. London, Spec. Publ. 13, 101–111.

Whitney, D.L., Evans, B.W., 2010. Abbreviations for names of rock-forming minerals. Am. Mineral. 95, 185–187. https://doi.org/10.2138/am.2010.3371

Whitney, D.L., Teyssier, C., Seaton, N.C.A., Fornash, K.F., 2014. Petrofabrics of high-pressure rocks exhumed at the slab-mantle interface from the “ point of no return ” in a subduction zone (Sivrihisar, Turkey). Tectonics 33, 2315–2341. https://doi.org/10.1002/2014TC003677.Received

Whitney, J.A., 1975. The effects of pressure, temperature, and XH2O on phase assemblage in four synthetic rock compositions. J. Geol. 83, 1–31.

Wilson, J.T., 1965. A new class of faults and their bearing on continental drift. Nature 207, 343–347. https://doi.org/10.1038/207343a0

Windley, B.F., Allen, M.B., Zhang, C., Zhao, Z.Y., Wang, G.R., 1990. Paleozoic accretion and Cenozoic redeformation of the Chinese Tien Shan range, central Asia. Geology 18, 128–131.

Woodhead, J.D., Fraser, D.G., 1985. Pb , Sr and 10Be isotopic studies of volcanic rocks from the Northern Mariana Islands . Implications for magma genesis and crustal recycling in the Western Pacific. Geochim. Cosmochim. Acta 49, 1925–1930.

Xia, B., Zhang, L., Bader, T., 2014. Zircon U–Pb ages and Hf isotopic analyses of migmatite from the “paired metamorphic belt” in Chinese SWTianshan: Constraints on partial melting associated with orogeny. Lithos 192, 15–179.

Xiao, W., Santosh, M., 2014. The western Central Asian Orogenic Belt: A window to accretionary orogenesis and continental growth. Gondwana Res. 25, 1429–1444. https://doi.org/10.1016/j.gr.2014.01.008

Xiao, W.J., Windley, B.F., Huang, B.C., Han, C.M., Yuan, C., Chen, H.L., Sun, M., Sun, S., Li, J.L., 2009. End-Permian to mid-Triassic termination of the accretionary processes of the southern Altaids: implications for the geodynamic evolution, Phanerozoic continental growth, and metallogeny of Central Asia. Int. J. Earth Sci. 98, 1189–1217.

Yamato, P., Burov, E., Agard, P., Pourhiet, L. Le, Jolivet, L., 2008. HP-UHP exhumation during slow continental subduction: Self-consistent thermodynamically and thermomechanically coupled model with application to the Western Alps. Earth Planet. Sci. Lett. 271, 63–74. https://doi.org/10.1016/j.epsl.2008.03.049

Yang, X., Zhang, L., Tian, Z., Bader, T., 2013. Petrology and U-Pb zircon dating of coesite-bearing metapelite from the Kebuerte Valley, Western Tianshan, China. J. Asian Earth Sci. 70–71, 295–307. https://doi.org/10.1016/j.jseaes.2013.03.020

Yong, W., Zhang, L., Hall, C.M., Mukasa, S.B., Essene, E.J., 2013. The40Ar/39Ar and Rb-Sr chronology of the Precambrian Aksu blueschists in western China. J. Asian Earth Sci. 63, 197–205. https://doi.org/10.1016/j.jseaes.2012.05.024

Yuan, X., Sobolev, S. V, Kind, R., Oncken, O., Bock, G., Asch, G., Schurr, B., Graeber, F., Rudloff, A., Hanka, W., Wylegalla, K., Tibi, R., Haberland, C., Rietbrock, A., Giese, P., Wigger, P., Röwer, P., Zandt, G., Beck, S., Wallace, T., Pardo, M., Comte, D., 2000. Subduction and collision processes in the Central Andes constrained by converted seismic phases. Nature 408, 958–961.

Zack, T., John, T., 2007. An evaluation of reactive fluid flow and trace element mobility in subducting slabs. Chem. Geol. 237, 5–22. https://doi.org/10.1016/j.chemgeo.2006.06.013

Zack, T., Kronz, A., Foley, S.F., Rivers, T., 2002. Trace element abundances in rutiles from eclogites and associated garnet mica schists. Chem. Geol. 184, 97–122. https://doi.org/10.1016/S0009-2541(01)00357-6

Zack, T., Moraes, R., Kronz, A., 2004. Temperature dependence of Zr in rutile: Empirical calibration of a rutile thermometer. Contrib. to Mineral. Petrol. 148, 471–488. https://doi.org/10.1007/s00410-004-0617-8

Zack, T., Stockli, D.F., Luvizotto, G.L., Barth, M.G., Belousova, E., Wolfe, M.R., Hinton, R.W., 2011. In situ U-Pb rutile dating by LA-ICP-MS:208Pb correction and prospects for geological applications. Contrib. to Mineral. Petrol. 162, 515–530. https://doi.org/10.1007/s00410-011-0609-4

Zhang, L., Ai, Y., Li, X., Rubatto, D., Song, B., Williams, S., Song, S., Ellis, D., Liou, J.G., 2007. Triassic collision of western Tianshan orogenic belt, China: Evidence from SHRIMP U-Pb dating of zircon from HP/UHP eclogitic rocks. Lithos 96, 266–280.

Appendix

The following appendix present supplementary data of fieldwork and analysis realized for this study. The main contacts, i.e., SCTS, GHPD and km-scale shear zone sare reported on each map for reference. Abbreviations: AMC: Akeyazi Metamorphic Complex; SCTS: South Central Tianshan Suture; GHPD: Greeenschist – high-pressure detachment.

Appendix A: Additional information on field data

A1. Map of the GPS data points location
A2. Map of the sample location and names
A3. Map of the lithology data points in the AMC
A4. Detailed map of the structures in the AMC
A5. Detailed of the stereodiagrams
A6. Supplementary field pictures of rocks in the AMC

A1. Map of the GPS data points during the two field campaigns

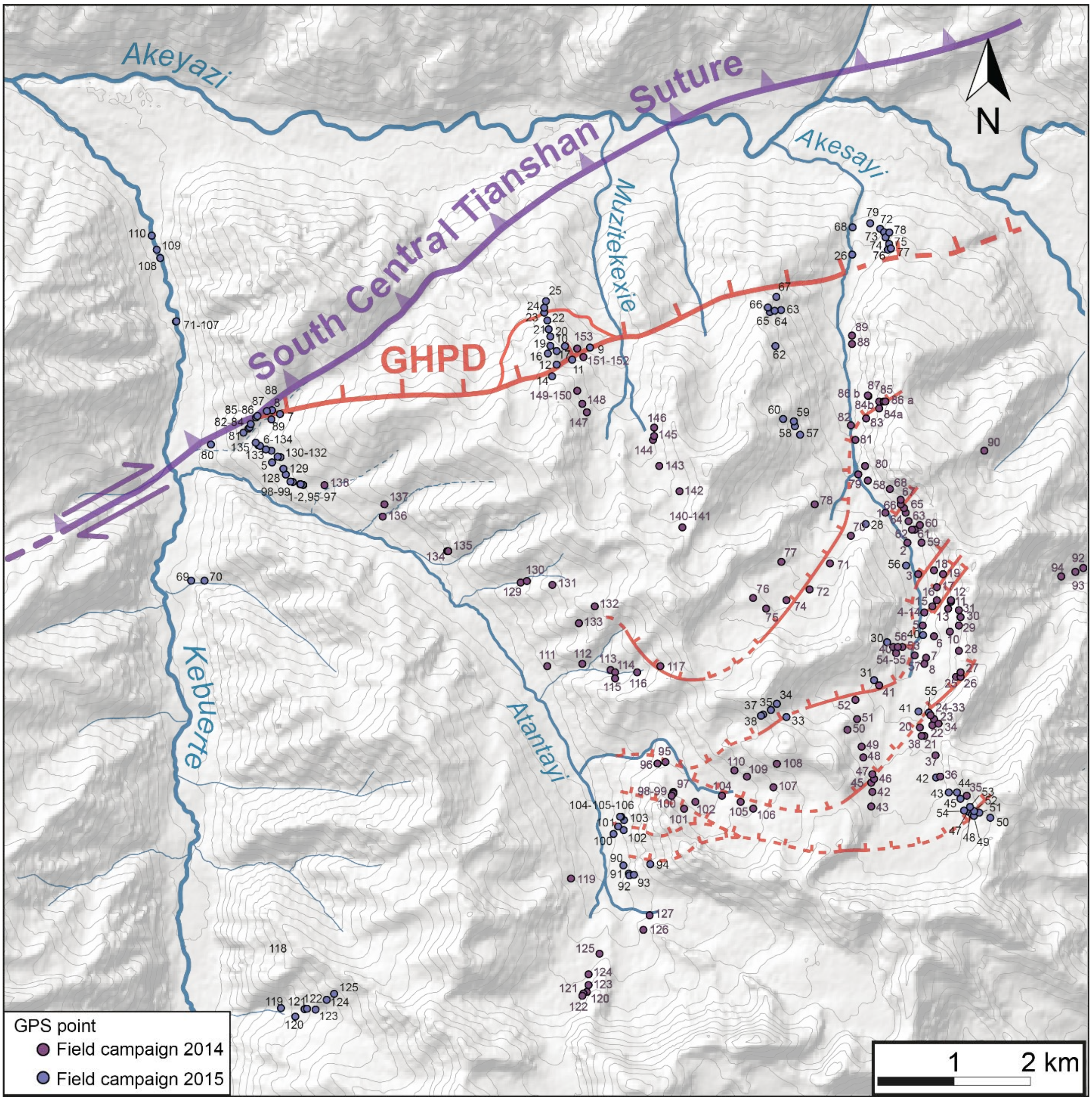

Appendix A1: Map of the AMC with location of the GPS data points of the field campaigns of 2014 (purple circles) and 2015 (blue circles).

A2. Map sample location and name

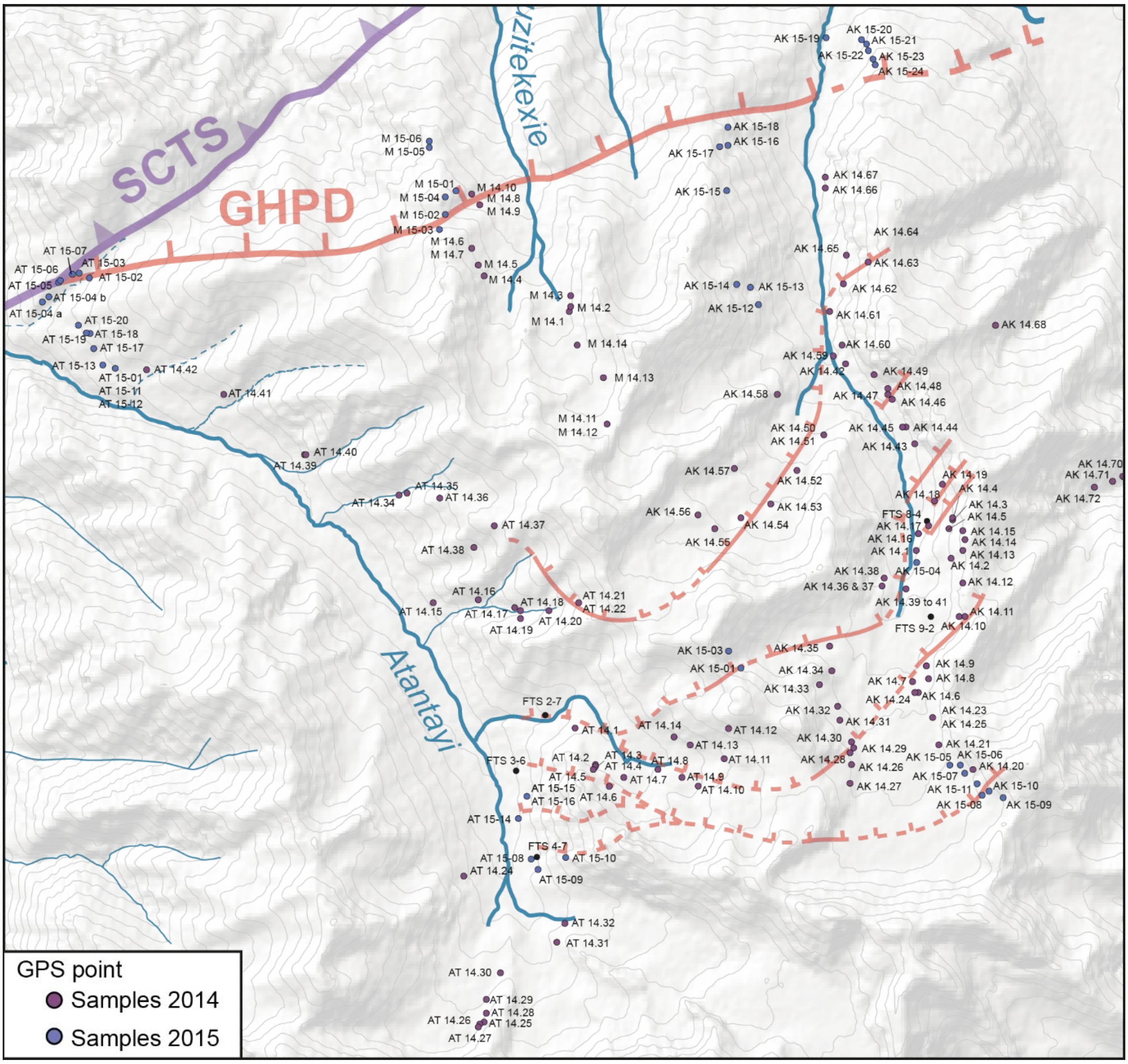

Appendix A2: Map of the AMC with location and names of samples collected during the field campaigns of 2014 (purple circles) and 2015 (blue circles). AT: Atantayi; M: Muzitekexie; AK: Akezayi.

A3. Map of the lithology in the AMC

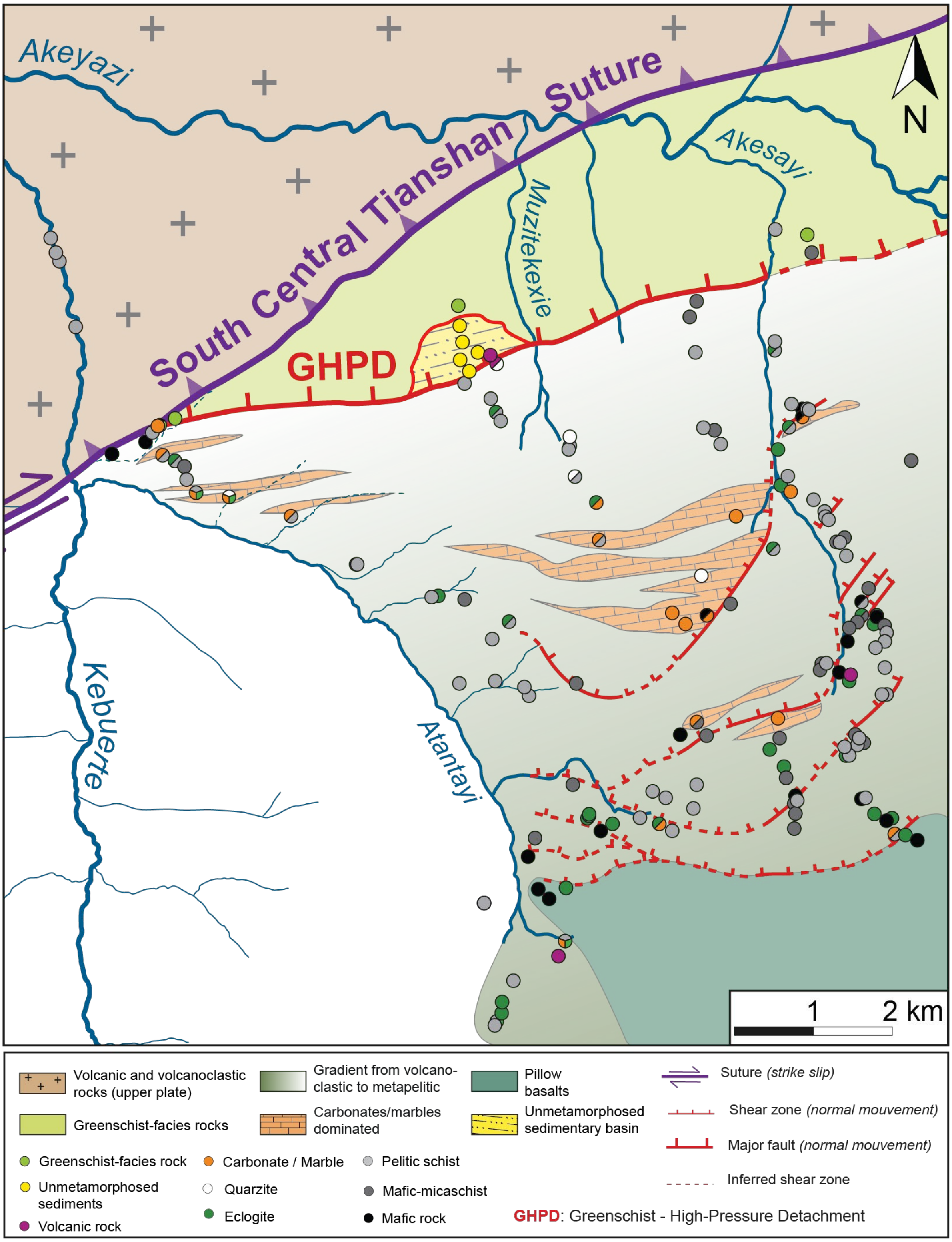

Appendix A3: Map of the AMC illustrating the main lithologies and detailed lithological data points (circles).

A4. Detailed map of the structures in the AMC

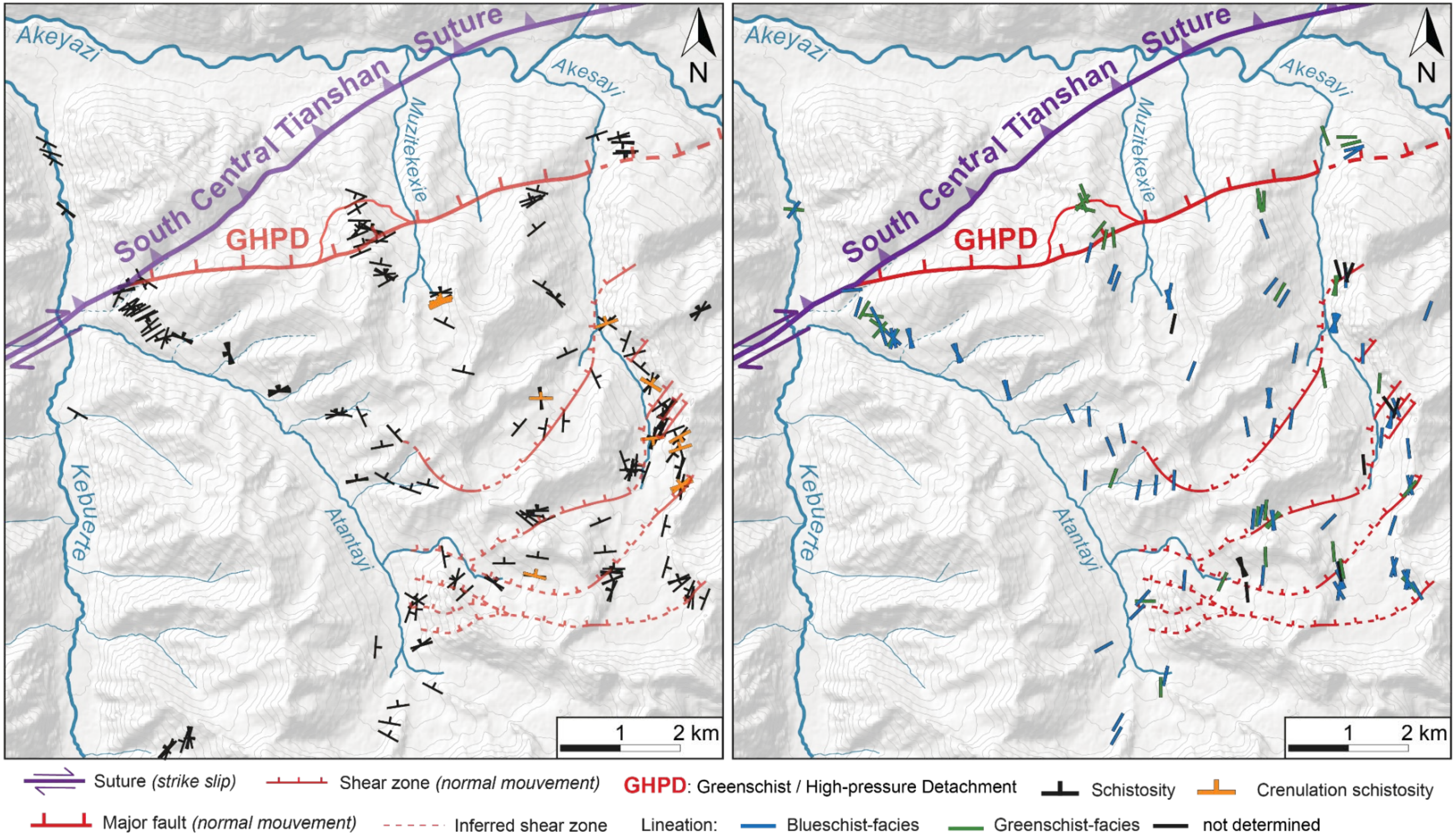

Appendix A4: Map depicting the main contacts observed and detailed structures measured in the AMC (a) Map of the schistosity measurements (black) and crenulation schistosity (orange). (b) Map of the lineation measurements formed at blueschist-facies (blue), greenschist-facies (green) and not determined conditions (black).

A5. Stereodiagrams details

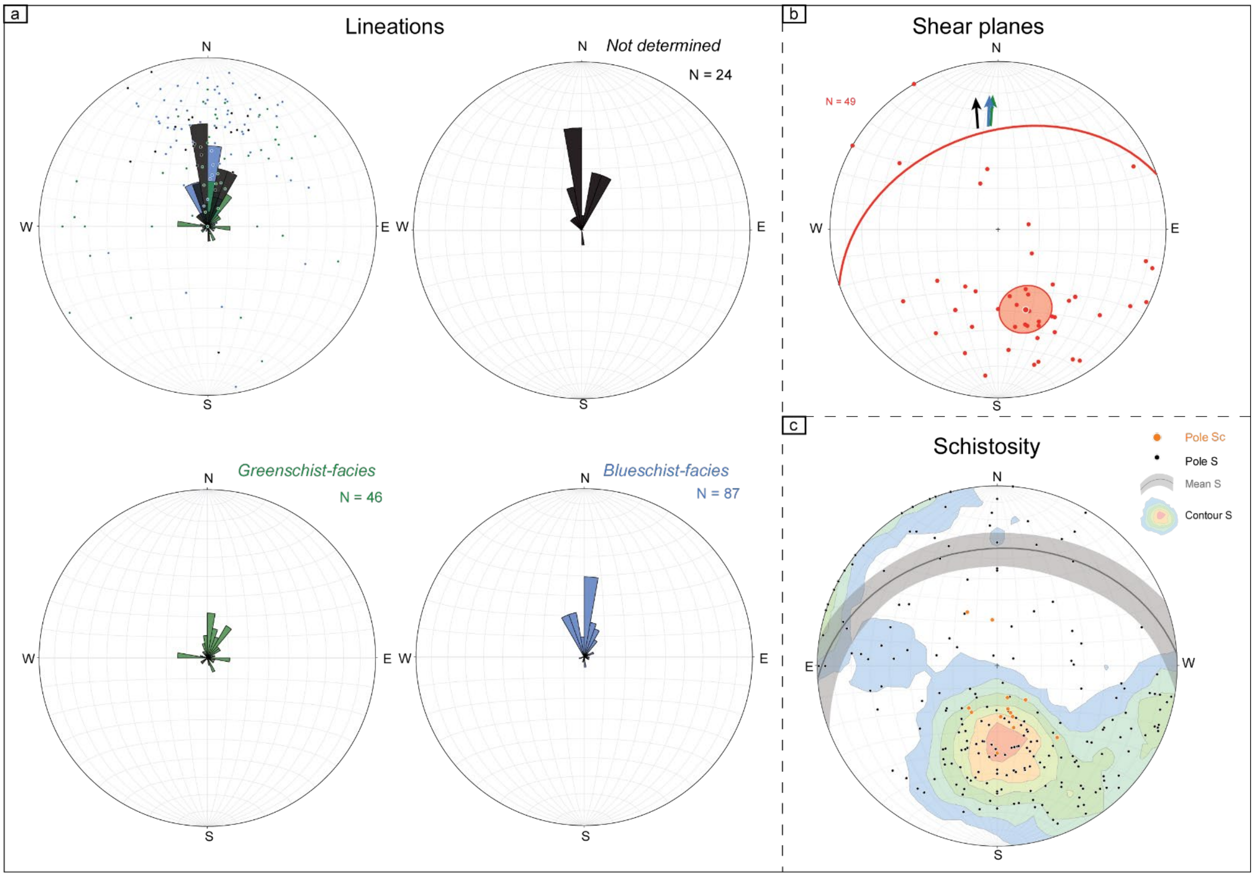

Appendix A5: Detailed stereodiagrams. (a) lineations according to their formation conditions at blueschist-facies (blue), greenschist-facies (green) and not determined conditions (black). N; number of measurements; note the coherent top-to-the-north direction. (b) shear planes measurements (red dots) and calculated average (red plane), with clear top top-to-the-north sense of shearing independently from metamorphic condition (arrows). (c) Details of schistosity (balc dots) and crenulation schistosity poles (orange dots); average schistosity (grey line and area) is calculated from the main cluster.

A6. Supplementary field pictures of rocks in the AMC

Appendix A6: Supplementary field pictures of lithology, deformation features and fluid-rock interactions observed in the AMC. (a) Intimate interlayering of mafic-micaschists rocks, the darker parts mark a larger mafic component. (b) pillow breccias observed in the southernmost part of the Akeyazi valley. Fluid-rock interactions in the AMC is illustrated by (c) deformed quartz veins in a schistosed micaschist host; (d) rutile large crystals (a few cm) growth; (e) omphacite-quartz veins and carbonatic metacomatism in a blueschist rock, and (f) quartz and ankerite veins in an eclogite. Deformation features of (g) shearing and folding at blueschist-facies conditions in a mafic micaschist dominated by the mafic component, (h) shearing and S/C structures in a micaschist, (i) crenulation schistosity at meter-scale.

Appendix B: Petrography and pressure-temperature conditions supplementary material

- B1. Table of the pressure-temperature estimates for this study
- B2. Table of pressure-temperature estimates from literature
- B3. Diagram of the pressure-temperature estimates from literature
- B4. Map of the Si (pfu) of phengite for this study
- B5. Mineral assemblage of eclogite and garnet compositional zoning in the AMC
- B6. Garnet profiles of Fe, Ca, Mg and Mn composition from core to rim

B1. Pressure-temperature estimates for this study

TABLE B1. SAMPLE NUMBER, LOCALISATION, TEMPERATURE AND PRESSURE ESTIMATES

Sample number	**Sample locality**		**T Zr in rutile (T_{Zr}) ± std *(°C)***	**T Carbonaceo *(°C)***	**T used for map**	**P Qtz in Gt (P_R) *(GPa)***	**P Gt-Omp-Phg (P_{GOP}) *(GPa)***	**P from coesite**	**P used for map**
	Latitude (°N)	***Longitude (°E)***							
AK 14.04	42.5136	81.3133	N.D.*	N.D.	N.D.	2.36	N.D.	N.A.†	2.36
AK 14.06	42.4992	81.3136	N.D.	540 ± 24	540	N.D.	N.D.	N.A.	N.D.
AK 14.10	42.5069	81.3192	N.D.	573 ± 29	573	N.D.	N.D.	N.A.	N.D.
AK 14.13	42.5136	81.3197	N.D.	536 ± 25	536	N.D.	N.D.	N.A.	N.D.
AK 14.14	42.5147	81.3200	N.D.	537 ± 21	537	N.D.	N.D.	N.A.	N.D.
AK 14.19	42.5203	81.3169	N.D.	525 ± 20	525	N.D.	N.D.	N.A.	N.D.
AK 14.20	42.4914	81.3211	N.D.	N.D.	N.D.	2.20	2.26	N.A.	2.26
AK 14.30	42.4942	81.3044	530 ± 22	N.D.	530	N.D.	2.74	N.A.	2.74
AK 14.31	42.4964	81.3028	N.D.	530 ± 15	530	N.D.	N.D.	N.A.	N.D.
AK 14.35	42.5039	81.3014	528 ± 18	N.D.	528	2.32	N.D.	N.A.	2.32
AK 14.46	42.5289	81.3100	N.D.	539 ± 24	539	N.D.	N.D.	N.A.	N.D.
AK 14.47	42.5294	81.3094	520 ± 20	546 ± 32	546	*2.56*	N.D.	***2.70***	2.70
AK 14.50	42.5253	81.3006	N.D.	524 ± 32	524	N.D.	N.D.	N.A.	N.D.
AK 14.61	42.5378	81.3014	N.D.	530 ± 18	530	N.D.	N.D.	N.A.	N.D.
AK 14.63	42.5428	81.3067	N.D.	534 ± 22	534	N.D.	N.D.	N.A.	N.D.
AK 14.65	42.5436	81.3036	N.D.	531 ± 19	531	N.D.	N.D.	N.A.	N.D.
AK 14.66	42.5503	81.3008	532 ± 15	546 ± 25	546	*1.73*	N.D.	***2.70***	2.70
AK 15.03	42.5033	81.2878	N.D.	551 ± 30	551	N.D.	N.D.	N.A.	N.D.
AK 15.04	42.5125	81.3136	534 ± 32	N.D.	534	*1.48*	*2.98*	***2.70***	3.00
AK 15.07	42.4911	81.3203	N.D.	546 ± 25	546	N.D.	N.D.	N.A.	N.D.
AK 15.08	42.4889	81.3228	N.D.	N.D.	N.D.	2.06	N.D.	N.A.	2.06
AK 15.20	42.5653	81.3061	N.D.	544 ± 19	544	N.D.	N.D.	N.A.	N.D.
AT 14.05	42.4914	81.2689	522 ± 17	N.D.	522	2.79	N.D.	N.A.	2.79
AT 14.17	42.5078	81.2581	N.D.	546 ± 10	546	N.D.	N.D.	N.A.	N.D.
AT 14.22	42.5083	81.2669	N.D.	N.D.	N.D.	2.30	N.D.	N.A.	2.30
AT 14.25	42.4658	81.2539	N.D.	N.D.	N.D.	2.33	N.D.	N.A.	2.33
AT 14.27	42.4653	81.2531	N.D.	544 ± 14	544	N.D.	N.D.	N.A.	N.D.
AT 14.29	42.4681	81.2542	N.D.	N.D.	N.D.	2.29	N.D.	N.A.	2.29
AT 14.30	42.4683	81.2542	N.D.	509 ± 20	509	2.60	N.D.	N.A.	2.60
AT 14.32	42.4758	81.2650	525 ± 22	537 ± 18	537	2.48	N.D.	N.A.	2.48
AT 14.37	42.5161	81.2553	543 ± 14	553 ± 26	553	2.30	N.D.	N.A.	2.30
AT 14.39	42.5233	81.2292	N.D.	N.D.	N.D.	2.74	N.D.	N.A.	2.74
AT 14.41	42.5294	81.2181	N.D.	546 ± 19	546	2.81	N.D.	*2.70*	2.81
AT 14.42	42.5319	81.2075	529 ± 22	553 ± 25	553	*2.62*	N.D.	***2.70***	2.70
M 14.02	42.5383	81.2658	537 ± 21	N.D.	N.D.	*1.87*	*2.66*	***2.70***	2.70
M 14.06	42.5442	81.2522	N.D.	535 ± 30	535	N.D.	N.D.	N.A.	N.D.
M 14.10	42.5497	81.2522	N.D.	180 ± 35	180	N.D.	N.D.	N.A.	N.D.
FTS 3-6			N.D.	N.D.	N.D.	N.D.	2.31	N.A.	2.31
FTS 8-4			N.D.	N.D.	N.D.	N.D.	2.45	N.A.	2.45
Average			***530 ± 7***	***539 ± 13***	***3***	***2.33***	***2.57***		***2.50***

Note: The error for pressure estimates is of +-0.2 for all samples, considering intrumental and fitting errors

*N.D. = not determined; †N.A. = not applicable

B2. Pressure-temperature estimates from literature based on various methods

TABLE B2. P-T DATA FROM LITERATURE AND METHOD USED TO CONSTRAIN P & T

Literature	T	P	Method for P-T estimates		
	(°C)	*(GPa)*	* CGTP	Other	Pseudosection model /
Gao & Klemd, 2000	480-580	1.4-2.1	EG, H80	ased on mineral assemblage	
Klemd et al., 2002	490-570	1.8-2.1	W96, WM		
Wei et al., 2003	540-550	1.6		TC_std_HP98	THERMOCALC / std
	560	1.5-1.7			
	580	1.5-1.9			
John et al., 2008	530-560	1.9	EG, P85		
VanDerStraaten, 20	575-635	1.85-2.05	EG, P85		Perple_X / std
	625-655				
Lü et al., 2008	570-630	2.7-3.3	T, P85, WM		
Wei et al., 2009	550-570	3.2			HERMOCALC / MnK-st
	550	2.25			
	540-550	2.2-2.3			
Lu et al., 2009	420-520	2.7	R00		
	470-510	2.4-2.7			† Domino⁄Theriak / std
Beinlich et al., 2010	480-540	1.95-2.25			Perple_X / TiK-std
Klemd et al., 2011	500-580	1.6-2.0	R00, W96		
	540-600	2.0-2.4			
Lü et al., 2012 b	540–580	2.7		§ Zr in Rtl, presence of coesite	
Li et al., 2013	590	2.3			Perple_X / MnK-std
Tian-Wei., 2013	526–540	2.9–3.0			HERMOCALC / MnK-st
	518	2.82			
	590	2.4-2.7			
	540	2.2			
Yang et al., 2013	565	2.9			THERMOCALC / MnK-st
Du et al., 2014	460–590	2.4–2.7			THERMOCALC / MnK-st
Meyer et al., 2016	540-550	1.9-2.25		# RSCM and Average P-T (THERMOCALC)	
	555-575	2.2-2.5			
Soldner et al., 2016	425-500	2.5-2.6			Perple_X / MnK-std
Tan et al., 2017	490-530	2.93-2.97		verage P-T (THERMOCALC	THERMOCALC
	520-560	2.43-2.47			

** CGTP = conventionnal geothermo-barometry, abbreviations for the different methods: EG : Ellis & Green, 1979 ;*

All pseudosection calculationS with Perple_X (Connolly, 1990) and THERMOCALC were made with the database

§ Zr in Rtl = Zr in rutile thermometry, using the equation of Tomkins et al. (2007)

 # RSCM = Raman spectrscopy on carbonaceous material thermometry

† Domino⁄Theriak = Pseudosection calculated with Domino⁄Theriak (de Capitani & Brown, 1987), using the database of Berman (1988)

B3. Diagram of the pressure-temperature estimates from this study and literature

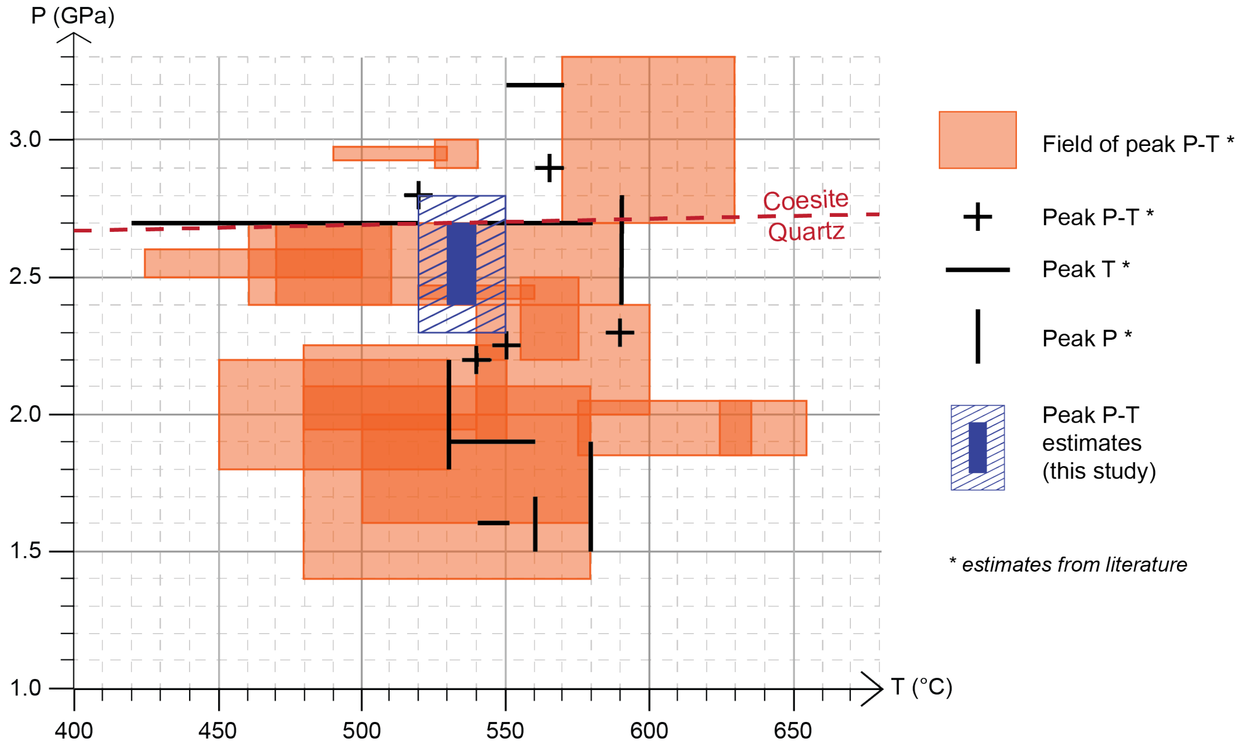

Appendix B3: Compilation of P-T estimates from the literature (Table DR2) and from this study. Note the very scattered P-T estimates results from previous studies.

B4. Map of the maximum Si (pfu) of phengite for this study

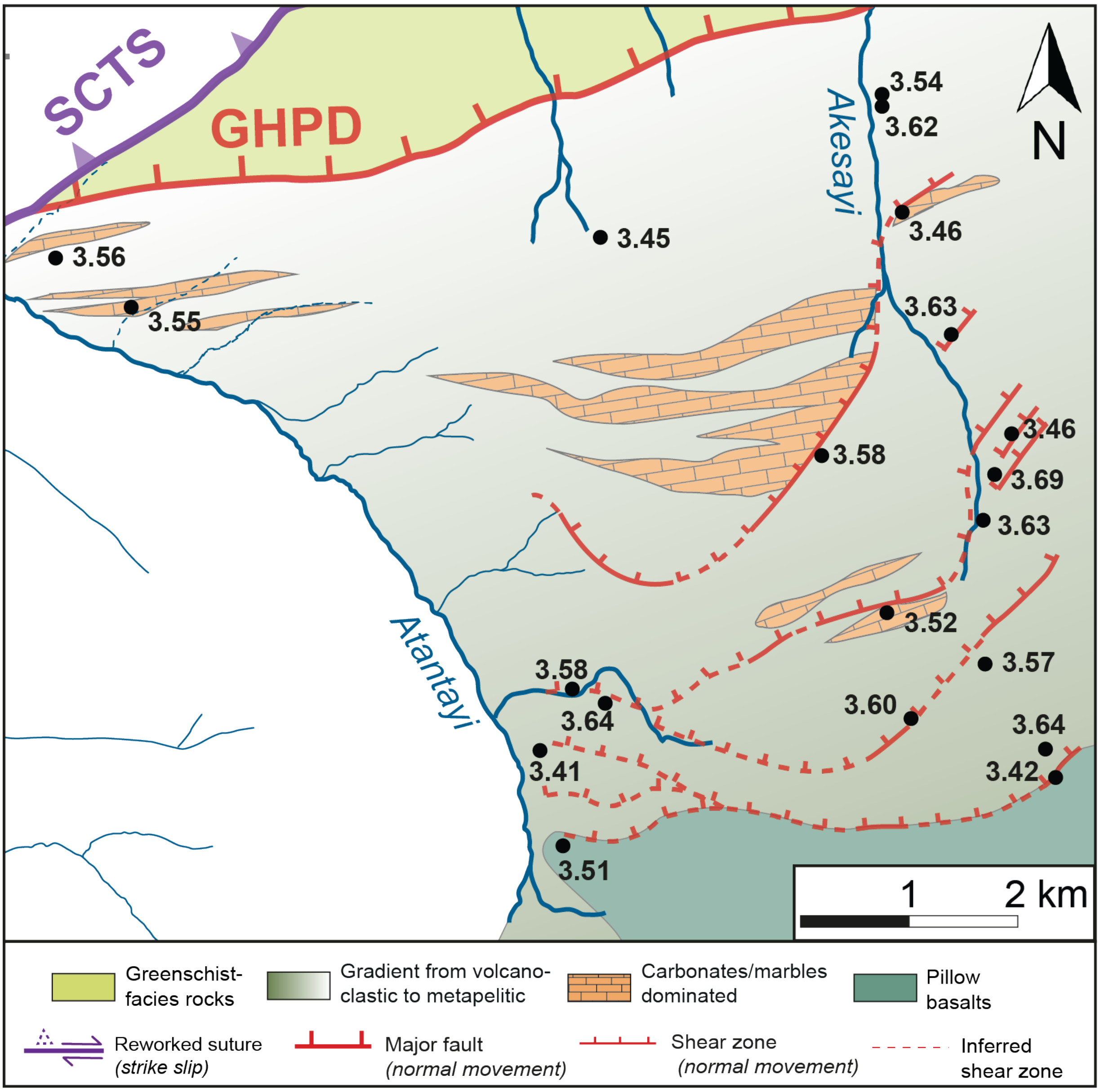

Appendix B4: Map of the AMC on which maximum Si per formula unit (pfu) are reported (black circles), ranging from 3.41 to 3.69, with 3.55 ± 0.08 in average.

Appendix B5: (a) to (d): Typical mineral assemblage observed for eclogite in the AMC. (a) microscopy picture. (b) SEM image with mineral present indicated in the figure and zooms (red squares) of (c) and (d). (c) Element composition maps of clinopyroxene matrix in textural equilibrium with phengite. (d) Element composition maps of an epidote presenting a zoning with an allanitic core. (e) to (g) Garnet growth microscopy picture (top left), SEM image (bottom left) illustrating the Mn, Mg, Ca and Fe compositional maps zoning. (e) Typical gradual prograde zoning. (f) Polycyclic zoning in two distinct phases of growth. (g) Polycyclic zoning presenting a Mn rim. (h) Prograde zoning with two distinct phases of garnet growth. Abbreviations: Ph: pehngite; Cpx: clinopyroxene; Qz: quartz; Pg: paragnoite; Ep: epidote; Gln: glaucophane.

B5. Typical eclogite mineral assemblage and garnet zoning of rocks in the AMC

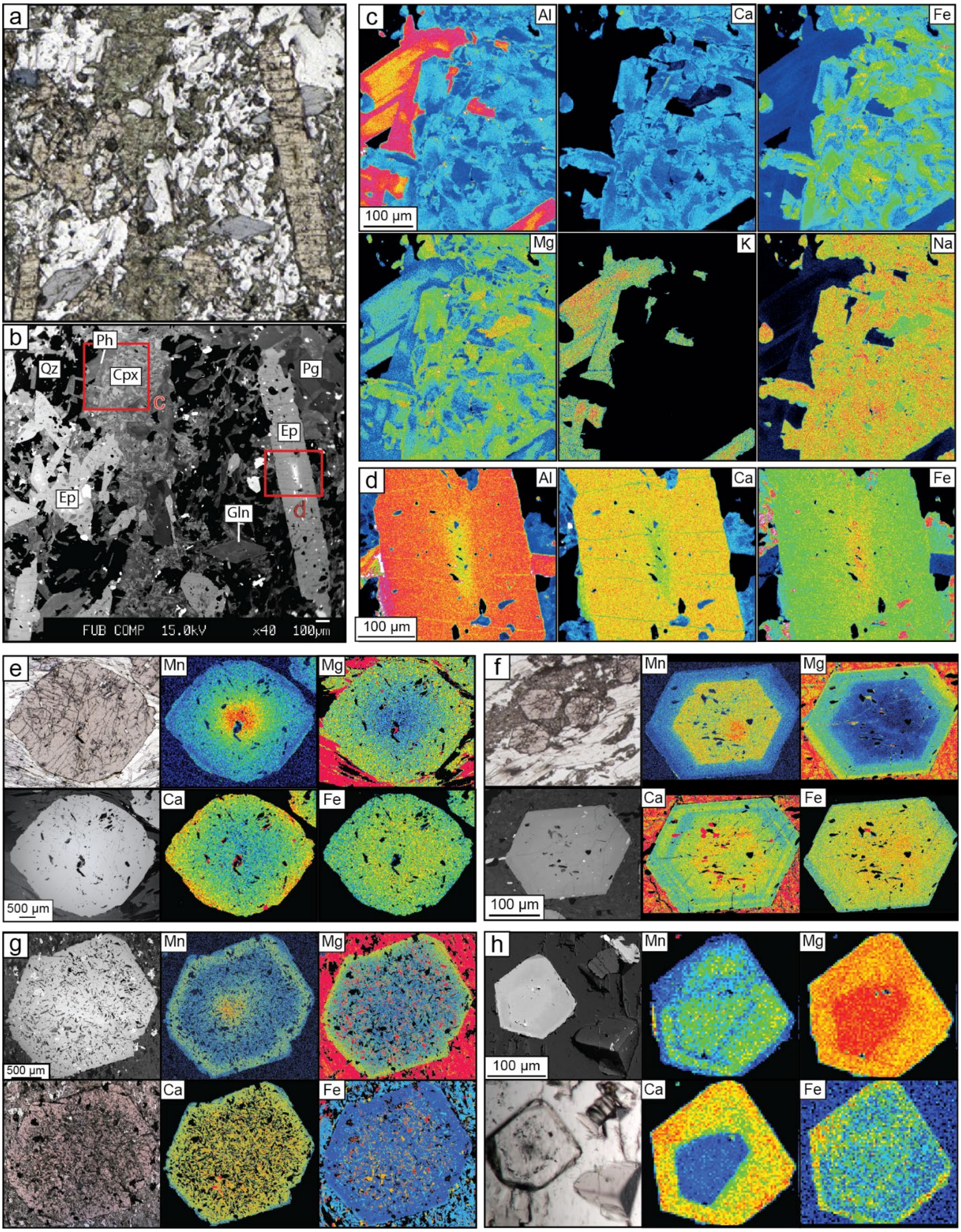

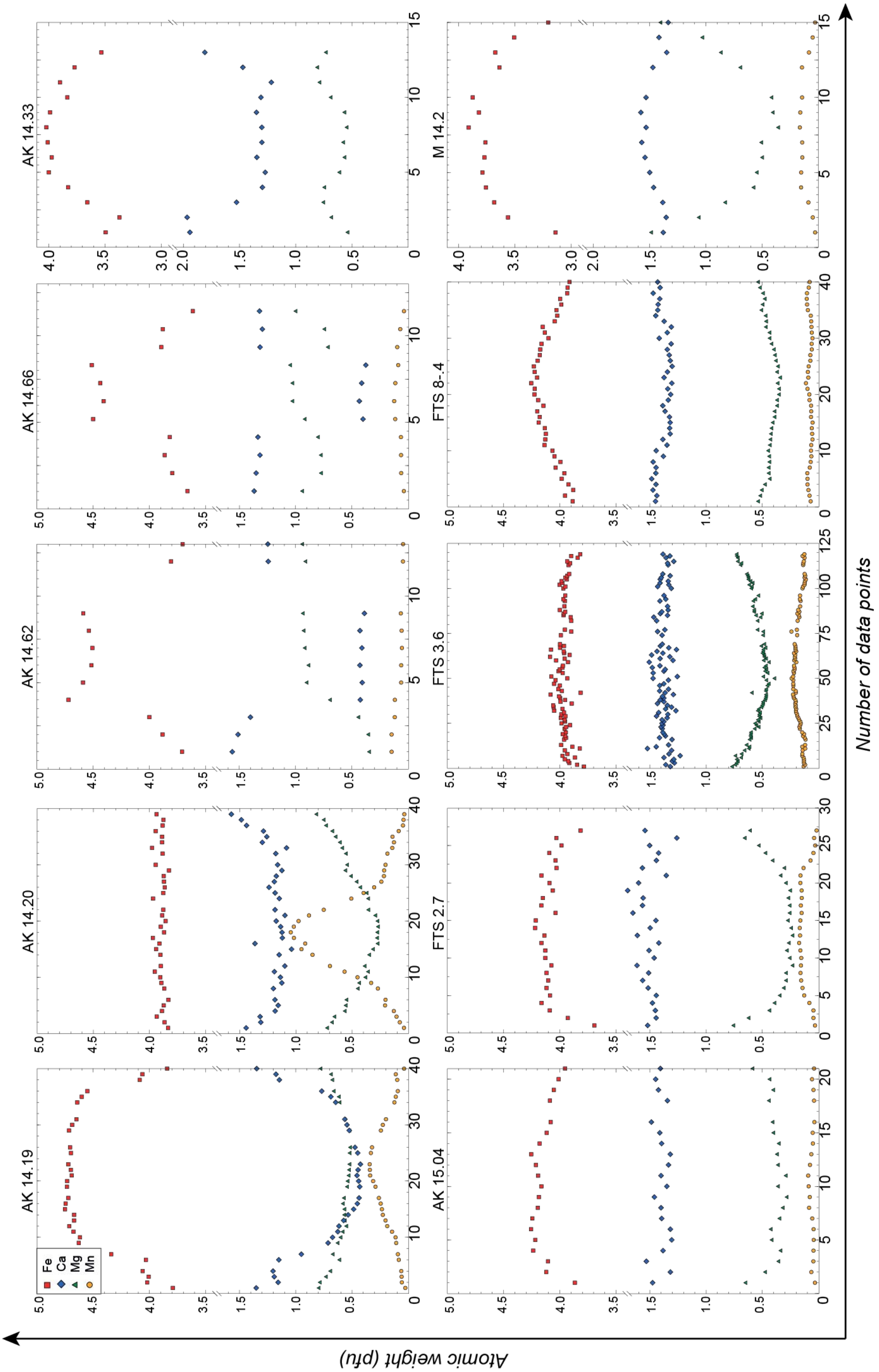

B6. Garnet profiles of Fe, Ca, Mg and Mn composition from core to rim

Appendix B6: Garnet composition profiles from rim to rim of Fe, Ca, Mg and Mn. Most samples present a typical prograde profile, with Fe and Mn rich-cores decreasing towards rim and increasing Mg and Ca towards rim. Samples AK 14.62 and 14.66 depict a step in composition, interpreted as nnew growth phase. Samples AK 14.33 and AK 15.04 illustrate a polycyclic zoning.

Appendix C: Dating supplementary material

C1. Table of dating from literature

C2. Fe+Mg (pfu) versus Si (pfu) of phengite for each sample used for Rb-Sr dating

C3. Table all mineral separates

C4. Isochrons regressed from all mineral separates

C1. Age estimates from literature and this study based on various methods

Table C1. Age estimates from literature and this study

Literature	**Number on Fig. 6.1**	**Age (Ma)**	+- (2σ)	**sample name**	**Radiometric method**
Klemd et al., Chicago Journals, 2005	1	**314.2**	2.3	GC 8-2	**Rb-Sr** on Ep-Gln-Wm
		315.8	3.2	GC 9-1	**Rb-Sr** on Ph-WR
		325.7	11.5	GC 10-1	**K-Ar** on Pg
		311.7	9.7	GC 3-2	**K-Ar** on Pg + Ph
		309.1	8.6	GC 8-5	
		327.1	9.1	GC 5-1	**K-Ar** on Ph
		323.9	7.4	GC 8-2	
		324.2	7.2	GC 9-1	
		311.3	0.9	GC 5-1	**40Ar/39Ar** on Phg + Pg
		311.6	0.9	GC 8-2	
		311.2	5	GC 9-1	
Zhang et al., LITHOS, 2007	2	**310**	6	841	**U-Pb Zrc, SHRIMP**
Su et al., EJM, 2010	3	**319.5**	2.9	071-6a	**U-Pb Zrc, SIMS - Zrc rim**
		318.7	3.3	071-8a	**U-Pb Zrc, SIMS - Zrc rim**
Klemd et al., EPSL, 2011	4	**315.8**	2.9	FTS9-2	**Lu-Hf** on 4Gt-1Omp-1WR
		313.9	4.8	FTS9-4	**Lu-Hf** on 3Gt-1Omp-1WR
		313	12	FTS9-3	**Lu-Hf** Gt on 2Gt-lOmp-1WR
Li et al., Lithos, 2011	5	**320.5**	14	Z53	**U-Pb Rtl, SIMS**
		320	10	07TU3	**U-Pb Rtl, SIMS**
John et al., LITHOS, 2012	6	**322**	5	JTS series	**Rb-Sr** on WR transect from blueschist to eclogite
Yang et al., JAES, 2013	7	**320.4**	3.7	K931	**U-Pb Zrc, SHRIMP**
Liu et al., Lithos, 2014	8	**321.4**	2.4	10LX5-5	**U-Pb Zrc, SIMS** - Zrc rim
Soldner et al., Gond.Res., 2017	9	**326**	2.9	TS1309b	**Lu-Hf** on 3Gt+1Gln+1WR
		318.4	3.9		**Sm-Nd** on 3Gt+1Gln+1WR
Tian-Wei, JMG, 2013	10	**318**	2.3	11AT06	**U-Pb Zrc, SIMS** - Zrc core
		316.8	0.8	11AT06	**U-Pb Zrc, SIMS** - Zrc core
		312.1	2.5	11AT06-2	**Sm-Nd** on 2Gt-2Omp-WR
This stuy	11	**315.9**	1.8	AK 14.6	**Rb-Sr** on 4Wm-1Ap
		321.1	1.7	AK 14.47	**Rb-Sr** on 3Wm-1Amp-1Ap
		321	1.9	AK 14.67	**Rb-Sr** on 3Wm-1Omp
		322.7	1.9	AT 14.1	**Rb-Sr** on 3Wm-1Ap
		310	2.5	AT 14.42	**Rb-Sr** on 2Wm-1Omp

Mineral abbreviations: Ep: epidote; Gln: glaucophane; Ph: phengite; Pg: paragonite; Zrc: zircon; Gt: garnet; WR: whole rock; Wm: white mica; Ap: apatite; Amp: amphibole; Omp: omphacite

Note that the numbers correspond to numbers for ages in Fig. 6.1

C2. Fe+Mg (pfu) versus Si (pfu) of phengite for each sample used for Rb-Sr dating

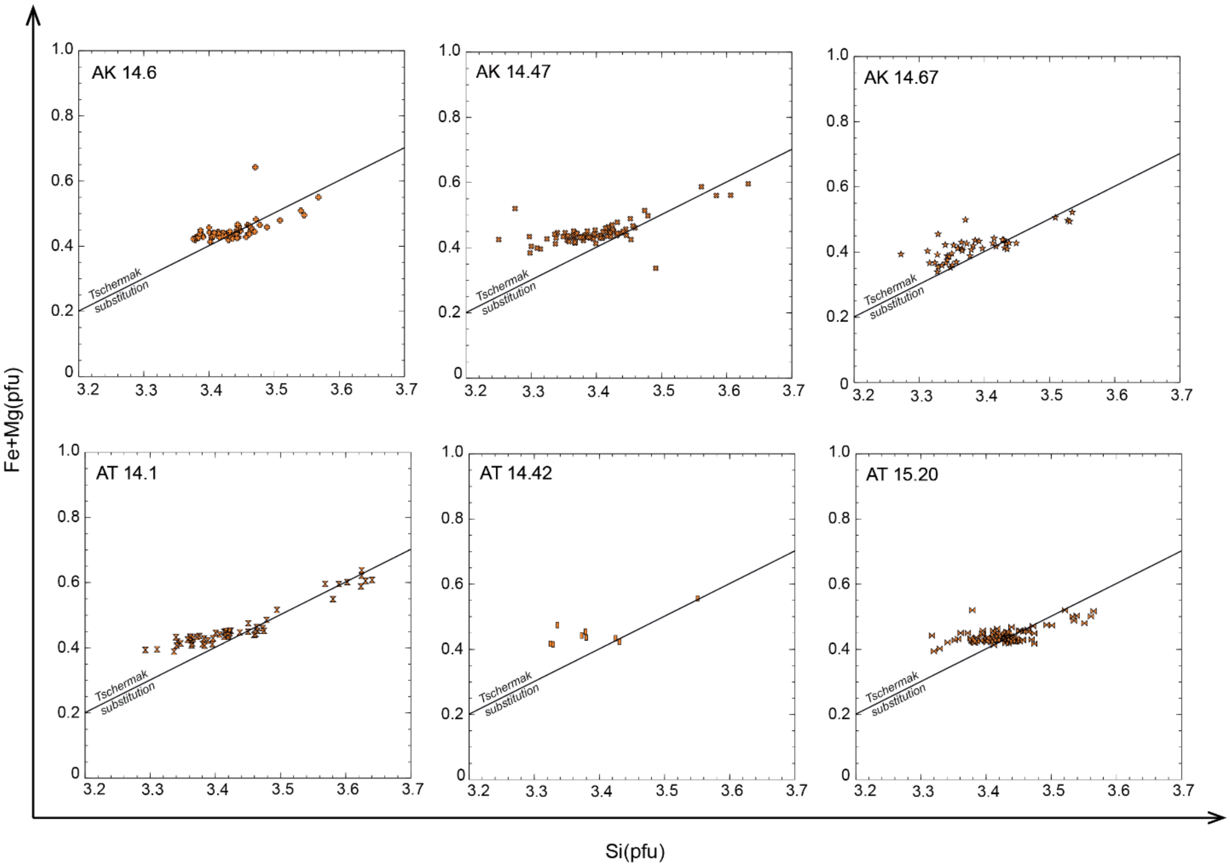

Appendix C2: Diagrams of Fe+Mg per formula unit (pfu) versus Si (pfu) of phengite in the different samples analyzed for Rb-Sr dating, with the tchsermak substitution line reported on each diagram (black line).

C3. Table all mineral separates

Table C3. Rb-Sr Isotope Data for Rocks from the Western Tianshan

Sample Mineral -fraction	Analysis number	Rb *(ppm)*	Sr *(ppm)*	^{87}Rb/^{86}Sr	^{87}Sr/^{86}Sr *(± 2σ)*	Ages *(Ma ± 2σ)*
AK 14.6-1						
Wm <115 µm	2276	45.2	811.2	0.161418	0.712962 (9)	314.0 ± 5.7
Wm 115-250 µm	2277	361.5	140.7	7.460666	0.745139 (10)	
Wm 100-280 µm	2230	267.9	378.7	2.050149	0.721572 (16)	
Wm 250-500 µm	2278	410.8	131.6	9.071209	0.752331 (11)	
Wm 280-500 µm	2231	322.8	293.0	3.194369	0.726809 (4)	
Wm >500 µm (1)	2233	349.0	157.9	6.418122	0.740160 (221)	
Wm >500 µm (2)	2279	384.4	149.6	7.463018	0.745384 (13)	
Ap 100-280 µm	2258	9.5	2357.9	0.011600	0.712290 (11)	
Amp 100-280 µm	2257	34.1	22.5	4.393600	0.731166 (8)	
AK 14.47-1						
Wm 100-280 µm	2234	316.1	220.1	4.164987	0.731738 (11)	321.1 ± 1.7
Wm 280-500 µm	2235	316.5	210.8	4.355155	0.732649 (7)	
Wm >500 µm	2236	347.5	150.0	6.728512	0.743141 (9)	
Ap 100-500 µm	2260	1.1	1971.5	0.001600	0.712996 (36)	
Amp 100-280 µm	2243	23.9	42.8	1.619959	0.720246 (13)	
AK 14.67-3						
Wm 100-280 µm	2237	195.7	82.1	6.924690	0.738965 (36)	321.0 ± 1.9
Wm 280-500 µm	2238	204.1	64.7	9.168297	0.749138 (11)	
Wm >500 µm	2239	177.7	152.4	3.379840	0.723208 (12)	
Omp 100-280 µm	2244	5.5	135.0	0.118071	0.708480 (4)	
AT 14.1-3						
Wm 40-280 µm	2256	201.6	82.7	7.075583	0.738471 (12)	321.4 ± 4.7
Wm 100-280 µm	2223-2224	189.8	96.6	5.701735	0.732869 (11)	
Wm 280-500 µm	2225	174.7	149.7	3.382655	0.722311 (8)	
Wm >500 µm	2226	193.2	122.3	4.582193	0.727582 (12)	
Ap 0-280 µm	2258	2.0	2485.3	0.002300	0.707009 (24)	
AT 14.42-11						
Wm 40-250 µm	2255	145.0	62.5	6.733406	0.736372 (9)	310 ± 16
Wm 100-280 µm	2227	160.7	92.0	5.064723	0.728278 (12)	
Wm 280-500 µm	2228	105.0	164.7	1.846378	0.714995 (12)	
Wm >500 µm	2229	22.9	330.0	0.201060	0.707436 (20)	
Omp 100-280 µm	2242	1.5	27.5	0.153514	0.707695 (23)	
AT 15.20-b						
Wm 70-140 µm	2270-71	100.7	69.0	4.235254	0,733329 (16)	316 ± 38
Wm 115-280 µm	2272	284.3	82.0	10.080637	0,761339 (8)	
Wm 250-500 µm	2273	271.7	81.2	9.732531	0,760465 (10)	
Wm >500 µm	2274	375.4	80.5	13.581951	0,777912 (12)	
Ap 140-280 µm	2280	1.7	1615.5	0.003000	0,718793 (24)	

Based on repeated measurements, the 87Rb/86Sr ratios were assigned an uncertainty of 1%. In the course of this study, repeated runs of NBS standard 987 gave an average 87Sr/86Sr ratio of 0.710278 ± 0.000024 (± 2σ, n= 35). Total procedural blanks were less than 0.1 ng for Rb and 0.24 ng for Sr. Wm: white mica; Ap: apatite; Amp: amphibole; Omp: omphacite.

C4. Isochrons regressed from all mineral separates

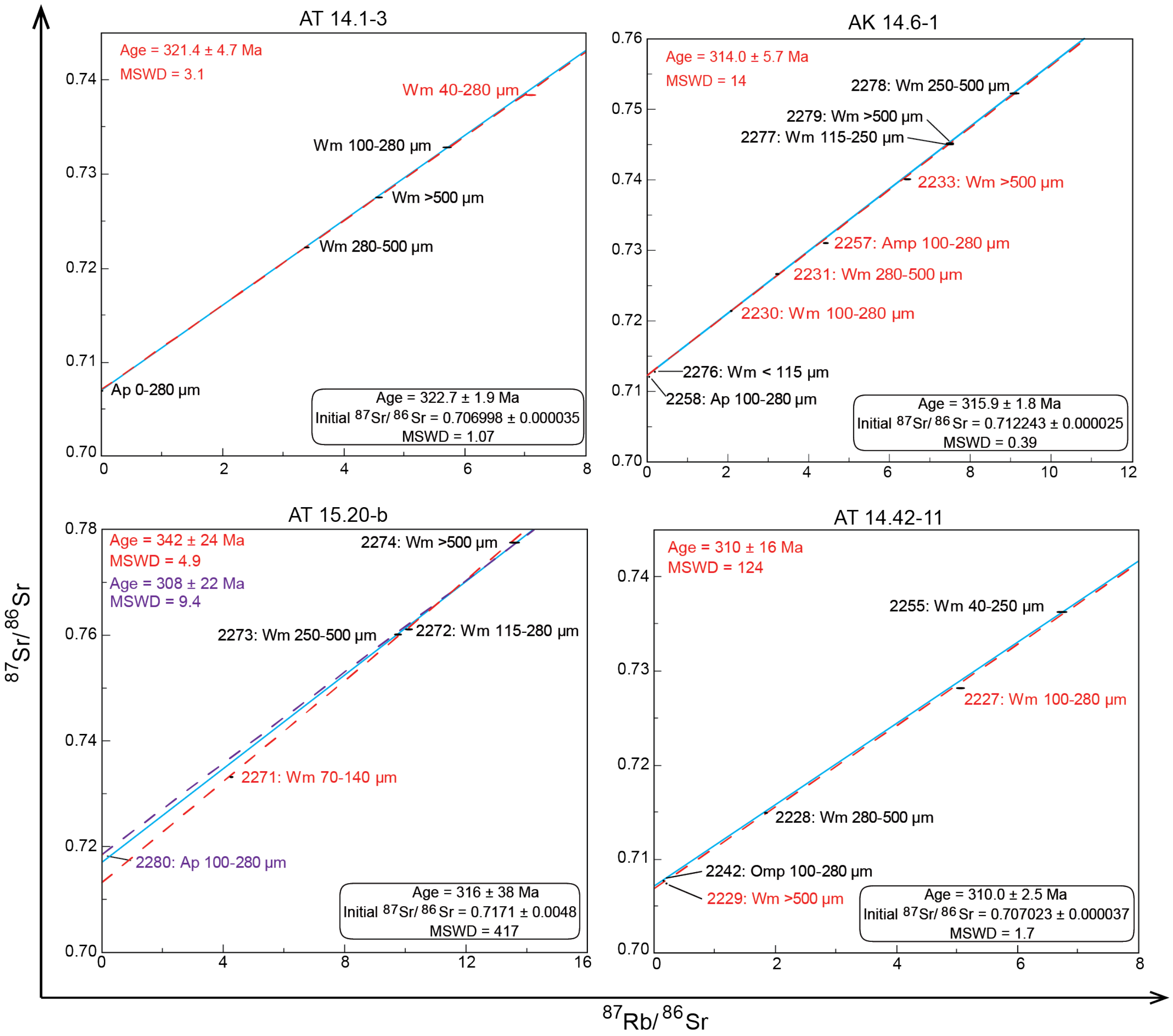

Appendix C4: Supplementary isochron regression calculation for samples AT 14.1-3, AK 14.6-1, AT 15.20-b and AT 14.42-11. The blue line represent the isochron regression used for chapter 6 of this study. Age calculation regression using all mineral fractions is illustrated by a red dashed line and correspond age calculation (red) for samples AT 14.1-3, AK 14.6-1 and AT 14.42-11. Sample AT 15.20-b regression calculations taking into account the white mica fraction 70-140 µm (red dashed line) or apatite fraction (purple dashed line) result in errorchrons with scattered age results in red and purple, respectively. Abbreviations: Wm: white mica; Ap: apatite; Amp: amphibole; Omp: omphacite.

See text of section 6.7 for details.